Advancing Magnetic Resonance Imaging for the in vivo Detection of Iron in Neurodegeneration

Michaelides, Christos Ioannou

Awarding institution:
King's College London

Advancing Magnetic Resonance Imaging for the *in vivo* Detection of Iron in Neurodegeneration

Christos Michaelides

Submitted for the degree of Doctor of Philosophy in

Neuroimaging

Institute of Psychiatry, Psychology and Neuroscience

King's College London

Supervised by:

Dr Po-Wah So and Dr David Lythgoe

June 2015

Abstract

With an increasingly ageing population, the prevalence of neurodegenerative diseases (NDDs) is set to rise. Diagnosis is still currently limited to clinical assessment and treatment options remain ineffective. Iron is thought to play a role in the progression of NDDs due to increased levels being discovered in the brain regions most affected by the specific disorders and exacerbating the loss of neurons, likely through oxidative stress mechanisms. Therefore, this research investigates magnetic resonance imaging (MRI) relaxometry methods to non-invasively and accurately, detect and quantify iron during neurodegeneration and to understand the role of iron-induced toxicity for neuronal death. This work is the first to link iron assessment using MRI in an *in vitro* model with *ex vivo* post-mortem tissue and *in vivo* assessment of iron, as well as providing further validation of inconclusive and conflicting studies evaluating differences in iron content in neurodegenerative disease pathology.

The accuracy of iron content measured using MRI relaxometry was assessed using a variety of model systems; ranging from the use of agarose standards, post-mortem human brain samples, and an *in vivo* animal model of iron-toxicity. Agarose standards containing different concentrations of iron demonstrated that iron linearly correlated to R1, R2 and R2*. This was the case for both ferrous and ferric iron forms, however ferric iron had a greater effect than ferrous iron. Human post-mortem brain tissue from the medial temporal gyrus (MTG) was then taken from control and Alzheimer's disease (AD) subjects and assessed by MRI relaxometry. The MTG is one of the brain regions affected in AD and contains both white (WM)

and grey matter (GM). Iron content was determined using synchrotron radiation X-ray fluorescence (SR-XRF) elemental mapping, a quantitative measure of iron content rather than using Perl's stain, a qualitative method of iron localisation. R2* correlation to iron content was strongest in both control and AD tissue, and was more sensitive within GM than in WM. Subsequent myelin assessment of brain samples using luxol fast blue demonstrated the effect of myelin content on iron-relaxometry correlations. Myelin was detectably lower in AD WM than control WM tissue, and contributed to an improved correlation of iron content to R2* measurements in AD samples. Finally, validation of iron content correlation to MRI relaxometry measurement was performed *in vivo* using a novel animal model by direct injection of ferric citrate into the mouse hippocampus. R2* and R2' provided the best method for detection of injected iron *ex vivo*, however no changes were observed *in vivo* after 10 days recovery due to conflicting signals from iron content and oedema. Greater levels of neuronal cell death and neuroinflammation were associated with the presence of iron in the brain, confirming the contribution of iron to toxicity.

Overall, this work improves our understanding of the relationship of iron to relaxometry measurement and the impact of myelin on such measurements. The work also confirms that the presence of high amounts of iron in the brain can lead to both neuronal cell death and neuroinflammation.

Acknowledgements

First and foremost, I'd like to extend a huge thanks to my supervisor, Dr Po-Wah So, for taking me on as part of her lab team, and for her indispensable help and advice throughout my PhD project. Additional thanks to Dr David Lythgoe and to Dr Amy Herlihy for their assistance and support in this work, and for reviewing the many pages of my thesis.

Thanks also to my parents for their tireless faith and encouragement motivating me throughout my studies. To Hristina, thank you for your loving support through the toughest times over the past few months, and for putting up with my strange working hours, during the PhD.

I'd like to acknowledge everyone at the James Black Centre for providing such a warm and stimulating environment during my studies, with a special mention to Jackie for her inspirational enthusiasm, helping me through PhD life over our very many Viet café lunches. A final thanks to all other family, friends and colleagues for providing me with encouragement, advice and support over the course of my PhD.

Accepted Abstracts Associated with Thesis

1. Michaelides C, Lythgoe DJ, Parkes HG, Troakes C, Bodi I, Geraki T, Herlihy AH & So PW (2015) Improved correlation of iron to R2 and R2* in Alzheimer's disease affected white matter. *ISMRM 23rd Annual Meeting;* p2228.
2. Michaelides C, Lythgoe DJ, Parkes HG, Troakes C, Bodi I, Geraki T, Herlihy AH & So PW (2014) MRI Relaxometry correlation against iron in Alzheimer's Disease. *Joint Annual Meeting ISMRM-ESMRMB*; p1933.
3. Michaelides C, Lythgoe DJ, Parkes HG, Troakes C, Bodi I, Geraki T, Herlihy AH & So PW (2013) MRI Relaxometry correlation to iron levels using synchrotron radiation X-ray fluorescence mapping in Alzheimer's Disease. *Magnetic Resonance Materials in Physics, Biology and Medicine*, 26(1):301. DOI: 10.1007/s10334-013-0383-6
4. Michaelides C, Lythgoe DJ, Parkes HG, Troakes C, Bodi I, Geraki T, Herlihy AH & So PW (2013) Evaluation of iron levels in Alzheimer's Disease using MRI relaxometry. *American Journal of Hematology*, 88(5):E162-3, DOI: 10.1002/ajh.23453
5. Michaelides C, Lythgoe DJ, Parkes HG, Troakes C, Bodi I, Geraki T, Herlihy AH & So PW (2013) Evaluation of iron levels in Alzheimer's Disease Medial Temporal Gyrus using MRI relaxometry. *Annual Meeting Alzheimer's Research UK*.

Published abstracts can be found in Appendix A.

Declaration of Contributors

Collaborations and assistance contributing to this work are detailed below:

Assessment of human Medial Temporal Gyrus (MTG) using MR relaxometry and SR-XRF elemental iron mapping

Synchrotron radiation X-ray fluorescence elemental mapping was performed in collaboration with Dr Tina Geraki at Diamond Light Source, who also performed much of the element quantification across the multiple visits to this synchrotron.

Human brain tissue samples were paraffin-embedded and underwent luxol fast blue staining at the MRC London Neurodegenerative Diseases Brain Bank, by Dr Claire Troakes, Dr Istvan Bodi and Mr Matthew Nolan.

MR detection of exogenous iron in the mouse hippocampus

Thanks to Fabio Vigil for his help and training to perform the animal surgeries.

Synchrotron radiation X-ray fluorescence elemental mapping was performed in collaboration with Dr Rolf Simon at the Karlsruhe Institute Technology (KIT) synchrotron in Germany.

Immunohistochemical and histological validation and assessment was performed in collaboration with Dr Antigoni Ekonomou, Miss Achvini Sriskanthanathan and Miss Semhar Abraha.

Microscope slide scanning of both human and mouse tissue sections were performed by Dr Matthew Ellis at University College London.

Abbreviations

4-HHE	4-hydroxyhexenal
4-HNE	4-hydroxynonenal
6-OHDA	6-hydroxydopamine
α-$_2$M	α-2-microgobulin
AAS	Atomic Absorption Spectroscopy
Aβ	β-amyloid protein
$A\beta_{1-42}$	Amyloidogenic form of the β-amyloid protein
AD	Alzheimer's disease
ADAM10	A Disintegrin and metalloproteinase domain-containing protein 10
ADAS	Alzheimer's Disease Assessment Scale
Al^{3+}	Aluminium ion
ALS	Amyotrophic Lateral Sclerosis
APH-1	Anterior pharynx-defective 1
APP	Amyloid precursor protein
ATP	Adenosine Triphosphate
B_0	External magnetic field
B_1	Radiofrequency pulse

BBB	Blood-brain barrier
BACE1	Beta-site APP-cleaving enzyme 1
CDR	Clinical Dementia Rating
CERAD	Consortium to Establish a Registry for Alzheimer's disease
CFH	Compliment Factor H
CJD	Creutzfeldt-Jakob disease
CP	Ceruloplasmin
CSF	Cerebrospinal fluid
Cu^{2+}	Copper ion
DAB	3,3-Diaminobenzidine
DG	Dentate gyrus
dGM	distal grey matter
DMT1	Divalent Metal Transporter 1
DNA	Deoxyribonucleic acid
EGCG	Epigallocatechin-3-gallate
ETL	Echo train length
FDG-PET	Fluorodeoxyglucose Positron Emission Tomography
FDRI	Field Dependent R2 Increase

Fe	Iron
Fe^{2+}	Ferrous iron ion
Fe^{3+}	Ferric iron ion
FOV	Field of view
FPN1	Ferroportin
GE	Gradient-Echo
GM	Grey matter
H-ferritin	Ferritin heavy chain
dH_2O	distilled water
HCl	Hydrochloric acid
HD	Huntington's disease
HFE	Haemochromatosis
HO-1	Haem Oxygenase 1
Iba-1	Ionized calcium binding adaptor molecule 1
ICP-MS	Inductively-coupled plasma mass spectroscopy
ID	Inner Diameter
IMS	Industrial Methylated Spirit
i.p	intra-peritoneal

IRE	Iron Responsive Element
IRP	Iron Regulatory Protein
KIT	Karlsruhe Institute Technology
LFB	Luxol fast blue
L-ferritin	Ferritin light chain
LA-ICP-MS	Laser-ablation inductively-coupled plasma mass spectroscopy
LAMMA	Laser microprobe mass analysis
LIP	Labile iron pool
LF	Lactoferrin
MAPT	Microtubule-associated protein tau
MBP	Myelin Basic Protein
MCI	Mild cognitive impairement
MCL	Mid-cortical layer
ME	Multi-echo
MFC	Magnetic Field Correlation
MGE	Multi gradient-echo
MMSE	Mini-Mental State Examination
MPTP	1-methyl-4-phenyl-1,2,3,6-tetrahydropyridine

MoCA	Montreal Cognitive Assessment
Mol. Rel.	Molar Relaxivity
MRI	Magnetic Resonance Imaging
mRNA	messenger ribonucleic acid
MS	Multiple Sclerosis
MW	Molecular Weight
M_z	Net magnetization vector
NaZ	Sodium Azide
NDD	Neurodegenerative disease
NFT	Neurofibrillary tangles
PBS	Phosphate Buffered Saline
PD	Parkinson's disease
PEDM	Proton Exchange Dephasing Model
PEN-2	Presenilin enhancer 2
PET	Positron Emission Tomography
PFA	Paraformaldehyde
PHF	Paired Helical Filaments
PiB	Pittsburgh compound B

PIL	Procedure Individual License
PIXE	Particle induced X-ray emission
PMI/ PMD	Post Mortem Interval/ Post Mortem Delay
PPL	Procedure Project License
ppm	parts per million
PS-1/ 2	Presenilin 1/ 2
QSM	Quantitative susceptibility mapping
r_1, r_2, r_2*, r_2'	Molar relaxivity using R1, R2, R2* or R2', respectively
RF	Radiofrequency
ROI	Region of interest
ROS	Reactive oxygen species
SD	Standard deviation
SE	Spin-Echo
SMP	Skimmed Milk Powder
SNR	Signal to Noise Ratio
SOD	Superoxide Dismutase
SR-XRF	Synchrotron radiation X-ray fluorescence
SWI	Susceptibility weighted imaging

T	Tesla
T1/ R1	Longitudinal relaxation time/ rate
T2/ R2	Intrinsic transverse relaxation time/ rate
T2*/ R2*	Transverse relaxation time/ rate including inhomogeneities
T2'/ R2'	Transverse relaxation time/ rate of inhomogeneities
TBARS	Thiobarbituric acid-reactive substances
TBS	Tris buffer saline
TE	Echo Time
TF	Transferrin
TfR	Transferrin receptor
TICS-M	Modified Telephone Interview for Cognitive Status
TR	Repetition Time
UTR	Untranslated region
WHO	World Health Organisation
WM	White matter
XANES	X-ray Absorption Near Edge Spectroscopy
Zn^{2+}	Zinc ion

Contents

Table of Figures

Table of Tables

1. Introduction

1.1. Overview

The World Health Organisation (WHO) recently reported that 36.5 million people worldwide currently have dementia, the most common manifestation of neurodegeneration (WHO, 2012). With globally ageing populations, especially in developing countries (Alzheimer's Disease International, 2013), neurodegenerative diseases represent a growing health and economic challenge, with approximately 7.7 million new cases each year (WHO, 2012). It is expected that the number of patients with dementia will double to 65.7 million by 2030 and triple to 115.4 million by 2050 (WHO, 2012). In the UK, over 800,000 people have been diagnosed with dementia and by 2051, this figure is set to exceed 2 million patients (Alzheimer's Society, 2014a).

Not only are there huge numbers of patients and families that will be affected by the debilitating features of dementia and neurodegenerative diseases, but huge economic burdens are placed on countries to deal with dementia sufferers, with economic impact at £26.3 billion annually in the UK alone (Alzheimer's Society, 2014a). This is equivalent to approximately £30,000 annually per patient, with only one third of these costs coming from the government (Alzheimer's Society, 2014a). The total cost of care for neurodegenerative diseases globally in 2010 was around $604 billion (Alzheimer's Disease International, 2010).

Furthermore, these diseases have huge emotional and financial effects on the family members and caregivers of those with dementia, as they have limited

support to help provide sufferers with continued good quality of life (Alzheimer's Society, 2014b).

No therapeutics currently exist that have been demonstrated to either prevent or cure neurodegenerative disorders, which include certain forms of dementia, let alone to recover lost capabilities (Alzheimer's Association, 2014). Treatment strategies currently in place are predominantly aimed towards alleviating symptoms (see section 1.2.6). More concerning, is the lack of understanding of the precise cellular and molecular causes of neuronal cell death that occur in neurodegenerative diseases. In part, this limited understanding of disease progression, has led to inaccurate assessments and biomarkers for the diagnosis of patients with dementia, such as Alzheimer's disease (AD), with pre-symptomatic diagnosis of patients still not currently possible. Moreover, with patients only being diagnosed towards the end stages of disease, with greater levels of neurodegeneration, the window for successful therapeutic intervention is substantially reduced. As such, there is a pressing need to identify and stratify at-risk individuals earlier during disease progression, prior to the memory impairments characteristic of disease, as well as gaining a greater understanding of the precise molecular changes occurring in order to develop effective therapeutics.

My own interests lie in gaining both an understanding of the causative roles of neurodegeneration across multiple disorders and in the validation of methods for detecting and predicting their appearances within the population earlier during disease progression. Assessment of potential causative changes between normal and neurodegenerative disease patients may lead to the identification of certain

characteristics that may not only play roles in the underlying pathology, but may be directly measureable as an early diagnostic biomarker.

The basis of this thesis therefore revolves around the hypotheses that there is a consistent, causative change in multiple neurodegenerative diseases due to metal ion dyshomeostasis, such as iron, in the brain. A role for iron during neurodegenerative diseases has been hypothesised since the 1950s when it was discovered that non-haem iron content increases in the brain during the normal ageing process. An increase in iron is found in the cortex, globus pallidus, putamen and substantia nigra up to approximately 40 years of age, at which point, the levels plateau (Hallgren and Sourander, 1958). Whilst there is a plateau in iron content during normal ageing, it was identified that this non-haem iron content was further increased in certain cell types within regions of the cortex of Alzheimer's disease patients (Goodman, 1953, Hallgren and Sourander, 1960). Since then, it has also been demonstrated that increased iron content can be detected in the substantia nigra of Parkinson's disease (PD) patients above that of healthy controls (Dexter *et al.*, 1987, Dexter *et al.*, 1989, Hirsch *et al.*, 1991). Subsequently, studies of other neurodegenerative diseases have shown changes in iron content related to pathology. These diseases include Multiple Sclerosis (MS) (Craelius *et al.*, 1982, Adams, 1988, LeVine, 1997), Huntington's Disease (HD) (Dexter *et al.*, 1991, Bartzokis *et al.*, 2007b, Chen *et al.*, 2013), as well as Amyotrophic Lateral Sclerosis (ALS) (Kasarskis *et al.*, 1995). Given that the localisation of iron content changes in the brain seems to be regionally and pathologically relevant to each of the specific

diseases, iron, along with other trace metals have been hypothesised to play causative roles during neurodegeneration.

With the non-invasive assessment of iron being possible using magnetic resonance imaging (MRI) methods, this thesis specifically focusses on the possibility for the quantitative detection of iron using MRI for potential clinical diagnosis during AD. Furthermore, the role of iron during neurodegeneration is also evaluated within the work of this thesis.

1.2. Alzheimer's Disease

1.2.1. AD pathology

Alzheimer's disease (AD), first described in 1907 by Alois Alzheimer (Alzheimer, 1907), involves the gradual loss of neurons throughout the brain, especially within the cortical and hippocampal regions. This loss of neurons causes a gradual decline in cognitive functioning, leading to semantic and spatial memory loss (Hodges and Patterson, 1995, de Toledo-Morrell *et al.*, 2000), as well as mood and anxiety alterations (Chen *et al.*, 2000).

AD progression can be broadly characterised into three stages (WHO, 2012). In the first and earliest stage, patients become forgetful of things that have just happened, can get lost in familiar places and can show mood changes with lower motivation and activity levels (WHO, 2006). This is largely due to pathology affecting neurons in hippocampus (Hyman *et al.*, 1984, Ball *et al.*, 1985), amygdala

(Emre *et al.*, 1993) and in the entorhinal cortex (Van Hoesen *et al.*, 1991). In the middle stage of disease, pathology becomes clearer to identify, with patients becoming very forgetful of recent events and names, and becoming lost at home or in familiar places (WHO, 2006). Some speech and language difficulties can occur, signifying greater atrophy of the medial temporal lobe (Smith *et al.*, 1986, Krasuski *et al.*, 1998), which is involved in semantic and language functions. Furthermore, continued degeneration of the hippocampus, amygdala and entorhinal cortex occurs. The final stage requires full time care of patients, with almost complete loss of awareness and aggressive mood changes (WHO, 2006).

A prodromal stage between normal ageing and Alzheimer's disease has recently been conceptualised identifying patients with Mild Cognitive Impairment (MCI), where patients exhibit a greater degree of memory loss than in normal ageing, but not yet to the point for clinical diagnosis of dementia (Petersen, 2004, Gauthier *et al.*, 2006, Petersen *et al.*, 2009). MCI has been described as a precursor stage towards AD, due to the high propensity of patients that progress from MCI to AD later in life (Bozoki *et al.*, 2001). However, conversion to AD will not occur in all patients or within the same timeframes (Morris *et al.*, 2001). Furthermore, similar pathological hallmarks are found in post mortem tissue of MCI patients as with AD, with increased β-amyloid and tau protein deposits compared with control patients (see section 1.2.2), and cognition correlating to neurofibrillary tangle (NFT) burden (Guillozet *et al.*, 2003). However, this is still to a lesser extent than AD itself (Petersen *et al.*, 2006).

Whilst there are limitations in understanding the causative processes and time scales for MCI conversion to AD, ultimately, this period represents an important interval to treat patients with novel therapeutic strategies or to evaluate novel biomarkers for assessment of the conversion into AD, given that MCI may be the earliest identifiable indicator of dementia.

Whilst the brain regions showing greatest atrophy during AD progression have been elucidated, (as described above) along with a growing understanding of some of the molecular processes that occur during pathology; namely that of the two major hallmarks of AD, β-amyloid plaques and tau neurofibrillary tangles, (see section 1.2.2.1 and 1.2.2.2), the fundamental cause of neuronal cell death in AD, or any other neurodegenerative disease, has yet to be elucidated. There are two main hypotheses for the cause of neurodegeneration in AD, focussed on accumulation of β-amyloid and tau neurofibrillary tangles (see section 1.2.2), and the relatively recent hypothesis focussed on metal dysregulation (see section 1.2.3). These hypotheses however, are mechanistically not exclusive, and demonstrate considerable overlap.

1.2.2. Protein accumulation

Many of the most common neurodegenerative diseases involve accumulation of protein aggregates either intra- or extra-cellularly, as the major hallmarks of pathology on post-mortem examination of brain tissue (see review by Ross (Ross and Poirier, 2004)). In AD, extracellular senile plaques and intracellular

neurofibrillary tangles (NFT) are detected, comprised of β-amyloid and tau proteins respectively (see review by Selkoe (Selkoe, 2004)). Similarly, Parkinson's disease patients display α-synuclein aggregates (Baba *et al.*, 1998, Spillantini *et al.*, 1998), Huntington's disease patients display Huntingtin aggregates (Scherzinger *et al.*, 1997) and Creutzfeldt-Jakob disease (CJD) patients develop prion protein aggregates (Prusiner *et al.*, 1998). Whilst the causes behind these protein aggregations are yet to be fully understood, all have been implicated with enhanced neuronal cell death.

1.2.2.1. β-amyloid plaques

β-amyloid plaques are one of the primary hallmarks of AD pathology. The protein itself, as well as the regulatory processes surrounding its expression, has been the predominant focus of research efforts to date. The aggregation product is formed from a strong, insoluble β-sheet structure, comprised of accumulated oligomers from the amyloid precursor protein (APP) cleavage products. Whilst the specific function of APP remains elusive, the processing steps involved in the formation of the β-amyloid product have been well defined (see review by O'Brien (O'Brien and Wong, 2011)).

The APP protein is a single transmembrane protein that is trafficked onto the extracellular membrane of neurons from the Golgi apparatus. Here, the APP protein can be variably cleaved, first by either α- or β-secretase, and then by γ-secretase (Figure 1-1) (Cole and Vassar, 2008). APP cleavage by the β-secretase BACE1 (Beta-

site APP-cleaving enzyme 1), allows for the formation of the amyloidogenic form of the β-amyloid (Aβ) protein comprised in plaques, $A\beta_{1-42}$ (Figure 1-1B). A secreted product of the APP protein is also released as part of BACE1 cleavage, termed APPsβ (Vassar, 2004). The γ-secretase, comprised of the four essential subunits, presenilin 1 or 2 (PS-1, PS-2), nicastrin, APH-1 and PEN-2, normally produces predominantly non-amyloidogenic Aβ form of $A\beta_{1-40}$, however cleavage of the slightly longer $A\beta_{1-42}$ leads to the form predominantly found accumulated in AD plaques (Thinakaran and Koo, 2008).

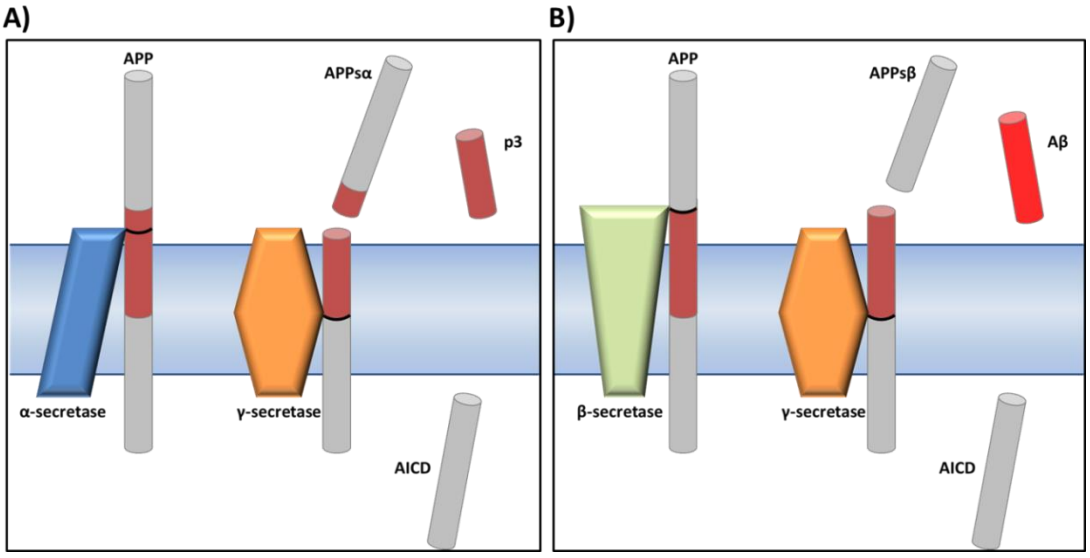

Figure 1-1 Amyloid processing pathways

Different cleavage products can be formed through alternative APP processing. (A) Formation of APPsα and p3 via initial α-secretase cleavage of APP, whilst (B) APPsβ and Aβ are formed following β-secretase (BACE1) cleavage of APP. Adapted from (Thinakaran and Koo, 2008).

Genetic mutations within the APP gene (Citron *et al.*, 1992, Mullan *et al.*, 1992, Nilsberth *et al.*, 2001), as well as in proteins responsible for the variable cleavage of APP (e.g. in PS-1 and PS-2 (Scheuner *et al.*, 1996, Hardy, 1997, Cruts and Van Broeckhoven, 1998) result in the familial inheritance of AD due to increased prevalence of the disease in families with these mutations.

It has recently been identified that the soluble oligomers of Aβ can exert neurotoxic effects by activating a number of cell surface receptors, increasing the permeability of the cell membrane, or blocking correct cellular functions (see review by Kayed, and by Klein (Kayed and Lasagna-Reeves, 2013, Klein, 2013)). Each of these mechanisms is able to disrupt cellular signalling pathways and ions, induce hyperphosphorylation of tau protein in sites relevant for aggregation (De Felice *et al.*, 2008), lead to mitochondrial dysfunction and activate apoptotic pathways (Kayed and Lasagna-Reeves, 2013). The formation of plaques has therefore, been suggested to be a protective measure to isolate these soluble Aβ oligomers together, to prevent toxicity and neuronal cell death (Treusch *et al.*, 2009).

1.2.2.2. Tau neurofibrillary tangles

Neurofibrillary tangles (NFT) are the second hallmark protein aggregations found during AD pathology and are comprised of the tau protein (Serrano-Pozo *et al.*, 2011). The function of the tau protein has been specified as a microtubule associated protein involved in the assembly of tubulin monomers into microtubules in neuronal axons (Cleveland *et al.*, 1977). Tau is transcribed from the MAPT

(microtubule-associated protein tau) gene and has a number of alternative splicing constructs (Buee *et al.*, 2000). Furthermore, the tau protein has a large number of phosphorylation sites predominantly on serine and threonine residues, controlling the activity of its microtubule assembling capabilities. Greater phosphorylation of tau leads to decreased microtubule formation (Beharry *et al.*, 2014). During AD pathology, tau becomes hyperphosphorylated, causing aggregation and the formation of paired helical filaments, which make up pre-tangles (Alonso *et al.*, 2001). Whether these insoluble paired helical filaments and tangles, or soluble oligomers of hyperphosphorylated tau, are the cause of neurotoxicity is also in debate, with many studies currently suggesting protective roles for the insoluble accumulations (Kopeikina *et al.*, 2012). Toxicity due to tau misregulation has been indicated through disrupted organelle and cellular material transport, e.g. mitochondria, therefore causing incorrect localisation, decline in cell function, synaptic loss and ultimately cell death (Mandelkow *et al.*, 2003, Reddy, 2011). Furthermore, tau has been identified as a downstream component to β-amyloid induced cell death (Rapoport *et al.*, 2002, Chong *et al.*, 2006).

1.2.3. Metal hypothesis of neurodegeneration

Another mechanism that has been highlighted as potentially playing a role during neurodegeneration in AD is through metal ion dysregulation. Metal ions implicated in neurodegeneration range from those that are present ordinarily at trace levels, holding toxic potential at increased concentrations such as lead or aluminium, to

those which are found as part of normal metabolic and cellular processes, such as zinc, copper and iron (Adlard and Bush, 2006).

From studies investigating trace metal ions, lowering of cognitive performance in both children and adults has been correlated to lead accumulation in the blood and in bone samples (Lanphear *et al.*, 2005, Weisskopf *et al.*, 2007). Similarly, aluminium has been linked to AD (see review by Gupta (Gupta *et al.*, 2005)) both through observations of greater cognitive decline or dementia risk with high aluminium intake (Rondeau *et al.*, 2009) and also through the observation that injected aluminium salts leads to NFT aggregation (Klatzo *et al.*, 1965) as well as the presence of aluminium in both NFT and Aβ plaques in AD (Tokutake *et al.*, 1995). Whilst studies on trace metals do seem to show correlation against cognitive decline and greater dementia risks, their applicability to all AD cases is still limited and requires further evaluation.

Biologically active metals however, such as iron, copper and zinc have been implicated in neurodegeneration and cognitive decline in both human patients and in animal models of disease (Zecca *et al.*, 2004, Rivera-Mancia *et al.*, 2010). Furthermore, it has been identified that all three of these metal ions are accumulated with amyloid plaque cores, therefore highlighting their involvement during AD (Lovell *et al.*, 1998). The role of iron and copper is based on their enhancement of reactive oxygen species (ROS) production and resultant oxidative stress (see section 1.2.3.1), while zinc tends to be related to antioxidant processes. Iron content has been suggested to be increased in certain brain areas relevant for AD pathology using chemical methods (see section 1.4.1.1) as well as MRI based

approaches (see section 1.6.5). Elevated iron contents are linked directly to increased production of ROS (Smith *et al.*, 1997, Sayre *et al.*, 2000) (see section 1.4.3.1), which has ultimately been implicated as a cause of cell and neuronal death. Furthermore, iron content has also been directly linked to amyloid processing (see section 1.4.3). Copper ion content has also been suggested to be altered in AD patients compared with controls (see review by Pal (Pal *et al.*, 2015)), (Brewer, 2012), with copper ions undergoing the same chemical processes as iron to increase ROS levels to drive neuronal death (see section 1.2.3.1). Zinc involvement in AD is complicated given that there is no consensus on whether there is an increased or decreased concentration observed in comparison to controls (see review by Watt (Watt *et al.*, 2010)). Zinc has been predominantly implicated in AD based on its involvement on amyloid processing, accumulation and degradation (Watt *et al.*, 2010), with zinc being a cofactor for β-amyloid degrading enzymes (Leissring, 2008). Alternatively, changes in zinc translocation through transporters have been highlighted to play a role in cognitive decline and neuronal death (Lyubartseva and Lovell, 2012, Bush, 2013).

1.2.3.1. Reactive Oxygen Species mechanisms

Reactive Oxygen Species (ROS) are normally formed as part of oxidative phosphorylation, a critical process in cellular respiration and therefore for functioning of all cells (Bonda *et al.*, 2011). They include a number of different species, all of which have a free unpaired electron, making them highly reactive compounds. The predominant ROS produced during oxidative phosphorylation is

the superoxide anion radical ($O_2^{\bullet -}$) within the mitochondria, the site of cellular respiration (Jomova *et al.*, 2010). Cells ordinarily have very tight control over the levels of ROS, given the highly reactive nature of free radicals. SODs act to reduce levels of superoxide anion radical by catalysing conversion to the more stable product, hydrogen peroxide (H_2O_2) and then to water by glutathione peroxidases and catalases. However, in the presence of increased ferrous iron or cuprous copper (Cu^+) within the cell, hydrogen peroxide can undergo the Fenton reaction (Figure 1-2), forming the hydroxyl free radical ($OH^{\bullet}$) (Jomova and Valko, 2011).

$$H_2O_2 + Fe^{2+} \longrightarrow Fe^{3+} + OH^- + OH^{\bullet} \quad (1)$$

$$O_2^{\bullet -} + Fe^{3+} \longrightarrow Fe^{2+} + O_2 \quad (2)$$

Figure 1-2 Fenton and Haber-Weiss reaction

(1) The Fenton reaction involves the conversion of hydrogen peroxide to produce the hydroxyl free radical under high levels of ferrous iron. (2) The superoxide anion can react with ferric iron producing the ferrous iron and oxygen in the Haber-Weiss reaction.

This ROS is highly reactive causing lipid peroxidation, protein degradation and DNA damage. Lipid peroxidation occurs when the hydroxyl free radical is able to initiate and propagate the breakdown of lipids into further toxic products, such as 4-hydroxynonenal (4-HNE) or 4-hydroxyhexenal (4-HHE) (Markesbery and Lovell, 1998, Catala, 2009). Other evidence of lipid peroxidation assayed has been shown to be an increase in malondialdeyde and thiobarbituric acid-reactive substances

(TBARS). Protein damage can occur through ROS reactions with both the amino acid polypeptide chain and with the side chains (Pratico, 2008). ROS action on DNA can cause DNA-DNA or DNA-protein cross linkages, DNA strand breaks and oxidation of the base pairs (Lovell and Markesbery, 2007).

Cell death from increased ROS and oxidative stress mechanisms has also been suggested to occur through excitotoxic mechanisms, due to loss of mitochondria membrane potential and ultimately apoptosis (Markesbery, 1997). Treatment of neuronal cells with hydrogen peroxide led to an increase in ROS production and eventually cell death by apoptosis, which could be limited using Coenzyme Q10 to maintain the mitochondria membrane potential (Somayajulu *et al.*, 2005). Furthermore, mitochondria extracted from AD subjects that were subsequently transformed into control cells, demonstrated defects and reduced activity in Complex IV of the electron transport chain and increased basal intracellular calcium concentration (Sheehan *et al.*, 1997).

1.2.4. Evidence of ROS production in AD

Evidence for oxidative stress in the pathology of AD has long been demonstrated in many studies. Increased lipid peroxidation products such as TBARS have been found in regions specific for AD, such as the hippocampus, cortex and amygdala (Subbarao *et al.*, 1990, Lovell *et al.*, 1995). Furthermore, enzymes involved in the reduction of ROS, including glutathione peroxidase and reductase and catalase showed elevated expressed in the hippocampus of AD patients (Lovell *et al.*, 1995). Additionally,

evidence suggests that lipid peroxidation may occur prior to onset of AD, given the identification of lipid peroxidation products, malondialdehyde and TBARS in MCI and early AD patients' superior and medial temporal gyri (Keller *et al.*, 2005). Preclinical AD patients also showed increased 4-HNE and acrolein lipid peroxidation products in the hippocampus compared with controls (Bradley *et al.*, 2010).

Evidence of protein oxidation products has been demonstrated in the hippocampus of AD patients (Hensley *et al.*, 1995, Butterfield *et al.*, 2007) compared with control, whilst the cerebellum showed no change. More recently, changes in protein oxidation between MCI and control samples have been identified, highlighting this as a potential early occurrence in cognitive decline and AD (Butterfield *et al.*, 2006). Furthermore, direct injection of $A\beta_{1\text{-}42}$ into the rat brain induced the generation of protein oxidation products (Boyd-Kimball *et al.*, 2005).

DNA mutations can be detected in both nuclear and in mitochondrial DNA in AD cortical samples through the detection of oxidised base products (Mecocci *et al.*, 1994, Gabbita *et al.*, 1998). Similarly, MCI subjects were also found to contain elevated oxidised base pairs in various cortical regions, again highlighting that oxidative stress may be occurring in the earliest points of cognitive decline and AD (Wang *et al.*, 2006). DNA fragmentation was identified at greater levels in AD hippocampal tissue and this was colocalised to increased expression of pro-apoptotic protein, Bax, highlighting potential causes towards neuronal cell death (Su *et al.*, 1997).

1.2.5. Clinical diagnosis and biomarkers of AD

The sensitivity and specificity of a diagnostic test needs to be considered prior to its adoption into the clinic. The sensitivity of a test is its ability to correctly detect AD in a given population, i.e. will it detect all individuals with AD, and is measured by assessment of the number of positive cases detected compared with the number of patients in total with AD. The specificity of a test is its ability to detect only patients with AD as opposed to normal subjects, and is measured by assessment of the number of negative cases detected compared with the total number of patients without AD. Clinical tests can be compared using these measurements to evaluate which provides the best diagnostic capabilities.

Current methods for diagnosis of AD remain predominantly based on memory and cognitive function assessment (McKhann *et al.*, 1984). Numerous cognitive tests exist to understand the scope of dementia in patients. The predominant test routinely used is the Mini-Mental State Exam (MMSE) (Folstein *et al.*, 1975), which was developed to be a short assessment of the cognitive functions of psychiatric patients. This test however, was eventually shown to hold limited differentiation between MCI patients and normal subjects (Mitchell, 2009) and has therefore allowed for the development of other cognitive tests. The Alzheimer's Disease Assessment Scale (ADAS) (Rosen *et al.*, 1984), was developed to be used in AD clinical trials. The Montreal Cognitive Assessment (MoCA) (Nasreddine *et al.*, 2005) was later developed as a means to better distinguish MCI patients from normal subjects. Other tests in use include the Clinical Dementia Rating (CDR) (Morris, 1993) and cognitive tests have even been developed for application over the

telephone, such as the modified Telephone Interview for Cognitive Status (TICS-M) (Brandt *et al.*, 1988, Welsh *et al.*, 1993), which was also able to identify patients with MCI (Cook *et al.*, 2009).

Whilst these tests are able to somewhat stratify between patients with MCI and AD, as well as to distinguish between these and normal subjects with relatively high accuracy, all the tests are non-quantitative and subject to bias. Furthermore, as the decline in cognitive function only manifests towards the end stages of disease (Figure 1-3), therapeutic intervention has been thought to only hold limited efficacy for patients, due to the significantly decreased population of neuronal cells remaining (Sperling *et al.*, 2011).

Definitive diagnosis of AD can only be performed post-mortem, by assessing the presence of amyloid plaques and NFT in different brain areas. Categorisation using systems such as the CERAD system, or using Braak staging allow for confirmed diagnosis of AD; at CERAD stage C and Braak stages V-VI (Braak and Braak, 1991, Alafuzoff *et al.*, 2008).

Given that memory assessments are non-quantitative, late stage and hold low specificity, alternative approaches have been evaluated for quantification of AD biomarkers, including the use of imaging modalities, such as MRI or PET (see section 1.2.5.1), or by examining protein levels in either CSF or blood (see section 1.2.5.2). With elevated iron content though to play a role in AD (see section 1.4), the possibility for the early detection of brain iron content using MRI is currently being evaluated (see section 1.6.5).

A model for AD or dementia onset was proposed to highlight how novel biomarkers may be utilised to identify "at risk" individuals earlier (Figure 1-3), or to identify patients that have increased likelihood for conversion from MCI to AD (Jack *et al.*, 2010). Whilst earlier detection of alternative pathological hallmarks of AD may ultimately require a greater biological and temporal understanding of AD progression, these biomarkers may also provide a basis for the development of better therapeutic strategies against the earliest treatable stages of pathology (Jack *et al.*, 2010). Indeed, if iron, or any other metal ion, is found to hold critical roles for AD pathology prior to $A\beta_{1\text{-}42}$ generation or accumulation, this model may be amended to incorporate earlier biomarkers to incorporate these findings (Figure 1-3). Roles for iron early on during pathology have already been suggested through increased iron staining in post-mortem human tissue from preclinical AD and MCI subjects, and correlation of iron staining levels to declining cognitive memory (Smith *et al.*, 2010).

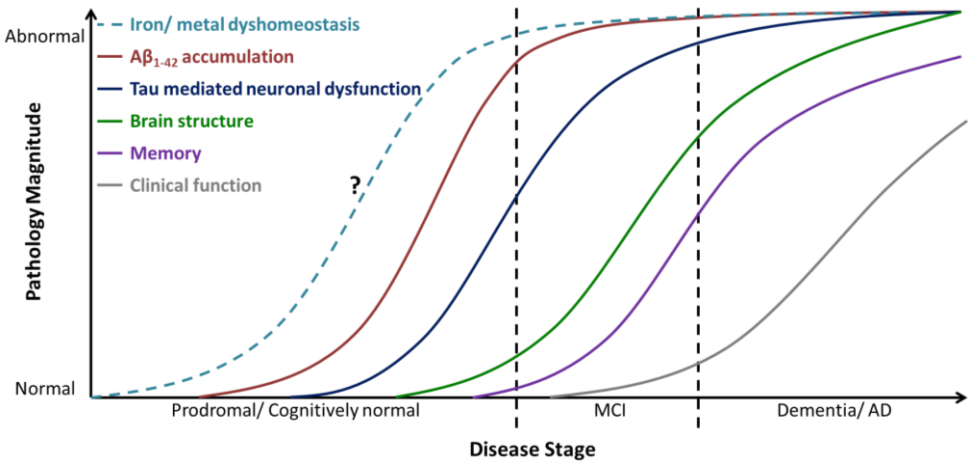

Figure 1-3 Model for AD biomarkers expression cascade

This model has been proposed as a method of detecting different pathological processes throughout AD, prior to the onset of symptomatic memory and cognitive

deficits (adapted from Jack et al., 2010). If greater evidence is found to support iron, or other metal ion, dyshomeostasis prior to Aβ accumulation, the model can be amended to incorporate this expression from an earlier time point.

1.2.5.1. Imaging methods

Many studies have used non-invasive imaging modalities, including positron emission tomography (PET) and MRI, to evaluate and monitor the neurodegenerative damage in AD. Frequently, these parameters are correlated against cognitive tests, and in some cases, against post mortem histological assessment. In general, volume loss has been highlighted as the major correlator to cognitive decline, with cortical and medial temporal systems showing the greatest rate and overall loss, attributed predominantly to synapse loss (Terry *et al.*, 1991).

Computational assessment of brain atrophy has allowed rates between AD and control patients to be detected by MRI (Fox and Freeborough, 1997). Measurement of hippocampal volume atrophy was able to predict conversion of MCI patients to AD (Jack *et al.*, 1999). Furthermore, whole brain atrophy, as well as atrophy in the hippocampus, entorhinal cortex and ventricles was greater in patients that progressed from normal cognition into MCI or AD, than normal subjects during ageing. MCI patients converting to AD also showed greater atrophy in the brain regions highlighted above (Jack *et al.*, 2004). Not only was MRI assessment of atrophy well correlated to cognitive testing scores, it was demonstrated to provide a more robust measurement (Fox *et al.*, 1999, Jack *et al.*, 2004). Evaluation of

atrophy rates in normal ageing individuals can even be detected, with whole-brain, temporal lobe and hippocampal volumes decreasing and ventricular volume increasing with increasing age, especially over 70 years (Scahill *et al.*, 2003).

PET imaging has been used in a small cohort to identify MCI conversion to AD, based on lower fluorodeoxyglucose (FDG) uptake into certain brain areas (Chetelat *et al.*, 2003). Pittsburgh compound B (PiB) has been recently used in PET imaging to highlight amyloid plaques in the brain, alongside MRI based ventricle expansion rate determination (Jack *et al.*, 2009). It was demonstrated that whilst amyloid plaque levels show very poor correlation to cognitive decline, as assessed using the CDR and MMSE, MRI based ventricular expansion assessment correlated strongly, highlighting that the level of neurodegeneration is likely to be the link to cognitive scores, whilst amyloid plaque load is not (Jack *et al.*, 2009).

Given the wide applicability for the use of both MRI and PET imaging systems for non-invasive assessment of AD, larger scale studies have been carried out over longer time courses, to allow for greater understanding of the clinical diagnostic potential of AD and dementia. Recently, hippocampal volume and hippocampal atrophy were shown to predict the conversion of normal aged subjects to AD over a 10 year period (den Heijer *et al.*, 2010). This study demonstrates that changes within the brain may be occurring well in advance of the appearance of clinical symptoms. Furthermore, within the same longitudinal study of patients, hippocampal shape was shown to provide additional predictive capability of subjects converting from normal cognition to dementia, than assessment of hippocampal volume alone over the 10 year period (Achterberg *et al.*, 2013).

1.2.5.2. Other biomarkers

Assessment of $A\beta_{1-42}$ and tau levels from the CSF of AD, MCI and control patients demonstrates that these measures can provide a cut-off for AD detection, as well as being able to predict patients that will convert from MCI to AD (Shaw *et al.*, 2009). Furthermore, similar to Aβ protein contents or plaque load assessed histologically, CSF Aβ did not correlate to hippocampal atrophy, whereas CSF measurement of tau, did correlate (de Souza *et al.*, 2012). However, clinical CSF contents assessed in different centres still remain variable, and whilst $A\beta_{1-42}$ and tau levels could be used to identify AD individuals from control groups, substantial overlap between different dementia types has been observed using this approach, due to overlapping biological phenotypes (Ewers *et al.*, 2015).

The use of blood-based biomarkers has also been evaluated in AD, with Aβ again demonstrating only minimal diagnostic or prognostic potential longitudinally (Rissman *et al.*, 2012). Similarly, tau levels demonstrated substantial overlap between control and AD patients, despite significantly higher concentrations within the AD population (Zetterberg *et al.*, 2013). The use of blood-based biomarkers may be severely hampered by the inherent heterogeneity of patient populations, as well as the numerous potential comorbidities that are associated with aged patients from either disease, or control groups (Henriksen *et al.*, 2014).

More recently however, higher-throughput methods have been employed utilizing proteomics approaches to identify blood-based biomarkers to differentiate between AD and control groups, with the identification of complement factor H (CFH) and α-2-macroglobulin (α-$_2$M) differing between AD and control patients (Hye

et al., 2006). Indeed, panels of blood-based biomarkers are beginning to show reproducibility across multiple cohorts for detection of AD compared to controls (Kiddle *et al.*, 2014).

Metal ion detection has also been employed, with copper serum levels detectably increased in AD patients versus control samples in a small cohort study (Squitti *et al.*, 2002), and additional evidence gleaned in monozygotic twins discordant for AD (Squitti *et al.*, 2004). Additionally, altered miRNA expression patterns have been assessed from the brain and blood to establish a method for diagnosis of AD (Delay *et al.*, 2012, Geekiyanage *et al.*, 2012).

Clearly, it is reasonable to postulate that no single biomarker will be sufficient to diagnose, stratify and evaluate the progression of AD between controls and all other diseases and it therefore seems likely that certain tests used individually, or in combination, will be required to satisfy the necessary requirements for novel biomarkers.

1.2.6. Current AD therapies

As neurodegeneration in AD severely impacts cholinergic systems, current AD treatments, such as Donepezil and Galantamine, have been directed towards enhancement of cholinergic neurotransmission. These function by inhibiting acetylcholinesterases, or modulating acetylcholine receptors to increase the levels of acetylcholine neurotransmitter at synapses (Mangialasche *et al.*, 2010). Whilst

these treatments provide some benefits to patients, they tend to be anti-symptomatic, with limited impact against neurodegeneration observed.

More recently, therapeutics designed to target β-amyloid and tau aggregations have been developed, however none have provided clinical efficacy to reduce or prevent cognitive decline in AD (Mangialasche *et al.*, 2010). Indeed, follow up of patients with $A\beta_{1-42}$ immunisation demonstrated lower levels of β-amyloid plaques post-mortem, however no sign of improved cognition, or changes in mortality rate were detected (Holmes *et al.*, 2008). Many other trials since, have also investigated the clearance of Aβ monomers, oligomers and fibrils from AD patients using immunotherapies, however all have showed similar limited efficacy at reducing the cognitive decline associated with pathology (Panza *et al.*, 2014). Alternative methods for reducing the amyloid burden in AD, including secretase modulators and aggregation inhibitors, and more recently methods to interrupt tau phosphorylation and aggregation have also demonstrated limited efficacy in clinical trials (Mangialasche *et al.*, 2010, Schneider *et al.*, 2014). Therefore, given the considerable failures in clinical trials against AD, it seems clear that a greater understanding of the fundamental causes of neuronal death are required, with better preclinical models of disease to evaluate potential therapies, as well as to identify relevant biomarkers.

1.3. Iron, Uptake, Regulation and Distribution

Iron is a critical element required throughout the body for a variety of key functions. A major role of iron in the body is for oxygen transport within the haemoglobin of erythrocytes, where the iron exists bound to a haem group (Perutz, 1979). Iron ions can also make up the functional elements of essential proteins and enzymes within all cell types, either singly, or as part of iron-sulphur clusters. Examples of iron-containing proteins include: DNA polymerases (Netz *et al.*, 2012), cytochrome P450 enzymes (Meunier *et al.*, 2004) and iron regulatory proteins (IRPs) (Anderson *et al.*, 2012, Lill *et al.*, 2012).

1.3.1. Iron in biological tissues

There are a number of different forms of iron that exist within biological tissues. The two main classes described are haem iron and non-haem iron. Haem iron simply describes iron that is in complex with haem groups, such as those in haemoglobin, whilst non-haem iron describes all the other forms of iron, including low molecular weight complexes, metalloproteins, storage proteins and ionic complexes (Haacke *et al.*, 2005):

1) Low molecular weight complexes include iron associated with citrate, ascorbate and ATP present in cells (Bradbury, 1997, Moos *et al.*, 2007) and is sometimes termed as ‘free’ iron, and forms the labile iron pool (LIP). This form of iron is considered to be at extremely low concentrations, compared with the overall presence of iron in cells (Schenck, 2003).

2) A key metalloprotein that binds iron is the transport protein, transferrin. Transferrin (TF) is a 79kDa protein consisting of two lobes (N- and C- lobe) and functions to transport iron in the body (Gomme and McCann, 2005). Serum TF protein is predominantly synthesised by the liver and without any iron bound, is known as apotransferrin (Beutler *et al.*, 2000). A maximum of two iron atoms in the ferric form can bind to transferrin, one to each lobe (Nunez *et al.*, 2012), Mutations in the transferrin gene give rise to the rare disease, atransferrinemia, causing reduced delivery of iron to the bone marrow and reduced haemoglobin synthesis (Beutler *et al.*, 2000).

3) Ferritin is the predominant storage protein for iron within all cell types and contains most of the iron present in cells. It consists of 24 protein subunits, comprised of heavy (H-) and light (L-) chains arranged into a spherical cage. The 80Å core is capable of holding up to 4500 iron atoms in the ferric form as a crystalline structure, ferrihydrite ($5Fe_2O_3.9H_2O$) (Harrison and Arosio, 1996). The heavy chain is involved in catalysis of ferrous iron to the ferric form, due to a ferroxidase activity, whilst the light chain is predominantly involved in the storage of iron. Ferritins are expressed across most tissue types, including the heart, spleen, pancreas and liver, and are composed of different combinations of the H- and L- ferritins, owing to post-translational regulation (Cairo *et al.*, 1991). The storage of iron in ferritin occurs by ferrous iron transport through ion entry channels of the protein cage, followed by ferroxidase catalysis to bind the growing ferrihydrite cores that are initiated at the nucleation sites inside the protein (Theil, 2011). Iron export from ferritin can also occur, however this process is less understood than the mechanism of iron entry (Theil, 2011). It

has been demonstrated that mutations in the ferritin light chain cause a series of neurodegenerative diseases clinically, known as neuroferritinopathies, which are characterised by iron overload, movement disorders and cognitive decline (Curtis *et al.*, 2001).

4) Hemosiderin is another storage form of iron, however has been suggested to be a degradation product of ferritin (Haacke *et al.*, 2005). It remains unclear as to the true nature of hemosiderin, however it exists as an insoluble form and is more apparent during iron overload pathologies, such as haemochromatosis (Quintana, 2007).
5) Finally, another form of iron that has been established to exist in biological tissues is magnetite, a crystal structure of Fe_3O_4 (Kirschvink *et al.*, 1992). This form of iron was identified in both control and AD brains and has highly ferromagnetic properties.

Critically, it should be noted that not all forms of iron exhibit similar effects on the MRI signal and this has added complexity to the application of MRI for understanding iron content changes in the brain during neurodegenerative diseases (see section 1.6.5).

1.3.2. Normal brain iron uptake

Specific functions within the brain can be attributed to iron-containing enzymes, such as those involved in neurotransmitter synthesis including tyrosine hydroxylase synthesis of dopamine (Daubner *et al.*, 2011), and those involved in myelin

synthesis, including fatty acid hydroxylases (Connor and Menzies, 1996, Alderson *et al.*, 2004, Todorich *et al.*, 2009). As such, oligodendrocytes were found to hold greater levels of transferrin, ferritin and iron than any other cell types in both adult (28-49 years) and aged (60-90 years) brains (Connor *et al.*, 1990). This is likely due to the high metabolic demands for iron required in myelin synthesis and maintenance, as well as the continued cell survival requirements, especially within the white matter regions of the human brain.

As the brain is comprised of numerous cell types and regions, iron content is heavily varied across the brain, likely reflecting the different cellular and physiological functions. Furthermore, as iron can be toxic at high concentrations, (see section 1.4.3.1) iron uptake and regulation into the brain must be tightly regulated.

Whilst iron uptake into systemic tissues including heart and liver, can occur through the direct uptake of iron from blood plasma, uptake into the brain is further complicated due to the presence of the blood brain barrier (BBB), acting to prevent the passage of toxins and unnecessary proteins into the brain (Ward *et al.*, 2014).

Iron initially enters the blood through the duodenum endothelial cells following ingestion (see review by Anderson, and by Rouault (Rouault, 2001, Anderson *et al.*, 2012))Export of ferrous (Fe^{2+}) iron from the duodenal endothelial cells occurs through ferroportin (FPN1), for loading onto transferrin, via the ferroxidase activity of hephaestin (Anderson *et al.*, 2012). Hephaestin oxidises exported ferrous iron to the ferric (Fe^{3+}) form, to load a capacity maximum of two ferric iron atoms per transferrin molecule (Nunez *et al.*, 2012) for transporting iron to tissues with iron demand. Iron-bound TF circulating within the blood serum binds with high affinity

to the Transferrin Receptor (TfR) located on the BBB endothelial cell membrane (Figure 1-4). The TfR is then internalised via a clathrin-mediated mechanism. Acidification of the internalised endosome by a proton pump causes ferric iron release from the TF-TfR complex and following reduction to ferrous iron by a ferric reductase inside the endosome, is transported into the cytoplasm by the divalent metal transporter 1 (DMT1) transporter. Here, ferrous iron is either stored within ferritin or can be transported into the brain interstitial fluid by FPN1.

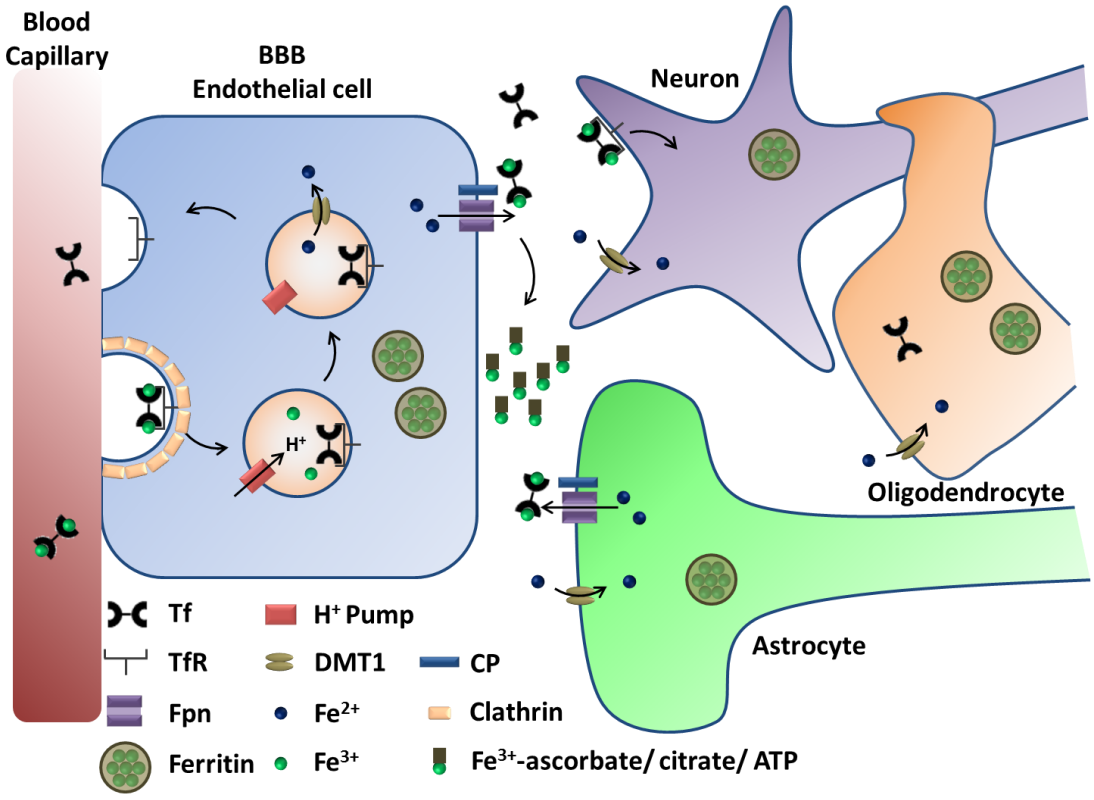

Figure 1-4 Brain iron uptake, transport and storage mechanisms between different cell types

Tf, Transferrin; TfR, Transferrin Receptor; Fpn, Ferroportin; H^+ pump, proton pump; DMT1, divalent metal transporter 1; CP, ceruloplasmin; Fe^{2+}, ferrous iron; Fe^{3+}, ferric iron (adapted from Ward et al., 2014).

Iron exported into the interstitial fluid by FPN1 from the BBB endothelial cells can either be bound to TF, or is found in complex with citrate, ascorbate or ATP (Bradbury, 1997, Moos *et al.*, 2007). From the interstitial fluid, iron can be transported through various mechanisms into neurons, astrocytes, oligodendrocytes and microglial cells.

It has been demonstrated that TF is produced by oligodendrocytes (Connor *et al.*, 1990) and astrocytes, however only neurons express the TfR in the brain to therefore allow uptake of iron via this method. Neuronal uptake of iron can also occur by a non-Tf bound method, via ferrous iron transport through DMT1, given the expression of this protein in neurons (Moos *et al.*, 2007). Iron uptake into neurons is also supported due to the storage of iron provided by ferritin expression (Moos *et al.*, 2007). Ferrous iron is also able to be transported into microglia for storage in ferritin, due to detected expression of DMT1 and ferritin in these cell types similarly to neuronal cells (Urrutia *et al.*, 2013).

Ceruloplasmin (CP) expression is predominantly found in astrocytes, allowing conversion of ferrous iron to the ferric state, and subsequent binding of ferric iron to TF for iron export from cells (Loeffler *et al.*, 2001, Vassiliev *et al.*, 2005). Iron export from other cell types is less well understood however, some studies have also highlighted the expression of FPN1 on neuronal cells (Wu *et al.*, 2004).

1.3.3. Iron regulation of protein expression

Iron content is able to provide direct feedback to cells for careful regulation of the uptake, storage and export of iron (Anderson *et al.*, 2012). It has been demonstrated that cells under low iron content increase expression of the transferrin receptor and lower expression of ferritin, to promote iron uptake and availability within the cell (Figure 1-5) (Theil, 1990, Klausner *et al.*, 1993, Zecca *et al.*, 2004). This occurs through the presence of an iron responsive element (IRE) in the 3'-untranslated region (UTR) of the transferrin receptor mRNA transcript, which is bound by iron response proteins (IRPs) to stabilize the transcript (Casey *et al.*, 1989). An IRE in the 5'-UTR of the ferritin mRNA transcript inhibits expression of this protein due to IRP binding (Theil, 1990). Conversely, under high iron conditions, low IRE binding by IRPs leads to unstable transferrin receptor mRNA (Casey *et al.*, 1989), and a rise in the expression of ferritin, through IRP promotion of translation (Thomson *et al.*, 1999), thus reducing cellular iron (Hentze *et al.*, 2004) (Figure 1-5).

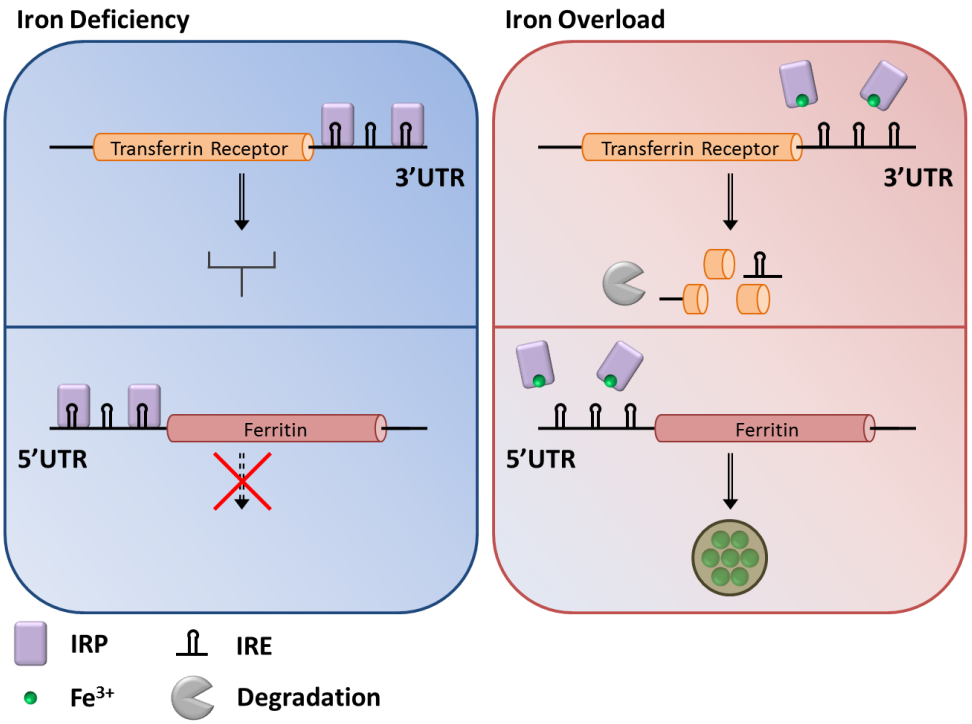

Figure 1-5 Translational regulation by iron

IREs present in the 3'-UTR of transferrin receptor and 5'-UTR of ferritin regulates the translational expression of these mRNA transcripts in dependence with iron content in the cell, based on IRP binding to IREs (adapted from Zecca et al. 2004).

1.4. Iron and AD

1.4.1. Iron regulation in the aged and AD brain

Given the hypothesis of iron involvement in AD, many studies have evaluated iron localisation, as well as the localisation and functioning of iron regulatory proteins (IRPs), such as ferritin and transferrin, between normal ageing (Connor *et al.*, 1990) and AD (Connor *et al.*, 1992b).

1.4.1.1. Iron

A number of brain regions, including the prefrontal, temporal, sensory and motor cortex, as well as the caudate nucleus, the putamen and the globus pallidus have been reported to show high accumulation of iron levels during the first 20-30 years of normal ageing, whilst the medulla oblongata showed no change in iron levels (Hallgren and Sourander, 1958). After 40 years of age, the increase in iron levels plateaus in all brain regions. Although greater levels of stainable iron have been identified histologically in cells within cortical areas from AD samples (Goodman, 1953), global cortical iron levels remained comparable to normal (Hallgren and Sourander, 1960). This implies that a local redistribution of stainable iron may be occurring in AD in areas that demonstrate the greatest level of neuronal loss.

The use of histochemical methods for iron evaluation has demonstrated elevated iron content within the cortex of AD samples, compared with age-matched controls, and was correlated to worsening CDR (Clinical Dementia Rating) scores (Smith *et al.*, 2010). Furthermore, whilst a difference in stainable iron was detected in PD substantia nigra, no changes in stainable iron was detected in AD samples from the hippocampus, frontal cortex, substantia nigra, globus pallidus or putamen (Jellinger *et al.*, 1990). The latter study contained slightly more patients than the prior, perhaps accounting for the discrepancy.

Quantitative evaluation of iron has also been contradictory for iron content changes between control and AD patients (Deibel *et al.*, 1996, Magaki *et al.*, 2007, House *et al.*, 2008, Schrag *et al.*, 2011). Raised iron content was shown in the hippocampus (Deibel *et al.*, 1996), and in the temporal cortex (House *et al.*, 2008),

of AD patients compared with controls, however both studies were performed in small group of patients. Furthermore, whilst an increase in iron was reported within AD patients' frontal cortex and globus pallidus, the results were normalised to protein content, and this protein content was also detectably lower in the frontal cortex (Loeffler *et al.*, 1995). Equally, iron contents have been demonstrated to increase in some regions of AD samples, whilst decreasing in other regions, e.g. in the occipital cortex (Connor *et al.*, 1992b). More recently, assessments for "loosely-bound iron" demonstrated a decrease within hippocampal white matter from AD patients compared with control, whereas the overall iron contents were similar between the groups (Magaki *et al.*, 2007). Similar levels of iron have also been demonstrated by other studies in cortical regions (Religa *et al.*, 2006). Likewise, overall cerebrospinal fluid (CSF) iron levels were similar between control, MCI and AD, however "redox-active" iron was higher in MCI patients compared with controls (Lavados *et al.*, 2008).

Comprehensive assessments of iron content throughout the adult human brain have also recently been performed, again demonstrating the heterogeneous ranges of iron present in different brain areas (Krebs *et al.*, 2014, Ramos *et al.*, 2014). Comparison of controls against AD samples provided evidence of greater iron content in the hippocampus of AD patients, however only two AD patients were compared, limiting the certainty of these results (Ramos *et al.*, 2014). Furthermore, no differences were observed between the genders, a parameter overlooked by most other studies (Ramos *et al.*, 2014). Adding to the controversial and contradictory evidence for iron changes during AD, a meta-analysis of the

quantitative literature investigating iron contents within the AD human brain, recently identified the possibility of citation bias towards positive results for an increase in iron content in AD compared with controls (Schrag *et al.*, 2011). A more recent meta-analysis of quantitative research provided evidence for lower serum iron levels in AD compared with control patients, whilst also highlighting raised iron contents in eight brain regions; including the globus pallidus, caudate nucleus, amygdala, putamen and the frontal, parietal and temporal cortex (Tao *et al.*, 2014). The discrepancies observed between these two meta-analyses likely draw from the differences in inclusion criteria. The more recent study includes research performed subsequent to the earlier meta-analysis, but it also includes quantitative research data from the primary source of citation bias mentioned in the earlier meta study. Furthermore, whilst no citation bias was reported by the more recent study, this can be attributed to the exclusion of review articles, which was found to be the source of citation bias in the first article (Schrag *et al.*, 2011, Tao *et al.*, 2014).

1.4.1.2. Iron storage

During ageing, oligodendrocytes in the basal ganglia have been found with less iron, ferritin and transferrin staining, whilst no changes were observed from any other brain regions (Connor *et al.*, 1990). Microglial ferritin staining was increased in a number of brain areas, whilst astrocytic ferritin expression was only increased in the cerebral cortex, basal ganglia, hippocampus and amygdala during ageing (Connor *et al.*, 1990). The changes associated with decreased ferritin and iron in the basal ganglia oligodendrocytes, with a concomitant increase of ferritin in microglia

and astrocytes supports a potential notion of altered iron localisation in the brain during ageing, which has been hypothesised by other studies (Hallgren and Sourander, 1960). Furthermore, increased microglial ferritin with ageing supports the interaction of inflammatory processes during ageing and disease (Zecca *et al.*, 2004).

H-ferritin has been predominantly found in neuronal cells and oligodendrocytes, whilst L-ferritin was mainly localised to microglia (Han *et al.*, 2002). Whilst neurons expressed greater levels of H- than L- ferritin, oligodendrocytes contained similar levels of each of these ferritin isoforms (Connor *et al.*, 1994). The differences in ferritin isoform expression in the brain have been thought to reflect the function of ferritin within each of these cell types, with H-ferritin indicative of stress response, whilst L-ferritin suggesting a greater role for iron storage (Connor *et al.*, 1994). Indeed subsequent studies suggest that long term iron storage is maintained in microglia, expressing high proportions of L-ferritin as a readily available method for iron storage (Lopes *et al.*, 2008).

1.4.1.3. Iron transport

TF protein in AD samples was increased in frontal cortex compared with elderly controls, and iron accumulation was detected in the frontal cortex and globus pallidus. Furthermore, correlation values of TF to iron were decreased in AD frontal cortex and globus pallidus compared to control, indicating a change in the mobilisation of iron in AD (Loeffler *et al.*, 1995). Decreased correlation of TF to iron

was also observed in a number of regions in PD (Loeffler *et al.*, 1995), again indicating a change in iron mobilisation.

TF binding has also been identified around plaques in AD grey matter (Connor *et al.*, 1992a). TF was found expressed in astrocytes rather than in oligodendrocytes in AD white matter, however, this wasn't the case in the hippocampus where TF was expressed predominantly in oligodendrocytes, as expected (Connor *et al.*, 1992a).

Finally, the TF gene is also implicated in a greater risk for AD, with the C2 allele, along with a mutation in the hemochromatosis (HFE) gene increasing risk (Robson *et al.*, 2004). This is thought to be due to the C2 allele causing a change in the affinity of TF for iron, leading to accumulation.

1.4.2. Iron accumulation and aggregation with Aβ and tau

It has been demonstrated that both amyloid plaques and neurofibrillary tangles, are associated with iron (Good *et al.*, 1992, Smith *et al.*, 1997, Lovell *et al.*, 1998). These studies have ranged from demonstrating association using histological methods, to chemical analyses. Using the chemical analytical method micro-PIXE (Particle Induced X-ray Emission) (see section 1.5.2), iron, copper and zinc were found accumulated within the cores and rim of amyloid plaques in AD amygdala compared with AD and control neuropil (Lovell *et al.*, 1998). The accumulation of these metals was also confirmed to be localised to regions of β-sheet conformation in AD tissue (Miller *et al.*, 2006). NFT containing neurons showed selective accumulation of iron and aluminium in AD hippocampus compared with control

using laser microprobe mass analysis (LAMMA) (Good *et al.*, 1992). Furthermore, the accumulation of iron in plaques and tangles in the hippocampus has been shown histologically (Smith *et al.*, 1997).

It was identified that ferric iron, as well as Al^{3+} (aluminium ion) and Zn^{2+} (zinc ion) ions may hold a direct role in the aggregation of β-amyloid, as shown by a radiolabelled peptide aggregation assay using the βA4 peptide (Mantyh *et al.*, 1993). Furthermore, ferric iron, along with Al^{3+} were shown to increase amyloid aggregation into fibrillary oligomers, whereas Zn^{2+} and Cu^{2+} (copper ion) ions did not (Bolognin *et al.*, 2011).

Ferric iron was shown to bind and cause aggregation of tau into soluble paired helical filaments (PHF), dependent on the phosphorylation state of tau (Yamamoto *et al.*, 2002). Furthermore, reduction of ferric iron to the ferrous form led to the solubilisation of insoluble PHF of tau, indicating that the presence of ferric iron may be involved in forming insoluble PHF (Yamamoto *et al.*, 2002).

1.4.3. Direct links between iron to APP and tau biology

Most recently, direct regulatory links between iron and APP expression and processing have been identified that may promote the expression of Aβ during AD. An IRE was discovered on the APP mRNA transcript, highlighting a direct mechanism by which iron can affect expression of the APP transcript (Rogers *et al.*, 2002). The location of the IRE is present in the 5'UTR, promoting translational expression under high cellular iron content, similar to ferritin expression (Rogers *et al.*, 2002,

Rogers *et al.*, 2008). Furthermore, links between the homeostasis of iron and specifically Aβ processing have been highlighted to occur through regulation of the proprotein convertase, furin. Furin is able to cleave and activate ADAM10, which is involved in the functioning of the α-secretase complex for APPα production (Anders *et al.*, 2001, Hwang *et al.*, 2006). Excess iron content can reduce furin expression (Silvestri *et al.*, 2008), therefore reducing α-secretase activity and promotion of APP processing through BACE1 cleavage into Aβ (Silvestri and Camaschella, 2008).

Whilst the function of APP has still not been confirmed, recent reports have highlighted it to be potentially involved with iron export from cells (Duce *et al.*, 2010). Ferroxidase activity was identified in APP, whereby catalysis of the ferrous to ferric form of iron could occur in a similar manner as that by ceruloplasmin for cellular export. APP was then identified to be involved in loading iron onto transferrin and exporting iron from cells via ferroportin (Duce *et al.*, 2010). Iron overload in cells was rescued by administration of APP in cell models and primary neuronal cultures of $APP^{-/-}$ mice (Duce *et al.*, 2010). Subsequently, a role for tau in iron export has also been suggested using primary cortical neurons, as $tau^{-/-}$ cells showed decreased surface trafficking of APP (Lei *et al.*, 2012).

1.4.3.1. Evidence for iron-related oxidative stress through ROS production

Iron, along with other metal ions, is thought to lead to increased oxidative damage during brain ageing (von Bernhardi *et al.*, 2010), and contribute to the "alternate

hypothesis" of neurodegeneration in AD (Lee *et al.*, 2007) (see section 1.2.3 and 1.2.3.1).

The accumulation of iron in plaques and tangles described above was shown histologically to have redox capabilities, highlighting potential as a source for ROS production (Smith *et al.*, 1997). In fact, both amyloid plaques and tangles only demonstrated redox potential following the addition of iron or copper salts, demonstrating that the metal ions bound in these protein aggregates are bound in a redox active manner in AD tissue. Also, tau protein was highlighted to make a contribution to the redox activity, assessed using a hydrogen peroxide-based assay (Sayre *et al.*, 2000).

Even more convincingly, $A\beta_{1-42}$, the amyloidogenic form of amyloid, was shown to have an enhanced capability to cause redox reactions with iron and copper than $A\beta_{1-40}$. Not only were redox active iron and copper demonstrated in a hydrogen peroxide detection assay in conjunction with $A\beta_{1-42}$, but the reaction products were shown to generate the hydroxyl radical through increased TBARS measurement (Huang *et al.*, 1999). Finally, it has also been demonstrated that $A\beta_{1-42}$ may only show cell toxicity when iron is bound (Rottkamp *et al.*, 2001).

With iron's suggested role in oxidative stress within the brain during ageing and disease, stress response proteins, such as heme oxygenase 1 (HO-1) have been evaluated (Smith *et al.*, 1994, Hirose *et al.*, 2003). HO-1 is a 32kDa protein and is able to catalyse the formation of biliverdin, iron and carbon monoxide from heme (Hirose *et al.*, 2003). Its expression has been shown to increase with ageing in the

cerebral cortex and hippocampus, and was associated with higher levels of ferritin in the cortex, but not in the hippocampus (Hirose *et al.*, 2003).

In AD, HO-1 was associated with plaques and tangles in hippocampal tissue, and supports the possibility that iron mediates oxidative damage and ROS formation in areas relevant for disease pathology (Smith *et al.*, 1994). Indeed the expression of HO-1 seems somewhat specific to disease pathology, with increased expression identified in both neurons and astrocytes found in the hippocampus and temporal cortex, but not in substantia nigra, of AD samples (Schipper *et al.*, 1995).

1.4.4. Role of iron in AD and neurodegenerative diseases from preclinical research

The use of animal models in neurodegenerative disease research is paramount for greater understanding of the pathological processes underpinning disease, as well as for evaluation of novel therapies and in establishment of biomarkers to diagnose and monitor progression (Jucker, 2010). As neurodegenerative diseases only appear in humans in their fullest form, many genetically engineered models have been created, that comprise certain aspects of the disease. Frequently used models in AD research are mice that have been engineered to express mutant proteins that have been identified as strong risk factors for familial forms of AD in humans (Hardy and Selkoe, 2002). These are mostly based around the amyloid processing pathways, with many different gene mutations expressed in APP, PS-1 and PS-2 (Jucker, 2010). Mice have been created containing mutated forms of one, or even combinations of

genes, such as the APP/ PS-1 mouse, which contains an overexpressed mutated APP and mutated PS-1 protein (Borchelt *et al.*, 1997). Similarly, fragments of APP have been expressed to yield β-amyloid accumulations and cognitive pathology in mice, by expressing the C100 fragment in mice (Neve *et al.*, 1996). Furthermore, transgenic mice containing mutated tau protein, either alone, or in combination with APP, have demonstrated similar AD phenotypes (Ballatore *et al.*, 2007). These animals tend to be characterised with accumulated β-amyloid protein or tau, loss of synapses, and declines in cognitive and memory tests (Oddo *et al.*, 2003).

Many of these animal models have been utilised for assessment of the role of iron during neurodegeneration, especially as iron accumulation is detected within the amyloid plaques from preclinical models, such as in the APP/PS-1 model (Falangola *et al.*, 2005, Wengenack *et al.*, 2011). Furthermore, transgenic mice overexpressing mutated ferritin light chains give rise to similar iron overload, ferritin aggregates (as inclusion bodies) and motor dysfunction as that observed with neuroferritinopathies, (outlined in section 1.3.2 (Curtis *et al.*, 2001)), therefore highlighting the impact that incorrectly functioning ferritin holds within the brain (Vidal *et al.*, 2008).

However, using these animal models has also provided evidence for Aβ plaque formation as a protective role against iron toxicity (Maynard *et al.*, 2002, Bishop and Robinson, 2003). Overexpression of APP lead to a reduction in iron content, as well as a reduction in the levels of other metal ions, in the Tg2576, C100.V717F and C100.wt transgenic mice lines (Maynard *et al.*, 2002). Aβ also had a protective role when co-injected into rat cortex with iron (Bishop and Robinson, 2003).

1.4.5. Role of iron forms in AD

AD patients also show differences in composition of ferritin and hemosiderin to control subjects and these changes were predominantly located to the oligodendrocytes of the hippocampus (Quintana *et al.*, 2004, Quintana *et al.*, 2006). Furthermore, X-ray Absorption Near Edge Spectroscopy (XANES) was used to establish the presence of unusual iron cores, such as magnetite, near senile plaques in AD compared to control samples (Collingwood *et al.*, 2005). Similarly, magnetite levels were found to be elevated in female AD subjects compared with controls, however male AD subjects did not show elevated magnetite levels (Pankhurst *et al.*, 2008). From these studies, a direct role for iron overload and abnormal biochemical changes is apparent, leading to dysfunction of neuronal cells involved in cognitive memory (Quintana, 2007). Some of the chemical mechanisms underlying the generation of these unusual iron cores have been suggested to be due to β-amyloid plaque interaction with ferrihydrite iron, the form of iron found in ferritin, (see section 1.3.2) to reduce this iron form to magnetite (Everett *et al.*, 2014a). Indeed, these processes may even outline novel mechanisms of cell death, whereby magnetite was found to affect microtubule formation and stability *in vitro*, and led to abnormal cell morphology and reductions in cell viability (Dadras *et al.*, 2013). Furthermore, ferric iron can be catalyzed into ferrous iron by β-amyloid, which may allow a greater role for participation in the Fenton reaction enhancing ROS production (see section 1.2.3.1) (Everett *et al.*, 2014b).

1.4.6. Chelation therapy potential

Clinical, as well as preclinical studies have established a possible therapeutic benefit of iron chelation therapy against neurodegenerative disorders, whereby these compounds are able to bind and sequester heavy metals from taking part in any further, potentially damaging, reactions. Much of this research has been developed in PD models of disease, where ferritin overexpression, or the metal chelator Clioquinol, were able to reduce the effects of a 1-methyl-4-phenyl-1,2,3,6-tetrahydropyridine (MPTP) lesion in the substantia nigra (Kaur *et al.*, 2003). Furthermore, pre-treatment with the BBB permeable, iron-specific chelator VK-28, was used to prevent loss of dopamine within the striatal regions in the 6-hydroxydopamine (6-OHDA) lesioned rat (Shachar *et al.*, 2004) leading to further development of BBB permeable iron chelators (Youdim *et al.*, 2005).

Deferoxamine is a bacterial siderophore, used for the treatment of iron overload by chelation, and has been used clinically in a small study of 48 subjects to slow the progress of AD by two-fold (McLachlan *et al.*, 1991). Furthermore, Clioquinol, which has been shown to produce a significant decrease in iron levels in mice brains upon treatment (Yassin *et al.*, 2000), has also provided stabilisation or even some symptomatic improvement for AD patients (Regland *et al.*, 2001, Ibach *et al.*, 2005). Drawbacks to these studies however, are that they use small patient numbers and were performed without control subjects. Novel iron chelators, VK-28 and M30 have also shown neuroprotective roles in APP/PS-1 mice models of AD, and were similar to epigallocatechin-3-gallate (EGCG) to lower the expression of APP (Avramovich-Tirosh *et al.*, 2007). Perhaps the most encouraging finding towards the

positive use of iron chelation strategies against neurodegenerative diseases stems from the positive outcomes observed during a recent 12 month double-blind placebo-controlled clinical trial, in which Deferiprone demonstrated efficacy using motor scores for PD patients (Devos *et al.*, 2014).

1.5. Iron Quantification in Biology

Many approaches for iron detection in biological tissues have been employed, to evaluate both the concentration, as well as in understanding the form, of iron within tissue. Furthermore, by using these methods to qualitatively and quantitatively assess iron within biological tissues, any changes to iron biology can be assessed during disease, including during neurodegenerative diseases and dementia.

1.5.1. Histological method assessments

Histological approaches for iron evaluation utilise the redox potential of iron for staining. Perls iron stain uses soluble ferrocyanide addition to tissue, which reacts with ferric ions released by acid treatment, to form the blue crystal precipitate Prussian blue (van Duijn *et al.*, 2013). Furthermore, the Turnbull blue method utilises a ferricyanide reaction with ferrous ions, for ferrous iron specific detection following acid treatment (Jellinger *et al.*, 1990, Meguro *et al.*, 2003). Enhancement of both Prussian blue and Turnbull blue stains can be performed through the

hydrogen peroxide dependent oxidation of 3,3-diaminobenzidine (DAB) producing a brown precipitate (Meguro *et al.*, 2007, van Duijn *et al.*, 2013). Using a similar method, the redox-potential of iron in plaques and tangles has been evaluated using hydrogen peroxide based assays coupled with DAB (Smith *et al.*, 1997, Sayre *et al.*, 2000).

Whilst these methods are able to provide excellent understanding of the localisation of iron within tissue, quantification of iron content is complicated due to the inconsistency of staining methods and their dependence on many external factors (Meguro *et al.*, 2007). Iron staining in brain tissue was found to be affected by factors such as fixation time length in 4% formalin, with fixation for longer than 24 hours leading to a marked reduction in staining (Morris *et al.*, 1992). Furthermore, different metals have been found to leach into fixative at different rates and the form in which they are bound can affect their rate of loss (Gellein *et al.*, 2008). Fixation time has not, however, been shown to affect iron contents in brain tissue up to 18 months (Bush *et al.*, 1995, Chua-anusorn *et al.*, 1997, Gellein *et al.*, 2008), although evidence does exist demonstrating decreased iron content following 4-6 years fixation (Schrag *et al.*, 2010). Finally, it has also been noted that assessment of the chemical state of iron can be complicated by changes in oxidation environment in post mortem tissue, as well as by fixation and staining processes of biological tissue (Dobson and Grassi, 1996, Collingwood and Dobson, 2006). It has also been shown that the Perls and Turnbull stains demonstrate some degree of cross reactivity for the different forms of iron (Meguro *et al.*, 2003).

1.5.2. Chemical method assessments

More recently, quantitative chemical approaches have been used to evaluate iron content within post-mortem tissue, using methods such as, inductively-coupled-plasma mass spectrometry (ICP-MS), atomic absorption spectroscopy (AAS), micro-particle induced X-ray emission (micro-PIXE) and synchrotron-radiation X-ray fluorescence (SR-XRF) (Lovell *et al.*, 1998, House *et al.*, 2007, Langkammer *et al.*, 2010, Antharam *et al.*, 2012, Zheng *et al.*, 2013, Stuber *et al.*, 2014).

ICP-MS involves the ionisation of atoms from a sample, prior to performing mass spectrometry analysis for various elements. This approach has been used to investigate the concentration of iron, as well as many other elements in the brain (Corrigan *et al.*, 1993, Langkammer *et al.*, 2010). AAS measures the concentration of elements in a sample by assessing the amount of light at a specific wavelength that is absorbed, and has similarly been used to assess the iron content in brain samples (House *et al.*, 2007). Whilst these two methods are highly sensitive for iron, and other metal quantification, both require the excision of tissue for chemical assessment and therefore cannot be directly spatially correlated to other techniques, for example, to compare against MRI. Furthermore, whilst adaptations can be made for spatial assessment, e.g. using laser ablation ICP-MS (LA-ICP-MS) (Becker *et al.*, 2010), all these techniques are also destructive, leading to the loss of material for any subsequent assessment, such as using histology.

Micro-PIXE uses a high energy proton beam to collide with atoms in a sample, thus emitting X-rays that are specific for each chemical element that can be detected (Stuber *et al.*, 2014). This technique has been used to quantify the iron content in

plaques and tangles (Lovell *et al.*, 1998), as well as to quantitatively map iron, sulphur and phosphorus content in human cortical samples (Stuber *et al.*, 2014), and allows for the non-destructive, and spatial assessment of iron. Similarly, SR-XRF can be used to spatially and quantitatively assess brain iron content and also provides the benefit of being a non-destructive technique. This approach uses high energy electron beams to produce X-ray photons that are able to eject inner shell electrons from atoms within a sample (Figure 1-6). The ejection of an inner shell electron allows outer shell electrons to drop into the inner shell, thus releasing photons that can be detected (Figure 1-6). The energy released from atoms is specific to the energy change and to the element, with the primary observation being Kα energy detection, whereby an electron from the L shell, drops into the K shell orbitals (Figure 1-6). Furthermore, the amount of energy released is directly proportional to the concentration of the element in the sample. This technique has recently been used to quantitatively correlate MRI measurements against iron content and to assess brain samples from AD tissue (Antharam *et al.*, 2012, Zheng *et al.*, 2013) (see section 1.6.5.1).

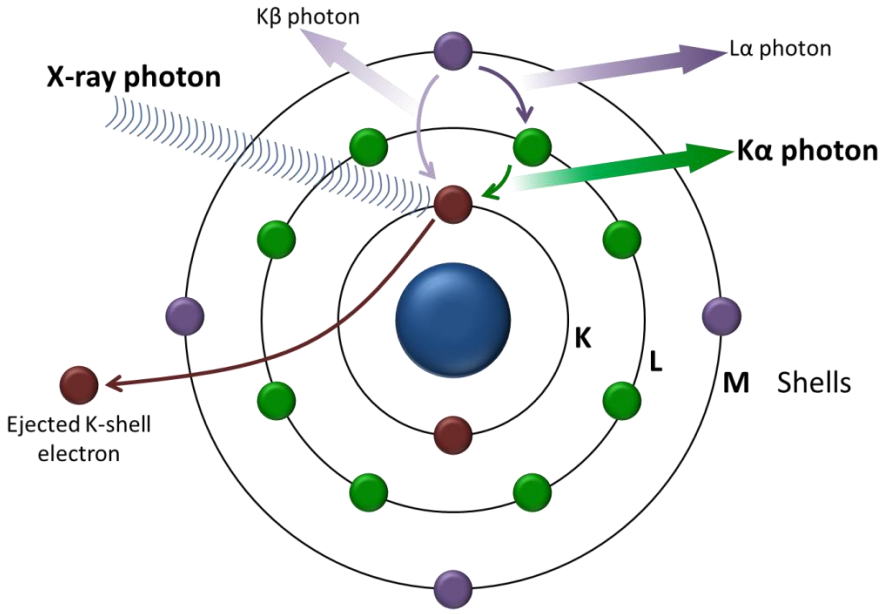

Figure 1-6 SR-XRF method for detection of specific elements

High energy X-ray photons cause inner shell electrons to be ejected from an atom. Electrons from higher energy shells move into the inner K shell in place of lost electrons, which involves an energy release in the form of photons. Kα photons are produced when an electron moves from the L shell to the K shell. Kβ photons are produced when an electron moves from the M shell to the L shell. Lα photons are produced when an electron moves directly from the M shell to the K shell. Detection of these photons allows quantification of elements in a sample.

1.6. MRI and Iron Quantification

MRI is a non-invasive method for detection of magnetic nuclei, the most abundant of which are water protons in the body. Changes in the magnetic properties of water due to interaction with cellular components can be detected using various MRI acquisition methods that therefore highlight tissue microstructure. Due to the

paramagnetic effects of iron on water protons, a number of studies have established the potential for detection of iron using MR methods (Bartzokis *et al.*, 1993, Clark *et al.*, 2003, Haacke *et al.*, 2005, Wood, 2007, Langkammer *et al.*, 2010).

1.6.1. Relaxometry

The most studied methods for imaging iron involves the shortening of the transverse relaxation times T2 and T2*, or increased rates R2 and R2* (Ordidge *et al.*, 1994, Schenck *et al.*, 2006). A basic overview of MRI relaxometry is provided here (see review by Deoni (Deoni, 2010)).

Protons and neutrons spin randomly within atomic nuclei. In nuclei that have an even mass number, these spins cancel each other out, whilst within nuclei with an odd mass number, they do not. It is these nuclei that are MR active, as they therefore demonstrate net spin. Given that atomic nuclei have a positive charge due to the presence of protons, a magnetic moment is created around the spinning nuclei, induced by the spinning charged particle. Protons are the most frequently utilised nuclei in MRI due to the large net magnetic moment created by a single proton and their high abundance in both water and fat found within the body.

When outside of a magnetic field, protons show no alignment. When placed inside a magnetic field however, protons will orientate either parallel or antiparallel with the applied magnetic field (B_0). There is an excess in the population of protons orientated in the parallel orientation due to the lower energy requirement in this direction compared with the anti-parallel orientation. The excess of protons

orientated parallel to B_0 creates a net magnetisation (M_Z) in the direction of the external magnetic field. The overall size of the net magnetization vector increases with greater B_0 magnetic field strength, since the population difference between parallel and anti-parallel magnetic moments is proportional to B_0.

Furthermore, proton spin axes precess when in an external magnetic field, due to interaction of the magnetic moments with the external field. The precessional frequency of protons can be determined through the Larmor frequency, shown below:

$$\omega = \gamma B_0$$

Where, ω is the Larmor, or precessional frequency (rad s^{-1}), B_0 is the magnetic field strength and γ is the gyromagnetic ratio, a constant for each atom defined as the frequency of a particular nucleus at 1 Tesla (T).

The gyromagnetic ratio is specific for each magnetic nuclei, and so each nuclei has its own Larmor frequency at a given field strength. The Larmor frequency of protons at 1T is 42.57 MHz, and therefore at 7T, will be 297.99 MHz. By applying a radiofrequency (RF) pulse (termed B_1) at the Larmor frequency for protons at a given B_0, protons resonate, with two events occurring simultaneously (Figure 1-7). The RF pulse 'tips' the net magnetization, M_Z, through an angle, θ (e.g. by 90°, Figure 1-7A), towards the transverse, M_{XY}, plane. Furthermore, the proton spins become coherent, therefore showing the same phase (Figure 1-7B). With the magnetization vector now solely in the transverse plane and coherent, image acquisition can occur due to the transverse magnetization inducing an electrical

signal in the receiver coil. Two intrinsic characteristics of nuclei can be detected following this application of a 90° RF pulse; the T1, spin-lattice (or longitudinal) relaxation time, and the T2, spin-spin (or transverse) relaxation time (Figure 1-8).

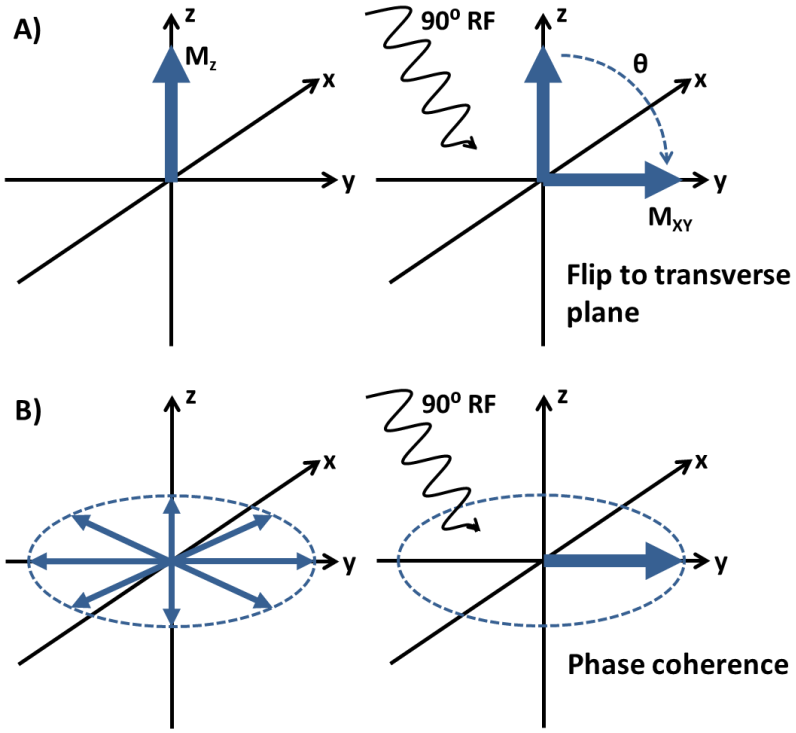

Figure 1-7 Net magnetisation vector and effects of 90° RF pulse application

(A) The net magnetisation vector (M_z) is flipped ϑ° (90° in this example) into the transverse (M_{XY}) plane following application of an RF pulse of sufficient energy, and at the corresponding Larmor frequency. (B) A RF pulse also causes protons to precess coherently, in the same phase.

T1 is the time constant required for the magnetization to recover in the longitudinal, z direction, back up to M_z (Figure 1-8A), whilst T2 is the time constant for the decay of M_{XY} coherence (Figure 1-8B), following RF pulse application.

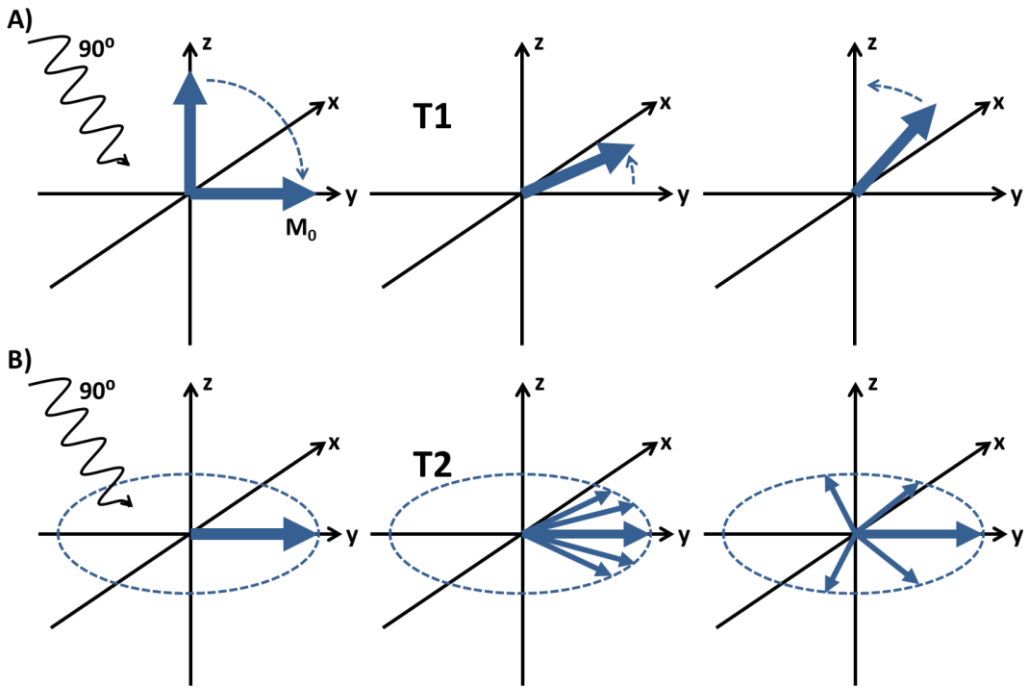

Figure 1-8 T1 and T2 relaxation mechanisms

This figure shows (A) the application of a 90° RF pulse causing the direction of proton magnetisation to fall into the x,y plane and M_z = 0, followed by T1 longitudinal relaxation, and (B) T2 transverse relaxation, and decay of M_{XY}.

Evaluation of T1 and T2 relaxation times is commonly performed using a spin-echo (SE) based sequence (see section 1.6.2). Similarly, M_{xy} can be evaluated using a gradient-echo (GE) sequence to provide the T2* relaxation time (see section 1.6.3).

1.6.2. Spin-echo (SE) acquisition of T1 and T2

Spin-echo (SE) imaging is a commonly-used standard method for acquisition of T1 and T2 weighted images, or for T1 and T2 quantification. Due to magnetic field inhomogeneities and spins acting on each other to speed up or slow down

precessional frequencies, dephasing of spins begins as soon as the 90° RF pulse has completed (Figure 1-9A-C). Therefore, a rephasing step is performed by applying another RF pulse, flipping spins 180° (Figure 1-9D). The different spin speeds continue at the same rate; faster spins continue to precess fast, slower spins continue to precess slowly, providing an echo when the spins rephase back to coherence (Figure 1-9E-F). At this point, image acquisition can occur at full transverse signal.

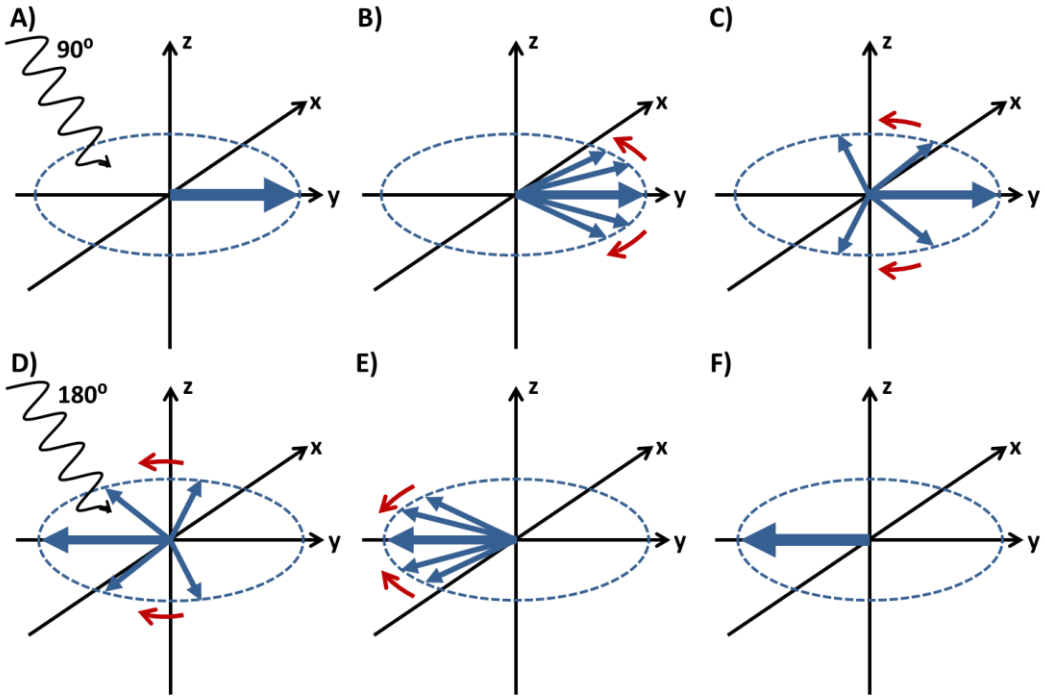

Figure 1-9 SE acquisition mechanisms

(A) A 90° RF pulse causes the net magnetisation vector to move into the transverse plane. (B) Dephasing of spins occurs immediately on completion of RF pulse, with (C) precessional spins fanning out at different speeds with time. (D) A 180° RF pulse causes the spins to flip around the transverse plane axes, (E) refocussing the precessional spins for (F) image acquisition.

The T1 and T2 of samples can be measured using spin-echo acquisitions by changing the two parameters necessary for generating image contrast; the repetition time (TR), and the echo time (TE). The TR is the time between 90^{o} flips, controlling the longitudinal relaxation signal recovery (Figure 1-10), such that at low TRs, minimal recovery of T1 relaxation has occurred, compared with long TRs which allow for full recovery of M_z. The TRs are much longer than the TE, which is the time between the 90^{o} flips of precessional spins, and image acquisition (Figure 1-10). The 180^{o} flip occurs at TE/2, to ensure image acquisition occurs at maximal signal availability.

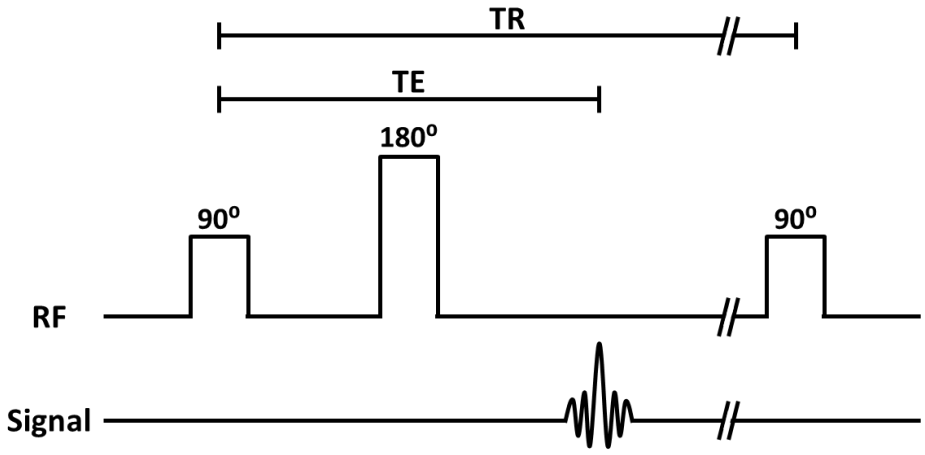

Figure 1-10 Basic SE acquisition sequence

RF pulses on the top line and signal acquisition on the bottom line. The two main parameters contributing to image contrast are shown; the repetition time (TR) and the echo time (TE), in correspondence with when RF pulses are provided (top line) and signal acquisition occurs (bottom line). Double line gaps indicate that the TR is much longer than the TE.

Acquisition of several SE images with different TRs and a constant, short, TE allows the measurement of T1 relaxation (Figure 1-11A). A short TE is optimal for T1 measurement, to ensure limited effects on the obtained signal due to T2 effects. Signal intensity increases with an exponential function according to $Y = M_0 \times [1 - e^{(-X/T1)}]$, where Y is the signal intensity of the image, M_0 is the proton density and X is the TR (Figure 1-11A). By solving the equation with each TR, the T1 value can be obtained, corresponding to recovery of 63% of the z-component of the magnetisation, M_z. Similarly, acquisition of several SE images with different TEs and a constant, long, TR allows the measurement of T2 relaxation (Figure 1-11B). A long TR is optimal for T2 measurement, to ensure full recovery of longitudinal relaxation thus limiting T1 effects on the obtained signal. Signal intensity decreases with an exponential function according to $Y = M_0 \times e^{(-X/T2)}$, where Y is the signal intensity of the image, M_0 is the proton density and X is the TE (Figure 1-11B). By solving the equation with each TE, the T2 value can be obtained, corresponding to a 63% reduction of the total relaxation in the transverse plane. The reciprocal of T1 and T2 relaxation times provides the R1 and R2 relaxation rates, and these have been demonstrated to show direct linear correlation to iron content both *in vivo* and *ex vivo* (Ogg and Steen, 1998, Langkammer *et al.*, 2010).

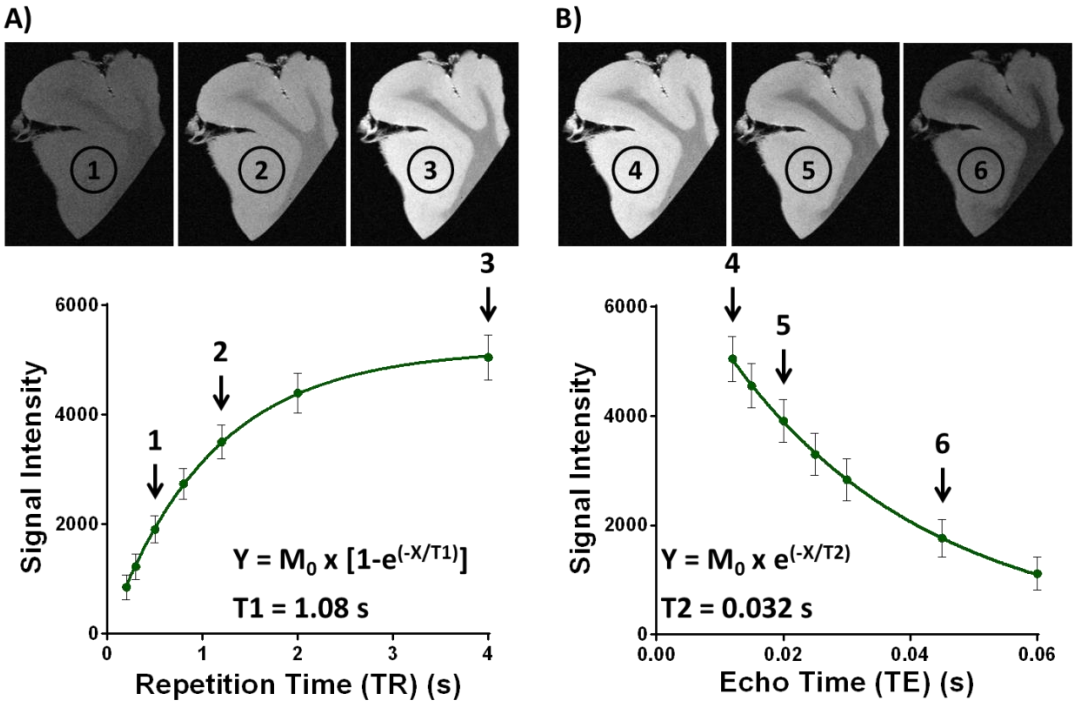

Figure 1-11 Overview of SE measurement of T1 and T2 values in samples

(A) Representative images at three increasing TRs (1 – 3) for T1 measurement and (B) representative images at three increasing TEs (4 – 6) for T2 measurement are shown. Mean signal intensity for each of the regions of interest (ROIs) (red circles) are plotted against TR or TE, for calculation of T1 or T2 values, respectively (graphs).

1.6.3. Gradient-echo (GE) acquisition of T2*

Gradient-echo (GE) acquisition provides another way of assessing the M_{xy} component of samples. The sequence is initiated in a similar way to SE sequences, with a RF pulse to flip the magnetization vector towards the transverse plane. Again, spins start to dephase as soon as the RF pulse is removed, however whilst a 180^{o} RF pulse is applied in SE sequences to refocus spins, a GE sequence applies a negative gradient immediately after the original 90^{o} RF pulse to cause rapid

dephasing of transverse magnetisation. A positive gradient in the opposite direction can then be applied to reverse this dephasing and leads to echo formation for signal acquisition.

The GE method is therefore only able to refocus dephasing that was caused by the negative gradient, and does not refocus spins that have been affected by magnetic field inhomogeneities. SE sequences however rephase spins based on their natural environments therefore limiting the effects from local inhomogeneities. Hence, T2* acquisition incorporates T2 effects, as well as effects from inhomogeneities and magnetic susceptibility.

1.6.4. Fast acquisition of T2 and T2*

Whilst the SE and GE acquisition methods described above provide standard approaches for evaluation of T1, T2 and T2*, these sequences have long acquisition times making their feasibility for clinical use difficult (Deoni, 2010). Furthermore, scan time is limited when performing preclinical animal studies, due to the use of anaesthesia to prevent unwanted movement during MR acquisition *in vivo*. Home Office regulations limit the amount of time that an animal can be left under anaesthesia, limiting the time available for scanning by MRI. Faster acquisition methods can therefore be used to acquire T1, T2 and T2* relaxometry. Multi echo (ME) T2 and multi gradient echo (MGE) T2* evaluation are described here, given the applicability of these particular measurements for iron detection and quantification.

Both fast ME and MGE acquisitions begin by flipping the net magnetisation into the transverse plane, using a 90^{o} RF pulse, as described above. Spins are then rephased time and time again (Figure 1-12), by either using 180^{o} RF rephasing pulses (for T2 measurement) or by utilising gradients to perform 180^{o} rephasing steps (for T2* measurement). The number of rephased echoes is the echo train length (ETL).

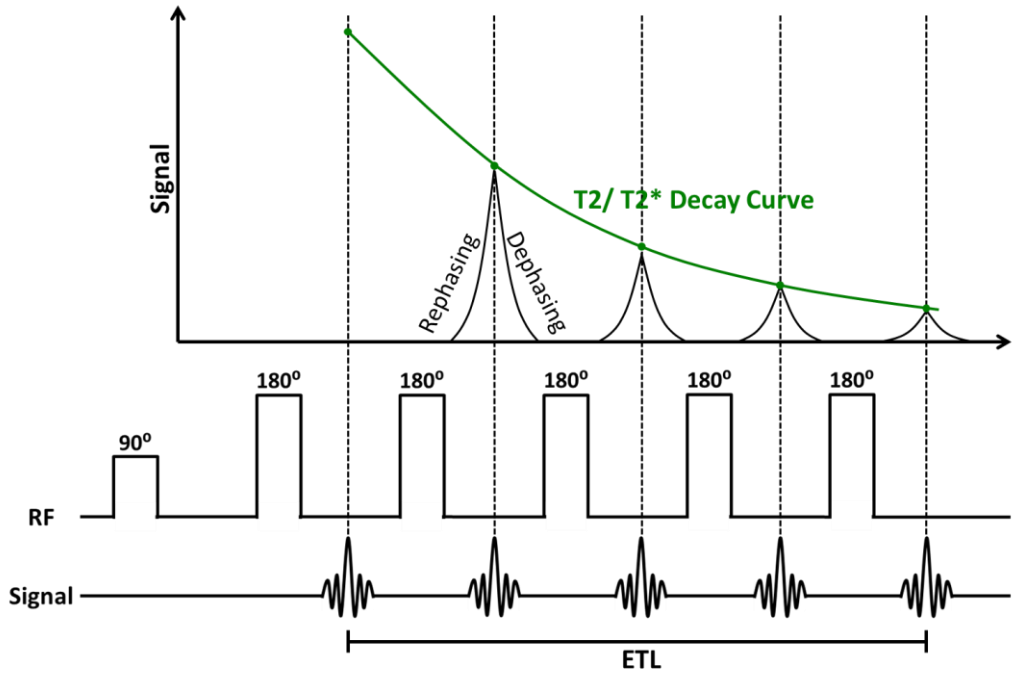

Figure 1-12 Fast ME T2 and MGE T2* acquisition sequence and method

Sequence begins with a 90^{o} RF pulse to move net magnetisation vector into the transverse plane. A series of echoes (see the signal line) are then created by using repeated 180^{o} RF pulses to dephase and then rephase spins during this acquisition. Signal acquisition mid-way through each 180^{o} rephasing pulse therefore allows acquisition of multi-echo data, from one initial 90^{o} pulse. MGE data is acquired in the same way, however using gradients to rephase spins instead of RF pulses. ETL are the number of echoes created within the acquisition sequence.

1.6.5. Assessment of brain iron using MRI in ageing and AD

Many studies investigating brain iron content against MRI rely upon previously published post-mortem data to correlate observed *in vivo* MRI results with iron contents (Schenker *et al.*, 1993, Ogg and Steen, 1998, Jensen *et al.*, 2009, House *et al.*, 2010, Qin *et al.*, 2011). Iron contents quantified across multiple brain regions and ages tend to be taken from the Hallgren and Sourander study, from 1958 (Hallgren and Sourander, 1958).

1.6.5.1. Relaxometry

Relaxometry measurements in tissues depend on the tissue water content, as well as the interactions of water protons with macromolecules (Haacke *et al.*, 2005). Furthermore, small amounts of paramagnetic material, such as iron, can strongly impact the relaxometry of protons given their large magnetic moments compared with protons (Haacke *et al.*, 2005). As highlighted in section 1.3.1, non-haem iron is predominantly present within ferritin and hemosiderin in the brain (Dedman *et al.*, 1992, Vymazal *et al.*, 1996b) and these are considered to be the main iron sources in biological tissues that provide MRI contrast (Schenck, 2003). The other sources of non-haem iron in the brain, transferrin and iron within the LIP (see section 1.3.1), are considered to be at concentrations that are too low to impact MRI contrast.

The relaxation mechanism for iron in ferritin has been attributed to the Proton Exchange Dephasing Model (PEDM), in which relaxation occurs between water protons at the surface of the iron oxide ferritin core and exchange with the bulk

water protons (Gossuin *et al.*, 2002). The impact of this model is that it provides first order relaxation mechanism whereby R2 linearly increase with magnetic field strength (Gossuin *et al.*, 2002).

R1 was directly correlated to iron content in multiple brain regions and was found to correlate to age with a similar exponential fitting as that observed for iron contents during ageing from the Hallgren and Sourander post-mortem study (Ogg and Steen, 1998). Furthermore, T2 values were correlated against Hallgren and Sourander post-mortem iron contents, to demonstrate similar changes in T2, as that found for iron contents with age, in both the globus pallidus and putamen (Schenker *et al.*, 1993). In both studies, a large change in T1 or T2 was observed in the first 20-30 years, which then plateaus by 40 years, similar to iron contents (Schenker *et al.*, 1993, Ogg and Steen, 1998). The decrease in T2 values has not only been demonstrated to be similar in nature to the changes in iron content within the brain during ageing, however differences in iron content were also related to motor and cognitive functioning in normal ageing, with decreased T2 values providing decreasing scores in these tests (Pujol *et al.*, 1992). A mathematical model developed involving iron deposition in the brain, as assessed using T2*, demonstrated that this may precede decreases in hippocampal volume, that in turn correlated to worsening memory scores in normal ageing adults (Rodrigue *et al.*, 2012). Furthermore, more prominent iron deposition, assessed by T2* quantification, was also observed in aged patients with hypertension across a number of brain areas (Rodrigue *et al.*, 2011).

Evidence for iron deposition in the hippocampus of AD patients was suggested using T2-weighted imaging compared to control subjects (Schenck *et al.*, 2006). Similarly, the iron contents from Hallgren and Sourander were correlated to R2' values in a small cohort and then used to demonstrate increased R2' values in the hippocampus, caudate, putamen and parietal cortex of both MCI and AD patients (Qin *et al.*, 2011). Furthermore, R2' values were shown to be strongly correlated against declining MMSE scores in this cohort.

More recently however, research efforts have involved attempts to validate MRI methods using quantitative assessments of iron, to understand and validate the specific impact iron has on various MRI parameters. Iron content, assessed by AAS, was correlated against R2, determined in a 4.7T MRI scanner, using post-mortem AD tissue to define the content of iron required to cause correlative changes as 55μg/g wet tissue (House *et al.*, 2007). A comprehensive investigation performed R2 and R2* relaxometry on deceased subjects, followed by the bulk analysis of small areas of brain regions using ICP-MS from a single brain slice (Langkammer *et al.*, 2010). Strong correlations between iron content and both R2 and R2* were found across multiple brain regions and subjects, with R2* showing greater sensitivity (Langkammer *et al.*, 2010). Whilst these studies clearly show correlation of iron content across different brain regions, they do not evaluate the spatial correlation of iron content to MRI measurements within brain regions, to understand whether different tissue-dependent factors may be affecting relaxometry values. To address this, one study has evaluated the differences in iron

content correlation to R1 and R2 values either within WM or GM tissue (House *et al.*, 2008).

More recently, quantification of iron content, as well as myelin content, spatially using micro-PIXE has been performed to attempt to model relaxivities based on the contributing factors from these two variables (Stuber *et al.*, 2014). Strong correlations between iron content and relaxometry were again identified and linear regression was utilised to model iron and myelin contents from relaxometry maps in these control cortical samples. These spatial quantitative methods for iron detection are also now being used to evaluate samples from neurodegenerative diseases, such as Alzheimer's or Parkinson's disease. Indeed, hippocampal sections from Alzheimer's disease patients were assessed by both R2 and R2* with SR-XRF elemental mapping performed subsequently (Antharam *et al.*, 2012). Whilst no global differences in iron content or relaxometry were detected between control and AD samples here, strong correlations to R2 and R2* were observed and detectable pixel hyper intensities were identified in a greater proportion of AD samples than control, potentially highlighting amyloid plaques containing accumulated iron.

1.6.5.2. Field dependence of R2

Non-standard methods, such as field dependent R2 increase (FDRI) have also been used to detect iron. FDRI is the measurement of R2 values at different field strengths, and has been suggested as a specific detection method for ferritin iron.

This specificity for ferritin iron is attributed to the linear increase of R2 with field strength due to the PEDM (see section 1.6.5.1). Furthermore, given that ferritin is the predominant source of non-haem iron in biological tissues (see section 1.3.1) FDRI may provide an excellent method for iron detection *in vivo*. Indeed, FDRI proved sensitive for ferritin iron above other types of iron, including transferrin bound iron and ferric iron (Bartzokis *et al.*, 1993).

FDRI has been used to assess brain ferritin levels (Bartzokis *et al.*, 1993) and post-mortem iron concentrations in the frontal white matter, caudate nucleus, putamen, and globus pallidus of normal ageing in the human brain (Bartzokis *et al.*, 1994a). FDRI has also been used to identify increased ferritin iron in the caudate, globus pallidus and putamen in AD (Bartzokis *et al.*, 1994b, Bartzokis *et al.*, 2000) and in the basal ganglia in HD (Bartzokis *et al.*, 1999), compared to control subjects. Furthermore, the age and gender differences observed with neurodegenerative diseases has been attributed to differences in ferritin iron levels, as detected using this approach (Bartzokis *et al.*, 2007a). The limitation for performing FDRI however, is the need for MRI scanning at different field strengths.

1.6.5.3. Susceptibility

Due to the highly paramagnetic nature of iron, measurement of susceptibility effects can also provide a means for iron detection and quantification (Haacke *et al.*, 2004, Wallis *et al.*, 2008). R2' is the contribution of susceptibility effects due to local inhomogeneities, which is incorporated with the intrinsic transverse relaxation

from R2* measurement, and can therefore be simply calculated by subtracting R2 from R2* (Miszkiel *et al.*, 1997). Another, more recent approach for measuring susceptibility uses susceptibility weighted imaging (SWI) or quantitative susceptibility mapping (QSM), which utilises phase imaging for the detection of substances with different magnetic susceptibilities in adjacent tissues (Haacke *et al.*, 2004, Haacke *et al.*, 2005).

Using SWI, differences were identified in brain iron deposition with age and even between brain hemispheres (Xu *et al.*, 2008), however no differences due to gender were observed, unlike that shown by FDRI (Bartzokis *et al.*, 2007a). In healthy subjects, R2* and phase from SWI showed high correlation values against iron concentration within the brain at a variety of field strengths (Yao *et al.*, 2009). Furthermore, given the potential of SWI to detect iron in the brain, baseline phase behaviour in a number of brain regions has been acquired from 75 normal subjects, for future possible comparisons against neurological pathologies, including neurodegeneration (Haacke *et al.*, 2007). Quantitative susceptibility mapping (QSM) has been developed as an approach to quantify the levels of iron in the brain (de Rochefort *et al.*, 2010) with the red nucleus, substantia nigra and cerebellar nuclei showing increased iron levels compared to the rest of the brain tissue. Comparison of QSM to SR-XRF elemental iron contents in a whole post-mortem human brain slice, showed very strong correlation (Zheng *et al.*, 2013).

Using the APP/PS-1 mouse model of AD, SWI was compared against T2 and T2*-weighted imaging for amyloid plaque detection and showed improved contrast to noise ratio in plaques with iron staining (Chamberlain *et al.*, 2009). Whilst this study

provides strong evidence for the optimal detection of plaques by comparison against Perls stain, assessment of sensitivity can only be performed using quantitative measurements of iron content, such as using SR-XRF, which has been shown to correlate iron levels with SWI in AD transgenic mice (McCrea *et al.*, 2008).

1.6.5.4. Magnetic Field Correlation

Magnetic Field Correlation (MFC) is another approach for iron detection by imaging of the magnetic field inhomogeneities within tissue (Helpern *et al.*, 2004, Jensen *et al.*, 2006). Whilst both R2* and R2' measurements incorporate signal from inhomogenities, they are both also affected by transverse relaxation mechanisms caused by dipole-dipole interactions with water protons (Jensen *et al.*, 2006). MFC was designed to provide a better method for inhomogeneity imaging than using R2* or R2', and relies on the ability to measure the effect of inhomogeneities on the magnetic field, temporally (Jensen *et al.*, 2006).

MFC showed linear correlation to iron content in the basal ganglia of normal adults and was found to be significantly greater in regions from an aceruloplasminemia patient, in which greater brain iron levels are found (Jensen *et al.*, 2009). Limited evidence for the application of MFC in AD has previously been performed, however MFC values were found to be higher in the globus pallidus, putamen and thalamus of MS patients than controls, and correlated to both MS lesions and to neuropsychological scores (Ge *et al.*, 2007).

1.6.5.5. Imaging plaques

It has been suggested that detection of plaques using MRI is due to iron accumulation raising the intrinsic paramagnetic properties of amyloid. Animal models of AD have again been invaluable for determining and validating transverse relaxation methods for plaque detection during pathology. In the first instance, imaging of plaques has highlighted differences in T2 and T2* weighted images in a longitudinal study of the APP/PS-1 mouse (Wengenack *et al.*, 2011). These MR images were correlated against Perl's stain for iron, Thioflavin S fluorescence for β-sheet aggregated protein and Aβ-plaques using an antibody and showed that whilst T2 imaging was able to detect plaques in all brain regions, T2* images could only reliably detect iron loaded plaques in the thalamic areas but not those in the cortex and hippocampus (Wengenack *et al.*, 2011). Similar findings were observed for iron loaded plaque detection in the APP(V717I) AD mouse model (Vanhoutte *et al.*, 2005). Calcium and iron accumulation have been suggested to create contrast in T2* quantification of plaques in APP/PS-1 mice (Dhenain *et al.*, 2009). More recently however, disparity between human AD plaques and plaques from APP/PS-1 mice was shown by evaluating R2* relaxivity and contrast. Whilst human plaques demonstrated R2* contrast associated with iron accumulation, R2* contrast in plaques from the APP/PS-1 mouse were not (Meadowcroft *et al.*, 2009). Using deferoxamine to chelate iron from human AD plaques still provided contrast using R2* mapping, therefore suggesting that amyloid plaques are able to impact R2* relaxation alone, without iron presence (Meadowcroft *et al.*, 2015).

1.6.5.6. Confounding effects for detection of iron in the brain

It should be noted however that whilst MRI methods to assess iron content have been extensively reported in the literature, many other factors also affect relaxometry values in tissue, including water content, e.g. oedema (Kato *et al.*, 1986), or tissue microstructure (Deoni, 2010). White matter (WM) demonstrates very different composition to grey matter (GM) and has therefore been shown to strongly impact R1, R2, R2* and susceptibility quantification (Rooney *et al.*, 2007, Schmierer *et al.*, 2007, Fukunaga *et al.*, 2010). Furthermore, given that oligodendrocytes contain high levels of iron for myelin production and maintenance (see section 1.3), attempts have been performed to understand the signal attributed to iron compared with myelin, mostly through the use of iron chelation to extract iron and leave myelin. Indeed, WM regions from post-mortem occipital cortex showed strong effects on R2* and susceptibility, which were substantially, but not completely, removed following iron chelation (Fukunaga *et al.*, 2010). More recently, attempts to quantitatively model myelin content using sulphur and phosphorus, alongside iron content have been trialled using micro-PIXE, and showed that WM provides substantial influence on relaxation values (Stuber *et al.*, 2014).

Additional complexity in the assessment of relaxometry values within regions of WM, are the discoveries that WM orientation can also substantially affect R2* values, which may equally need to be taken into account in quantifying iron contents using this (Wharton and Bowtell, 2012, de Pasquale *et al.*, 2013).

1.7. Methodology Considerations

1.7.1. Post-mortem evaluation

1.7.1.1. Post-mortem interval (PMI)

When using post-mortem human or mouse tissue, various factors must be taken into account. One such factor is the post mortem interval (PMI) which is the time taken from death until the brain is fixed or frozen at the brain bank. The post-mortem delay (PMD) is the time taken from death until the brain is removed from the skull. During the PMI, many biochemical changes can occur, ranging from short term changes in protein and metabolite concentrations, to longer term tissue degradation (Perry *et al.*, 1981, Petroff *et al.*, 1988, Thompson *et al.*, 2013). Metabolite changes in tissue composition have even been detected using ^{1}H-MRS, from 3 days onwards in post mortem sheep and human brain (Ith *et al.*, 2002) and used in attempts to estimate the PMI, purely based on metabolic profiles (Scheurer *et al.*, 2005). However, very few studies have investigated the effect of PMI length on relaxometry assessment. An early study discovered that a minor decrease in T2, but not in T1 relaxivity values was observed between a two and 90 hour PMI in porcine brain tissue, however these samples were maintained at 8^{o}C potentially attenuating any likely changes in relaxometry (Gyorffy-Wagner *et al.*, 1986). More recently, conflicting evidence has been demonstrated using rat brain samples for the effects of PMI length on relaxometry values (Fagan *et al.*, 2008, Shepherd *et al.*, 2009). *In situ* assessment of T1 and T2 values in the rat corpus callosum, striatum and cortex, decreased with PMI length during a 24 hour period of repeated

scanning (Fagan *et al.*, 2008). T1 and T2 values continued to decrease even after stabilization of core body temperatures to the magnet temperature, after 10 hours post mortem (Fagan *et al.*, 2008). Conversely, T1 and T2 values were increased using rat cortical samples immersed in formaldehyde fixation at increasing PMI lengths up to 24 hours (Shepherd *et al.*, 2009). No effects of PMI directly on iron content exists from the limited literature (Loeffler *et al.*, 1995).

1.7.1.2. Fixation time

Other factors that may affect MR results include the fixation time of samples. The fixation time of human post-mortem tissue indicates the period that samples have been submerged in formalin fixative solution. Fixation of tissues is a commonly performed technique for tissue preservation, to stop decomposition, whilst also maintaining protein interactions and localisation (Fox *et al.*, 1985, Puchtler and Meloan, 1985). The fixation of samples using formalin involves the cross-linking of proteins together to preserve tissue in its initial form. As MRI involves the measurement of proton spins to generate contrast based on water proton environments, it has been well documented that changes in MR contrast and relaxometry can occur as a result of the fixation process compared with fresh tissue (Tovi and Ericsson, 1992, Blamire *et al.*, 1999, Dawe *et al.*, 2009). T1 and T2 values have been shown to decline with fixation time, although the decline is greater for T1 (Tovi and Ericsson, 1992, Blamire *et al.*, 1999). Furthermore, T2 values were shown to change differently depending on the depth of tissue, highlighting longer times required for fixative to reach the deeper brain regions (Dawe *et al.*, 2009).

These relaxometry changes are associated with decreased water proton availability and movement during fixation.

1.7.2. Subjects' age at death

Few studies have been specifically performed evaluating any impacts of adult or aged subjects' ages on relaxometry or iron contents. In general, these effects have only been determined from young, through to adult and old patients, where a steep increase in iron is detected for the first 20-30 years of age, until iron levels plateau (Hallgren and Sourander, 1958). Similar observations for T2 relaxation with age, as that in the Hallgren and Sourander study, have been observed (Pujol *et al.*, 1992, Schenker *et al.*, 1993). More recently however, an age dependent effect on normal iron contents has been observed in adult samples, which was also dependent on gender (Ramos *et al.*, 2014).

2. Thesis Aims, Objectives and Hypotheses

The overall aim of this thesis is to evaluate the application of MRI methods to non-invasively and accurately, detect and quantify iron during neurodegeneration. This work is the first to link iron assessment using MRI in an *in vitro* model with *ex vivo* post-mortem tissue and *in vivo* assessment of iron, within the same work. This work also provides further validation of studies which have so far provided inconclusive and conflicting results with respect to detectable changes in iron content in the brain during neurodegenerative diseases. It is also the first to demonstrate and spatially assess elemental iron levels in the medial temporal gyrus, a region involved in Alzheimer's disease alongside MRI data from the same region and includes a greater number of both control and Alzheimer's disease human tissue samples than other studies, giving greater statistical power in the conclusions being drawn.

Specific objectives are detailed in the relevant chapter for each study described in this thesis.

Brain iron content appears to be elevated in neurodegenerative diseases (see section 1.4.1) and hence there is great interest in measuring iron non-invasively within the brain (see section 1.6.5). Evaluation of iron content by MRI in live, biological tissue however can be complex due to the heterogeneous localisation and forms of iron (see section 1.3.1), as well as the varied tissue environments. Thus, in the first instance, the ability of MRI to measure iron in a simple model using

agarose gel standards containing various concentrations of iron, will be assessed. Having explored the relationships between various MRI metrics with different iron concentrations and forms in simple *in vitro* models, the associations of iron with these MRI measures will be assessed in neurodegeneration in humans and in an iron induced mouse model of neuronal death.

Whilst there is consistency in the use of MR methods as surrogate measures of iron during neurodegeneration, most involve clinical studies where correlation with iron is performed against previously published post-mortem iron data (see section 1.6.5), or using histochemical Perl's stain (see section 1.5.1). Whilst Perl's stain provides important characterisation of iron localisation, this technique may be limited by non-specific staining and non-linear responses to varying iron concentrations, limiting analysis of the precise impact of iron content on MRI. Thus, the second objective of this project is to quantitatively assess iron content using SR-XRF in AD compared with control tissue, and to correlate this with the detection of iron using MRI, for each group. This assessment was focussed on material from the medial temporal gyrus (MTG) given this region's involvement in AD pathology (see section 1.2.1), as well as the presence of both WM and GM tissue in this region. The presence of both WM and GM in the MTG allows comparisons of influencing factors within human tissue that can also affect iron detection using MRI measurements, such as myelin content (see section 1.6.5.6). These observations can help understand how MRI measurements are affected by iron content in the brain, within different tissue types.

Finally, as it is impossible to validate iron-sensitive MR acquisition methods in the brain and to assess neurodegeneration directly due to iron *in vivo* in a clinical environment, an animal model will be utilised (see section 1.4.4). Animal models provide a useful tool to perform investigations within a controlled, *in vivo*, system and thus, the third objective of this project will be to validate iron-sensitive MR measurements *in vivo* and understand how iron may cause neuronal cell death. This study will be performed by directly injecting ferric citrate bilaterally into the mouse hippocampus, to explore the direct effect of iron induced neuronal death, without the detrimental effects associated with transgenic animal models of neurodegeneration that also give rise to iron overload.

The hypotheses for this work are that:

- Iron-sensitive MRI relaxometry methods will show strong, positive correlation to known amounts of iron in solution, or associated with ferritin, in simple agarose standards.
- Iron-sensitive MRI relaxometry methods will positively correlate with SR-XRF elemental mapping of iron in control and AD post-mortem human MTG.
- Myelination will affect iron-sensitive MRI relaxometry methods in control and AD post-mortem human MTG.
- Iron sensitive MRI relaxometry methods will be able to quantify, and will correlate with, iron content detected by SR-XRF in an iron induced animal model of neuronal cell death.

- Iron content will show correlation to pathology severity, assessed using animal behaviour methods and histological staining for markers of neuronal death and neuroinflammation.

3. Materials and Methods

3.1. Materials

3.1.1. Animals

Male C57Bl/6 mice were used in all animal studies performed and were obtained from Harlan (Bicester, UK). Animal studies were performed in accordance with the Animals (Scientific Procedures) Act 1986 (UK) under project license (PPL) number 70/7085 and personal license (PIL) number 70/24270. All mice were housed in pairs in standard cages under a 12 hour light and dark cycle with *ad libitum* access to RM1 food pellets (SDS, Essex, UK) and water.

3.1.2. Reagents

The following reagents were purchased for performing laboratory experiments.

Agarose (low melting point; Life Technologies Ltd, UK), ferric chloride (Sigma, Poole, UK), ferrous chloride (Sigma, Poole, UK), hydroxylamine hydrochloride (Sigma, Poole, UK), 1,10-phenanthroline (Sigma, Poole, UK), sodium acetate (Sigma, Poole, UK), QG buffer (Qiagen, Venlo, Netherlands), ferritin from equine spleen in saline (Sigma, Poole, UK), sodium citrate (Sigma, Poole, UK), sucrose (Sigma, Poole, UK), phosphate buffered saline (PBS) tablets (Oxoid Ltd, Basingstoke, UK), sodium azide (NaZ) (Sigma, Poole, UK), sodium hydroxide (BDH, UK), 12M hydrochloric acid (HCl) (Fisher Scientific, UK), neg-50 cryoembedding medium (Thermo Scientific, UK).

The following reagents and antibodies were used for histological and immunohistochemical assessment.

Xylene (general purpose grade; Fisher Scientific, UK), 30% solution hydrogen peroxide (Sigma, Poole, UK), tris (hydroxymethyl) methylamine powder (VWR International, Leicestershire, UK), triton-X100 (Sigma, Poole, UK), NaCl (VWR International, Leicestershire, UK), normal donkey serum (Jackson Laboratories, UK), rabbit polyclonal anti-Iba-1 antibody (019-19741; Wako Pure Chemical Industries, Richmond, VA), cresyl violet (VWR International, Leicestershire, UK), luxol fast blue (Sigma, Poole, UK), lithium carbonate (Sigma, Poole, UK), haematoxylin (VWR International, Leicestershire, UK), Immpact DAB peroxidase substrate kit (Vector Laboratories, UK), skimmed milk powder (SMP) (Marvel, UK), 100% industrial methylated spirit (IMS) (Fisher Scientific, UK), 100% acetic acid (VWR International, Leicestershire, UK), absolute ethanol (Fisher Scientific, UK), DPX mountant (Sigma, Poole, UK), swine anti-rabbit IgG (DAKO, High Wycombe, UK), anti-rabbit IgG VECTASTAIN Elite avidin-biotin peroxidase complex kit (ABC kit) (Vector Laboratories, UK), Impress Reagent ready-made kit horse anti-mouse peroxidise-conjugated IgGs (Vector Laboratories, UK).

The following reagents were purchased for performing animal work and surgeries.

5% EMLA® cream (25mg/g Lidocaine, 25mg/g Prilocaine; AstraZeneca UK, Luton, UK), Lacri-lube preservative-free eye ointment (Allergan Ltd, Marlow, Bucks, UK), Vetergesic® (0.3mg/ml buprenorphine hydrochloride; Reckitt Benckiser Healthcare

(UK) Ltd, York, UK), heparin sodium 5,000 IU/ml (Wockhardt Ltd, UK), 100% w/w isoflurane (Abbott Animal Health, Kent, UK), Vetasept 0.75% w/w Povidone-Iodine solution (Animalcare Ltd, York, UK), Medical air and Medical oxygen (BOC Ltd, Guilford, Surrey), 4% paraformaldehyde (Pioneer Research Chemicals, UK), Aquapharm® 0.9% sterile saline solution (Animal Care, York, UK), Euthatal (sodium pentobarbital; Merian Animal Health, UK), Vetasept chlorhexidine clear spray (Animalcare Ltd, York, UK).

The following reagents were purchased for performing MRI scanning:

Galden® perfluorinated fluid PFS-1 (Solvay Solexis, UK).

3.1.3. Equipment

MR hardware

The following equipment was used during both *in vivo* and *ex vivo* MRI scanning:

7T Agilent MRIS system (Agilent Technologies, Oxford, UK), 43 mm inner diameter (ID) quadrature volume coil (MRL, Oxford), 26 mm/ 33 mm/ 39 mm quadrature coils (Rapid Technologies, Ohio, US), 25 mm quadrature coil (PulseTeq, Surrey, UK).

Physiological monitoring

Blease Frontline Genius and Blease vaporiser (Spacelabs Healthcare, WA, USA), Fan Module (High Output) (SA Instruments, NY, USA), Heater Module (SA Instruments, NY, USA), ECG/Temperature module (SA Instruments, NY, USA), Control/ Gating Module (SA Instruments, NY, USA).

The following items were only required for *ex vivo* MRI scanning:

1 ml, 10 ml, 20 ml and 30 ml syringes (BD, NJ, USA), 1 ml heparinised syringes (Protech Medical Ltd, Glossop, UK), parafilm (Bemis Flexible Packaging, Neenah, WI), single edge razor blades (Fisher Scientific, UK).

Surgical Procedures

Equipment required for animal surgical procedures included:

Stereotaxic frame (David Kopf Instrument, Tujunga, CA) with platform (Stoelting, Wood Dale, IL, USA), Contura electric razor (Wella, UK), 2.5µl Hamilton syringe (Hamilton Medical, Reno, NV), microsyringe pump and Micro4 pump controller (World Precision Instruments, Sarasota, FL, USA), homeothermic blanket control unit and blanket (Harvard Apparatus, Cambridge, MA, USA), V-Lux 1000 swan neck lighting unit (Volpi, USA), Microtorque II drill unit and Tech 2000 drill handpiece (Smooth N Sleek SDN BHD, Penang, Malaysia), micro drill steel burr (0.5mm) (Hager & Meisinger GmbH, Neuss, Germany), SES Little sister 3 autoclave unit (Eschmann Equipment, West Sussex, UK), sterile gloves (Latex Biogel, Mölnlycke Health Care

Limited, Bedfordshire, UK), cotton buds (Johnson and Johnson, Maidenhead, UK), scalpel (Swann-Morton Limited, Sheffield, UK), 0.20µm pore filter (Sartorius Stedim Biotech, UK), 4-0 vicryl sutures (Ethicon, USA), Fear Conditioning System (TSE Systems GmbH, Bad Homburg, Germany), metal gavage needle of 0.9mm gauge (Instech, PA, USA), perfusion equipment (AutoMate Scientific Inc., CA, USA).

Laboratory based work required the following equipment:

Leica SCN400F slide scanner (Leica, UK), pH meter 240 (Corning, MA, USA), benchtop centrifuge 5415D (Eppendorf, Stevenage, UK), Micro Centaur bench top centrifuge (MSE (UK) Ltd, London, UK), vortex (Jencons PLC, UK), Microm HM550 cryostat (Thermo Scientific, MA, USA), SmartSpec Plus spectrophotometer (Bio-Rad Laboratories, CA, USA), plastic cuvettes (VWR International Leicestershire, UK), magnetic stirrer (Jencons, PLC, UK), staining tray (VWR International, Leicestershire, UK), superfrost plus glass microscopy slides (Fisher Scientific, UK), 4µm thick Ultralene® (SPEX SamplePrep, NJ, USA), C35 disposable microtome blades (Cellpath, UK), coverslips (VWR International, Leicestershire, UK), 15ml and 50ml centrifuge tubes (Corning, MA, USA), 50ml and 1000ml measuring cylinders (VWR International, Leicestershire, UK), Costar® 10ml stripette serological pipettes (Corning, MA, USA), glass bottles (VWR International, Leicestershire, UK), 0.5ml, 1.5ml and 2ml tubes (Eppendorf, Stevenage, UK).

3.1.3.1. Customised equipment

Mouse brain holder

In order to increase efficiency of scanning, a brain holder was developed to scan multiple brains within one acquisition time, rather than single scanning of one brain at a time (Figure 3-1) by modification of a 20 ml syringe tube.

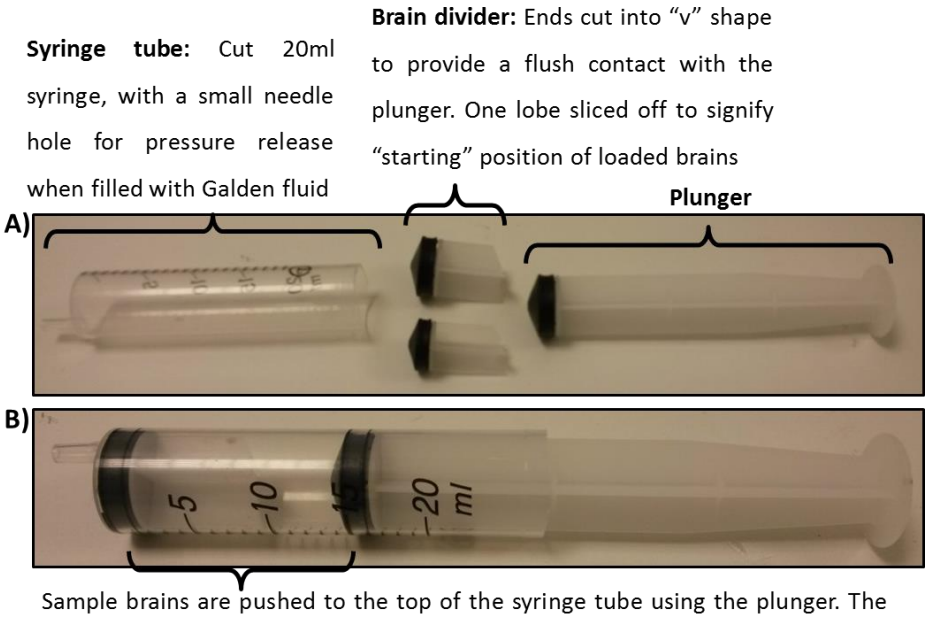

Figure 3-1 Customised brain holder

(A) Individual components of the brain holder are shown, comprised of the syringe tube, brain divider and plunger. (B) Brain holder with the components together for scanning up to four brains at once.

A plunger from either a 10 ml or 20 ml syringe was cut to a length of approximately 3 cm to allow a mouse brain to sit within the length of the divider (Brain divider,

Figure 3-1A) and one lobe of the divider was sliced off to signify a “number 1” position, allowing identification of each brain within the holder to the user. Loading of the brains was performed from position 1, next to the sliced lobe of the divider and the divider pushed to the end of a 20 ml syringe tube with the end cut off (Figure 3-1A). Parafilm was used to seal the top of the syringe tube before Galden® was poured in. The 20 ml plunger was then used to seal the Galden® in at the end and pushed all the way down to the brain divider. The needle hole allows the plunger to be pushed down without a build-up of pressure in the tube. Any remaining bubbles could be removed by adding Galden® using a small syringe with needle into the needle hole. This hole in the tube was then sealed using tape, followed by using parafilm to ensure no leakage from the brain holder during scanning.

Custom-made XRF slides

Custom made slides were used for XRF elemental analyses, due to the high sensitivity of this analytical technique and the possibility of metal contamination of samples. Acrylic slides with identical dimensions to normal histological slides (76 x 25 mm) were made, with a square hole in the centre of the slide with dimension 50 x 18 mm (Vet Tech solutions, UK) (Figure 3-2). Acrylic slides were first washed in 100% IMS before Ultralene® XRF film was glued across the slides so that samples could be mounted in the area with the gap. This provided an open area for XRF analysis of tissue samples, without any possibility of contamination from glass, or any other medium.

Figure 3-2 Image of custom-made slide for XRF elemental mapping

An acrylic slide with a gap of 50 x 18 mm was custom made for XRF elemental mapping and Ultralene® XRF film glued over the top to mount samples within the open region of the slide, limiting possible contaminants during analysis.

3.1.4. Software

Computer software used included; JIM 5.0 (Xinapse Systems, Alwincle, UK), ImageJ (National Institute of Health, Maryland, USA), FSL (FMRIB Software Library, Oxford, UK), PyMCA (ESRF, France), Prism (GraphPad, SD, USA) and cocor (comparing correlation) (Diedenhofen and Musch, 2015).

3.1.5. Preparation of Solutions

Heparin solution for cardiac perfusions

1. 1 ml Heparin (5000 IU/ml) was added per 100 ml saline producing a final concentration of 50 IU/ml.

70% ethanol solution

1. 30 ml distilled water (dH_2O) added to 70 ml ethanol in a measuring cylinder.

PBS and PBS + sodium azide (0.05%) solutions

1. Add one PBS tablet per 100 ml dH_2O.
2. Add a stirring magnet into the bottle and stir for 5 minutes until the tablet fully dissolves.
3. If sodium azide (NaZ) was also required to be added to the PBS to help prevent bacterial growth during long-term storage of samples, 0.05 g sodium azide was added per 100 ml PBS.

30% sucrose + sodium azide (0.05%) solution

1. Weigh out 150 g sucrose powder.
2. Add the powder to 400 ml PBS in a bottle.
3. Add a stirring magnet into the bottle and stir the solution for 5-10 minutes until the sugar fully dissolves into the PBS.
4. Weigh out and add 0.25 g Sodium Azide to the bottle.
5. Pour the clear solution into a measuring cylinder and top up with PBS to 500 ml.
6. Pour back into bottle and store at 4^{o}C until ready to use.

2% agarose solution

1. 1 g of agarose is weighed per 50 ml H_2O
2. Shake bottle well.
3. Dissolve agarose powder by microwaving for approximately 1 minute, until the solution begins to boil and becomes clear.
4. Allow the agarose solution to cool to near gelling point before use.

7.5% gelatin solution

1. 3.25g of gelatin is weighed per 50ml dH_2O.
2. Shake bottle well.
3. Dissolve gelatin powder by microwaving for approximately 1 minute, until the solution begins to boil and becomes clear.
4. Allow the gelatin solution to cool to near gelling point before use.

100 mM ferric or ferrous iron stock solution

1. Weigh out each form of iron to formulate a 100 mM solution in 10ml dH_2O (Table 3-1).
2. 10ml of dH_2O was then added and solutions inverted and vortexed to ensure the iron fully dissolved to formulate 100 mM stock solution

Table 3-1 Table of ferric and ferrous chloride formulae, molecular mass and weights measured for producing top iron stock solutions at 100 mM

	Formula	MW	Weight measured (g)
Ferric chloride (Fe^{3+})	$FeCl_3$	162.3	0.1623
Ferrous chloride (Fe^{2+})	$FeCl_2.4H_2O$	198.8	0.1988

MW = Molecular Weight

1,10-phenanthroline solution

1. Add 0.1802 g 1,10-phenanthroline to 200 ml dH_2O to make 5 mM stock.
2. Solution heated to 60^{o}C for 1 – 2 hours until 1,10-phenanthroline was fully dissolved.

Sodium acetate solution

1. Add 10.206 g sodium acetate to 75 ml dH_2O to make 1 M stock.

Hydroxylamine hydrochloride solution

1. Add 2.6059 g hydroxylamine hydrochloride to 50 ml dH_2O to make 0.75 M stock.

Tris buffer saline (TBS) (+/- triton X-100) solutions

1. Made from 20 mM Tris base, 150 mM NaCl, pH: 7.4
2. Add 2.422 g Tris base to approximately 950 ml dH_2O in a bottle.
3. Add 8.766 g NaCl to the Tris base solution.
4. Add a stirring magnet into the bottle and stir the solution until powder fully dissolves.
5. Adjust the pH of the solution to 7.4 by adding HCl.
6. Add dH_2O up to 1000 ml (TBS(-)).
7. TBS(+) made by addition of 0.2% triton X-100. Triton X-100 is used to make membranes permeable during IHC.

Blocking buffer solution

1. Add 10 ml dH_2O to powdered Normal Donkey serum, according to manufacturer's instructions.
2. 10% Normal Donkey serum added into 90% TBS(+).

Primary and secondary antibody buffer solution

1. 5% Normal Donkey serum added into to 90% TBS(+).

DAB solution

1. DAB solution made up by adding 1 drop DAB reagent to 1ml DAB diluent, according to manufacturer's instructions.

0.1% luxol fast blue

1. Add 0.1 g luxol fast blue to 100 ml IMS.
2. Add 0.5 ml 10% aqueous acetic acid and mix solution well before use.

0.05% lithium carbonate

1. Add 0. 05 g lithium carbonate to 100 ml dH_2O.

Sodium citrate buffer for antigen retrieval

1. Add 1.92 g/L sodium citrate into dH_2O to make 10 mM solution.
2. Adjust the pH to 6 using sodium hydroxide solution whilst stirring with a magnet.

Nissl stain

1. Weigh 0.05% cresyl fast violet powder into dH_2O, with 0.1% acetic acid.
2. Solution is heated up to 56^{o}C in the microwave for full dissolution. Care was taken not to overheat the solution above this temperature. The solution was filtered prior to use to remove large clumps of cresyl violet in the solution.
3. Prior to use, 0.5 ml of 10% acetic acid per 100 ml of cresyl violet solution is added and mixed to make up the working solution.

Ferric citrate solution formulation for animal injections

The pH of ferric and ferrous sulphate solutions were measured dissolved in PBS, dH_2O, or saline (Table 3-2). The pH meter was calibrated at pH 4.00, 7.00 and 10.00, prior to performing these measurements.

Table 3-2 pH values of different ferric and ferrous iron solutions tested

	Concentration (mM)	PBS	dH_2O	Saline
Ferrous Sulphate	0	7.19	5.02	4.69
	0.5	7.01	4.05	4.40
	1	6.85	4.09	4.37
Ferric Sulphate	0	7.21	5.20	4.76
	2	6.20	2.47	2.75

Both ferric and ferrous iron addition led to lowering pH values, which cannot be injected into the brain due to greater acidity. Furthermore, iron precipitated when adjusting the pH to 7.

Therefore, ferric citrate was synthesised ourselves by addition of aqueous ferric chloride solution with equimolar sodium citrate (Armstrong *et al.*, 2001). 4 mM and 2 mM ferric citrate solutions were created for injections, whilst 4 mM sodium citrate solution was used for control dosing.

1. Ferric chloride powder was weighed out to create a 2 x molar concentration of iron required (i.e. 8 mM ferric chloride for 4 mM final concentration of ferric citrate).

2. Sodium citrate at equimolar concentration to the iron solution was made (i.e. at 8 mM).
3. Equal volumes of ferric citrate and sodium citrate solutions were combined, to form a 4 mM ferric citrate solution.
4. The pH was adjusted to pH 7.4 using aqueous sodium hydroxide.
5. Solutions were filter-sterilized using a 0.20µm pore filter, prior to injections.

3.2. Methods

3.2.1. Iron agarose standards

Iron standards were formulated in 2% agarose to allow MRI relaxometry to be performed in a model substance with relaxivity values close to that of brain tissue.

3.2.1.1. Iron solutions

In the first set of studies, 100 mM ferric chloride or ferrous chloride solutions were formulated in 10 ml ultrapure MilliQ water. These solutions were used as the highest stock dilutions. 40, 20, 10, 5 and 2 mM solutions were produced by serial dilution of the 100 mM stock iron solutions providing a consistent dilution factor within each study (Table 3-3). These standards were scanned three times.

Table 3-3 Table of dilutions for production of iron agarose standards

Iron concentrations (mM)	100	40	20	10	5	2	0
Dilution factor for serial dilution	-	2.5	2	2	2	2.5	-
Serial dilution volume (ml)	10	1	1	1	1	1	-
MilliQ water volume (ml)	-	1.5	1	1	1	1.5	10
Dilution factor into 2% agarose	20	20	20	20	20	20	20
Final concentration (mM)	**5**	**2**	**1**	**0.5**	**0.25**	**0.1**	**0**

In a subsequent study, 100 mM ferric chloride or ferrous chloride solutions were produced in 10 ml ultrapure MilliQ water for a two-fold serial dilution, to provide further top solutions of 50, 25, 12.5, 6.25 and 3.13 mM. These provided final iron concentrations of 5, 2.5, 1.25, 0.63, 0.31 and 0.16 mM in the agarose standards. A control agarose standard with 0 mM iron was always prepared alongside iron concentrations to ensure reliability and reproducibility of iron agarose standard assessments.

Monitoring of ferric and ferrous iron pH

The pH of iron agarose standards were measured to evaluate any impact on relaxometry parameters. Measurement of the pH of ferric and ferrous iron directly in agarose was not performed due to the possibility of contaminating the pH sensor with agarose. Therefore, aqueous solutions of the ferric and ferrous iron were

formulated at the same concentrations as the final agarose standards and the pH of these solutions measured as a surrogate model to the agarose standards.

Validation of the oxidation states of iron in agarose standards

The oxidation states of iron in the agarose standards were validated using 1,10-phenanthroline. 1,10-phenanthroline turns red in the presence of ferrous (Fe^{2+}) iron ions and can be measured spectrophotometrically at an absorbance of 510nm. Hydroxylamine hydrochloride can be added into the assay mixture to reduce ferric (Fe^{3+}) iron ions to the ferrous form, for subsequent detection with 1,10-phenanthroline.

To validate the oxidation states of iron in the agarose standards, 100 µl of each agarose standard was sliced off using a clean metal blade and the slice transferred into a centrifuge tube. 300 µl QG buffer was added to each tube and allowed to heat up to 60^{o}C for 10 minutes. This QG buffer dissolves the agarose and prevents gelling under these conditions. Sodium acetate was added to 20 mM final concentration and the 1,10-phenanthroline to 0.75 mM final concentration. Water was added to a final assay volume of 5 ml. Hydroxylamine hydrochloride was not added to this assay mix to prevent the reduction of iron from the ferric to ferrous form and therefore allow validation of the oxidation states of iron in the standards. Final absorbance measurements were adjusted for the slight variations in weight of agarose standard dissolved.

Validation of iron content present in agarose standards

To validate the accuracy of iron content present in the agarose standards, a standard curve of ferrous iron was formulated at the following concentrations; 10.00, 7.50, 5.00, 3.75, 2.50, 1.25, 0.63, 0.31, 0.16 and 0.00 mM. The 1,10-phenanthroline assay was performed as above, with the addition of 0.015 M hydroxylamine hydrochloride to ensure the full reduction of iron to the ferrous form for reaction with 1,10-phenanthroline.

The absorbance was measured spectrophotometrically at a wavelength of 510 nm.

Examination of iron agarose standards for precipitation

Approximately 200 µl of each concentration of freshly made ferric and ferrous iron agarose standards were transferred to glass microscopy slides and a coverslip added on top prior to gelling. Once the agarose had gelled, the slides were evaluated using microscopy at 40X magnification for the appearance of iron precipitation or accumulation.

Ferric/ ferrous iron combinations

Combinations of ferric iron to ferrous iron agarose standards were formed to evaluate how the two forms of iron affect MRI measurements. These were made first by making 100 mM combinations of ferric/ ferrous iron at 100/ 0, 80/ 20, 50/

50, 20/ 80 and 0/ 100 %. These 100 mM stock solutions were then each serially diluted by two-fold, as described above.

Ferritin iron agarose standard

Ferritin iron agarose standard was formed by using ferritin from equine spleen (see materials). The iron content of ferritin was provided by the manufacturer and diluted to a stock solution of 100 mM iron content, for serial dilution by two-fold using dH_2O, alongside fresh ferric iron chloride and ferrous iron chloride agarose standards, as study controls.

3.2.1.2. 2% agarose iron standard samples

200 µl of each ferric or ferrous iron solution was transferred into a new 15ml centrifuge tube, and freshly made 2% agarose added up to 4ml to provide a 1:20 dilution of stock iron solutions. Solutions were then gently inverted two or three times to ensure full mixing of the iron solutions with the agarose.

Prior to full gelling, 1 ml syringes were filled using each ferric or ferrous 2% agarose solution and then allowed to cool and gel fully in an upright orientation at room temperature. Once solid, the ends of each syringe were covered with parafilm to prevent water loss from the gels over time. These standards were each labelled and stored at 4^oC until use.

3.2.1.3. MRI relaxometry

MRI acquisition

The seven 1 ml syringes were held together tightly using autoclave tape for all the standards (Figure 3-3). These were placed into the 25 mm ID RF coil and secured. Relaxometry assessment was performed using a multi-slice spin-echo (SE) sequence for T1 and T2 measurement; T1 measured using TR: 70, 100, 150, 200, 400, 600, 800, 1200, 2000, 4000 and 8000 ms and TE: 9 ms, T2 measured using TR: 4000 ms, TE: 9, 12, 15, 20, 25, 30, 45, 60, 90, 120, 180 and 250 ms. FOV = 26 x 26 mm, Matrix = 128 x 128, Averages = 1, Thickness = 2 mm, 5 adjacent slices acquired. A multi-echo (ME) SE sequence was also used to assess T2, to provide a faster T2 measurement than using a series of single echo time SE acquisitions. Acquisition parameters for this sequence were TR: 4000 ms, first TE = 9 ms, with 16 echos equally spaced by 9 ms.

T2* was assessed using a single echo gradient-echo (GE) RF-spoiled sequence with TR: 4000 ms, TE: 3, 6, 9, 12, 15, 20, 30, 50, 75, 100 and 150 ms. FOV = 26 x 26 mm, Matrix = 128 x 128, Averages = 1, Thickness = 2 mm, 5 slices acquired, flip angle = 20^{o}. A multi-gradient-echo (MGE) sequence was also used to assess T2*, to provide a faster approach for T2* measurement than using a series of single echo time gradient-echo acquisitions. TR: 2000 ms, first TE = 2.5 ms, with equally spaced TEs = 6 ms, 5 echoes, flip angle = 90^{o}. Both GE and MGE sequences were acquired with thickness = 2 mm and 5 contiguous slices acquired, as well as thickness = 0.5 mm over 20 contiguous slices, due to imaging artefacts observed in 2mm thick slices (see section 4.4.2).

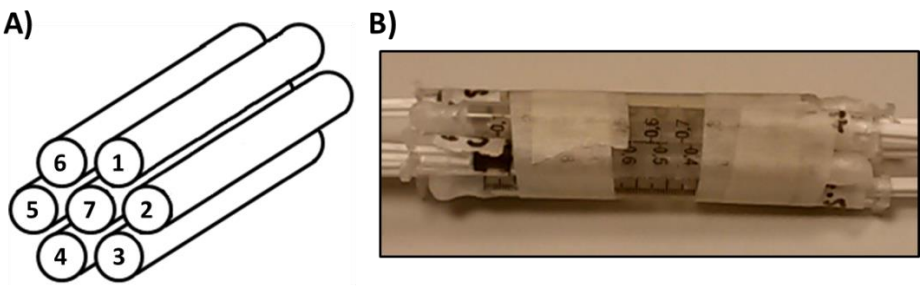

Figure 3-3 Schematic diagram of iron agarose standards MRI acquisition

(A) Schematic diagram of syringes showing how standards were placed into the RF coil for scanning and (B) photograph of iron agarose standard syringes taped together.

MRI relaxometry analysis

Calculation of relaxometry maps was performed by a pixel-by-pixel least-squares fitting method using JIM 5.0. Images were first converted to ANALYZE 7.5 format in JIM 5.0 and T1, T2 and T2* maps generated by fitting to $y=M_0*[1-e^{(-TR/T1)}]$, $y=M_0*e^{(-TE/T2)}$ and $y=M_0*e^{(-TE/T2^*)}$, respectively, where y is the voxel intensity and M_0 is the proton density at each corresponding TR or TE. R1, R2 and R2* maps were generated by calculating the reciprocal of T1, T2 and T2* maps. R2' maps were calculated by subtracting SE R2 maps from GE R2* maps.

3.2.1.4. Analysis

Statistical testing was performed in Prism. Correlations were assessed using r^2 linear regression analysis and Pearson's correlation, with significance level set at $P \leq$

0.05. Number of asterisks denotes significance level; * $P \leq 0.05$, ** $P < 0.01$, *** $P < 0.001$ and **** $P < 0.0001$. Bland-Altman plots were produced by calculating the percentage difference between the two MR imaging methods (either SE R2 with ME R2, or GE R2* with MGE R2*) against the average of the measurements. Multiple t-tests were used to compare the relaxometry values at each concentration of ferric to ferrous iron, with significance assessed using Holm-Sidak to $\alpha \leq 0.05$. Molar relaxivities (r_1, r_2, r_2* and r_2') were assessed as the gradient of linear correlation regression lines, as relaxivity values per iron concentration ($s^{-1}mM^{-1}$). One-way ANOVA was used to assess differences between the relaxivity slopes of the different proportions of ferrous to ferric iron contents.

3.2.2. Assessment of control and AD human MTG using MR relaxometry and SR-XRF elemental iron mapping

Assessment of post-mortem human brain tissue was performed by using medial temporal gyrus (MTG) samples from control subjects and comparing against samples from the same region of Alzheimer's disease (AD) patients. The post-mortem samples were obtained from the MRC London Neurodegenerative Diseases Brain Bank and consent was obtained from all subjects for autopsy, neuropathological assessment and research. Tissues were taken for histological and neuropathological assessment for degenerative diseases, performed in accordance with institutional guidelines. AD pathology was classified using CERAD (Consortium to Establish a Registry for Alzheimer's disease) pathological criteria assessing the presence of plaques (Alafuzoff *et al.*, 2008), with staging based on Braak and Braak

classification (Braak and Braak, 1991). All AD samples used in this study showed Braak stages V-VI. Control cases are defined as having no history of neurological disease or cognitive decline clinically, and showing no, or only minor age-related, pathology following neuropathological assessment.

3.2.2.1. MRI relaxometry

Sample preparation

Post-mortem formalin-fixed human brain samples (approximately 15mm x 15mm x 5mm) from the MTG of Alzheimer's Disease (AD) patients (n=15) and control subjects (n=15) were age, fixation time and post-mortem interval (PMI) matched (see section 1.7; see Appendix B for full list of human samples).

Samples were carefully wrapped in tissue paper to limit susceptibility and inhomogeneity artefacts from the sample holder cassettes, and immersed in Galden® in a 50 ml tube. Samples were oriented perpendicular to the magnetic field for MRI. After MRI, samples were prepared for elemental mapping by SR-XRF and histological analysis.

MRI Acquisition

Human brain samples underwent MRI using the 43mm ID quadrature volume coil. T1-relaxometry was performed using a spin-echo saturation recovery sequence with TR values of 300, 500, 800, 1200, 2000 and 4000 ms, and TE 12 ms. T2-

relaxometry was also performed as above, but using TEs of 12, 15, 20, 25, 30, 45 and 60 ms, with a TR of 4000 ms. T2*-relaxometry was performed using a single echo gradient-echo sequence with TE values of 5, 10, 15, 20, 25, 30 and 50 ms and a TR of 4000 ms. For T1-, T2- and T2*- relaxometry measurements, FOV = 28 x 28 mm, matrix size = 256 x 192, 2 averages were used and 13 contiguous 0.5 mm thick slices obtained. T2-weighted MRI was also performed to obtain good white and grey matter contrast images for placement of regions of interest (ROIs), at TR/ TE = 4000/ 30 ms.

Relaxometry map generation

All quantitative MRI measures were calculated as described in section 3.2.1.3.

3.2.2.2. Synchrotron-radiation X-ray fluorescence elemental mapping

Sample preparation

Following MRI, the samples were processed on a 40 hour cycle going through alcohol, then chloroform, and then infiltration using a paraffin wax blend (70% soft paraffin wax, 20% beeswax and 10% dental wax). Molten paraffin wax was then used to embed the tissue in moulds and allowed to cool. Sample blocks were sectioned using a microtome to the central region of each brain sample and a 7 µm section was mounted onto the custom made XRF slides with Ultralene® film (Figure

3-2) for synchrotron-radiation XRF on the I18 beamline at the Diamond Light Source synchrotron (Didcot, Oxfordshire, UK).

SR-XRF acquisition

A ROI containing both grey and white matter of each sample was selected for XRF using the T2-weighted image. The beam energy was tuned to 11 keV and focussed to 100 x 100 μm and the sample scanned at constant time per pixel in a rastor fashion. Samples were mounted at 45^{o} with respect to the incoming X-ray beam in the plane of the orbiting electrons to minimise scatter contribution to the detected signal. Data collected is in the form of a spectrum showing the characteristic emission radiation from individual elements in the sample. Quantitative maps were generated using PyMCA (ESRF, France) to fit the characteristic Kα and Kβ peak areas for each element and quantify the iron content using the peak at energy level 6.40 keV. Quantitative data was normalised to data obtained from a reference metal film (AXO, Dresden, GmbH) and adjusting the flux accordingly.

Following XRF spectra acquisition across samples, the output data were converted to TIF images using a script to substitute each pixel with acquired parts per million (ppm) values.

3.2.2.3. XRF-MRI correlation

Registration

The T2-weighted image was aligned with SR-XRF elemental iron maps by eye to a position of similar orientation to the corresponding iron elemental maps, using cropping, resizing and transform tools in ImageJ. Relaxometry maps were then registered according to the same slice and settings as required for the T2-weighted image.

Group comparisons

For each brain sample, regions of interest (ROIs) were manually selected around all the white (WM) or grey matter (GM) from the T2-weighted image using JIM 5.0. ROIs were drawn with a 1-2 pixel gap from the tissue boundaries, to avoid partial volume effects at these interfaces. The ROIs were then overlaid for each of the R1, R2, R2* and R2' maps and a comparison of WM to GM was performed. Data from each WM and GM region was then separated between AD and control to compare group differences. Minor adjustments were made to ROIs applied in R2* maps, to avoid the enhanced susceptibility artefacts at the edges of samples, likely due to small air bubbles caught between the sample and paper tissue interface.

Correlation

Twenty-four square ROIs of 3 x 3, or 5 x 5 pixels were placed across the white and grey matter regions of elemental iron maps and the mean intensities and standard deviations generated from each using ImageJ. Identical ROIs were placed in the same positions across T2-weighted images and then overlaid onto R1, R2, R2* and R2' maps to extract mean values and standard deviations for correlation of each ROI between iron and relaxometry measurements. Twenty-four ROIs were used for this assessment to place an equal number of ROIs (eight) across each of the tissue regions identified; in the WM, MCL and dGM (see section 5.4.1), therefore avoiding bias when comparing correlations across samples.

3.2.2.4. Immunohistochemical assessment

Luxol fast blue (LFB) staining

Adjacent sections to that used for XRF elemental mapping were sectioned at 14 µm thickness and mounted onto glass microscopy slides for standard histopathological assessment. Following dewaxing using 100% Xylene, samples were part rehydrated in 95% IMS, and stained overnight using luxol fast blue solution at 56^{o}C. Sections were then washed in dH_2O and differentiated using 0.05% lithium carbonate for 10 seconds. Differentiation was continued using 70% IMS until dye stopped coming out and then sections washed in dH_2O. Sections were counter stained using Nissl staining (0.05% cresyl fast violet solution; preheated to 60°C) for 3 minutes, before

differentiating in 95% IMS (with acetic acid) for 10-15 seconds. Slides were then dehydrated in 100% IMS and cleared in xylene for mounting with coverslips.

Histopathological analysis

Images of each sample were imaged using a Leica SCN400F slide scanner, acquiring at x40 magnification across each sample, at Institute of Neurology, University College London, UK. Images were obtained using auto-focus settings with a 65% compression for outputs, in the form of the .scn pyramidal tiff file format. Images were stored and could be retrieved using the Leica Digital Image Hub for correct orientation of samples and generation of magnified images.

Analysis of luxol fast blue staining in the human tissue sample was performed by first cropping, rotating and registering the histological images by eye against the iron elemental maps using ImageJ. Images then had their resolution reduced to the equivalent resolution as the iron elemental maps for each corresponding sample. Image intensities were then inverted to provide a measure of myelin content. Whole region ROIs (for WM and GM tissue) were drawn and mean intensities obtained. Furthermore, twenty-four similarly placed 5x5 pixel ROIs as those used on both elemental iron and relaxometry maps were redrawn onto the LFB images for a semi-quantitative correlation of iron to myelin staining.

3.2.2.5. Statistical data analysis

Differences in the R1, R2, R2* and R2' relaxometry measures and iron levels between whole white and grey matter regions were tested for statistical significance using Student's unpaired t-test or one-way ANOVA. In all comparisons, number of asterisks denotes significance level of unpaired data; * $P \leq 0.05$, ** $P < 0.01$, *** $P < 0.001$ and **** $P < 0.0001$. Paired t-test or repeated-measures one-way ANOVA were also used to evaluate the consistency of differences between regions within each individual sample. Number of hashtags denotes significance level of paired data; # $P \leq 0.05$, ## $P < 0.01$, ### $P < 0.001$ and #### $P < 0.0001$. These statistical measures were also used to evaluate differences in relaxometry or iron content between AD and control samples. Tukey's test for multiple comparisons was performed following one-way ANOVA testing. A value of $P \leq 0.05$ was considered statistically significant and all statistical tests were performed using Prism. Values are shown in mean ± standard deviation (SD).

Using results from the twenty-four square ROIs of 5 x 5 pixels each, correlation plots were calculated for each sample between iron and relaxometry values and r^2 correlation coefficients and gradients were used for assessment of correlation. Group comparisons were made from the mean r^2 values from each patient group.

To evaluate overall correlation of iron against different relaxometry measures, all the twenty-four ROI mean values from either AD or control samples were correlated together against each relaxometry measurement. Graphs show correlation coefficients with significance level assessed using Pearson correlation. In all correlations, * $P \leq 0.05$, ** $P < 0.01$, *** $P < 0.001$ and **** $P < 0.0001$.

Histopathological assessment using the twenty-four square 5 x 5 pixels was performed in a similar way as above, however using the luxol fast blue average values within the acquired image.

Correlation comparisons were performed using cocor software available online (Diedenhofen and Musch, 2015) and using Pearson and Filon's z comparison for statistical significance to $P \leq 0.05$.

3.2.3. MR detection of exogenous iron in the mouse hippocampus

3.2.3.1. Animals and treatment

Ten week old C57Bl/6J male mice were obtained and housed under a 12-hour light/ dark cycle, with *ad libitum* access to food and water. All procedures were performed in accordance with the Animals (Scientific Procedures) Act 1986.

3.2.3.2. Surgery

Preparation

To perform surgery under asepsis, all metal items to be used were sterilised by autoclaving at 141^{o}C with sonication prior to surgeries. The surgery table was wiped down using chlorhexidine clear and covered with a sterile drape. Equipment required for surgery was then placed onto the table, including; stereotaxic frame, heating unit and blanket, swan neck lighting unit, drill unit and drill and the syringe plunger pump. The heating blanket was placed below the platform of the

stereotaxic frame to help maintain animal body temperature whilst under anaesthesia. A sterile drape was also used to cover the animal for warmth and prevent contamination from other body areas. A sterile gown, hair net, mask and gloves were worn throughout the duration of surgeries.

Bilateral hippocampal injection

Mice were first weighed and randomly assigned to 3 groups (n = 6 per group); two groups received 2 mM and 4 mM ferric citrate injections, and one received 4 mM sodium citrate (control/ vehicle) solution. Anaesthesia was induced using 5%:95% isoflurane: oxygen and the head shaved to observe the skull location. The mouse head was then placed into the stereotaxic frame, with ear pins holding the head in place and anaesthesia was maintained with 1.5%: 98.5% isoflurane: oxygen for the duration of surgery.

100 µl Vetergesic analgesic was injected i.p to prevent pain to the animal and Lacrilube gel covered over the eyes to prevent drying and damage to the eyes, during the long surgical procedure. Sterile PBS was used to wipe loose hair away from the top of the head and iodine solution used to clean and sterilise the area of scalp for surgery. A small incision was made dorso-ventrally across the mouse head to expose the skull. Sterile PBS was used to clean the skull of excess iodine. The needle was placed gently onto the skull above each hemisphere to ensure a flat head orientation medio-laterally. If a difference in height greater than 0.2 mm was

observed between each hemisphere, the head position was adjusted slightly by moving each of the ear pins up or down.

The position of bregma was identified from the point in which the three skull plates join and was confirmed by placing the injection needle lightly on top, to observe a slight movement of all three skull plates (Figure 3-4A). Once confirmed, coordinates were recorded from the stereotaxic frame and injections were performed 2.1 mm caudal to bregma, ± 1.5 mm lateral to the midline (Figure 3-4B).

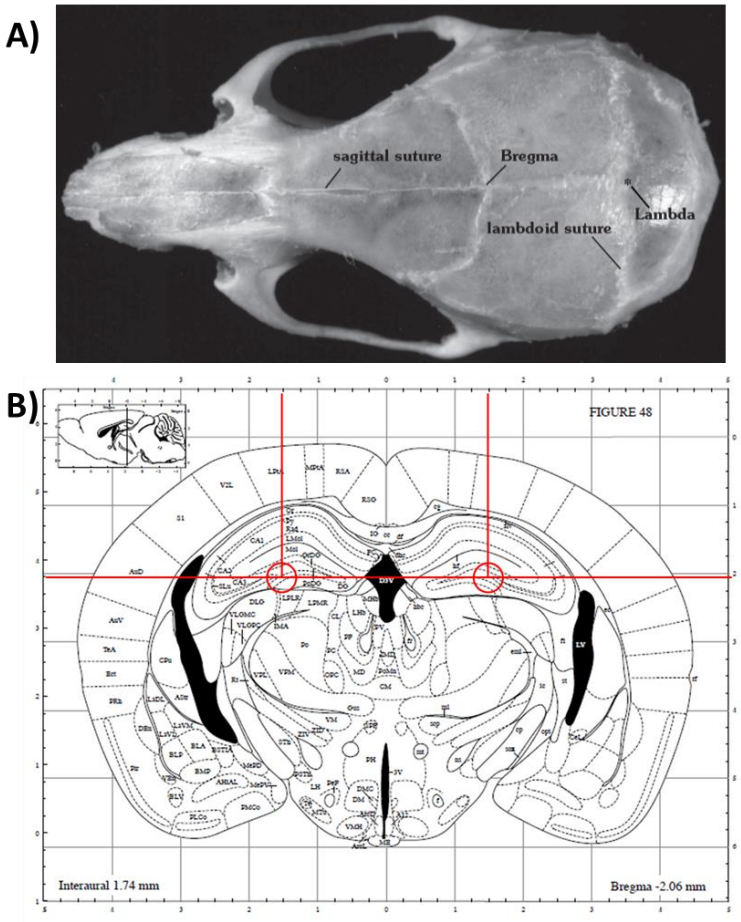

Figure 3-4 Positioning of ferric citrate injections into the mouse hippocampus

(A) Image of the skull highlighting the positions of bregma and the midline, used as markers for locating site of drilling, and (B) position in the hippocampus of the ferric

citrate injection (images obtained from the Paxinos Mouse Brain Atlas (Paxinos and Franklin, 2001)).

The drill bit was cleaned by dipping into 70% ethanol, followed by dipping into sterile PBS. A hole was then made in the skull by gently drilling at the confirmed sites of injection. The needle was inserted to 1.8 mm below the dura (Figure 3-4B) for a 500 nl injection at a rate of 500 nl/minute using the injection pump. Solutions were injected bilaterally into the hippocampus. After injection, the needle was left in place for an additional minute to limit leakage of solution within the needle tract. The needle was also lifted out from the brain very slowly over the course of a minute to prevent fluid being drawn out from the syringe. The skin over the skull was then sutured together using sterile 4-0 vicryl sutures.

Animals were allowed to recover in a warm box for 45 minutes after surgery, before being returned back into their cage with mashed pellets in water to aid recovery post-surgery. Published literature has shown serious side effects following iron injection (Armstrong *et al.*, 2001) and therefore mice were monitored daily during their recovery period. We observed minor seizures in 5 of the 12 treated mice (two in the 2 mM and three in the 4 mM iron group) immediately following surgery. No recurrent long term movement or behavioural effects were observed after the first 24 hours following surgery. Animal weights were monitored throughout the recovery period as a measure of animal health.

3.2.3.3. Fear conditioning behaviour assessment

Fear conditioning was performed to evaluate contextual memory function following ferric citrate injection, due to the critical role the hippocampus plays in contextual memory. The protocol was adapted from Izquierdo *et al.* (Izquierdo *et al.*, 2006) and from previous lab experiments.

Fear conditioning training

The fear-conditioning box was wiped down using 70% IMS prior to conditioning each animal. Mice were left in their cage until the conditioning was to be performed. Cages were kept outside of the fear-conditioning room to avoid long-term distress to animals. Mice were placed into the fear conditioning box, the camera recording started and the Day 1 procedure initiated. The procedure provides three electric shocks; one after 90 seconds acclimatisation, a second electric shock another 90 second pause, and a third electric shock after 150 second pause. Electric shocks were administered at 0.60 mA Direct Current (DC). A final 60 second pause was allowed before returning mice to their cage. 48 hours was then allowed before contextual memory testing.

Contextual memory

Hippocampal based contextual memory was measured 48 hours post conditioning. Prior to contextual memory recall, the fear conditioning box was wiped down using

70% IMS and each animal was placed into the box and recorded for 5 minutes without any external stimulus or shock to evaluate contextual memory recall.

Behaviour assessment

Assessment of fear conditioning behaviour was performed by evaluation of the freeze fear response. Typically, mice will freeze and prevent all movement when exposed to a stressful environment (Izquierdo *et al.*, 2006). Scoring was performed by timing how long each animal spent frozen, as a percentage of total time for each phase of the behavioural study.

3.2.3.4. Magnetic Resonance Imaging

In vivo data acquisition

Mice were allowed to survive 10 days post-surgery before *in vivo* MRI acquisition was performed. Mice were anaesthetised using 5%:95% isoflurane: oxygen and placed into a head holder with anaesthetic mask in the MRI scanner. Anaesthesia was maintained using 1.5%:98.5% isoflurane: oxygen and mice were placed in a 25 mm ID radiofrequency (RF) coil. MRI was acquired using a ME SE sequence for T2 relaxometry, parameters were: 16 echoes with echo time (TE) 9 – 144 ms, step size 9 ms, repetition time (TR) 4600 ms and 2 averages. T2* relaxometry was performed using a MGE sequence with 5 echoes (3, 9, 15, 21, 27 ms), TR 2000 ms and 8 averages. For all scans, the matrix size was 128 x 128, FOV was 18 x 18 mm, with 31

contiguous slices throughout the brain at 0.5 mm thick in axial orientation. The respiration rate and temperature were monitored during MR acquisition using a respiration pillow and temperature probe next to the animal, respectively. Temperature in the MRI scanner was maintained at 37^{o}C using warm air from the heater module and fan.

Cardiac perfusion

Following the *in vivo* scans, mice were injected i.p. with 100 µl sodium pentobarbital. Once mice were terminally anaesthetised, by testing reflexes using the foot shock, an opening was made in the chest cavity to reveal the heart. A metal gavage needle of 0.9mm gauge was introduced into the left ventricle and heparinised-saline was used to wash out the blood before perfusion fixation with 4% paraformaldehyde (PFA). 4% PFA was allowed to wash through the circulation of the mouse for an additional 15 minutes, ensuring tissue was fully fixed. Mouse brains were then extracted from the skull and left in 4% PFA for at least 48 hours before *ex vivo* scanning.

Ex vivo data acquisition

Four brains were placed into the customised brain holder for MRI (see section 3.1.3.1), immersed in Galden®. *Ex vivo* scanning with a spin-echo (SE) sequence for T1 (TR = 550, 670, 800, 1000, 1200, 2000 and 4000 ms, TE = 11ms) and SE T2 (TR = 4000 ms, TE = 11, 15, 20, 25, 30, 45 and 60 ms) relaxometry was performed. T2*

assessment was performed using a single echo gradient-echo (GE) sequence (TR = 4000 ms, TE = 4, 8, 12, 20, 30 and 50 ms) with flip angle = 20^{o}. Both SE and GE sequence acquisitions had FOV = 30 x 30 mm, matrix size 256 x 256 and averages = 2, with 33 contiguous axial slices at 0.5 mm thickness.

Fast ME T2 and MGE T2* measurements were also performed for comparison against standard sequences with ME T2; 16 echoes with echo time (TE) 11.6 – 185.6 ms, repetition time (TR) 7000 ms and 4 averages, and MGE T2* using 5 echoes (2.5, 8.5, 14.5, 20.5 and 26.5 ms), TR 2000 ms and 10 averages. For all scans, matrix size was 256 x 256 with FOV of 30 x 30 mm with 33 contiguous axial slices at 0.5 mm thickness.

MRI image analysis

Relaxometry maps were generated as described in section 3.2.1.3.

Image registration

The SE T2-weighted images (TR = 4000ms, TE = 20ms) from each of the six control mice brains were registered into the same image space as a correctly oriented sample, and averaged together to create a template T2-weighted image in FSL.

A six parameter registration model (rigid body) was then used in FLIRT (FMRIB's Linear Image Registration Tool) to move each of the relaxometry maps into consistent image space according to the same transformation matrices as used to

register each brains' T2-weighted image to the T2-weighted template image. This method allowed the consistent overlay of ROIs between R1, R2, R2* and R2' relaxometry maps.

3.2.3.5. Synchrotron radiation X-ray fluorescence (SR-XRF) mapping

Sample preparation

Following *ex vivo* MRI, brains were immersed in 30% sucrose for 48 hours before cryosectioning at 40µm onto XRF film. XRF film was pre-mounted onto the custom made acrylic slides following cleaning using 100% IMS.

During cryosectioning, prior to a section being mounted onto XRF film, all surfaces and equipment were wiped down using 100% IMS to limit any possible contamination of metal elements within the sample or XRF slide.

Cryosectioning methodology

Once the front of the hippocampus had been reached by sectioning at 20 µm per slice, the following sequence of sectioning was performed. Five slides of 4 sections per slide were cut, with each slice separated by 100 µm within one slide (Figure 3-5). Following all these sections (5 slides x 4 sections = 20 sections; 20 sections at 20 µm each = 400 µm total) a 40 µm slice was obtained after cleaning down the cryostat, as explained above, as a "pre-XRF" section to ensure the cryostat was set to cut at the correct thickness. The second 40 µm section was then taken for XRF

(Figure 3-5; section 22) followed by a 20 µm "post-XRF" section obtained prior to starting a new "batch" of 5 slides (40 µm + 40 µm + 20 µm = 100 µm in total for acquisition of an XRF section). The slides with sections for histology were kept at -20^{o}C until use. The XRF slides were kept at room temperature until XRF scanning.

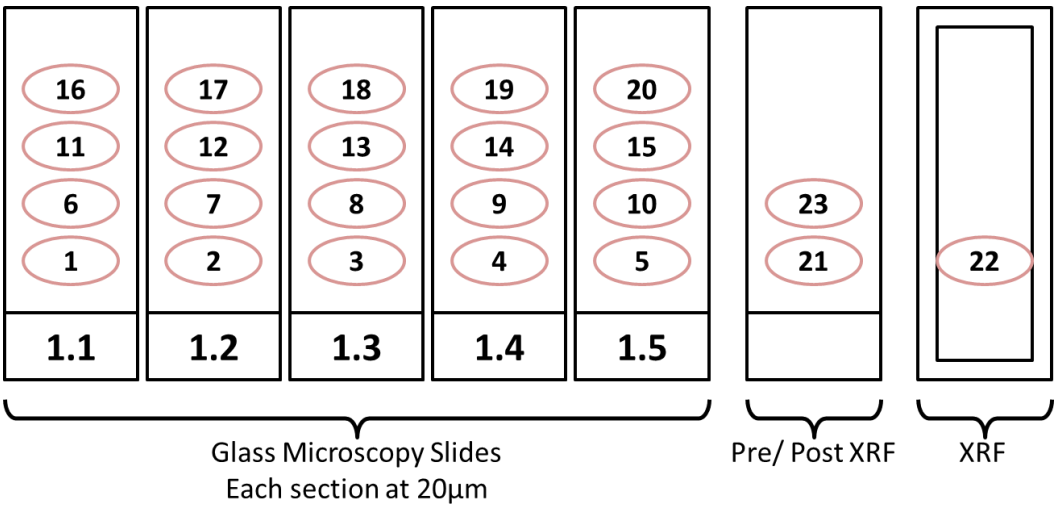

Figure 3-5 Cryosectioning method for histological and XRF elemental analysis

The cryosectioning method for the ferric iron injected mice brains is shown, where sections 1-20 were sectioned at 20µm, before changing the sections to be cut at 40µm for XRF (section 22). Section 21 and 23 were obtained immediately prior to or post to the XRF section, due to changing the cryosectioning thickness from 20µm to 40µm, and then back to 20µm. Numbers 1.1 – 1.5 at the bottom of each slide refer to the slide labelling process used.

SR-XRF acquisition

XRF mapping was performed on the Fluo X-ray fluorescence microprobe beamline at the ANKA synchrotron radiation facility (Karlsruhe Institute Technology (KIT),

Karlsruhe, Germany). The beam energy was tuned to 10keV and focussed to 100 x 100 µm and the sample scanned at constant time per pixel. XRF slides were attached to magnetic slide holders using tape and a ROI around the hippocampus of each slice was selected for XRF by low-power optical microscopy with a stage calibrated to the beam-line motor coordinates (Figure 3-6).

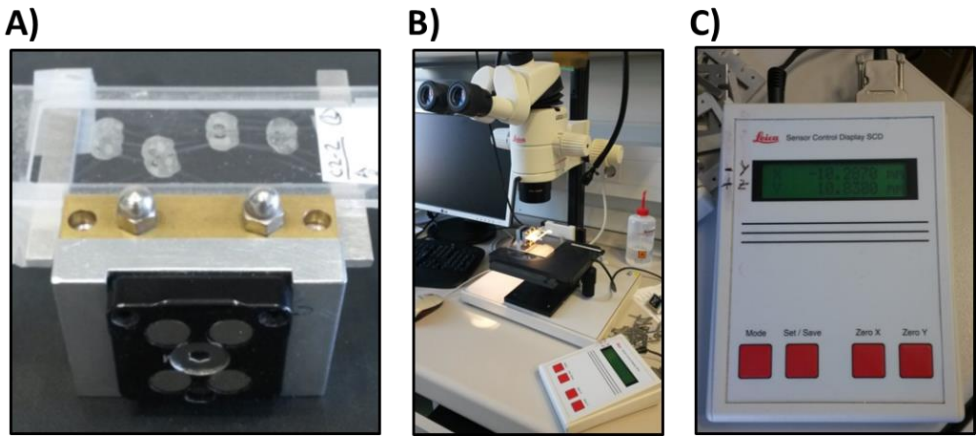

Figure 3-6 Method of selecting hippocampal area at KIT synchrotron

XRF slide holding 3-4 mouse sections was mounted onto magnetic slide holders using tape. (B) A low-powered optical microscope used to define an area around the hippocampus of mouse tissue sections, using (C) motor coordinates calibrated against the beamline scanning coordinates.

Data acquisition and analysis was the same as performed above (see section 3.2.2.2), however data was normalised against the transmitted monitor radiation to generate quantitative data using PyMCA. Three animals per treatment group and the three hippocampal slices relating to areas acquired by MRI in each animal, were assessed by SR-XRF due to time restrictions at the ANKA beamline.

3.2.3.6. Statistical data analysis

Iron content (in ppm) of hippocampal ROIs for both the whole hippocampus and lesion areas were obtained from iron elemental (n = 3 per group) and relaxometry (n = 6 per group) maps. Statistical testing between the control and treatment groups was determined using one-way ANOVA, followed by Tukey's test for multiple comparisons. One animal from each of the ferric citrate treatment groups was excluded from the relaxometry analyses, due to no lesion observed in one hemisphere based on R2* maps. Similar to the iron agarose standards and human post-mortem tissue results, the number of asterisks denotes significance level in graphs; * $P \leq 0.05$, ** $P < 0.01$, *** $P < 0.001$ and **** $P < 0.0001$. Total iron content in the treated animals was calculated by: lesion mean x lesion volume, for both elemental iron and relaxometry measurements, to assess the difference in total iron content detected using each measurement between the 2 mM and 4 mM treatment groups. Correlation of hippocampal relaxometry measures against iron was determined using both Pearson correlation coefficient and r^2 linear regression analysis from every ROI.

3.2.3.7. Histochemical assessment

Immunohistochemistry

Immunohistochemical staining was performed using antibodies detailed below. Sections were removed from the freezer and allowed to thaw to room temperature, before TBS(-) was added to each slide to rehydrate samples. Slides

were then dried using tissue, and a wax pen used to draw around samples on the slide. 1% hydrogen peroxide in TBS(-) was added and left for 30 minutes at room temperature to reduce background peroxidase activity prior to DAB staining. Slides were washed in TBS(-) for 5 minutes and then TBS(+) for 5 minutes. Blocking buffer was added (10% serum in TBS(+)) for 2 hours at room temperature. Primary antibodies were then added in 5% serum in TBS(+) and slides left at 4^{o}C overnight (Table 3-4).

Three washes for 15 minutes were performed in TBS(+) before the secondary antibody in 5% serum in TBS(+) was added and left on the sections for 2 hours at room temperature (Table 3-4). A further three washes were performed for 20 minutes each, in TBS(+) twice and then TBS(-) once at the end. DAB solution was added on each slide and the reaction time recorded (Table 3-4). Once positive staining could be observed under the microscope, the DAB solution was tapped off into a waste container, the time recorded and the slides left in tap water to terminate the reaction. These were then left in tap water for at least 5 more minutes. Counterstaining could then be performed using either haematoxylin or nissl staining, as outlined below.

Once immunohistochemical procedures were completed, samples could then be dehydrated and mounted by placing in 70% IMS for 5 minutes, then 95% IMS for 5 minutes and then twice in 100% IMS for a further 5 minutes of each wash. Slides were then transferred into 100% xylene for 6 minutes twice before mounting, by placing a small volume of DPX onto the sections and placing coverslips gently on

top, avoiding the creation of air bubbles. The slides were finally allowed to dry in a fume cupboard overnight.

Table 3-4 Outline of primary antibody dilutions, DAB staining times and counterstains applied onto mouse tissue from ferric citrate hippocampal injections

Primary antibody	Raised in	Dilutions	Secondary antibody	DAB stain time	Counterstain
Ferritin	Rabbit	1:2500	Impress kit	4 mins	Haematoxylin
Iba1	Rabbit	1:1500	Impress kit	2 mins 15 secs	Nissl

Haematoxylin staining

After at least 5 minutes in tap water following DAB staining, slides were counterstained in Harris' Haematoxylin for 5 minutes. Slides were washed again in running tap water before the staining was differentiated using 0.5% acid alcohol for about 15 seconds. Slides were again then left in running tap water for 5 minutes, followed by dehydration and mounting as described above.

Nissl staining

After at least 5 minutes in tap water following DAB staining, slides could be counterstained using Nissl staining (0.05% cresyl fast violet solution; preheated to 60°C) for 25 minutes at 60°C. Differentiation was then performed in 95% IMS for

10-15 seconds, with a few drops of 10% acetic acid added to accelerate the process. Sections were rinsed twice in dH_2O before differentiating sections in an ascending series of alcohols and xylene as described below:

a. 70% IMS for 5 minutes.
b. 80% IMS for 2 minutes.
c. 90% IMS for 2 minutes.
d. 95% IMS for 2 minutes.
e. 100% IMS for 2 minutes, twice.
f. 50% IMS/ 50% xylene for 2 minutes.
g. 100% xylene for 2 minutes.

Sections were then checked for clear background microscopically prior to mounting with DPX.

3.2.3.8. Microscopy evaluation

Stained sections were imaged using a Leica SCN400F slide scanner, as described in section 3.2.2.4. Images were then obtained from the Leica Digital Image Hub for assessment of immunohistochemical staining.

4. Results: Iron Agarose Standards

4.1. Introduction

In order to validate the MR relaxometry sequences to be used, it is necessary to understand the direct effect of different forms of iron on the MR signal without any other interfering effects. To do this, agarose standards have been used in a number of studies to investigate the correlation of a specific cell type or element to the produced signal.

4.2. Objectives

The objectives for the work with iron agarose standards were:

- To validate and assess iron-sensitive MRI relaxometry methods for measurement and quantification of iron content.
- To understand the different effects that different iron ions, and bound compared with unbound iron can elicit on MR relaxometry values.

4.3. Methods

The methods for this work can be found in section 3.2.1. In brief, different concentrations of ferric and ferrous iron chloride were formed in 2% agarose and filled into 1 ml syringes. Furthermore, standards with iron loaded ferritin, as well as

combinations of ferric to ferrous chloride, were also generated at different concentrations in 2% agarose. These iron agarose standards were then scanned for R1, R2 and R2* relaxometry assessment using standard SE and GE sequences, as well as using fast ME and MGE sequences for R2 and R2* evaluation, respectively. Iron concentrations were then correlated against R1, R2, R2* and R2' relaxivity values.

4.4. Results

4.4.1. T1- and T2- weighted qualitative observation of agarose standards

T1- and T2- weighted images of the seven different concentrations of ferrous and ferric iron were first compared for differences in contrast and signal intensity (Figure 4-1). Taking each of the T1- or T2- weighted images separately, the seven standards with different concentrations of iron show different signal intensities to each other (Figure 4-1A and B for ferrous iron standards).

Circular ROIs were placed over each iron agarose standard in MR images to obtain mean signal intensity values. Visually, curves for signal intensity versus TR and TE have higher initial slopes for higher iron concentration in the agarose standards (Figure 4-1C-D). Additionally, the signal intensity versus TR reaches a lower plateau level for higher iron concentration (Figure 4-1C). These observations pave the way for performing quantitative measurement of T1 and T2 values to correlate against iron content directly.

Relaxometry maps were generated by performing a pixel by pixel regression for T1 and T2 using SE acquisition, and T2* using GE acquisition. Reciprocal T1, T2 and T2* maps were generated to produce R1, R2 and R2* maps for further assessments, given the strong evidence for direct correlation of these measurements with iron content (see section 1.6.5; Figure 4-2).

Increased pixel intensities in the R1, R2 and R2* maps highlight regions with increased relaxivity values. Increasing concentrations of ferric or ferrous iron led to an increase in R1, R2 and R2* values within each map (Figure 4-2). A clear difference visually can be identified between the ferrous and ferric forms of iron, with the latter showing considerably higher R1, R2 and R2* relaxivity values by comparison to the ferrous form (Figure 4-2).

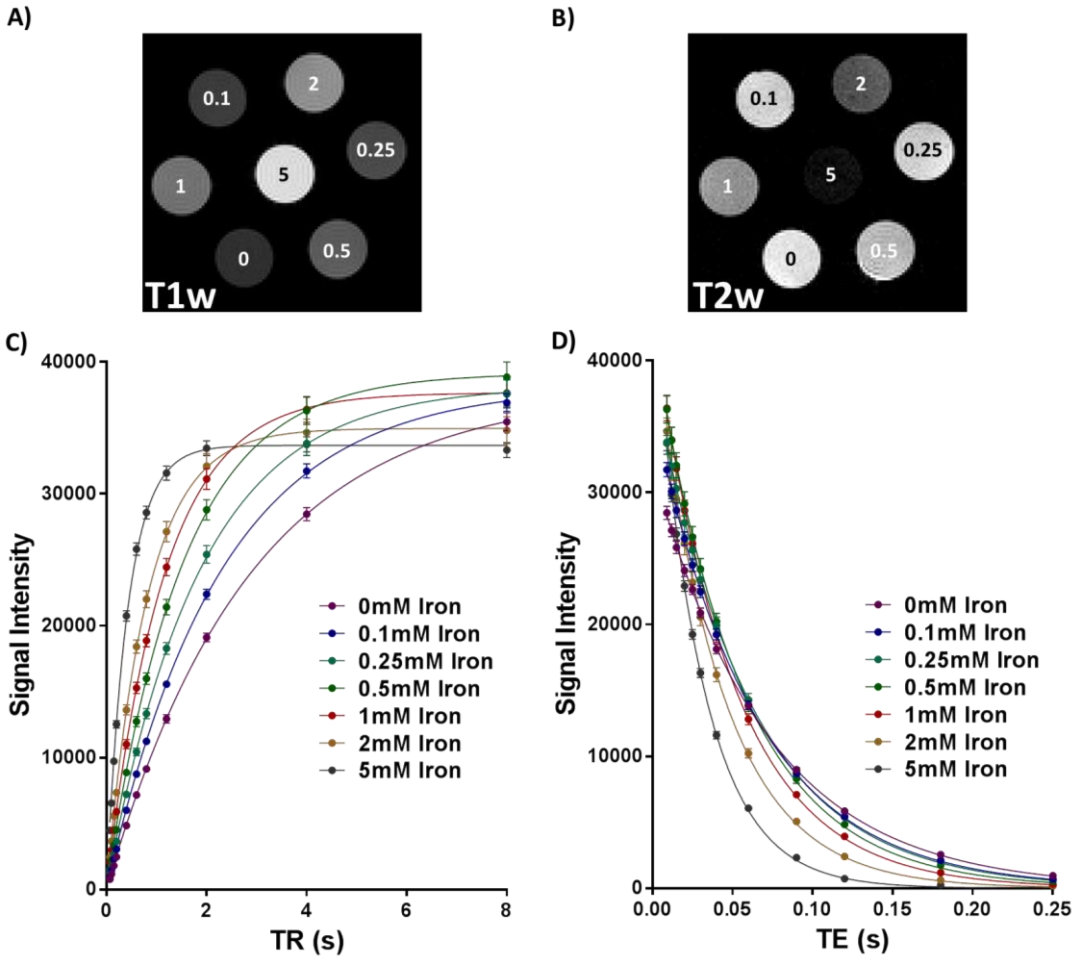

Figure 4-1 Ferrous iron agarose standards T1- and T2- relaxometry curves

(A) Axial T1- weighted (T1w) image of the ferrous iron agarose standards at TR/TE = 400/ 9 ms and (B) axial T2- weighted (T2W) image of the ferrous iron agarose standards at TR/TE = 4000/ 120 ms. Values overlaying T1 and T2 weighted images are ferrous iron concentrations in mM. Relaxivity curves for (C) T1 quantification and (D) T2 quantification of each concentration of the ferrous iron agarose standards. Graphs show mean values ± SD.

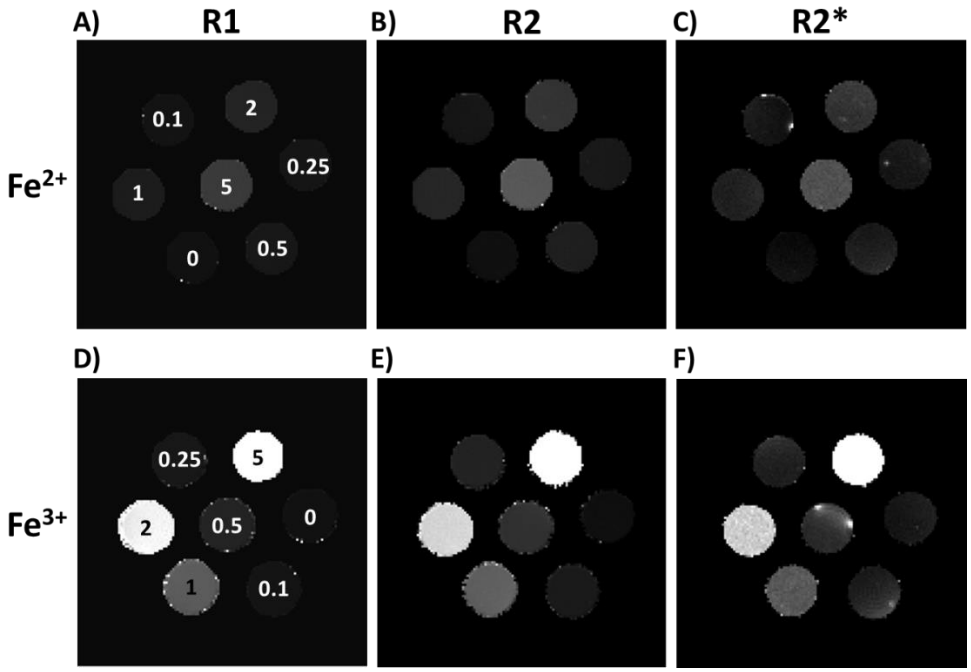

Figure 4-2 R1, R2 and R2* relaxometry maps of ferrous and ferric iron in agarose standards

R1, R2 and R2 axial relaxometry maps of (A-C) ferrous (Fe^{2+}) and (D-F) ferric (Fe^{3+}) iron chloride agarose standards. Values overlaying ferric and ferrous R1 relaxometry maps are iron concentrations in mM. Image contrasts are consistent between ferrous and ferric iron agarose standards for each relaxometry map.*

4.4.2. Quantification reproducibility

To provide an accurate assessment of iron using MRI relaxometry, the consistency of iron measurements was first tested across multiple slices through the standards. Assessment of the R1 and R2 values across the five adjacent slices demonstrated reliable acquisition and measurement, with clearly separable and non-overlapping

profiles between each concentration of both ferrous and ferric iron (Figure 4-3A-B, D-E).

R2* values however, were difficult to discern given the large image artefacts present, especially in the outermost agarose standards (Figure 4-4A-B, arrows). These image artefacts subsequently increased the variability of the mean relaxivity measurements for each standard (Figure 4-3C and F). None of the seven different concentrations of ferrous iron were discernible from each other, given the large variations in mean relaxivity values in each slice (Figure 4-3C, Figure 4-4A). Furthermore, none of the measurements were constant across slices, leading to overlapping profiles between concentrations. The 2 mM and 5 mM ferric iron standards are clearly separated, likely due to their substantially higher relaxivity values compared with the remaining standards (Figure 4-3F). The five remaining ferric iron standards however, were not discernible due to variability of mean relaxivities and overlapping profiles across the different slices (Figure 4-4B). R2* values below approximately 60 s^{-1} were therefore not consistent for a given agarose standard.

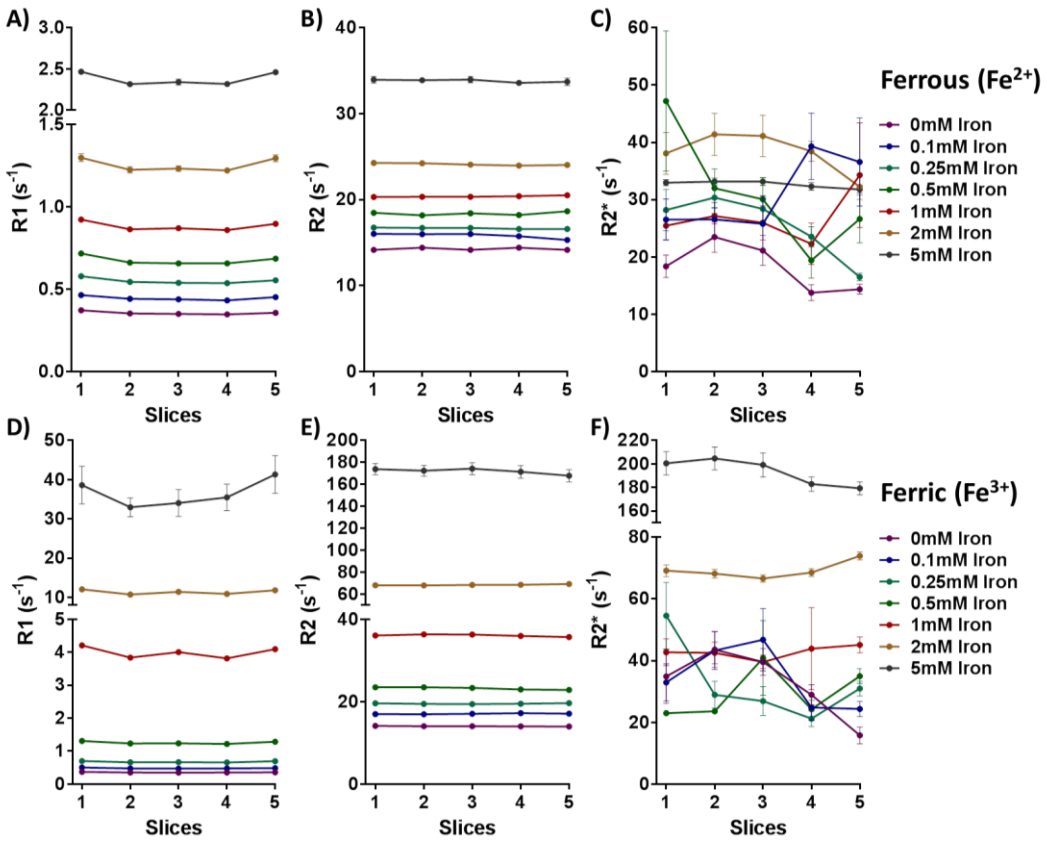

Figure 4-3 Mean R1, R2 and R2* quantification of iron agarose standards across multiple slices

(A) R1, (B) R2 and (C) R2 profiles for ferrous iron demonstrates consistent and reliable acquisition of R1 and R2 values, whilst R2* profiles overlap. (D) R1, (E) R2 and (F) R2* profiles for ferric iron demonstrates similar consistent and reliable acquisition of R1 and R2, whilst R2* values show substantial overlapping of profiles below 60 s^{-1}. Graphs show mean values ± SD.*

In order to quantify the R2* relaxivities in the iron standards, the slice thickness was reduced from 2 mm to 0.5 mm to limit artefacts potentially arising from B_0 inhomogeneities. The same length of standards were acquired, therefore providing 20 slices at 0.5 mm thickness (10 mm length total), instead of 5 slices at 2 mm

thickness (10 mm length total; Figure 4-4). Substantial improvements in the homogeneity of each standard were observed, with fewer artefacts observed than imaging 5 slices at 2 mm thickness (Figure 4-4; arrows).

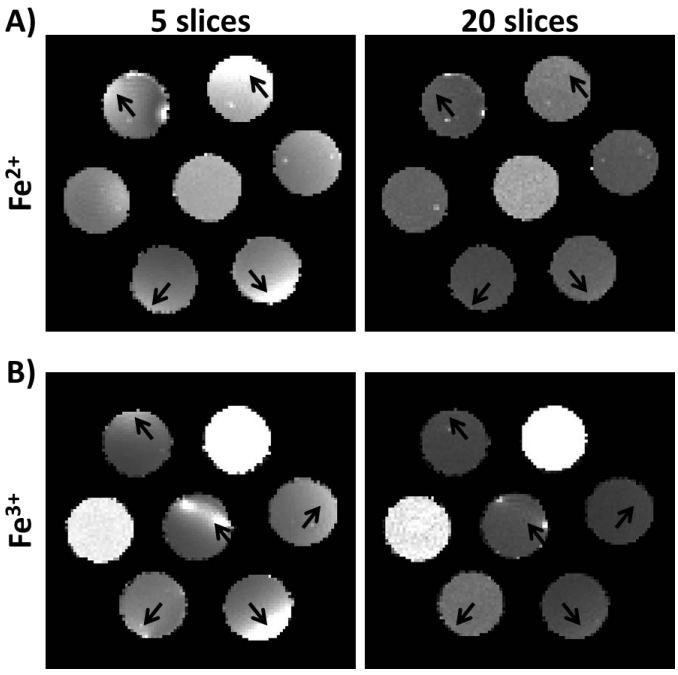

Figure 4-4 Image artefacts in R2* relaxometry maps dependent on thickness of slices

Artefacts were observed in the R2 maps for both (A) ferrous iron, and (B) ferric iron agarose standards when imaging was performed with 2 mm thickness (5 slices) (arrows). Imaging with 0.5 mm thickness (20 slices) led to greater homogeneity of R2* values within the standards.*

Mean R2* relaxivities across slices were therefore more clearly delineated by reducing the slice thickness (Figure 4-5). In both the ferrous and ferric standards, R2* values across slices were more consistent with fewer overlapping profiles,

allowing quantification of R2* relaxometry. Greater SD of individual slice mean relaxivities can be observed in the 0.5 mm thickness acquisition however, likely as a result of lower signal-to-noise ratio (SNR) due to the reduction in slice thickness (Figure 4-5B and D). However, as the data is considerably more consistent, this variability is unlikely to interfere with data analysis. As image artefacts were still observed to a limited degree using this acquisition method, data containing artefacts were monitored and slices excluded from analysis in cases where the artefacts produce interfering effects on quantification.

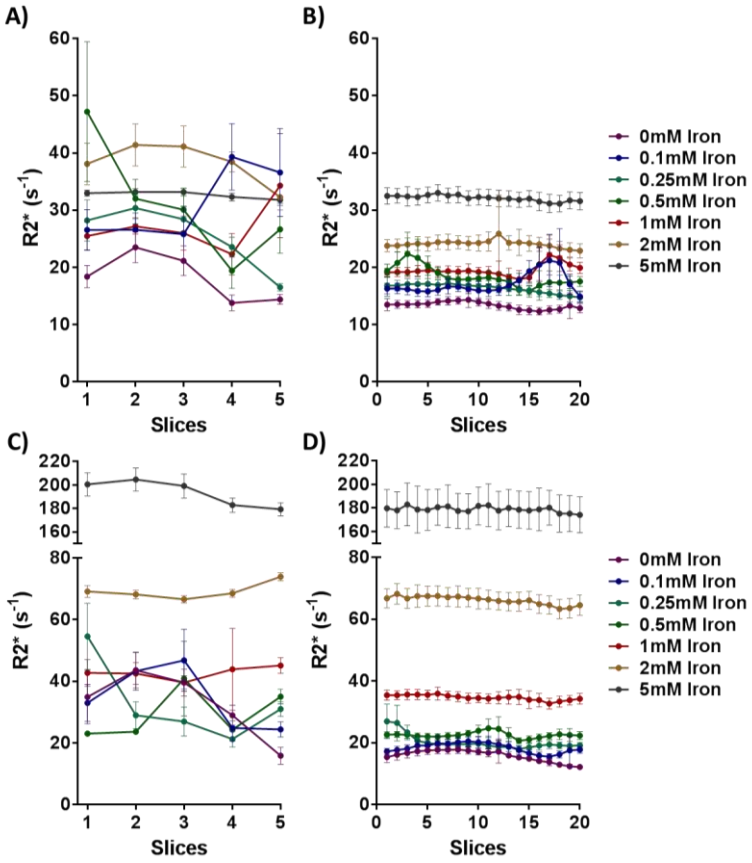

Figure 4-5 R2* measurement of iron agarose standards using different slice thickness

(A) R2 values of ferrous iron across five slices at 2 mm thickness and (B) R2* values of ferrous iron across twenty slices at 0.5 mm demonstrating the substantially*

improved profiles using 0.5 mm acquisition. (C) R2 values of ferric iron across five slices at 2 mm thickness and (D) R2* values of ferric iron across twenty slices at 0.5 mm. SD error bars are larger in the 20 slices data likely due to lower SNR from acquisition of 0.5 mm thickness slices. Graphs show mean values ± SD.*

4.4.3. Standard and fast relaxometry measurements

In vivo imaging requires faster scanning procedures to be employed in both clinical and preclinical settings. Therefore, faster measurements of R2 and R2* were performed using a multi-echo (ME) SE and a multi-gradient-echo (MGE) sequence respectively, for comparison against the standard spin-echo (SE) and gradient-echo (GE) acquisitions.

Comparing the R2 relaxivity values measured with SE and ME sequences demonstrates that there seems to be an under-estimation of R2 using the ME sequence for all iron concentrations in both the ferric and ferrous forms (Figure 4-6A-B). Furthermore, this under-estimation seems to be dependent on the R2 value itself. This was tested further by plotting Bland-Altman correlation comparisons using both the ferric and ferrous relaxometry data (Figure 4-7A-B). Whilst the correlation of ME R2 was directly and linearly proportional to SE R2 values (Figure 4-7A), consistent under-estimation of true R2 values were obtained using ME R2. The under-estimation of R2 was substantially greater at higher R2 values than at shorter R2 values (Figure 4-7B).

Comparison of the R2* relaxivity values measured with GE and MGE sequences seem to show similar values in both the ferric and ferrous standards (Figure 4-6C-D). Comparisons using Bland-Altman plots highlights MGE R2* to show a complicated relationship to GE R2* evaluation. The lowest R2* values are slightly under-estimated, whilst R2* values above $40s^{-1}$ are over-estimated (Figure 4-7C-D).

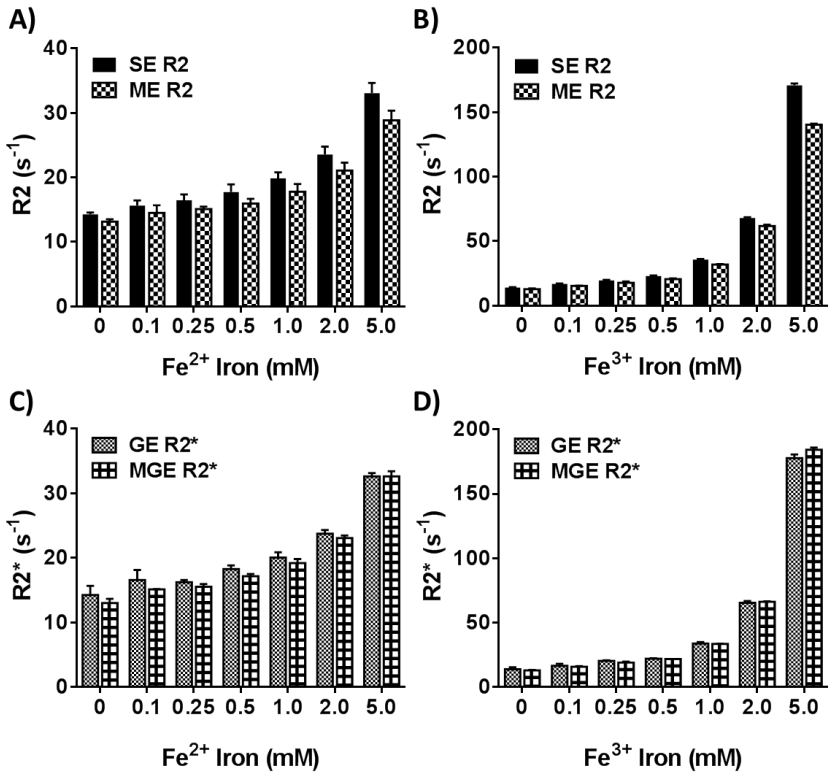

Figure 4-6 Comparison of standard and fast relaxometry measurements in iron agarose standards

SE and ME R2 measurement of (A) ferrous iron and (B) ferric iron agarose standards. GE and MGE R2 measurement of (C) ferrous iron and (D) ferric iron agarose standards. Graphs show mean values ± SD.*

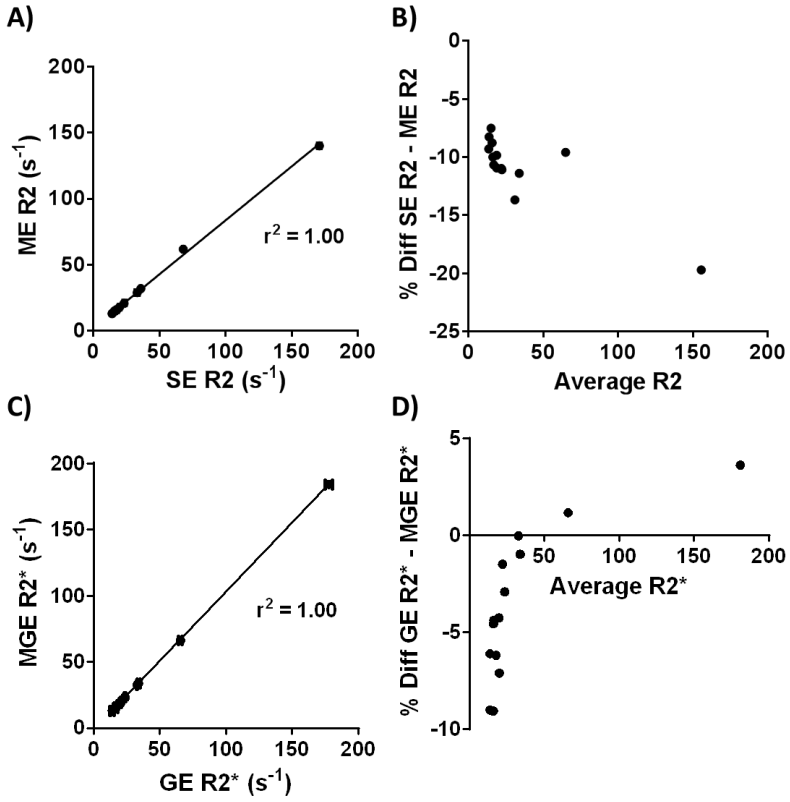

Figure 4-7 Bland-Altman correlation comparisons of standard and fast relaxometry measurements

(A) r^2 correlation of SE R2 compared with ME R2 measurement and (B) the percentage difference in SE to ME R2 values. (C) r^2 correlation of GE R2 compared with MGE R2* values and (D) percentage difference in GE R2* to MGE R2* values.*

4.4.4. Validation of pH, oxidation state and content of iron agarose standards

The pH of ferric and ferrous iron in aqueous solutions were measured as a surrogate model for the agarose standards (Figure 4-8, Table 4-1). Ferric solutions were significantly more acidic than ferrous solutions (mean ferrous solution pH = 4.27 ± 0.14, mean ferric solution pH = 2.55 ± 0.08, $P < 0.0001$). The ferric solutions

also show a gradual decline in pH with increasing concentrations of iron, however this decline in pH was not significant (ferrous, P = 0.378, ferric, P = 0.077).

Table 4-1 pH of ferric and ferrous iron aqueous solutions

Iron concentration (mM)	pH	
	Fe^{2+}	Fe^{3+}
5.00	4.22	2.46
2.50	4.15	2.52
1.25	4.26	2.51
0.63	4.21	2.53
0.31	4.24	2.60
0.16	4.55	2.68
0.00	3.75	3.85

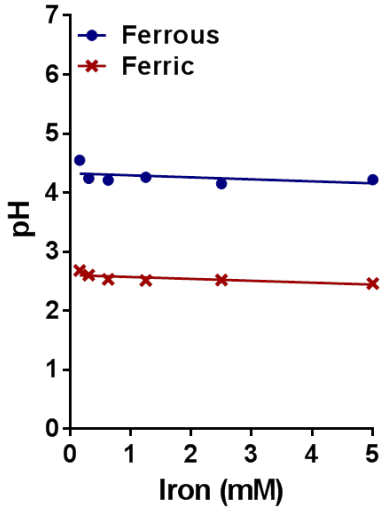

Figure 4-8 pH of ferric and ferrous iron aqueous solutions

Ferric iron solutions are more acidic than ferrous iron solutions.

Measurement of the oxidation states of iron in the agarose standards was performed using the 1,10-phenanthroline assay, without hydroxylamine hydrochloride (Figure 4-9). The 1,10-phenanthroline assay mix using agarose standards with ferric iron only appeared very slightly red by eye even at the top concentration (5mM) of iron (Figure 4-9A). In contrast, the 1,10-phenanthroline assay mix using agarose standards with ferrous iron appeared very clearly red (Figure 4-9A). Absorbance measurements at each iron concentration of the ferrous and ferric standards clearly validates the visual differences observed (Figure 4-9B).

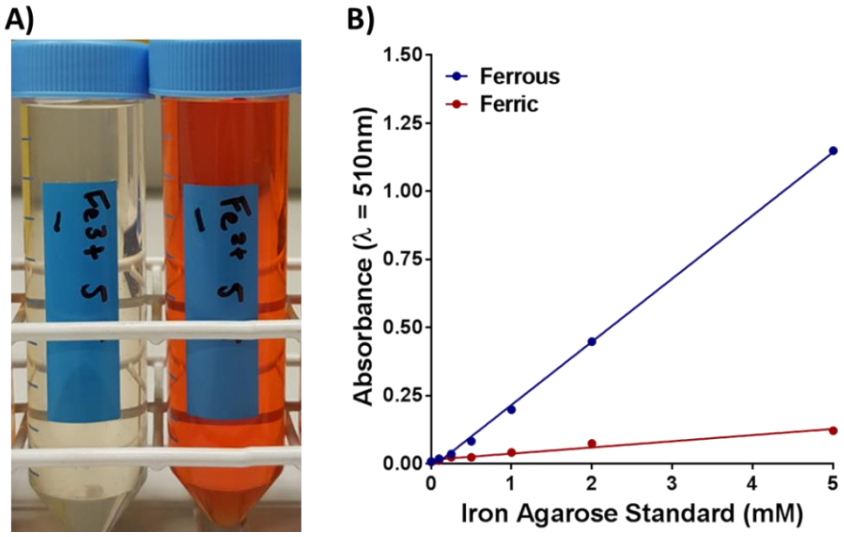

Figure 4-9 Measurement of the oxidation states of iron in the agarose standards

(A) Photograph of ferric (left) and ferrous (right) 1,10-phenanthroline assay without hydroxylamine hydrochloride. (B) Spectrophotometric absorbance measurements at 510 nm of the ferric and ferrous iron agarose standards.

In order to validate the actual final iron concentrations in the agarose standards, a standard curve was established using a series of ferrous iron chloride solutions, diluted from a single stock solution (Figure 4-10). The correlation value of the

standard curve was r^2 = 1.00 and demonstrates that if given an unknown absorbance value, the concentration of iron can be calculated using the regression line equation (Figure 4-10).

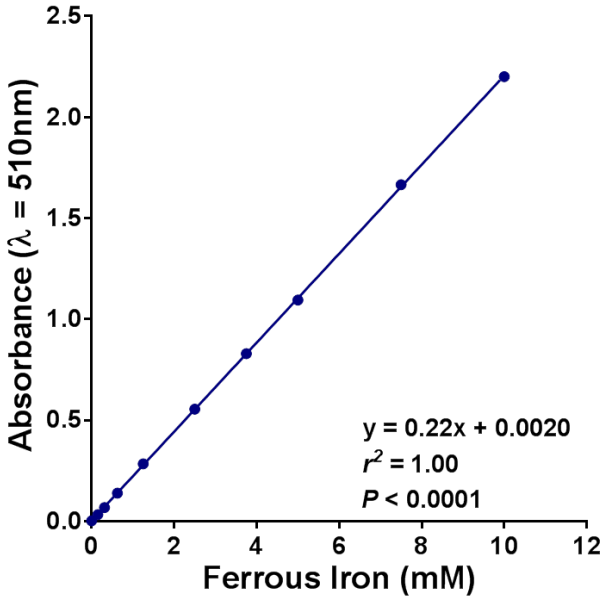

Figure 4-10 A standard curve of ferrous iron content compared with spectrophotometric measurement

Spectrophotometric measurement of the 1,10-phrenanthroline assay at a wavelength of 510 nm provided a perfectly linear relationship to ferrous iron concentrations.

Subsequently, the ferrous iron actual concentrations were calculated using the absorbance measurements taken above from the agarose standards (Figure 4-9) and comparing them to the standard curve. These actual concentrations were compared to the target concentrations (Figure 4-11). A correlation of r^2 = 1.00 was observed between the target iron concentration and the actual iron concentrations in the agarose standards (Figure 4-11). Furthermore, the slope of 1.05

demonstrates that the concentrations in the final agarose standards are extremely close to the target concentrations.

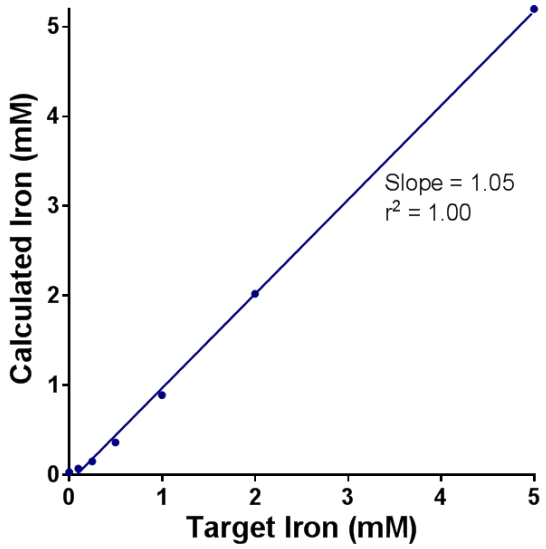

Figure 4-11 Calculated actual ferrous iron concentrations compared with target iron concentrations

The actual iron concentrations in the ferrous iron agarose standards were calculated from the 1,10-phenanthroline assay absorbance measurements with the standard curve absorbance measurements.

Microscopic evaluation of both the ferric and ferrous iron agarose standards demonstrated no evidence of precipitation or accumulation.

4.4.5. Iron quantification using relaxometry

Relaxometry maps were opened in ImageJ and circular ROIs placed over each iron agarose standard to obtain mean values across all the slices. Quantification of the

differences in relaxometry values between ferrous and ferric iron standards, and with increasing concentrations, were evaluated by averaging values across all slices from triplicate scans.

R1 values of ferrous iron increased from 0.35 ± 0.02 s^{-1} at 0 mM to 2.36 ± 0.06 s^{-1} at 5 mM with significant linear correlation of $r^2 = 1.00$ ($P < 0.0001$). By comparison, R1 values of ferric iron increased from 0.37 ± 0.01 s^{-1} at 0 mM to 37.12 ± 3.23 s^{-1} at 5 mM, with significant linear correlation of $r^2 = 0.99$ ($P < 0.0001$; Figure 4-12A). The slopes, defining the molar relaxivities (r_1) of ferrous and ferric iron were also significantly different (ferrous r_1 = 0.39 ± 0.01 $s^{-1}mM^{-1}$ and ferric r_1 = 7.48 ± 0.40 $s^{-1}mM^{-1}$, $P < 0.0001$). Ferric iron has significantly higher R1 values compared with ferrous iron from 0.1 mM up to 5 mM (Table 4-2).

Standard SE R2 values of ferrous iron increased from 14.27 ± 0.28 s^{-1} at 0 mM to 33.09 ± 1.58 s^{-1} at 5 mM with significant linear correlation of $r^2 = 0.99$ ($P < 0.0001$; Figure 4-12B). Ferric iron SE R2 values increased from 14.14 ± 0.29 s^{-1} at 0 mM to 170.93 ± 1.45 s^{-1} at 5 mM, with significant linear correlation of $r^2 = 0.99$ ($P < 0.0001$). The r_2 of ferrous and ferric correlations were also significantly different (ferrous r_2 = 3.61 ± 0.19 $s^{-1}mM^{-1}$ and ferric r_2 = 31.55 ± 1.08 $s^{-1}mM^{-1}$, $P < 0.0001$). Ferric iron has significantly higher SE R2 values compared with ferrous iron from 0.25 mM up to 5 mM (Table 4-2). Similar observations were made for ME R2 measurements, showing significantly different r_2 (ferrous r_2 = 3.01 ± 0.16 $s^{-1}mM^{-1}$ and ferric r_2 = 25.75 ± 0.64 $s^{-1}mM^{-1}$, $P < 0.0001$) and differences between ferric and ferrous iron detected upwards from 0.25 mM (Figure 4-12E and Table 4-2).

GE R2* values of ferrous iron increased from 14.28 ± 1.41 s^{-1} at 0 mM to 32.65 ± 0.50 s^{-1} at 5 mM with significant linear correlation of $r^2 = 0.98$ ($P < 0.0001$; Figure 4-12C). Ferric iron GE R2* values increased from 13.95 ± 1.55 s^{-1} at 0 mM to 177.84 ± 2.85 s^{-1} at 5 mM, with significant linear correlation of $r^2 = 0.99$ ($P < 0.0001$). The r_2* gradient of ferrous and ferric correlation were also significantly different (ferrous r_2* = 3.47 ± 0.23 $s^{-1}mM^{-1}$ and ferric r_2* = 32.86 ± 1.56 $s^{-1}mM^{-1}$, $P < 0.0001$). R2* of ferric iron was significantly higher compared with ferrous iron from 0.25 mM up to 5 mM (Table 4-2). Again, similar observations were made for MGE R2* measurements, showing significantly different r_2* gradient (ferrous r_2* = 3.70 ± 0.23 $s^{-1}mM^{-1}$ and ferric r_2* = 34.36 ± 1.67 $s^{-1}mM^{-1}$, $P < 0.0001$) and differences between ferric and ferrous iron detected upwards from 0.1 mM (Figure 4-12F and Table 4-2).

R2' values were calculated by subtracting mean SE R2 values from mean GE R2* values. No significant correlation or significant differences were observed either with increasing iron contents or between ferric and ferrous iron standards. The resultant R2' values were all approximately zero, giving evidence that the relaxivities obtained by R2* were similar to those acquired by R2 (Figure 4-12D).

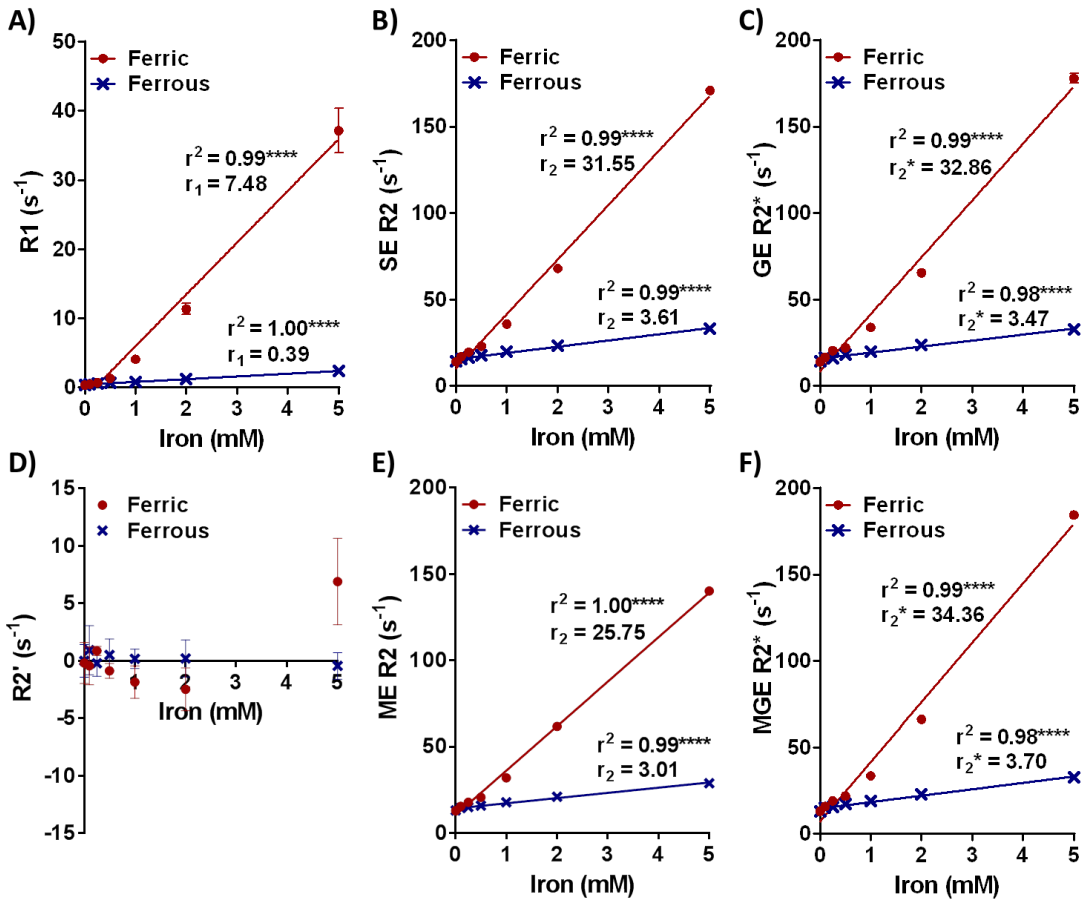

Figure 4-12 Ferrous and ferric iron agarose standards assessed by relaxometry measurements

Graphs showing (A) R1, (B) SE R2, (C) GE R2, (D) R2', (E) ME R2 and (F) MGE R2* relaxometry values against different concentrations of ferric and ferrous iron chloride in 2% agarose standards. r^2 are the correlation values; r_1, r_2 and r_2* are the molar relaxivities for each set of standards. Values are mean ± SD.*

Table 4-2 Statistical testing of relaxivity values between ferrous and ferric iron agarose standards

Iron concentration (mM)	P-values between Ferrous and Ferric				
	R1	SE R2	ME R2	GE R2*	MGE R2*
0	0.270	0.617	0.543	0.801	0.884
0.10	0.013[a]	0.040	0.246	0.965	0.020[a]
0.25	0.001[a]	0.006[a]	0.009[a]	< 0.001[a]	0.006[a]
0.50	< 0.001[a]	0.002[a]	< 0.001[a]	< 0.001[a]	< 0.001[a]
1.00	< 0.001[a]	< 0.001[a]	< 0.001[a]	< 0.001[a]	< 0.001[a]
2.00	< 0.001[a]	< 0.001[a]	< 0.001[a]	< 0.001[a]	< 0.001[a]
5.00	< 0.001[a]	< 0.001[a]	< 0.001[a]	< 0.001[a]	< 0.001[a]

[a] *denotes significance between ferric and ferrous iron reached using multiple t-tests, following Holm-Sidak method for multiple comparisons to $\alpha \leq 0.05$. Significant results highlighted blue.*

Assessment of uncertainty in R2, R2* and R2' measurements was performed by calculating the mean absolute deviation of the triplicate measurements from each ferric and ferrous agarose standard (Table 4-3). Low mean absolute deviations were apparent at each concentration of ferric or ferrous iron from R2 and R2* measurements, however R2' uncertainty was large compared with the mean value (Figure 4-13A-C). Very high percentage coefficients of variation of R2' values further substantiates the very high error in R2' compared to R2 and R2* values (Table 4-4).

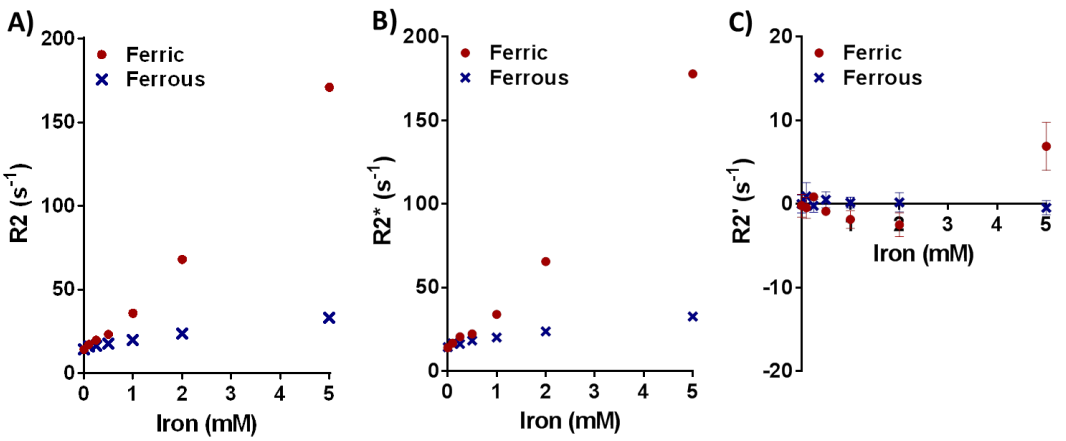

Figure 4-13 R2, R2* and R2' uncertainty across the triplicate measurements

The mean absolute deviation of each ferric and ferrous iron standard measurements was evaluated using (A) R2, (B) R2 and (C) R2' relaxometry.*

Table 4-3 Mean absolute deviations of ferric and ferrous iron standards using R2, R2* and R2'

Iron (mM)	Ferric			Ferrous		
	R2	R2*	R2'	R2	R2*	R2'
0.00	0.21	1.19	1.36	0.19	1.08	1.08
0.10	0.16	1.11	1.27	0.58	1.17	1.64
0.25	0.36	0.28	0.28	0.67	0.23	0.77
0.50	0.32	0.16	0.48	0.90	0.40	0.95
1.00	0.35	0.87	1.05	0.73	0.64	0.64
2.00	0.40	1.04	1.43	0.94	0.42	1.14
5.00	1.10	2.14	2.87	1.21	0.36	0.84

Table 4-4 Percentage coefficients of variation of ferric and ferrous iron standards using R2, R2 and R2'*

Iron (mM)	Ferric (%)			Ferrous (%)		
	R2	R2*	R2'	R2	R2*	R2'
0.00	2.1	11.1	952.4	2.0	9.9	13073.1
0.10	1.3	8.7	379.3	5.1	9.5	228.1
0.25	2.4	1.8	46.0	5.6	2.0	534.5
0.50	1.8	1.0	74.5	6.6	3.1	264.5
1.00	1.3	3.3	77.1	4.8	4.2	443.4
2.00	0.9	2.1	75.5	5.2	2.3	759.6
5.00	0.9	1.6	54.5	4.8	1.5	264.6

4.4.6. Combinations of ferric and ferrous iron agarose standards

To evaluate the differences observed between ferric and ferrous iron on relaxometry measurement further, combinations of these iron ions were formulated to evaluate the potential of ferric to ferrous ratio detection based on the differences in molar relaxivities between these ions. Combinations of ferric to ferrous iron were formulated at 100/0, 80/20, 50/50, 80/20 and 0/100 %, and serially diluted by a factor of 2 from the highest concentration.

Linear regression of iron concentration to relaxometry values for each ferric-to-ferrous combination, demonstrated significant linear correlation with R1, R2 and

R2* ($P < 0.0001$; Figure 4-14). The molar relaxivity slopes were found to be significantly different between the different proportions of ferrous to ferric iron contents tested across every relaxometry measurement taken (Table 4-5).

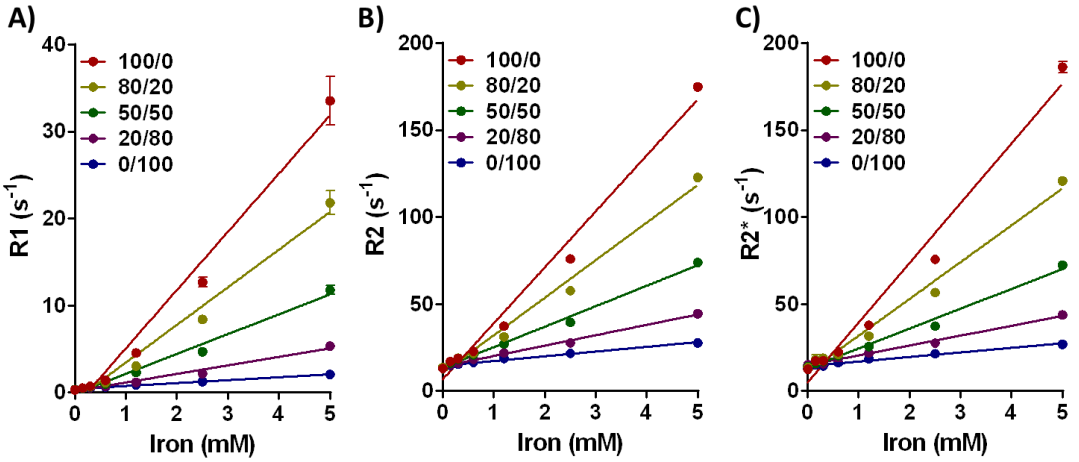

Figure 4-14 Molar relaxivity changes with different proportions of ferrous to ferric iron contents

(A) R1, (B) SE R2 and (C) GE R2 assessment demonstrate increasing molar relaxivity slopes with increasing proportion of ferric, compared to ferrous iron contents.*

Table 4-5 Molar relaxivity slopes of combinations of ferrous and ferric iron agarose standards

Fe^{3+}/Fe^{2+}	Molar relaxivities ($s^{-1}mM^{-1}$)				
(%)	SE r_1	SE r_2	ME r_2	GE r_2*	MGE r_2*
100/ 0	6.70 ± 0.43	32.15 ± 1.83	25.19 ± 0.84	34.32 ± 2.29	32.23 ± 1.99
80/ 20	4.32 ± 0.28	21.57 ± 1.10	19.79 ± 1.15	21.13 ± 1.11	21.44 ± 1.17
50/ 50	2.28 ± 0.12	11.75 ± 0.41	10.87 ± 0.46	11.40 ± 0.52	11.76 ± 0.38
20/ 80	0.98 ± 0.06	5.97 ± 0.19	5.37 ± 0.14	5.66 ± 0.21	5.79 ± 0.23
0/ 100	0.33 ± 0.01	2.72 ± 0.16	2.41 ± 0.18	2.63 ± 0.19	2.58 ± 0.11
P-value	P < 0.0001	P < 0.0001	P < 0.0001	P < 0.0001	P < 0.0001

Significance assessed using one-way ANOVA with significance reached at P ≤ 0.05.

4.4.7. Bound and unbound iron

To investigate the differences in relaxometry between iron ions, compared to bound iron, ferritin from equine spleen was used to formulate agarose standards as a form of bound iron. Ferritin contains iron in the form of ferrihydrite crystals (see section 1.3.2) which are in the ferric form. Ferric and ferrous iron agarose standards demonstrated similar correlations and molar relaxivity slopes to the previous set of standards (Table 4-6). Ferritin also demonstrates strong linear correlation with iron content (Figure 4-15 and Table 4-6). Ferritin r_1 was lower than that of both ferric and ferrous iron (Figure 4-15A), however ferritin r_2 and r_2* were only lower than the ferric form of iron, showing no significant difference compared with the ferrous

form (Figure 4-15B-C, Table 4-6). R2' values were, again, all approximately zero at each iron concentration, including using the ferritin iron standards (Figure 4-15D).

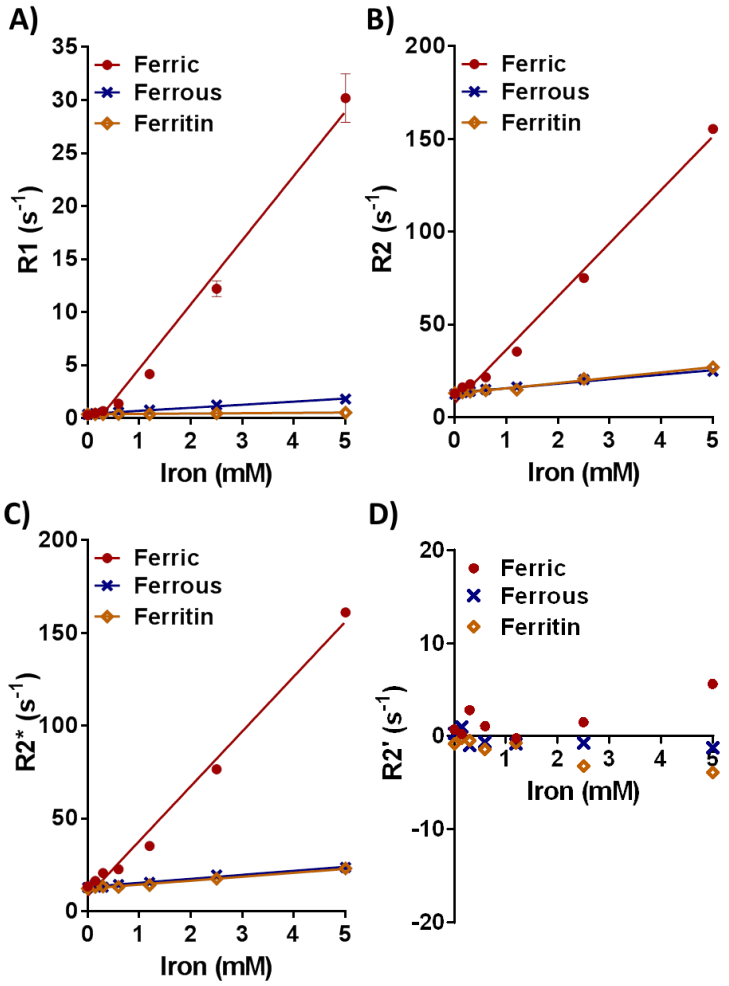

Figure 4-15 R1, R2, R2* and R2' relaxometry assessment of ferrous and ferric iron, compared with bound iron in ferritin

Table 4-6 Correlations and molar relaxivities of ferritin compared with ferric and ferrous iron agarose standards

		R1	R2	R2*
Ferric	r^2	0.98	0.99	0.99
	Mol. rel.	6.07 ± 0.34 [a]	28.74 ± 1.19 [a]	29.60 ± 1.40 [a]
Ferrous	r^2	0.99	0.98	0.97
	Mol. rel.	0.29 ± 0.01 [a]	2.43 ± 0.14	2.17 ± 0.16
Ferritin	r^2	0.95	0.98	0.99
	Mol. rel.	0.03 ± 0.00	2.86 ± 0.16	2.12 ± 0.11
P-value		P < 0.0001	P < 0.0001	P < 0.0001

Significance assessed using one-way ANOVA with significance reached at P ≤ 0.05. [a] denotes significance compared with ferritin, at P < 0.0001. Mol. rel. = molar relaxivity. Significant results highlighted blue.

4.5. Discussion

The main outcome from this chapter shows that iron concentration provides a strong, positive and linear impact on R1, R2 and R2* relaxometry measurements. Furthermore, the form of iron has been shown to directly affect the molar relaxivity values using r_1, r_2 and r_2* in agarose standards, with the ferric form of iron greatly increasing molar relaxivities, compared with the ferrous form of iron. Ferritin iron showed only minimal impact on all relaxometry assessments.

4.5.1. Quantitative MRI of standards

The application of MRI for detection of iron in biological tissue is complicated by the presence of different cell types, biochemical composition and water contents. Furthermore, assessment of iron content *in vivo* can be further complicated due to movements within tissue (e.g. blood) and due to difficulties in confirming iron contents for correlating against MRI. Therefore, to understand the fundamental impact of iron on MRI measurements, simple model standards are used (Bartzokis *et al.*, 1993, Zheng *et al.*, 2013). Agarose standards are a popular choice of standard, as the matrix has similar relaxation properties to that in biological tissues (Mitchell *et al.*, 1986).

Furthermore, the use of quantitative measurements of relaxation characteristics is far superior to T1- or T2- weighted imaging, as quantitative approaches provide measurements of intrinsic relaxation parameters, unaffected by differences in external factors, such as hardware (Kjos *et al.*, 1985, Cheng *et al.*, 2012). These approaches have therefore been used in this work, to evaluate the impact iron has on relaxometry measurements in iron agarose standards.

4.5.2. Quantitative relaxometry for iron detection

Using quantitative MR relaxometry methods, these results using agarose standards are in line with the literature highlighting direct, linear correlation of R1, R2 and R2* to iron contents (Bartzokis *et al.*, 1993, Vymazal *et al.*, 1996b, Haacke *et al.*, 2005, Langkammer *et al.*, 2010). R2 relaxation rate has been well documented to be

affected by iron content in standards and, in human tissue (Pujol *et al.*, 1992, Bartzokis *et al.*, 1993, Wood, 2007), and this has been attributed due to the paramagnetic nature of iron impacting proton spin dephasing, thus enhancing T2 relaxation. R2* has been shown to provide greater sensitivity to iron contents than R2 (Langkammer *et al.*, 2010) likely due to R2* dependence on both the intrinsic transverse relaxation, as well as T2' susceptibility effects provided by local inhomogeneities (Haacke *et al.*, 2005). Furthermore, R1 values have also been shown to correlate with iron contents (Vymazal *et al.*, 1996b, Ogg and Steen, 1998), highlighting that the paramagnetism of iron affects longitudinal relaxation, as well as transverse relaxation, although possibly to a lesser degree (Schenck, 2003).

4.5.3. Different forms of iron impact relaxometry measurements differently

Ferric iron ions demonstrated higher R1, R2 and R2* values than ferrous iron. The differences in R1 and R2 relaxation between ferric and ferrous iron have been suggested to be due to the greater correlation time of magnetic dipole-dipole interactions with water protons for ferric iron, compared to ferrous iron (Tokuhiro *et al.*, 1996). It was also suggested that the paramagnetism of iron was not the main cause of these differences (Tokuhiro *et al.*, 1996), and evidence exists showing susceptibility effects were similar between these two ions (Dietrich *et al.*, 2013). Unpaired electrons enhance relaxation and the 5 unpaired electrons in ferric iron give rise to the paramagnetic nature of this form of iron. The 4 unpaired electrons in the ferrous form of iron also makes this paramagnetic, however when bound by

certain ligands into an octahedral configuration, ferrous iron can become diamagnetic, showing minimal effects on proton relaxation.

The forms of iron within these agarose standards were confirmed using the 1,10-phenanthroline assay, with the ferric form predominantly present in the ferric agarose standards and the ferrous form present in the ferrous agarose standards. There was also no evidence of precipitation or accumulation of iron particles within the agarose standards upon evaluation using microscopy, highlighting that iron ion presence remained within solution.

With the pH of ferric solutions at approximately 2.55, the form of iron present within these agarose standards is likely to be predominantly as the ferric ion, Fe^{3+} (Hem and Cropper, 1962). It is likely, however, that alternative states of iron may have also been present at low concentrations within these solutions, such as $[Fe_2(OH)_2]^{4+}$, $[FeOH]^{2+}$ and $[Fe(OH)_2]^{+}$ (Snoeyink and Jenkins, 1980). The presence of any alternate forms of iron, even at low concentrations, may provide an explanation for the apparent deviation from linear correlation that seems to be observed using this ion. Furthermore, with the pH of the ferrous solutions at approximately 4.57, the form of iron present in these agarose standards is likely to be predominantly as the ferrous ion Fe^{2+} (Hem and Cropper, 1962). Linear regression has been used to evaluate the correlation of iron with relaxometry measurements due to the well-established literature present discussing this approach (Bartzokis *et al.*, 1993, Vymazal *et al.*, 1996b, Haacke *et al.*, 2005, Langkammer *et al.*, 2010).

R2 and R2* molar relaxivities were similar for both ferric iron (r_2 = 31.55 $s^{-1}mM^{-1}$; r_2* = 32.86 $s^{-1}mM^{-1}$) and ferrous iron (r_2 = 3.61 $s^{-1}mM^{-1}$; r_2* = 3.47 $s^{-1}mM^{-1}$) suggesting that there is no influence of field inhomogeneities detected in these standards, and that all the transverse relaxation can be associated to intrinsic T2 relaxation. Indeed, this was confirmed after calculating R2', to show that no correlation could be detected with iron content using these agarose standards. Further support for the lack of R2' correlation with iron content in these agarose standards was proven due to the extremely high error in R2' values, given the accumulation of error by subtracting R2 from R2* maps on a pixel by pixel basis. These observations were also apparent when using R2' to measure ferritin iron agarose standards. With these standards providing a very simple model for iron quantification, clearly the agarose matrix provides a homogeneous solution of iron ions, containing very few inhomogeneities (Tokuhiro *et al.*, 1996). Furthermore, this is in agreement with the similar susceptibilities detected for the two forms of iron, as highlighted above (Dietrich *et al.*, 2013).

It has also been demonstrated here that different proportions of ferric to ferrous iron can be detected based on their molar relaxivities, using agarose standards. This may provide a novel approach to determine the ferric to ferrous iron concentration in samples, by serial dilution of solutions and measurement of the molar relaxivities. A similar approach has already been used for measurement of radiation levels, through the conversion of ferrous to ferric iron upon application of radiation to a ferrous standard, and measurement of the NMR changes (Appleby *et al.*, 1987). These approaches may provide a non-invasive and readily available method to

determine proportional concentrations of ferric to ferrous iron, compared to the complex and restrictive chemical analyses also available. Whether this approach provides the same sensitivity using biological samples however, still requires evaluation (Dietrich *et al.*, 2013).

Finally, iron bound within ferritin storage protein was assessed for relaxivity values and molar relaxivity compared with iron ions. Whilst ferritin showed similar, strong positive correlation values as both ferrous and ferric iron, the r_1, r_2 and r_2* molar relaxivities were more similar to the ferrous form of iron, despite iron within ferritin being held as ferrihydrite crystals, in the ferric form (Harrison and Arosio, 1996). Ferritin has been shown to provide effects on R1 and R2 relaxivities based on its loading factor (Vymazal *et al.*, 1996a), as well as protein concentration (Gossuin *et al.*, 2004). The low impact of ferritin on relaxivity, especially in *in vitro* model systems is in agreement with other findings (Gossuin *et al.*, 2004, Bennett *et al.*, 2008). To obtain ferritin relaxivities *in vitro* closer to those detected in tissue, ferritin had to be aggregated either using trypsin or by binding ferritin to actin prior to polymerisation, leading to enhanced T2 relaxation (Gossuin *et al.*, 2007, Bennett *et al.*, 2008). However these methods still only enhanced T2 relaxation by 20-30%, remaining substantially less than that observed for ferric iron. This highlights that ferritin iron does not impact relaxometry values to the same extent as ferric iron.

The effects of ferritin on relaxivity values have been attributed due to a number of different theories, one of which, the proton exchange dephasing model, relies on exchange of bulk water protons, with exchangeable protons bound to the iron core

in ferritin, providing greater transverse relaxation effects (Gossuin *et al.*, 2002, Gossuin *et al.*, 2004).

It therefore seems plausible that if there is a misregulation of iron during diseases, including in AD, whereby normal-loaded, dispersed ferritin can be converted into various pathological forms, then this may strongly impact the MRI relaxation characteristics without a change in iron content. This is further supported by comparisons performed here between ferric and ferrous iron, with ferritin on R1, R2 and R2* relaxometry. Indeed, the discovery of greater levels of magnetite in the brains of AD patients (Collingwood *et al.*, 2005, Pankhurst *et al.*, 2008) may also be noteworthy, given that magnetite shows enhanced impact on relaxometry (Gossuin *et al.*, 2004).

4.5.4. Acquisition artefacts and sequence comparison

R2* measurements demonstrated image artefacts when acquired with slices of 2 mm thickness, which was attributed to B_0 inhomogeneities. Re-acquisition of agarose standards at 0.5 mm thickness led to the reduction of these artefacts. This was therefore due to lower impact of B_0 inhomogeneities within thinner slices, providing improved image acquisition. Despite the reduction in slice thickness affecting SNR and therefore the variability of pixels intensities within each ROI, the different iron concentrations could still be detected using this method of R2* assessment. To improve future acquisitions however, increasing the number of averages to improve SNR could be carried out.

Comparing R2 and R2* standard acquisition methods against fast acquisition methods demonstrates that the values from each technique are well correlated with each other, however they provide slightly different absolute values. This highlights that whilst these faster acquisition methods can be utilised as part of future experiments, especially when used consistently within a study, care should be taken if attempting to measure "true" relaxivity values, or if comparing against relaxometry values from different acquisition sequences. Similar to the detectably lower R2 values measured here with ME acquisition, it has been observed that T2 decay was slower using multiple echoes in the faster spin-echo acquisition methods, leading to higher signal intensity for later echoes than by using standard acquisition of T2 (Hennig, 1988, Poon and Henkelman, 1992). This therefore confirms the need to understand how the standard and fast acquisition methods compare to each other, when understanding the work within this project utilising both standard and fast MRI sequences.

4.5.5. Conclusion

R1, R2 and R2* relaxometry measurements have been validated for their use in assessment of iron content non-invasively using MRI, as outlined within the objectives (see section 4.2), and all showed strong, linear correlations to iron content. The impact of different forms of iron on these measurements has also been established, with the ferric form of iron showing greater influence on R1, R2 and R2* than the ferrous form. Using R2' measurements, it was not possible to assess the iron ion content within agarose standards, due to the relatively minimal

contribution of magnetic field inhomogeneities in these standards. Finally, ferritin iron demonstrated substantially lower longitudinal and transverse relaxation characteristics than ferric iron, despite the equally strong, linear correlation to iron content. As one of the objectives within this chapter was to gain an understanding of the different effects that different iron ions, and bound compared with unbound iron can elicit on MR relaxometry values (see section 4.2), it may therefore be important to consider that not all MR relaxometry changes observed within tissue may be solely due to iron concentration, given the varied measurements observed with different forms of iron here.

5. Results: Iron Measurement in Control and AD Human Medial Temporal Gyrus

5.1. Introduction

This chapter first assesses MR relaxometry values in aged healthy control samples from the medial temporal gyrus (MTG), and corroborates these with quantitative SR-XRF elemental iron mapping to understand how iron content directly affects relaxometry. The correlation of relaxometry values is also measured specifically against iron content. Subsequently, MR relaxometry of AD brain samples from the MTG are evaluated and again, corroborated and correlated with quantitative SR-XRF elemental iron mapping. Comparisons are made between control and AD tissue samples to explore changes in relaxivity values or iron content, or to evaluate any changes in the correlation between these measurements in neurodegenerative disease. Myelin content was also evaluated in these brain samples to understand the impact that tissue microstructure holds on relaxometry values.

5.2. Objectives

The objectives for the work with control and AD human post-mortem tissue were:

- To perform quantitative R1, R2, R2* and R2' relaxometry on control, and subsequently compared with AD, post-mortem human brain tissue from the MTG.

- To quantify SR-XRF elemental iron content in control, and subsequently compared with AD, post-mortem human brain tissue from the MTG.
- To correlate the spatial distribution of iron content with R1, R2, R2* and R2' relaxometry methods, both within individual samples, and across multiple samples, in control, and subsequently compared with AD, post-mortem human brain tissue.
- To evaluate the sensitivity of MRI relaxometry methods to assess iron content within specific tissue types, such as WM or GM, from control, and subsequently compared with AD, post-mortem human brain tissue.
- To determine the effect of tissue microstructure on MRI-iron correlations, in particular the degree of myelination, in control, and subsequently compared with AD, MTG brain tissue.

5.3. Methods

The majority of methods for this work can be found in section 3.2.2. In brief, human control samples underwent R1, R2, R2* and R2' relaxometry at 7T and were then sectioned for XRF elemental iron mapping and histology. Quantitative MRI relaxometry measurements and SR-XRF elemental iron contents were compared between tissue areas and correlated both within individual samples, as well as across multiple samples. The same assessments were also performed using AD human tissue samples from the MTG, and compared against the control samples. Luxol fast blue (LFB) staining was performed on adjacent sections to those taken for

XRF elemental iron mapping from both control and AD samples, for assessment of the impact myelin holds on relaxometry values in both control, and compared with AD tissue.

5.4. Results of Control Human MTG Assessment

5.4.1. Qualitative assessment of relaxometry and iron elemental maps in control samples

T2-weighted (T2W) images were each registered manually to their corresponding elemental iron maps by first re-orientating and then cropping images to match the iron maps (Figure 5-1A-C; see section 3.2.2.3). The T2W and XRF maps were then visually inspected to compare tissue architectural similarities. The same registration process was used to register R1, R2 and R2* maps with corresponding elemental iron maps (Figure 5-1D-F).

In both relaxometry and elemental iron maps, increased pixel intensities correspond to increased relaxivity values and iron contents, respectively (Figure 5-1C-F). The WM from brain tissue was clearly observed as dark areas in the T2W images of MTG (Figure 5-1B) corresponding to higher iron content in the elemental iron map (Figure 5-1C). The brighter GM regions in T2W images (Figure 5-1B) were localised at the outer areas of each tissue sample, with correspondingly lower iron contents (Figure 5-1C). R1, R2 and R2* maps matched the GM and WM localisation as shown in T2W images and in iron content maps, with higher relaxation rates in WM and lower relaxation rates in GM (Figure 5-1C-F). Only relaxivity values within

the cropped area of relaxometry maps were compared against elemental iron contents.

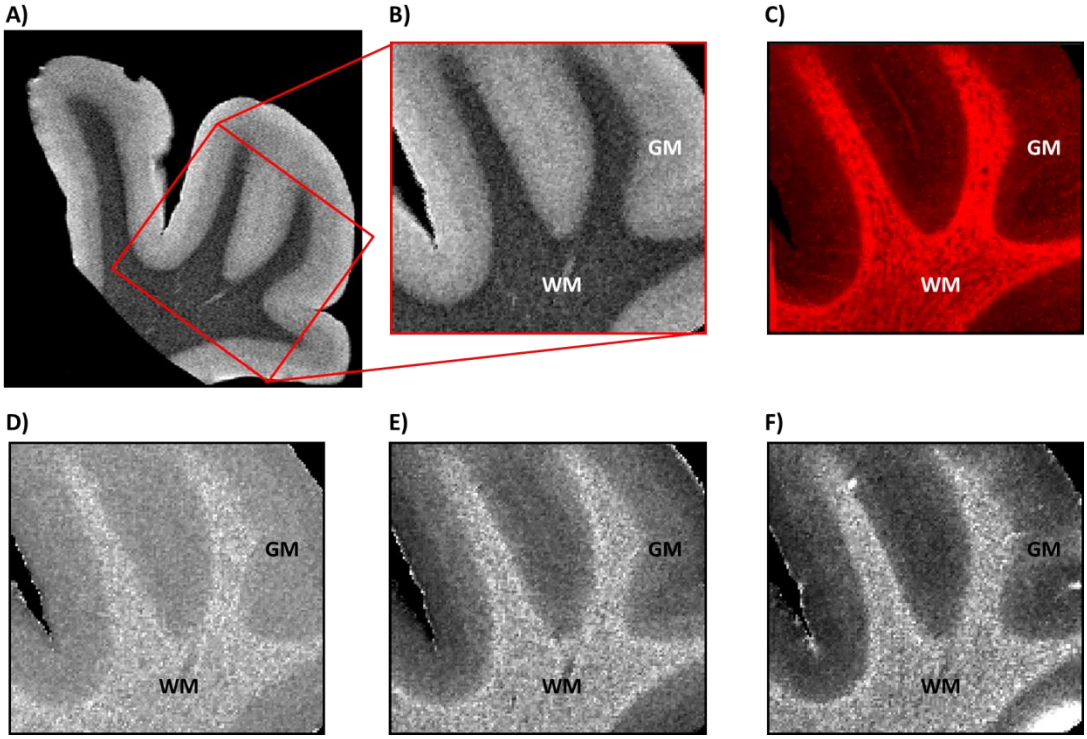

Figure 5-1 Alignment and qualitative comparison of relaxometry and iron elemental maps

(A) Full T2W image of a representative control human tissue sample from the medial temporal gyrus (MTG). (B) Registered region of T2W image that is comparable to the region acquired in (C) SR-XRF elemental iron mapping. (D) R1, (E) R2 and (F) R2 maps were then registered in the same way as T2W images to the acquired elemental iron map.*

Given that WM and GM regions are two of the dominant features observed in MR brain imaging *in vivo*, ROIs were drawn around these two tissue regions from all

samples acquired, on both elemental iron and relaxometry maps. Closer inspection of both T2W structural images and elemental iron maps allowed the delineation of distinct cortical layers within the GM, seemingly related to their iron content (Figure 5-2). Therefore, in addition to ROIs for WM and GM, two further ROIs were drawn corresponding to this mid-cortical layer (MCL), situated at cortical layers IV-V at the boundary between GM and WM, and to the distal GM layers (dGM), at the outermost edges of the cortex (Figure 5-2).

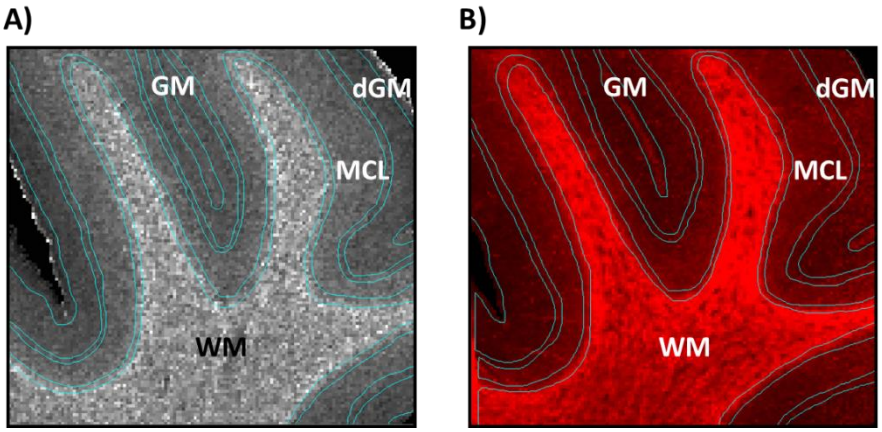

Figure 5-2 Whole ROI placement on R2 and elemental iron map of control sample

Typical WM, MCL and dGM ROI placement on (A) an R2 map and (B) an elemental iron map. The whole GM ROIs incorporate both the dGM and MCL ROIs.

5.4.2. Effect of PMI, fixation time and subjects' age on relaxometry and elemental iron content in control samples

As mentioned in section 1.7, a number of factors may influence relaxivity values and iron content in post-mortem human tissue. Therefore, the effects of post-

mortem interval (PMI), fixation time and subjects' age at death were evaluated initially, prior to quantitative analysis of tissue samples.

5.4.2.1. PMI

R1, R2, R2* and R2' relaxometry values, and elemental iron content were unaffected by PMI in our control human tissue samples (Figure 5-3, Table 5-1). PMI had no significant effects on any of the relaxivity values assessed using Pearson's correlation, in either GM (R1, P = 0.575; R2, P = 0.618; R2*, P = 0.683 and R2', P = 0.929) or WM (R1, P = 0.345; R2, P = 0.627; R2*, P = 0.831 and R2', P = 0.883; Figure 5-3A-D). Iron contents were also not significantly affected by PMI length in either GM regions (P = 0.480) or WM regions (P = 0.426; Figure 5-3E). The different GM cortical layers were also separately assessed, showing no significant effects of PMI on relaxometry or iron contents in these tissue areas (dGM: R1, P = 0.584; R2, P = 0.713; R2*, P = 0.361; R2', P = 0.316 and iron, P = 0.519, and MCL: R1, P = 0.612; R2, P = 0.413; R2*, P = 0.680; R2', P = 0.784 and iron, P = 0.423; Table 5-1).

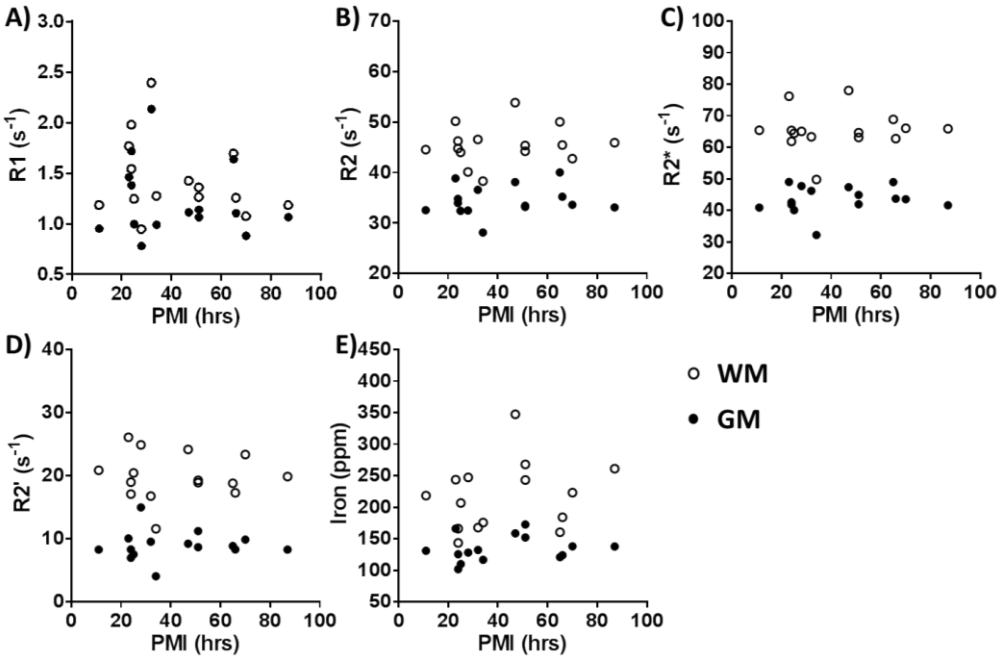

Figure 5-3 Effect of PMI on relaxometry values and elemental iron contents in control samples

The effect of PMI length of control tissue samples, against (A) R1, (B) R2, (C) R2 and (D) R2' relaxivity values, and against (E) elemental iron content. Correlation was assessed using Pearson's correlation with significance level set at P ≤ 0.05 (n =15).*

5.4.2.2. Fixation time

Increasing time in fixative significantly increased R1 relaxivity values in both GM and WM (GM: $r^2 = 0.59$, P = 0.0009 and WM: $r^2 = 0.59$, P = 0.0008; Figure 5-4A) and also of R2 relaxivity values in only GM (GM: $r^2 = 0.27$, P = 0.047 and WM, P = 0.085; Figure 5-4B, Table 5-1). No significant effects of fixation time were detected on R2* or R2' relaxivity values, or with iron content in GM (R2*, P = 0.440; R2', P = 0.360 and iron, P = 0.770) or WM of control human MTG samples (R2*, P = 0.588; R2', P = 0.440 and iron, P = 0.371; Figure 5-4C-E).

Again, the effects of length of fixation on relaxometry and iron measures were compared separately in dGM and MCL. Both dGM and MCL R1 values were significantly increased with increasing fixation times (dGM: $r^2 = 0.57$, P = 0.0012 and MCL: $r^2 = 0.59$, P = 0.0008). R2 values were also significantly increased in the dGM with increasing time in fixative ($r^2 = 0.40$, P = 0.011) but not in the MCL (P = 0.143). R2* relaxivity values (dGM, P = 0.165; MCL, P = 0.611), R2' values (dGM, P = 0.658; MCL, P = 0.356) and iron contents (dGM, P = 0.364; MCL, P = 0.935) were unaffected by fixation time (Table 5-1).

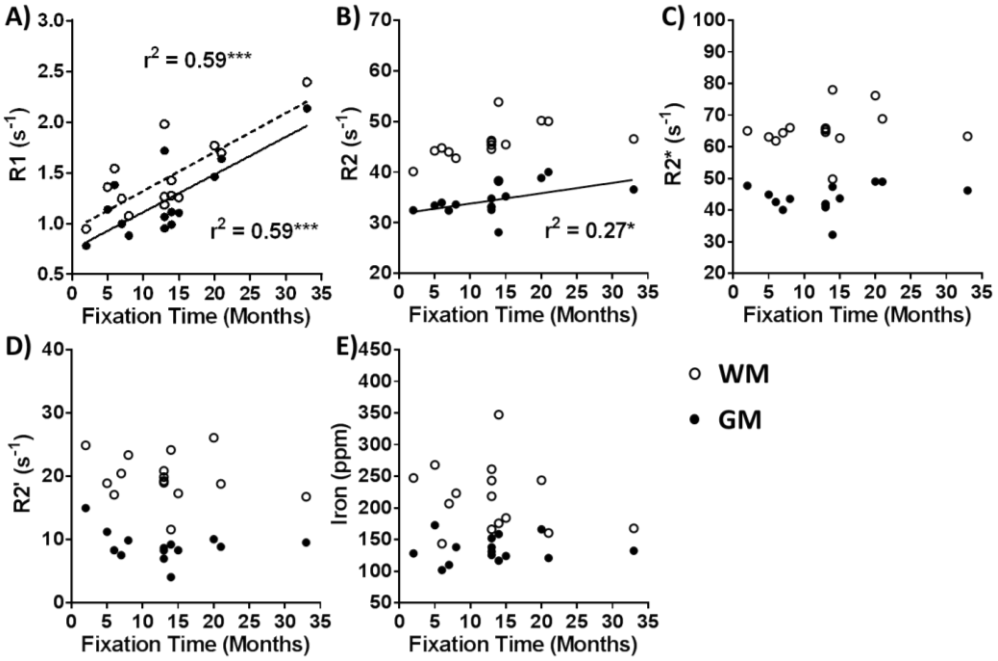

Figure 5-4 Effect of fixation time on relaxometry values and elemental iron contents in control samples

The effect of fixation time of control tissue samples, against (A) R1, (B) R2, (C) R2 and (D) R2' relaxivity values, and against (E) elemental iron content. Correlation was assessed using Pearson's correlation with significance level set at P ≤ 0.05. * P ≤ 0.05, ** P < 0.01, *** P < 0.001 and **** P < 0.0001 (n = 15).*

Samples with fixation time greater than 18 months were therefore excluded from subsequent assessments, given that iron content remains stable up to this point (Gellein *et al.*, 2008), and fixation time has less effect on results.

5.4.2.3. Age

The influence of the age of subjects at death on relaxometry values and iron content were also studied (Figure 5-5, Table 5-1). Age of subjects at death had no significant effects on GM or WM relaxivities (GM: R1, P = 0.169; R2, P = 0.903; R2*, P = 0.269 and R2', P = 0.051 and WM: R1, P = 0.104; R2, P = 0.641; R2*, P = 0.967 and R2', P = 0.575; Figure 5-5A-D). Iron contents were also unaffected by age in GM (P = 0.342) and WM (P = 0.985; Figure 5-5E). Individual correlations of dGM and MCL with subject age at death also showed no effect of age on relaxivities (dGM: R1, P = 0.178; R2, P = 0.913; R2*, P = 0.309 and R2', P = 0.162 and MCL: R1, P = 0.177; R2, P = 0.993; R2*, P = 0.408 and R2', P = 0.070) or on iron contents (dGM, P = 0.325 and MCL, P = 0.185; Table 5-1).

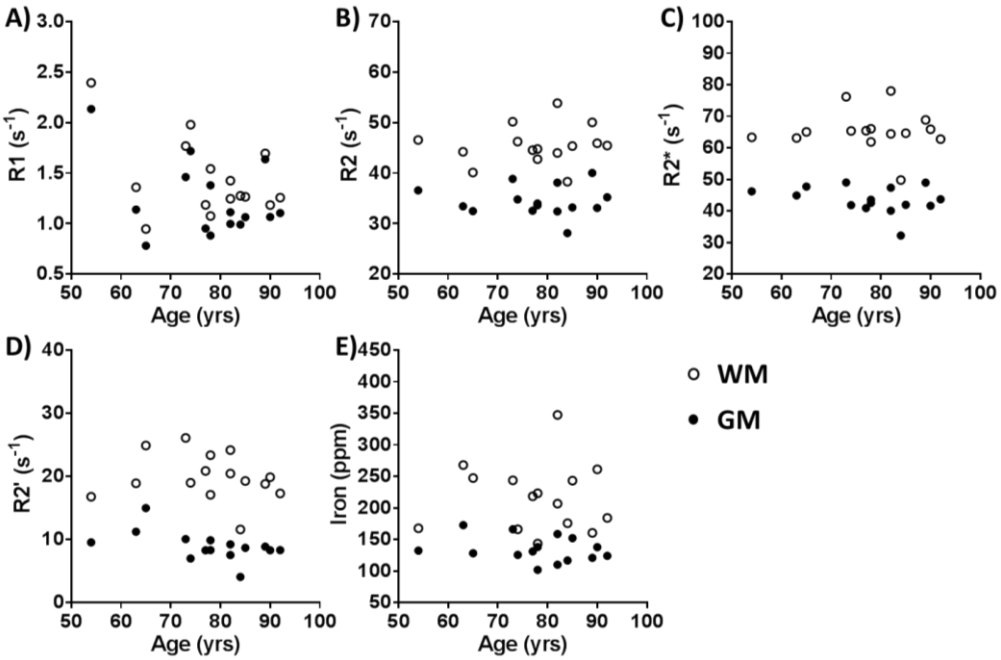

Figure 5-5 Effect of subjects' age at death on relaxometry values and elemental iron contents in control samples

The effect of control subjects' age at death, against (A) R1, (B) R2, (C) R2 and (D) R2' relaxivity values, and against (E) elemental iron content. Correlation was assessed using Pearson's correlation with significance level set at $P \leq 0.05$ (n = 15).*

Table 5-1 Summary table of the assessed factors' r^2 correlation values, on control sample relaxivity values and iron contents

		R1	R2	R2*	R2'	Iron
PMI	WM	0.07	0.02	0.00	0.00	0.05
	GM	0.02	0.02	0.01	0.00	0.04
	MCL	0.02	0.05	0.01	0.01	0.05
	dGM	0.02	0.01	0.06	0.08	0.04
Fixation Time	WM	0.59***	0.21	0.02	0.05	0.06
	GM	0.59***	0.27*	0.05	0.06	0.01
	MCL	0.59***	0.16	0.02	0.07	0.00
	dGM	0.57**	0.40*	0.14	0.02	0.07
Subjects' Age	WM	0.19	0.02	0.00	0.02	0.00
	GM	0.14	0.00	0.09	0.26	0.07
	MCL	0.14	0.00	0.05	0.23	0.14
	dGM	0.14	0.00	0.08	0.15	0.08

*Correlation was assessed using Pearson's correlation with significance level set at $P \leq 0.05$. * $P \leq 0.05$, ** $P < 0.01$, *** $P < 0.001$ and **** $P < 0.0001$. Significant results highlighted blue.*

5.4.3. Quantitative assessment of control tissue

5.4.3.1. R1, R2, R2 and R2' relaxivity value assessment*

Mean relaxometry values are summarised in Table 5-2. R1, R2, R2* and R2' WM values were all significantly higher when compared with overall GM values only (R1, P = 0.05; R2, P < 0.0001; R2*, P < 0.0001 and R2', P < 0.0001; Figure 5-6, Table 5-2). Separate comparison of the dGM and MCL sub regions with WM also demonstrated significant differences between these three tissue types using one-way ANOVA (R1, P = 0.045; R2, P < 0.0001; R2*, P < 0.0001 and R2', P < 0.0001; Figure 5-6, Table 5-2). More specifically, R2 and R2* values were consistently higher in WM compared with MCL (R2, P < 0.0001; R2*, P < 0.0001) and the MCL showed consistently higher values than dGM (R2, P < 0.0001; R2*, P = 0.0095; Figure 5-6B-C). R2' values in WM regions were significantly higher than both MCL and dGM (P < 0.0001), however the MCL did not show significantly different R2' values than the dGM region (P = 0.911; Figure 5-6D). Similarly, R1 values were only higher in WM compared to dGM (P = 0.040), whilst differences between WM and MCL (P = 0.197) and MCL and dGM (P = 0.711) were not significant (Figure 5-6A, Table 5-2).

To evaluate the consistency of higher relaxivities in WM compared to GM within each sample, paired statistics were also employed. Paired t-testing showed R1, R2, R2* and R2' relaxivities were found to increase significantly between GM and WM regions (P < 0.0001; Figure 5-6A-D). Furthermore, repeated-measures one-way ANOVA testing of dGM, MCL and WM regions demonstrated values consistently increasing in the order of dGM < MCL < WM for R1, R2 and R2* relaxometry (R1, P < 0.0001; R2, P < 0.0001 and R2*, P < 0.0001; Figure 5-6A-C). R2' values did not

consistently increase in this order across the three tissue regions, as values between dGM and MCL were similar (P = 0.761; Figure 5-6D).

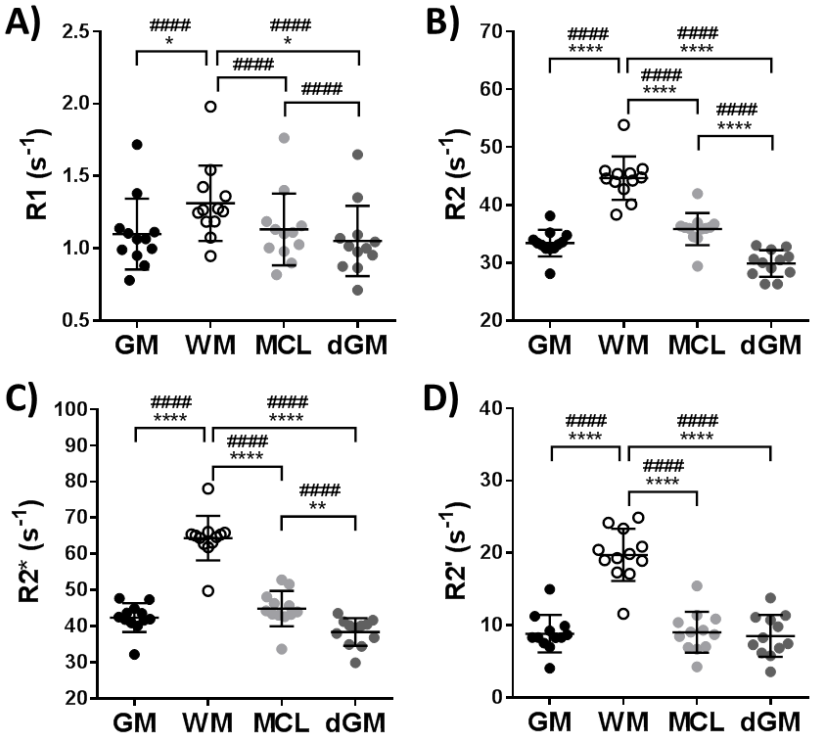

Figure 5-6 Relaxometry values in WM and GM tissue of control samples

Graphs showing the mean GM and WM region relaxivity values for (A) R1, (B) R2, (C) R2 and (D) R2' from control MTG samples. Significance was assessed using Student's unpaired (*), or paired (#) t-test between GM and WM. Mean MCL and dGM sub regions of GM ROIs were separately assessed with WM values, using one-way ANOVA (*), or repeated-measures one-way ANOVA (#), with Tukey's test for multiple comparisons. Graphs show mean values ± SD (n = 12).*

Table 5-2 Relaxivities and iron content from control MTG samples

Tissue Region	R1 (s^{-1})	R2 (s^{-1})	R2* (s^{-1})	R2' (s^{-1})	Iron (ppm)
GM	1.10 ± 0.25	33.42 ± 2.31	42.38 ± 3.98	8.82 ± 2.59	133.2 ± 20.4
WM	1.31 ± 0.26	44.64 ± 3.75	64.39 ± 6.16	19.74 ± 3.60	223.9 ± 55.2
P-value	0.050	< 0.0001	< 0.0001	< 0.0001	< 0.0001
WM	1.31 ± 0.26	44.64 ± 3.75	64.39 ± 6.16	19.74 ± 3.60	223.9 ± 55.2
MCL	1.13 ± 0.25	35.86 ± 2.78	44.92 ± 4.88	9.05 ± 2.84	150.1 ± 27.4
dGM	1.05 ± 0.24	29.89 ± 2.29	38.44 ± 3.82	8.53 ± 2.89	115.7 ± 16.3
P-value	0.045	< 0.0001	< 0.0001	< 0.0001	< 0.0001

(GM) grey matter, (WM) white matter, (MCL) mid-cortical layer and (dGM) distal grey matter regions. Values are mean ± SD. Statistical testing between GM and WM was performed using Student's unpaired t-test. Statistical testing between dGM, MCL and WM was performed using one-way ANOVA, with Tukey's test for multiple comparisons. Significance level set at $P \leq 0.05$ (n = 12).

5.4.3.2. XRF elemental iron assessment

Iron contents were also identified as being significantly higher in WM compared with GM regions from the MTG of control samples ($P < 0.0001$; Figure 5-7, Table 5-2). Subdivision of the GM region into the MCL and dGM demonstrated that mean iron content was significantly different between the three tissue regions ($P < 0.0001$; Figure 5-7, Table 5-2). Following Tukey's test for multiple comparisons however, only WM regions were significantly higher compared with both MCL and dGM ($P < 0.0001$), whilst iron content was similar between MCL and dGM ($P = 0.072$; Figure 5-7). Using paired statistics, iron content was consistently higher in the WM compared to GM for each sample ($P < 0.0001$; Figure 5-7). Repeated-measures one-way ANOVA testing of dGM, MCL and WM demonstrates values consistently increasing in the order of dGM < MCL < WM in iron content ($P < 0.0001$) between these three tissue types (Figure 5-7).

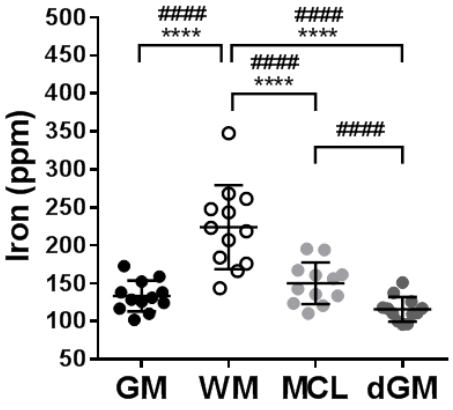

Figure 5-7 Elemental iron content in WM and GM tissue of control samples

Graphs showing the mean GM and WM region iron contents from control MTG samples. Significance was assessed using Student's unpaired (*), or paired (#) t-test. Mean MCL and dGM sub regions of the GM ROIs were separately assessed with WM

iron contents, using one-way ANOVA (*), or repeated-measures one-way ANOVA (#), with Tukey's test for multiple comparisons. Graphs show mean values ± SD (n = 12).

5.4.3.3. Gender comparison

Similar relaxometry values and iron contents were observed between male and female subjects within GM and WM regions of control MTG samples using two-way ANOVA, with Holm-Sidak test for multiple comparisons (R1, P = 0.158; R2, P = 0.240; R2*, P = 0.093; R2', P = 0.119 and iron, P = 0.793; Figure 5-8, Table 5-3). Furthermore, neither the dGM nor MCL layers demonstrated significant differences between male and female subjects (R1, P = 0.105; R2, P = 0.231; R2*, P = 0.084; R2', P = 0.120 and iron, P = 0.828; Figure 5-8, Table 5-3).

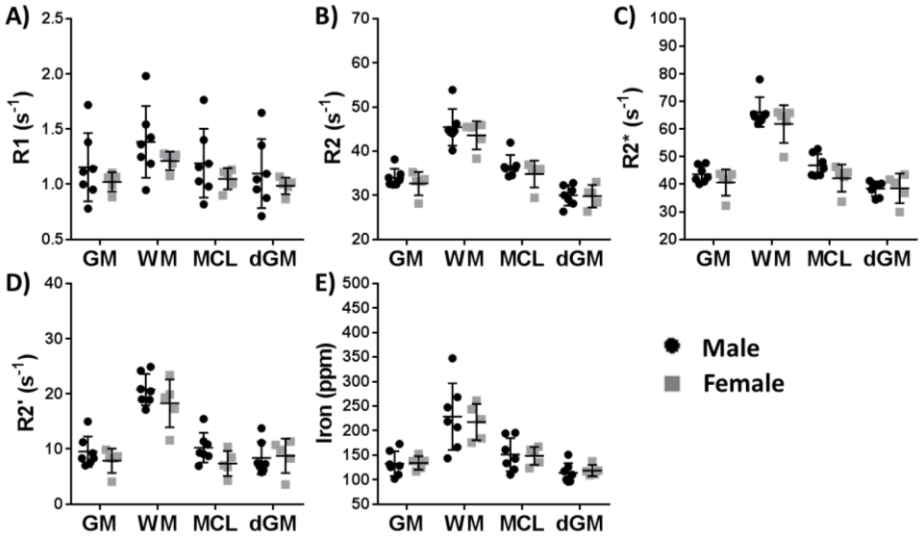

Figure 5-8 Gender comparison of relaxometry and elemental iron contents in control samples

(A) R1, (B) R2, (C) R2, (D) R2' relaxometry values, and (E) elemental iron contents, from male (n = 7) and female (n = 5) subjects in GM and WM tissue, and in the MCL and dGM sub regions. Graphs show mean values ± SD. Significance assessed using two-way ANOVA, with Holm-Sidak test for multiple comparisons with a level set to P ≤ 0.05 .*

Table 5-3 Relaxivities and iron content of control MTG from male and female subjects

GM	R1 (s^{-1})	R2 (s^{-1})	R2* (s^{-1})	R2' (s^{-1})	Iron (ppm)
Male	1.15 ± 0.31	33.97 ± 2.04	43.64 ± 3.06	9.52 ± 2.77	132.7 ± 25.2
Female	1.02 ± 0.09	32.65 ± 2.67	40.63 ± 4.79	7.86 ± 2.21	133.9 ± 13.8
WM					
Male	1.38 ± 0.33	45.41 ± 4.17	66.21 ± 5.38	20.78 ± 2.85	228.4 ± 68.0
Female	1.21 ± 0.08	43.57 ± 3.19	61.85 ± 6.86	18.29 ± 4.34	217.6 ± 37.0
MCL					
Male	1.19 ± 0.31	36.59 ± 2.55	46.86 ± 4.10	10.25 ± 2.72	151.1 ± 33.9
Female	1.05 ± 0.10	34.83 ± 3.05	42.20 ± 4.94	7.37 ± 2.26	148.6 ± 18.3
dGM					
Male	1.10 ± 0.31	29.97 ± 2.31	38.38 ± 2.69	8.36 ± 2.96	113.8 ± 19.9
Female	0.99 ± 0.08	29.78 ± 2.53	38.52 ± 5.40	8.76 ± 3.13	118.5 ± 11.2

Values are mean ± SD. Statistical testing performed using two-way ANOVA, with Holm-Sidak test for multiple comparisons with a level set to $P \leq 0.05$ (male (n = 7) and female (n = 5)).

5.4.4. Correlation of relaxometry to iron in control samples

5.4.4.1. Correlation of whole tissue type ROIs

Mean dGM, MCL and WM R2, R2* and R2' demonstrated significant positive correlations to iron (R2: $r^2 = 0.71$, $P < 0.0001$; R2*: $r^2 = 0.76$, $P < 0.0001$; R2': $r^2 =$

0.66, P < 0.0001; Figure 5-9B-D). R1 values were not significantly correlated (r^2 = 0.046, P = 0.211) across multiple control tissue samples (Figure 5-9A).

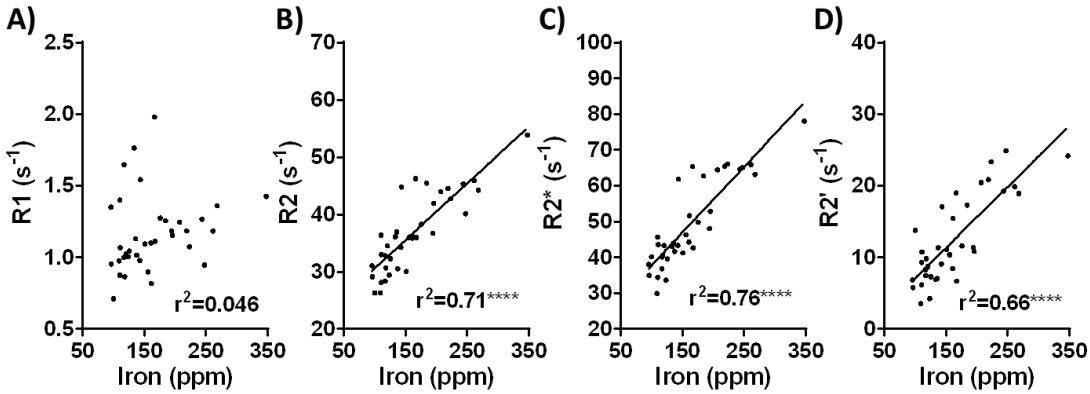

Figure 5-9 Whole tissue ROI correlations from control samples

Mean (A) R1, (B) R2, (C) R2 and (D) R2' values correlated against iron content for the control samples of all dGM, MCL and WM regions (n = 36). Correlation assessed using Pearson correlation with significance level set at P ≤ 0.05.*

In order to gain a greater understanding of the spatial correlation of relaxometry measurements to iron content in control samples (see section 1.6.5.1), equally sized square ROIs (see section 5.4.4.2) per tissue region (i.e. dGM, MCL and WM) were placed across each of the samples (Figure 5-10). Eight ROIs per tissue area were used to allow the variability of correlations within a single sample to be better understood (see section 5.4.4.3), whilst also preventing any bias in correlations within each sample (see section 3.2.2.3). Furthermore, eight ROIs per tissue area allows for tissue area-specific correlations to be performed (see section 5.4.4.5).

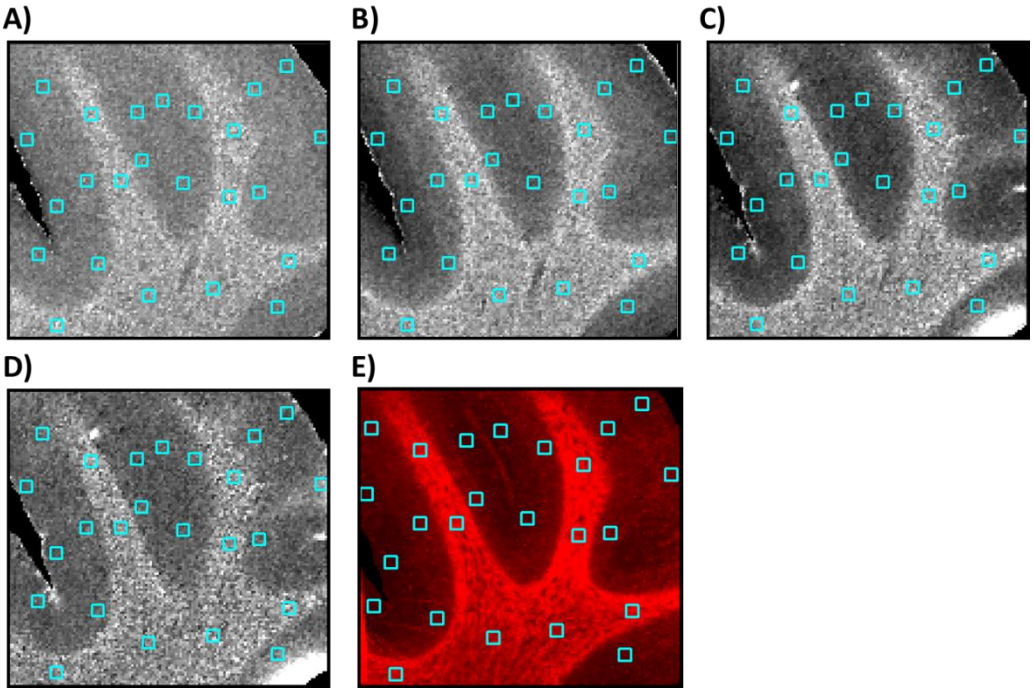

Figure 5-10 Representative relaxometry and elemental iron maps showing placement of 24 small ROIs in control sample

Representative (A) R1, (B) R2, (C) R2, (D) R2' and (E) elemental iron maps, demonstrating the placement of the eight equally sized ROIs within each tissue region (twenty four ROIs in total across each sample).*

5.4.4.2. Comparison of ROI sizes

Different sizes (3x3 and 5x5 pixel) of ROIs were used to evaluate whether relaxometry to iron correlations are affected by the size of the ROI used within a sample (Figure 5-11). Other work has used ROI sizes of 3x3 pixels (Antharam *et al.*, 2012). The regression correlation gradients and y-intercepts between relaxometry values and iron in individual samples were similar between 3x3 and 5x5 pixel ROIs, in all the control samples evaluated (representative correlations from one sample

are shown in Figure 5-11A-C). However the r^2 correlation values of each individual sample were significantly greater using 5x5 pixels compared to the 3x3 pixel ROIs for each of the samples (R1, P = 0.0032; R2, P = 0.0026; R2*, P = 0.0029; Figure 5-11D-F). This is likely due to the greater sampling of pixels using larger 5x5 pixel ROIs than the 3x3 pixel ROIs. Therefore, ROIs of 5x5 pixels were chosen for analyses, being more sensitive to correlations without affecting correlation gradients or y-intercepts.

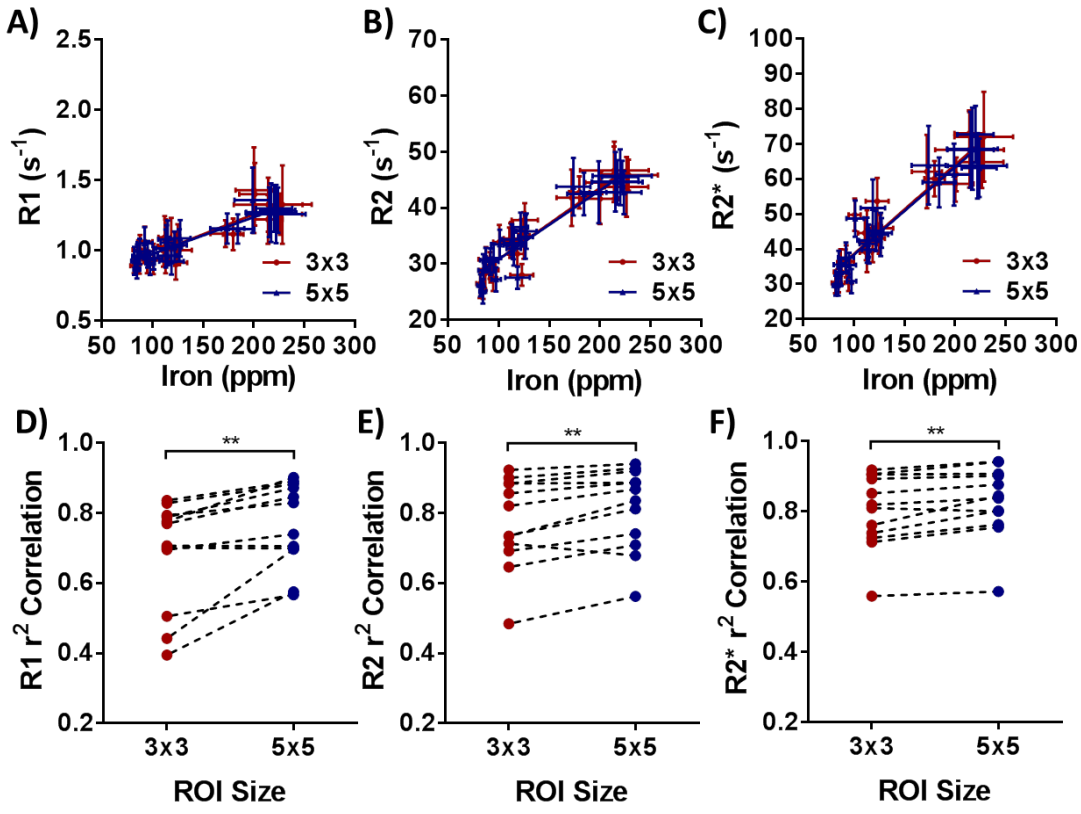

Figure 5-11 Comparison of 3x3 or 5x5 ROI sizes for spatial assessment across control tissue

Correlation of (A) R1, (B) R2 and (C) R2 values to elemental iron, in one sample, using twenty-four 3x3 (red) or 5x5 (blue) pixel ROIs. The r^2 correlation values were significantly improved using 5x5 (blue) pixel ROIs compared with 3x3 (red) pixels*

using (D) R1, (E) R2 and (F) R2 values to elemental iron content. (D-F) Each point represents the r^2 correlation of relaxometry values to iron within one sample and assessed for significance using paired t-test, with level set at $P \leq 0.05$ (n = 12).*

5.4.4.3. Individual sample correlations

Averaging all the individual r^2 correlations using the 5x5 pixel ROIs within each control sample (representative single sample ROI placement as shown in Figure 5-10, with individual correlation plots in Figure 5-12) demonstrated strongly significant correlations between each relaxometry measurement with iron content (R1, $r^2 = 0.77 \pm 0.12$; R2, $r^2 = 0.81 \pm 0.12$; R2*, $r^2 = 0.83 \pm 0.10$; R2', $r^2 = 0.65 \pm 0.18$; Table 5-4). Mean R2' correlations were found to be significantly lower than R2 and R2* correlations using one-way ANOVA with Tukey's multiple comparisons test (R2' compared with: R2, P = 0.024 and R2*, P = 0.012; Table 5-4). R1, R2 and R2* relaxometry were not significantly different in their individual correlations to iron across all the samples (R1 to R2, P = 0.848; R1 to R2*, P = 0.706; R1 to R2', P = 0.153 and R2 to R2*, P = 0.994; Table 5-4).

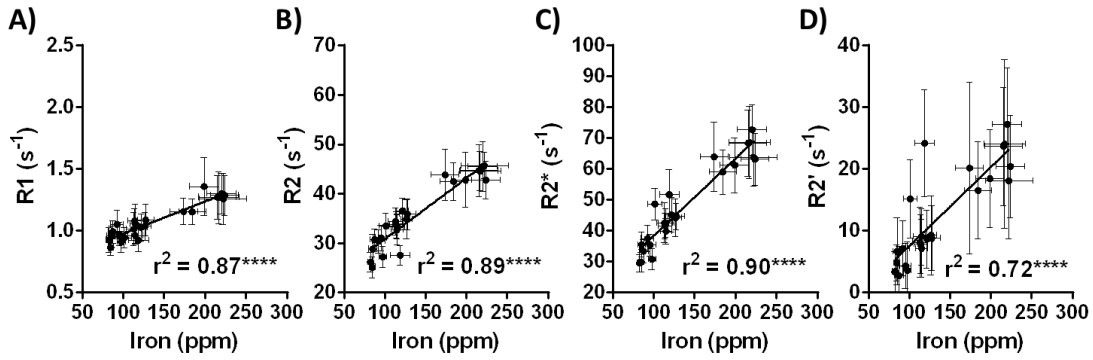

Figure 5-12 Representative relaxometry correlations against elemental iron for one control tissue sample

Representative (A) R1, (B) R2, (C) R2 and (D) R2' correlation graphs against iron content for one control post-mortem sample (see Figure 5-10). Correlation assessed using Pearson correlation with significance level set at $P \leq 0.05$.*

Table 5-4 The r^2 correlation values for relaxometry against iron content for each individual control sample

Sample	R1	R2	R2*	R2'
1	0.70	0.81	0.76	0.62
2	0.87	0.89	0.90	0.72
3	0.88	0.74	0.80	0.39
4	0.74	0.56	0.57	0.43
5	0.89	0.92	0.91	0.80
6	0.88	0.84	0.85	0.75
7	0.57	0.93	0.84	0.51
8	0.90	0.87	0.94	0.83
9	0.58	0.94	0.94	0.82
10	0.83	0.71	0.88	0.81
11	0.70	0.89	0.76	0.39
12	0.71	0.68	0.80	0.78
Mean ± SD	0.77 ± 0.12	0.81 ± 0.12 [a]	0.83 ± 0.10 [a]	0.65 ± 0.18

Significance assessed using one-way ANOVA with Tukey's multiple comparisons test to significance set at $P \leq 0.05$ ($n = 12$). [a] denotes significance compared with R2'. R2' correlations were lower than R2 and R2 correlations to iron, highlighted in blue.*

5.4.4.4. Grouped correlations of control samples

In order to evaluate the iron content correlations against relaxometry values for both intra- and inter- samples variation, rather than using the mean of each

samples' correlation (from Table 5-4), the individual 24 ROIs of all the samples together, were correlated with iron (Figure 5-13). Similar results to section 5.4.4.1 were obtained, with R2 and R2* demonstrating strongest correlation with iron content (R2, r^2 = 0.62, R2* r^2 = 0.68 and R2', r^2 = 0.54; all P < 0.0001) and R1 demonstrating very low correlation (r^2 = 0.05; Figure 5-13, Table 5-5). The correlation between R2* and iron was significantly higher than the correlation of R2 with iron (P = 0.005). Both R2 and R2* had higher correlation with iron content than R2' (R2' against R2, P = 0.046 and R2' against R2*, P < 0.0001; Table 5-5, Table 5-7). R1 values displayed much lower correlation across multiple samples (Figure 5-13A, Table 5-5) than was observed by evaluation of the individual sample correlations (Table 5-4). This indicates that other factors may impact the correlation of R1 with iron between samples. Indeed, an outlier seems to be apparent from the R1 correlation to iron content (Figure 5-13A), with the cluster of points between 1.5 and 2.0 s^{-1} all belonging to the same sample. This sample was investigated in greater detail, however could not be excluded as there was no evidence of β-amyloid, tau, or any other unusual pathology. Furthermore, the fixation time, PMI and age of death were within the range of other samples and there was no evidence of abnormal R2, R2* or R2' relaxometry measurements or unexpected iron contents. Molar relaxivities for each relaxometry measurement to iron are also summarised in Table 5-5, as a measure of sensitivity.

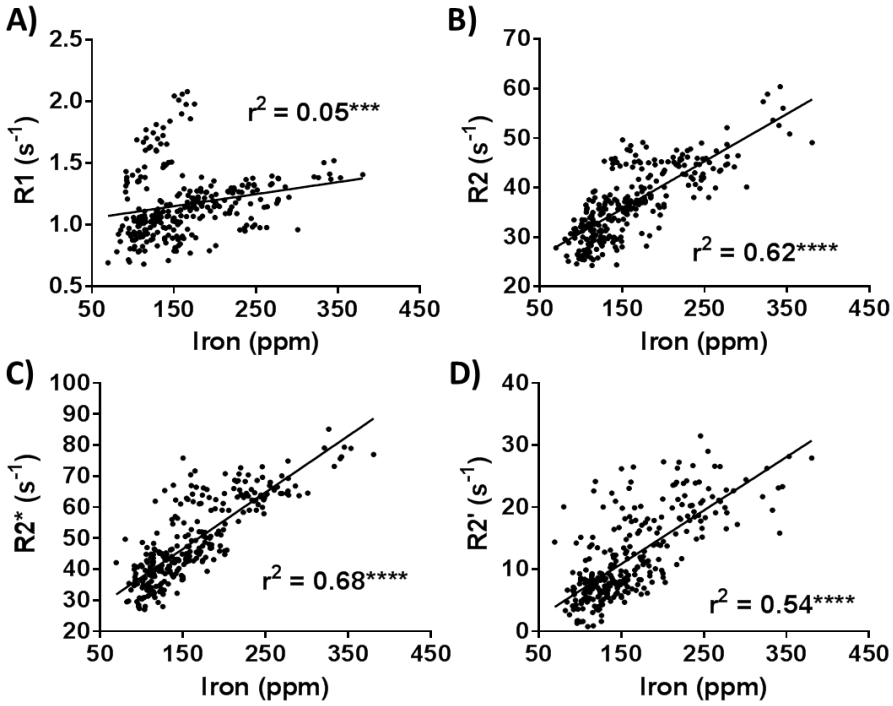

Figure 5-13 Correlation of relaxometry values against elemental iron content across all control samples

Graphs of (A) R1, (B) R2, (C) R2 and (D) R2' correlation with iron content, as assessed using the twenty-four 5x5 pixel ROIs for control samples. Each point corresponds to one ROI pairing between the relaxometry map and the elemental iron map. Correlation assessed using Pearson correlation with significance level set at $P \leq 0.05$ (n = 288).*

Individual sample regression lines (single representative correlation shown in Figure 5-12) were also displayed together to observe the inter-sample variability in correlations between relaxometry and iron (Figure 5-14). Wide variations in regression gradients, y-intercepts and ranges for R1, R2, R2* and R2' relaxometry and iron measurements are observed for the 12 individual samples (samples with

fixation times longer than 18 months have already been excluded) (Figure 5-14A-D). Furthermore, despite R2 and R2* correlating to iron content extremely consistently within samples (Table 5-4) and between samples (Figure 5-13B-C), both these measurements also demonstrated substantial variability in regression gradients between individual samples (Figure 5-14B-C). These variations in correlation highlight that other factors must clearly be affecting the correlation of relaxometry values with iron content, in a different manner per subject.

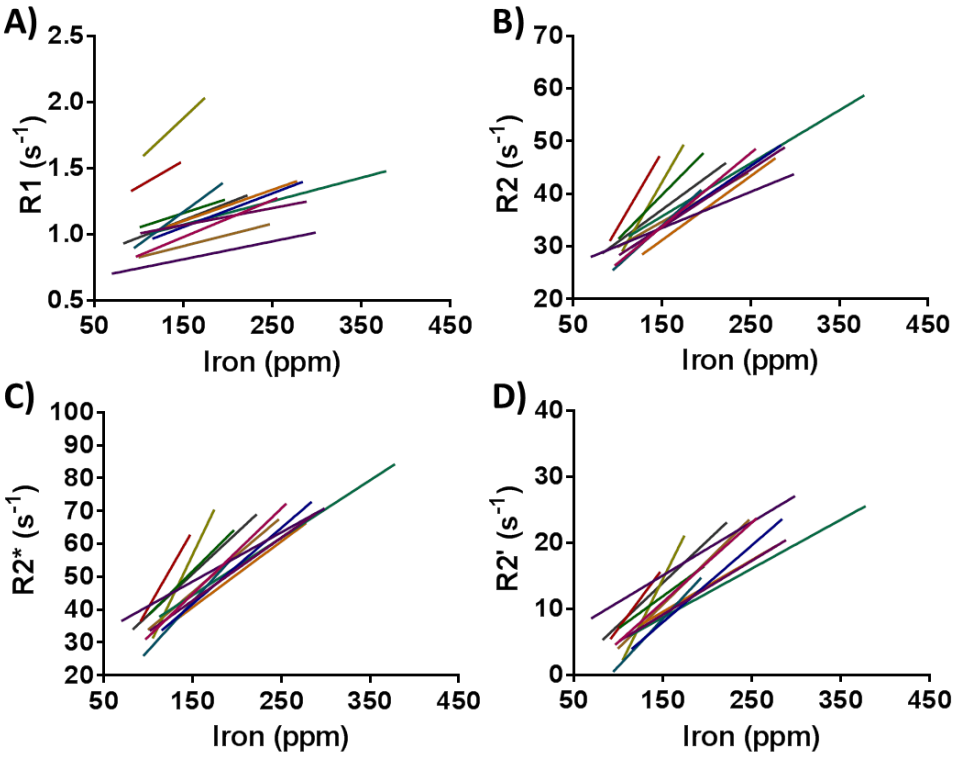

Figure 5-14 Variability in individual control sample correlations for relaxometry measurements against elemental iron contents

Regression lines for (A) R1, (B) R2, (C) R2 and (D) R2' relaxometry values against iron content, for the 12 individual control samples.*

5.4.4.5. Region-specific correlations in control tissue

To study correlations of relaxometry measurements with iron content in different tissue types, i.e. within WM or GM, the 5x5 ROIs from each region (Figure 5-10) were correlated separately with iron contents (Figure 5-15, Table 5-5). R2, R2* and R2' relaxometry measurements all continued to correlate significantly with iron levels, whether in the WM (R2, $r^2 = 0.19$; R2*, $r^2 = 0.34$ and R2', $r^2 = 0.20$, all $P < 0.0001$) or in the GM tissue types separately (R2, $r^2 = 0.38$; R2*, $r^2 = 0.37$ and R2', $r^2 = 0.11$, all $P < 0.0001$; Figure 5-15B-D and F-H, Table 5-5). However, these region-specific correlations were substantially lower than using ROIs from both WM and GM regions together (Table 5-5). R1 values displayed much lower correlation to iron in WM between multiple samples with a slight decreasing regression gradient ($r^2 = 0.09$, $P < 0.0001$; Figure 5-15A) and GM R1 values did not correlate to iron content (Figure 5-15E). Therefore, R1 values in separate tissue regions were not compared any further.

Molar relaxivities and correlation values were compared between the WM and GM tissue types for each relaxometry measurement to understand whether tissue microstructure effects the correlation of relaxometry with iron content. GM R2 correlation with iron content was greater than that for WM ($P = 0.041$), and with a higher molar relaxivity ($P < 0.0001$; Table 5-6). GM R2* correlation with iron was similar to that for WM ($P = 0.775$), but also had a higher molar relaxivity ($P = 0.0003$; Table 5-6). GM R2' values were correlated with iron similarly as that for WM R2' values ($P = 0.282$) and had similar molar relaxivities ($P = 0.692$; Table 5-6).

Evaluating for different relaxivity measurements in WM only, R2* values were significantly more correlated to iron content than R2 (P = 0.018) or R2' values (P = 0.016), and R2 and R2' values were correlated to iron similarly (P = 0.909; Table 5-5 and Table 5-7). In the GM regions only, R2* and R2 values were similarly correlated to iron (P = 0.786), and both were better correlated with iron content than R2' values (R2 and R2*, P < 0.0001; Table 5-5 and Table 5-7).

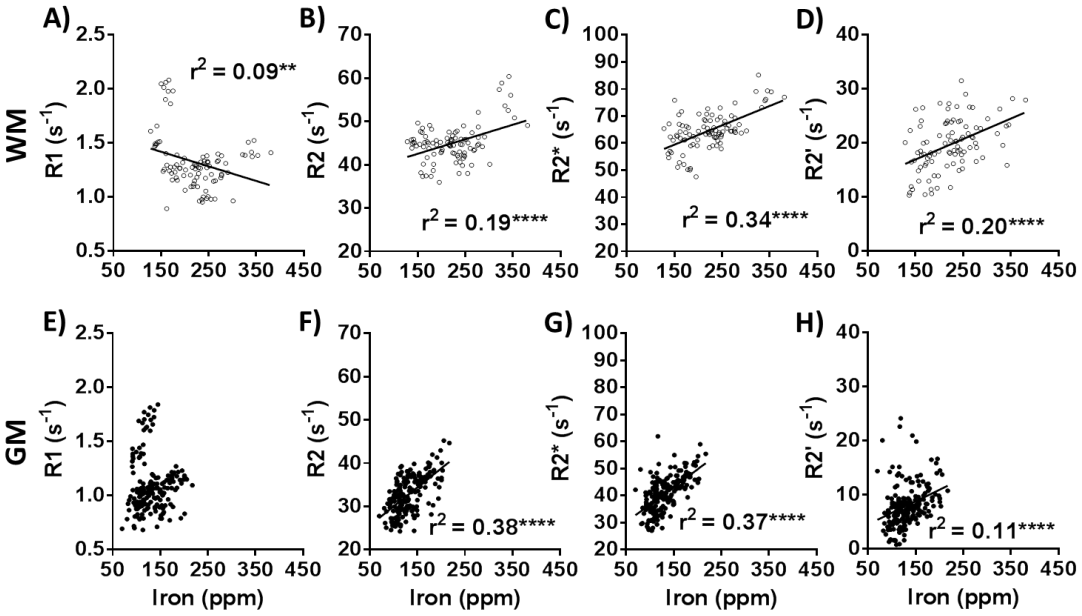

Figure 5-15 Correlation of relaxometry values against elemental iron content for all control samples in WM or GM tissue

Graphs showing (A-D) WM and (E-H) GM correlations to iron contents, using R1, R2, R2 and R2' relaxometry assessment in control samples. Correlation assessed using Pearson correlation with significance level set at P ≤ 0.05. Solid circles are GM ROIs (n = 192), hollow circles are WM ROIs (n = 96).*

Table 5-5 Summary of correlations for all regions, WM only, or GM only regions between relaxometry values and iron contents

Measure	All regions	WM only	GM only
R1 r^2	0.05	0.09	0.00
r_1 (s^{-1} ppm^{-1})	0.001	-0.001	0.00
R2 r^2	0.62	0.19	0.38
r_2 (s^{-1} ppm^{-1})	0.096	0.034	0.088
R2* r^2	0.68	0.34	0.37
r_2* (s^{-1} ppm^{-1})	0.182	0.072	0.130
R2' r^2	0.54	0.20	0.11
r_2' (s^{-1} ppm^{-1})	0.086	0.038	0.043

Significance between correlations was assessed using Pearson and Filon's z, with level set to $P \leq 0.05$, and significant values summarised in Table 5-7. R1 values were not compared due to low correlation values and regression gradients.

Table 5-6 Summary of significant differences comparing correlation values and molar relaxivities, between WM and GM control tissue

Measurement	r^2	Molar relaxivity
R1	-	-
R2	GM > WM	GM > WM
R2*	GM = WM	GM > WM
R2'	GM = WM	GM = WM

> denotes values are significantly different, = denotes values are similar.

Table 5-7 Summary table of relaxometry to iron correlation comparisons in different tissue regions

Region Selection	Order of significance						
All ROIs (WM and GM)	R2*	>	R2	>	R2'	>	R1
WM only	R2*	>	R2	=	R2'	>	R1
GM only	R2*	=	R2	>	R2'	>	R1

Significance between correlations was assessed using Pearson and Filon's z, with level set to $P \leq 0.05$. > denotes values are significantly different, = denotes values are similar.

5.4.5. Myelin assessment in control samples

Luxol fast blue (LFB) stain was used to assess myelin content in control MTG tissue samples to quantitatively compare and correlate against relaxometry measurements and iron contents.

5.4.5.1. Qualitative comparison of myelin

LFB was used to stain for myelin in tissue slices adjacent to elemental iron maps. Images obtained demonstrate clear distinction between GM and WM regions, with intensely stained WM and less intense staining in GM (Figure 5-16C). WM and GM were found in similar locations as observed by structural T2W MRI and XRF elemental iron mapping (Figure 5-16A-B). Furthermore, similar delineation of different cortical layers in the GM region can be observed in the LFB images (Figure

5-16C), separating the GM into MCL and dGM regions (as described in section 5.4.1, Figure 5-2).

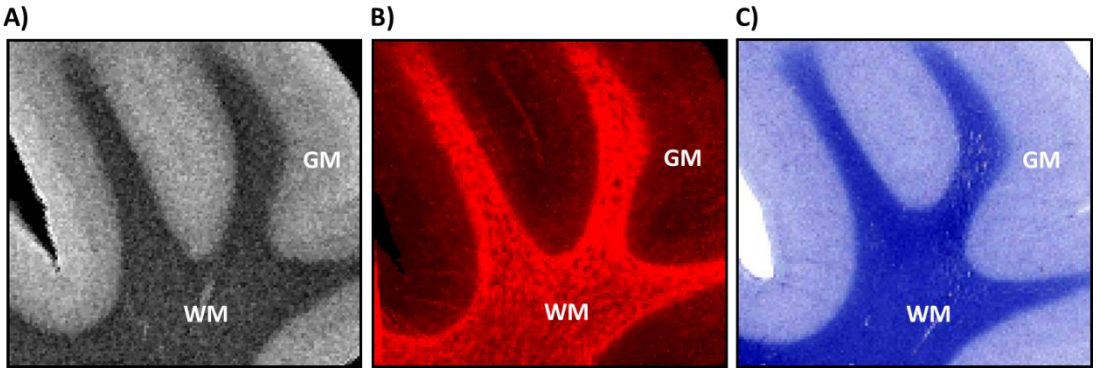

Figure 5-16 Representative T2W, elemental iron and LFB image of a control sample

Representative images of a (A) T2W, (B) an elemental iron map and (C) the corresponding adjacent tissue slice to iron maps stained for luxol fast blue (LFB). WM and GM regions are highlighted.

5.4.5.2. Effect of PMI, fixation time and subjects' age on myelin in control samples

Prior to quantitative analysis, the effects of PMI, fixation time and age of subjects' death on myelin were evaluated (as performed for relaxometry and iron contents, see section 5.4.2). Length of PMI had no significant effects on myelin content in either GM ($P = 0.052$) or WM ($P = 0.919$; Figure 5-17A). The separated dGM and MCL myelin contents were also not correlated with PMI length (dGM: $P = 0.078$ and MCL: $P = 0.106$). Fixation time lengths also demonstrated no significant correlations with myelin in either GM ($P = 0.484$) or WM ($P = 0.076$; Figure 5-17B), or following

separation of GM into dGM (P = 0.598) and MCL (P = 0.543). Finally, the age of subjects at death demonstrated no significant correlations with myelin in GM (P = 0.325) or WM (P = 0.763; Figure 5-17C), or through separation of GM into dGM (P = 0.361) or MCL (P = 0.345).

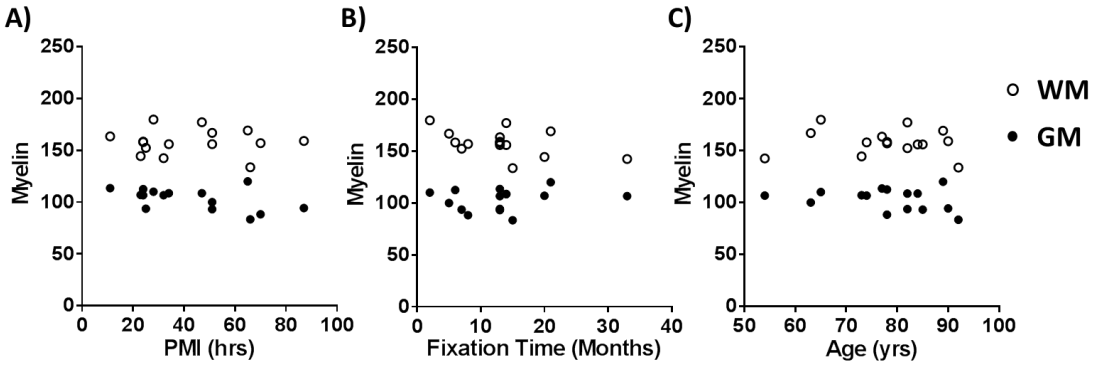

Figure 5-17 Effect of PMI, fixation time and subjects' age at death on myelin contents in control samples

Graphs showing (A) PMI, (B) fixation time, and (C) subjects' age at death of control samples, against myelin measurement. Correlation was assessed using Pearson's correlation with significance level set at P ≤ 0.05 (n = 15).

5.4.5.3. Quantitative assessment of myelin in control tissue

WM had significantly higher myelin content compared with GM (P < 0.0001; Figure 5-18) and when compared separately with MCL and dGM (MCL, P < 0.0001 and dGM, P < 0.0001; Figure 5-18). Whilst the MCL could be readily visualised in the LFB stained tissue samples, myelin was not significantly higher in the MCL compared to the dGM (P = 0.078) across all samples (Figure 5-18). However, using paired statistics, MCL was shown to have higher myelin content than dGM consistently

within each sample, in the order dGM < MCL < WM (repeated measures one-way ANOVA: dGM to MCL, P < 0.0001; MCL to WM, P < 0.0001 and dGM to WM, P < 0.0001; Figure 5-18).

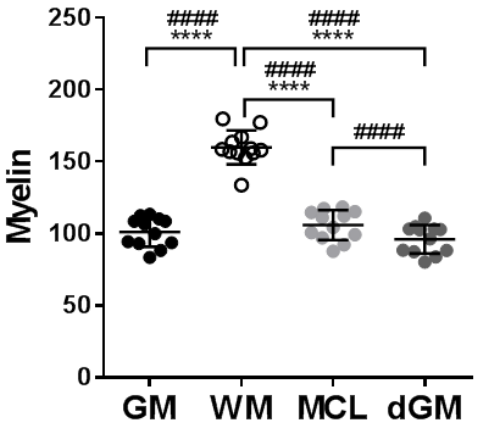

Figure 5-18 Myelin content in WM and GM tissue of control samples

Graphs showing the mean GM and WM region LFB staining of myelin from control MTG samples. Significance was assessed using Student's unpaired (*), or paired (#) t-test. Mean MCL and dGM sub regions of the GM ROIs were separately assessed with WM iron contents, using one-way ANOVA (*), or repeated-measures one-way ANOVA (#), with Tukey's test for multiple comparisons. Graphs show mean values ± SD (n = 12).

5.4.5.4. Gender comparison of myelin in control samples

Significantly lower myelin content was detected in female subjects compared with male subjects using two-way ANOVA across GM and WM tissue regions (P = 0.0033) and when comparing the dGM, MCL and WM tissue regions (P = 0.0003; GM: male, 106.44 ± 7.20; female, 93.58 ± 9.48; WM: male, 165.18 ± 10.17; female, 152.35 ±

10.46; dGM: male, 101.08 ± 6.92; female, 88.93 ± 9.45 and MCL: male, 111.15 ± 7.80; female, 98.45 ± 9.33; Figure 5-19). However, no individual tissue region was statistically different following Holm-Sidak's test for multiple comparisons (all regions, P = 0.060; Figure 5-19).

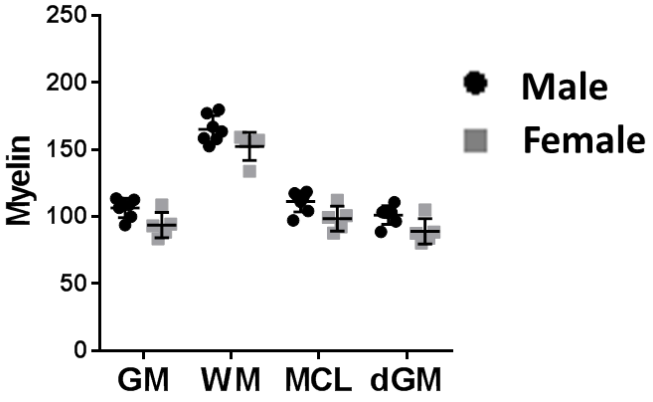

Figure 5-19 Gender comparison of myelin content in control tissue

Myelin contents in the GM and WM tissue regions, as well as GM sub regions, separated between male (n = 7) and female (n = 5) samples. Significance assessed using two-way ANOVA, with Holm-Sidak's test for multiple comparisons with the level set at P ≤ 0.05. Graphs show mean values ± SD.

5.4.6. Correlation of myelin against relaxometry and iron in control tissue

5.4.6.1. Correlation of whole tissue type ROIs

Myelin content demonstrated strong correlation to iron content (r^2 = 0.63) using the dGM, MCL and WM mean values (Figure 5-20A). Correlation to R1, R2, R2* and R2' relaxometry measurements were also significant, with greatest correlation to R2* (R1, r^2 = 0.17; R2, r^2 = 0.67; R2*, r^2 = 0.78 and R2', r^2 = 0.72; Figure 5-20B-E).

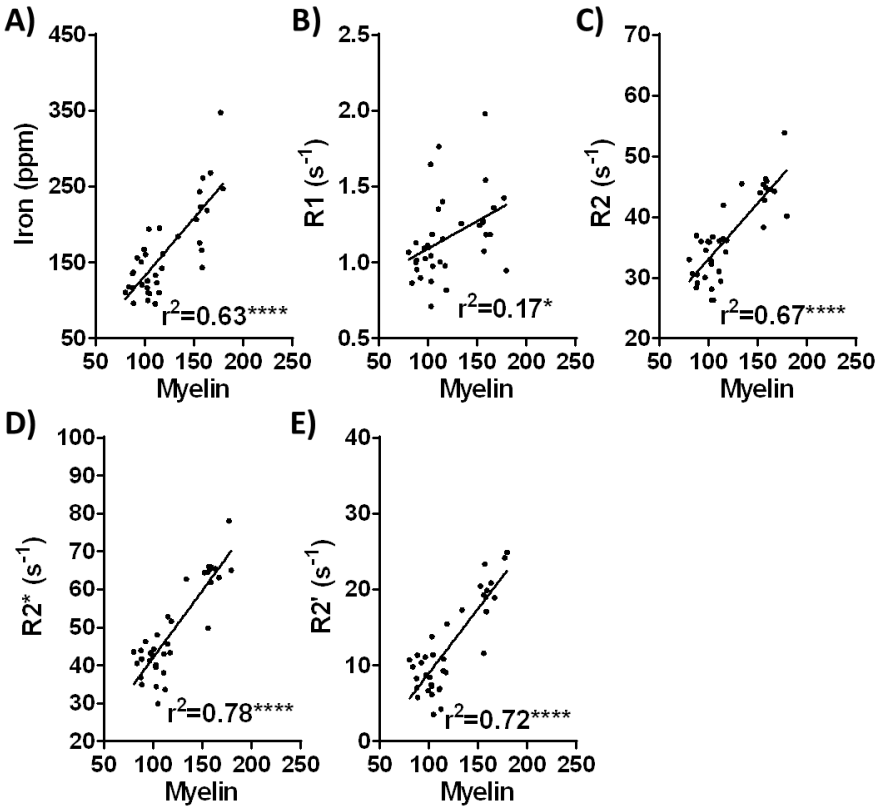

Figure 5-20 Whole tissue ROI correlations against myelin from control samples

Correlation of myelin with (A) mean elemental iron content and (B) R1, (C) R2, (D) R2 and (E) R2' relaxometry values for the control samples using the dGM, MCL and WM regions (n = 36). Correlation assessed using Pearson correlation with significance level set at P ≤ 0.05.*

5.4.6.2. Individual sample correlations

The same 5x5 pixel ROIs used to evaluate the individual sample correlations between elemental iron and relaxometry measurements (Figure 5-10) were placed over the LFB images to spatially correlate the variation in myelin content, compared with iron or relaxometry values. Significant correlations were demonstrated

between myelin and R1, R2, R2* and R2' across individual samples (R1, r^2 = 0.80 ± 0.11; R2, r^2 = 0.84 ± 0.10; R2*, r^2 = 0.88 ± 0.07 and R2', r^2 = 0.71 ± 0.16; Table 5-8). Myelin correlation to iron content was also very high (r^2 = 0.84 ± 0.10). R2' values correlated significantly less to myelin, than iron content, R2 and R2* did (iron to R2', P = 0.03; R2 to R2', P = 0.037 and R2* to R2', P = 0.002; Table 5-8). Iron content, R1, R2 and R2* correlations to myelin were similar (Table 5-8).

Table 5-8 The r^2 correlation values of myelin against relaxometry and iron content for each individual control sample

Sample	Iron	R1	R2	R2*	R2'
1	0.87	0.84	0.87	0.79	0.57
2	0.79	0.93	0.80	0.94	0.91
3	0.87	0.67	0.85	0.85	0.61
4	0.78	0.75	0.80	0.85	0.40
5	0.82	0.80	0.95	0.95	0.85
6	0.82	0.72	0.83	0.86	0.59
7	0.91	0.89	0.86	0.90	0.75
8	0.88	0.89	0.94	0.95	0.85
9	0.82	0.75	0.86	0.94	0.76
10	0.71	0.83	0.58	0.72	0.61
11	0.93	0.59	0.81	0.86	0.79
12	0.90	0.95	0.93	0.95	0.87
Mean ± SD	0.84 ± 0.06 [a]	0.80 ± 0.11	0.84 ± 0.10 [a]	0.88 ± 0.07 [a]	0.71 ± 0.16

Significance assessed using one-way ANOVA, with Tukey's multiple comparisons test with significance level at P ≤ 0.05 (n = 12). [a] denotes significance compared with R2'. R2' correlations were lower than iron content, R2 and R2 values correlations to myelin, highlighted in blue.*

5.4.6.3. Grouped sample correlations in control tissue

Correlation of myelin to both iron and relaxometry for inter- and intra- sample variability measurement using the twenty-four 5x5 pixel ROIs (as in section 5.4.4.4) demonstrated that myelin content correlated strongly with iron content (r^2 = 0.57, P < 0.0001) as well as R1, R2, R2* and R2' relaxometry measurements (R1, r^2 = 0.17; R2, r^2 = 0.63; R2*, r^2 = 0.71 and R2', r^2 = 0.58, all P < 0.0001), with the strongest correlation to R2* (Figure 5-21, Table 5-9).

R2* correlation to myelin was greater than iron (P < 0.0001), R2 (P = 0.0003) and R2' (P < 0.0001) correlations to myelin, whilst similar correlations with myelin were observed between iron and R2 (P = 0.061), iron and R2' (P = 0.739) and R2 and R2' (P = 0.179; Table 5-9 and Table 5-10). R1 correlation to myelin was much lower across multiple samples (r^2 = 0.17; Figure 5-21A) than by evaluation of the individual sample correlations (Table 5-8). Again, this indicates that other factors may impact the correlation of R1 with myelin between samples. R1 correlation with myelin was also substantially less than iron content, R2, R2*and R2' correlations with myelin (Figure 5-21; Table 5-10). Regression gradients of each measurement to myelin are summarised in Table 5-9.

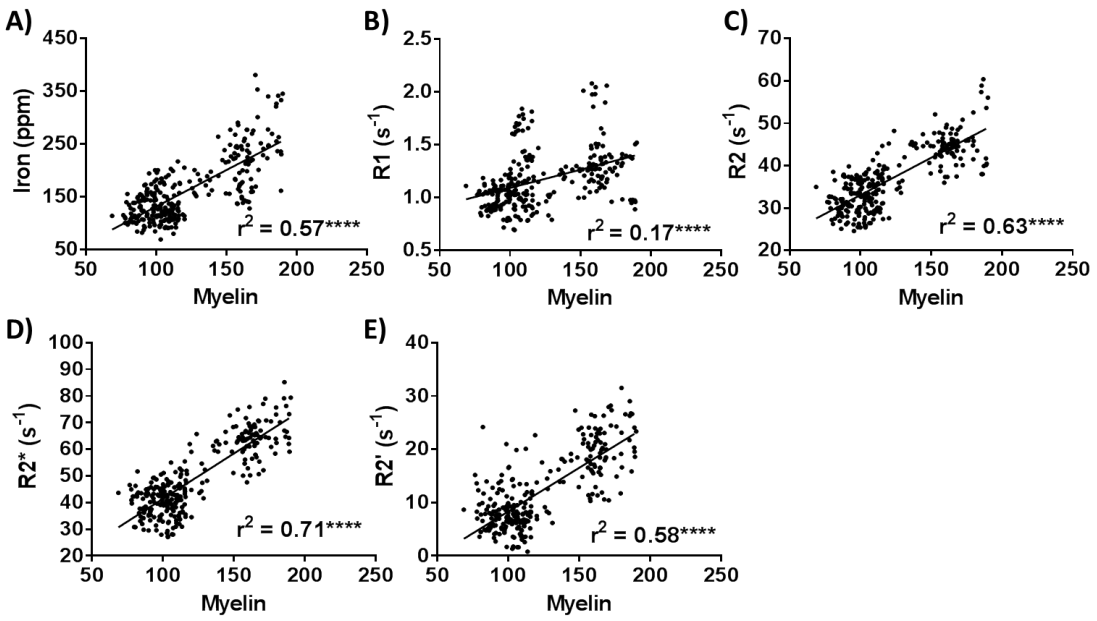

Figure 5-21 Correlation of relaxometry values and elemental iron contents against myelin across control samples

Graphs of (A) elemental iron, (B) R1, (C) R2, (D) R2 and (E) R2' against myelin content, as assessed using the twenty-four 5x5 pixel ROIs for control samples. Each point corresponds to one ROI pairing between the myelin image and elemental iron map/ relaxometry maps. Correlation assessed using Pearson correlation with significance level set at $P \leq 0.05$ ($n = 288$).*

5.4.6.4. Region-specific correlations to myelin in control tissue

Both WM and GM separated ROIs demonstrated substantially lower correlations compared with assessment of all ROIs together, indicating that correlation of iron content and relaxometry values against myelin is predominantly driven by GM and WM regions than specifically evaluating within each region in control samples

(values and regression gradients are summarised in Table 5-9). Therefore, individual region correlation comparisons were not explored further.

Table 5-9 Summary of r^2 correlation values for all regions, WM only, or GM only regions between relaxivities or iron contents, compared with myelin

	Iron	R1	R2	R2*	R2'
All regions r^2	0.57	0.17	0.63	0.71	0.58
All regions gradients	1.39	0.00	0.18	0.34	0.16
WM r^2	0.20	0.00	0.02	0.10	0.09
WM gradients	1.84	0.00	0.05	0.16	0.11
GM r^2	0.05	0.06	0.09	0.04	0.00
GM gradients	0.54	0.00	0.11	0.11	0.01

Significance between correlations was assessed using Pearson and Filon's z, with level set at $P \leq 0.05$. Significant values summarised in Table 5-10. R1 values were not compared due to low correlation values. WM and GM specific values were not compared due to substantially lower correlations to myelin.

Table 5-10 Summary table of comparisons between relaxometry or iron content correlation with myelin

Region Selection	Order of significance
All ROIs (WM and GM)	R2* > iron = R2 = R2' > R1

Significance between correlations was assessed using Pearson and Filon's z, with level set at $P \leq 0.05$. > denotes values are significantly different, = denotes values are similar.

5.4.7. Summary of control human MTG assessments

- Elemental iron maps demonstrated comparable tissue architecture to R1, R2, R2* and R2' relaxometry maps, identifying GM and WM tissue. Different cortical layers (MCL and dGM) were also detected (see section 5.4.1). Myelin content highlighted similar cortical architecture as that observed in both elemental iron and MR images.
- Fixation time of samples significantly increased R1 values across all tissue regions, and increased GM R2 values. PMI and subjects' age at death did not affect relaxometry values or iron contents (see section 5.4.2; Table 5-1). Myelin content was not affected by PMI, fixation time or subjects' age at death (see section 5.4.5.2).
- R1, R2, R2* and R2' relaxometry values, and iron contents, were all higher in WM than GM from control MTG. R1, R2 and R2* relaxometry values and iron contents increased in the order of dGM < MCL < WM within each sample. R2' values did not (see section 5.4.3). Myelin content was greater in WM than GM, and also consistently increased in the order of dGM < MCL < WM for each sample (see section 5.4.5.3).
- Males and females demonstrated similar levels of iron, as well as relaxometry values (see section 5.4.3.3), however myelin contents were lower overall in females compared with males (see section 5.4.5.4).
- Spatial correlation of samples was performed using twenty-four 5x5 pixel square ROIs across relaxometry and elemental iron maps.

- Mean correlations of individual samples between R1, R2 and R2* with iron content were similar, whilst R2' was less correlated to iron content than R2 and R2* (see section 5.4.4.3; Table 5-4). Mean correlations of individual samples between R1, R2, R2* and iron with myelin were similar, with R2, R2* and iron content correlating with myelin better than R2' (see section 5.4.6.2).
- Grouped correlations assessing inter- and intra- sample variation together demonstrated low R1 correlation to iron content, whilst R2, R2* and R2' correlation with iron content was strong. Relaxometry correlation to iron content was in the order of R2* > R2 > R2' (see section 5.4.4.4; Table 5-7).
- Substantial variation of individual sample ranges and regression gradients were observed between relaxometry and iron contents.
- Region-specific correlations were much lower than whole sample correlations. R2 and R2* were more sensitive for iron content in GM than in WM tissue (see section 5.4.4.5; Table 5-6). R2* showed greatest correlation to iron content within WM.
- Grouped correlations demonstrated that R2* was the most sensitive measurement for myelin (see section 5.4.6.3). Region-specific relaxometry and iron content correlations with myelin were very low by comparison to assessment of all the ROIs (see section 5.4.6.4).

5.5. Results of AD Human MTG Assessment

5.5.1. Qualitative assessment of relaxometry and iron elemental maps in AD samples

As described in section 5.4.1, both relaxometry and elemental iron maps show increasing pixel intensities corresponding to increasing relaxivity values and iron contents, respectively (Figure 5-1). WM can be clearly observed as dark areas in T2W images, with GM adjacent to these WM areas appearing as brighter pixels in the AD MTG tissue, as observed in control human brain samples (Figure 5-1). Similarly, iron contents match the tissue architecture of AD WM and GM from T2W images, with more intense pixels in WM areas compared to GM. Comparison of the T2W images and elemental iron maps together, again allowed delineation of a MCL, corresponding to cortical layers IV-V, at the boundary between GM and WM, as observed in control tissue (see section 5.4.1). ROIs were drawn around the WM and GM from each elemental iron and relaxometry maps, as well as around the MCL and dGM areas, following subdivision of the GM region into two zones (Figure 5-2).

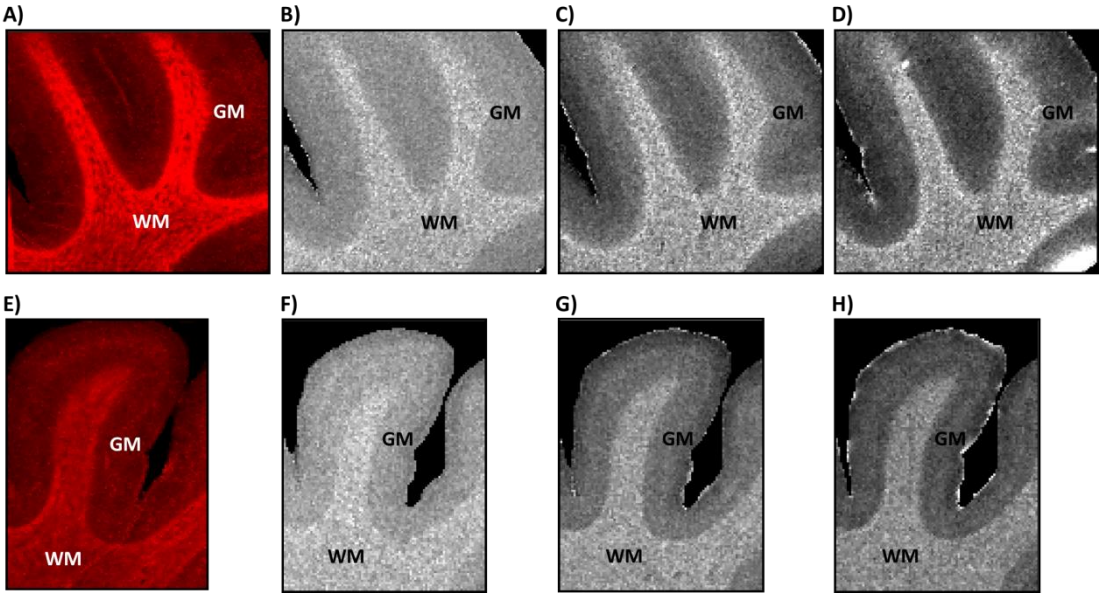

Figure 5-22 Qualitative comparison of control and AD iron elemental and relaxometry maps

(A) Iron elemental map, (B) R1, (C) R2 and (D) R2 maps of a control human tissue sample compared with (E) iron elemental map, (F) R1, (G) R2 and (H) R2* maps of a representative AD human tissue sample from the MTG.*

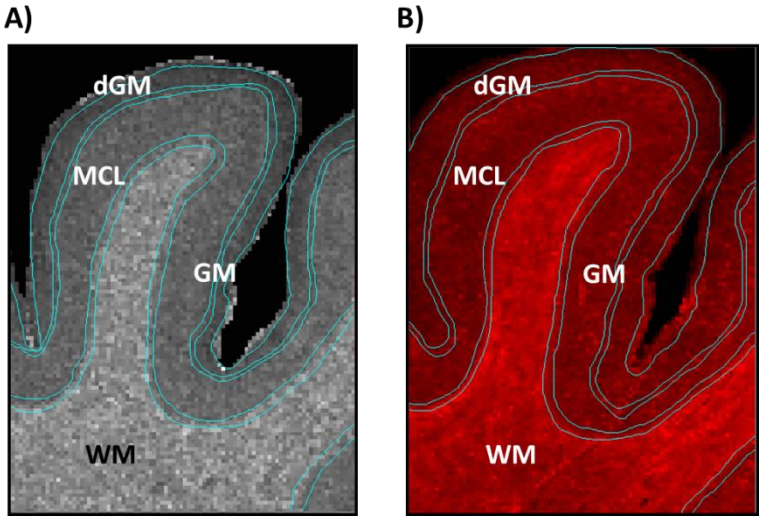

Figure 5-23 Whole ROI placement on R2 and elemental iron map of AD sample

Typical WM, MCL and dGM ROI placement on (A) an R2 map and (B) an elemental iron map. The whole GM ROIs incorporate both the dGM and MCL ROIs.

5.5.2. Effect of PMI, fixation time and subjects' age on relaxometry and elemental iron content in AD samples

A number of factors may affect relaxivity values and iron contents in post-mortem human tissue (see section 1.7), including PMI, fixation time and subjects' age at death. Whilst control samples have already been assessed (see section 5.4.2), the influence of these factors on measurements in AD tissue were also evaluated prior to subsequent data analyses, and to observe whether these factors may influence disease tissue differently than to control tissue.

5.5.2.1. PMI

PMI length did not significantly affect relaxivity values using Pearson correlation in GM (R1, P = 0.263; R2, P = 0.261; R2*, P = 0.247 and R2', P = 0.610), or WM (R1, P = 0.443; R2, P = 0.693; R2*, P = 0.641 and R2', P = 0.656; Figure 5-24A-D, Table 5-11). Iron contents were also unaffected by PMI in GM (P = 0.990) or WM (P = 0.863; Figure 5-24E). Separation of GM into two sub-regions demonstrated no significant correlations between relaxometry and PMI length in the dGM (R1, P = 0.291; R2, P = 0.294; R2*, P = 0.153 and R2', P = 0.585) or MCL (R1, P = 0.257; R2, P = 0.309; R2*, P = 0.334 and R2', P = 0.669; Table 5-11). Similarly, iron contents did not correlate with PMI in either of these areas (dGM, P = 0.813; MCL, P = 0.847; Table 5-11).

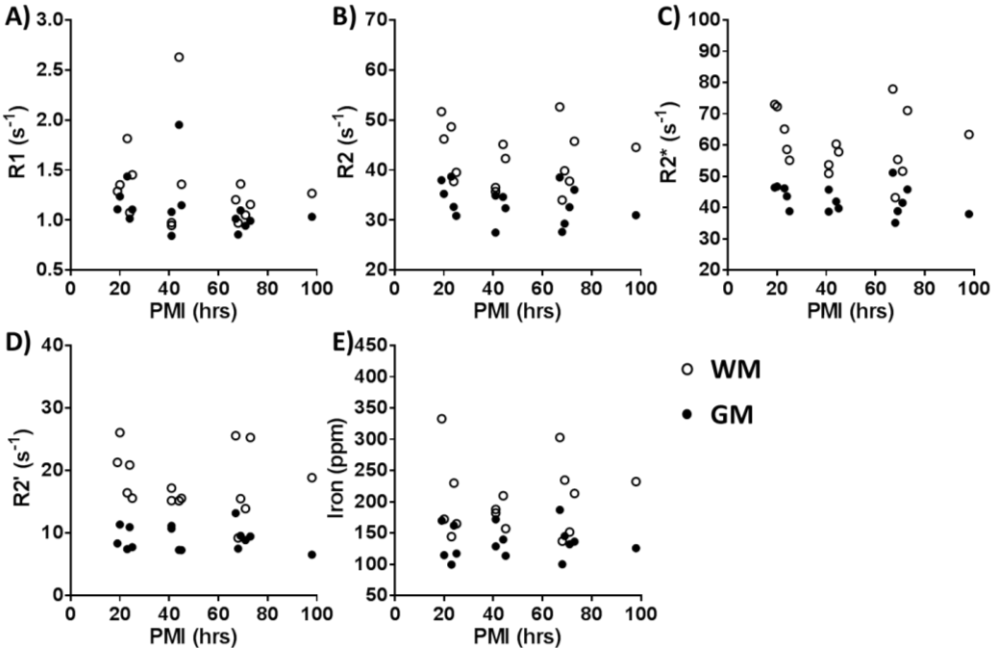

Figure 5-24 Effect of PMI on relaxometry values and elemental iron contents in AD samples

The effect of PMI length of AD samples, against (A) R1, (B) R2, (C) R2 and (D) R2' relaxivity values, and against (E) elemental iron content. Correlation was assessed using Pearson's correlation with significance level set at P ≤ 0.05 (n = 15).*

5.5.2.2. Fixation time

Increased R1 values were significantly correlated to increasing fixation times in AD tissue in both GM (r^2 = 0.52, P = 0.003) and WM (r^2 = 0.62, P = 0.001; Figure 5-25A, Table 5-11), as observed in control tissue (Figure 5-4). R2 and R2* were unaffected by fixation time in both GM (R2, P = 0.964 and R2*, P = 0.252) and WM (R2, P = 0.875 and R2*, P = 0.408; Figure 5-25B-C, Table 5-11). Decreased R2' values were significantly correlated with increased fixation times in both GM and WM (GM: r^2 =

0.49, P = 0.004 and WM: r^2 = 0.27, P = 0.04; Figure 5-25D). Iron was not affected by fixation times (GM, P = 0.105 and WM, P = 0.199; Figure 5-25E, Table 5-11).

Assessing the MCL and dGM areas separately demonstrated similar results as described above, with R1 values positively correlating to fixation time (dGM: r^2 = 0.51, P = 0.003 and MCL: r^2 = 0.52, P = 0.002) and R2 and R2* values showing no correlation (dGM: R2, P = 0.584 and R2*, P = 0.770; and MCL: R2, P = 0.843 and R2*, P = 0.283; Table 5-11). R2' values in the dGM did not correlate with fixation time (P = 0.148), whilst the R2' values in MCL did (r^2 = 0.38, P = 0.014; Table 5-11). Iron contents were unaffected by fixation time within dGM (P = 0.132) or MCL (P = 0.100; Table 5-11).

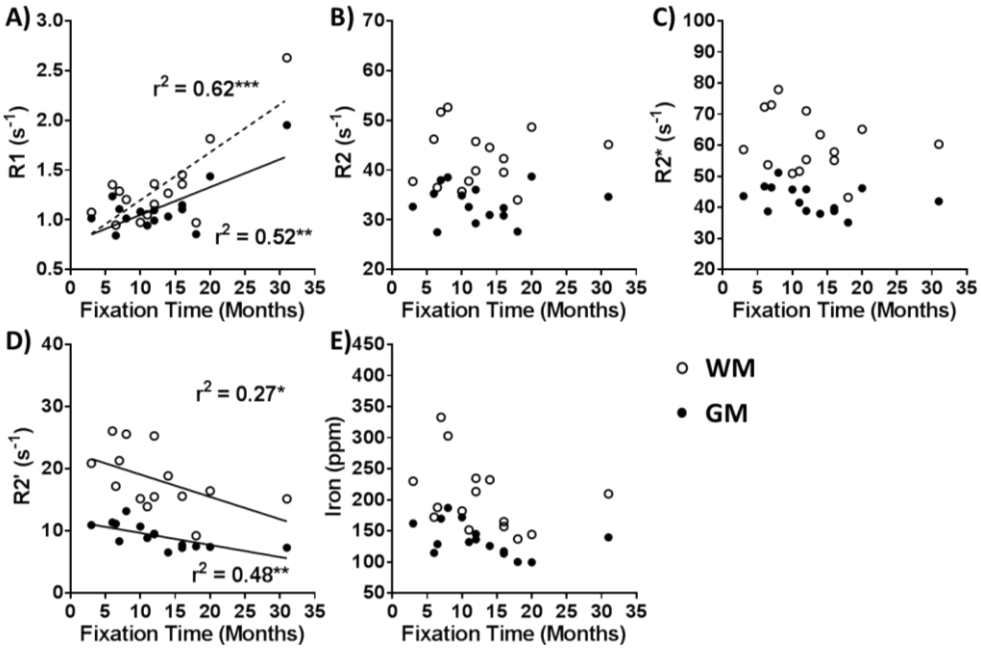

Figure 5-25 Effect of fixation time on relaxometry values and elemental iron contents in AD samples

The effect of fixation time of AD samples, against (A) R1, (B) R2, (C) R2 and (D) R2' relaxivity values, and against (E) elemental iron content. Correlation was assessed*

*using Pearson's correlation with significance level set at P ≤ 0.05. * P ≤ 0.05, ** P < 0.01, *** P < 0.001 and **** P < 0.0001 (n = 15).*

Prolonged tissue fixation of AD samples demonstrated similar correlations to relaxivity values as observed with control tissue samples (see section 5.4.2.2). Therefore again, samples with fixation time greater than 18 months were excluded from all further analyses and correlations under the same exclusion criteria (see section 5.4.2.2).

5.5.2.3. Age

Age of patients at death had no significant effects on any of the relaxometry values assessed in either GM (R1, P = 0.084; R2, P = 0.911; R2*, P = 0.839 and R2', P = 0.443) or WM (R1, P = 0.111; R2, P = 0.690; R2*, P = 0.637 and R2', P = 0.642) of AD MTG tissue (Figure 5-26A-D, Table 5-11). Iron contents were also unaffected by age in GM (P = 0.766) and WM (P = 0.977; Figure 5-26E). No significant correlations were observed compared with age in the dGM (R1, P = 0.096; R2, P = 0.791; R2*, P = 0.874; R2', P = 0.436 and iron, P = 0.602) or MCL sub-regions (R1, P = 0.085; R2, P = 0.944; R2*, P = 0.880; R2', P = 0.617 and iron, P = 0.726) of AD MTG samples either (Table 5-11).

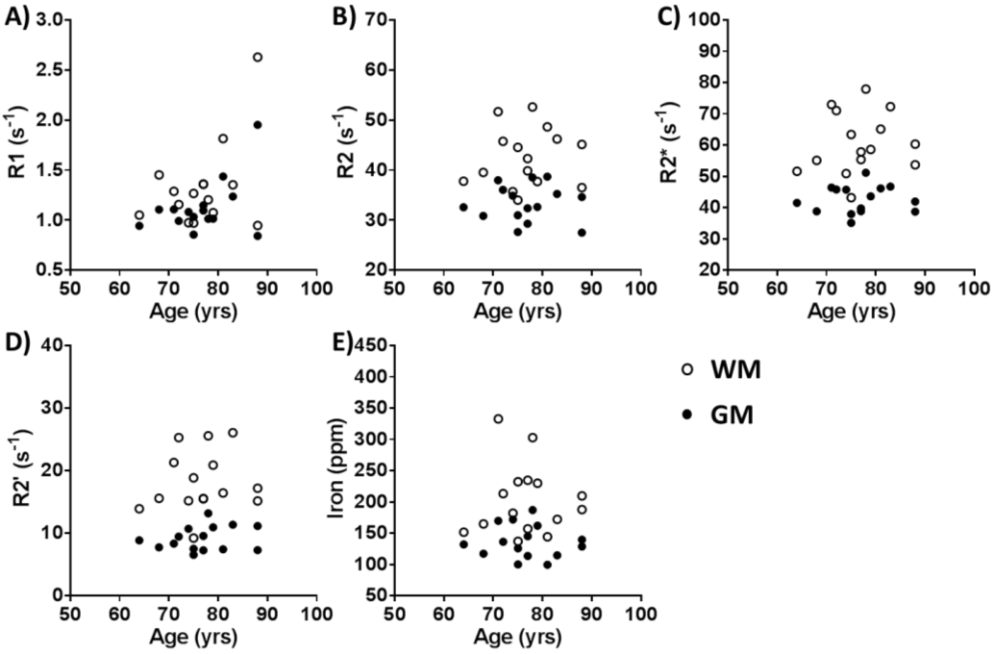

Figure 5-26 Effect of subjects' age at death on relaxometry values and elemental iron contents in AD samples

The effect of AD subjects' age at death, against (A) R1, (B) R2, (C) R2 and (D) R2' relaxivity values, and against (E) elemental iron content. Correlation was assessed using Pearson's correlation with significance level set at P ≤ 0.05 (n = 15).*

Table 5-11 Summary table of the assessed factors' r^2 correlation values, on AD sample relaxivity values and iron contents

		R1	R2	R2*	R2'	Iron
PMI	WM	0.05	0.01	0.02	0.02	0.00
	GM	0.10	0.10	0.10	0.02	0.00
	MCL	0.10	0.08	0.07	0.01	0.00
	dGM	0.09	0.08	0.15	0.02	0.00

Fixation Time	WM	0.62***	0.00	0.05	0.27*	0.12
	GM	0.52**	0.00	0.10	0.48**	0.19
	MCL	0.52**	0.00	0.09	0.38*	0.19
	dGM	0.51**	0.02	0.01	0.15	0.17
Subjects' Age	WM	0.20	0.01	0.02	0.02	0.00
	GM	0.21	0.00	0.00	0.05	0.01
	MCL	0.21	0.00	0.00	0.02	0.01
	dGM	0.18	0.01	0.00	0.05	0.02

*Correlation was assessed using Pearson's correlation with significance level set at P ≤ 0.05. * P ≤ 0.05, ** P < 0.01, *** P < 0.001 and **** P < 0.0001. Significant results highlighted blue.*

5.5.3. Quantitative assessment of AD tissue

5.5.3.1. R1, R2, R2 and R2' relaxivity value assessment*

R1, R2, R2* and R2' relaxivity values were all significantly higher in WM, compared with GM in AD MTG samples using unpaired t-test (R1, P = 0.011; R2, P < 0.0001; R2*, P < 0.0001 and R2', P < 0.0001; Figure 5-27, summarised in Table 5-12). Separation of GM into the MCL and dGM sub-regions also demonstrated significantly different R1, R2, R2* and R2' values across all three tissue regions, using one-way ANOVA (R1, P = 0.001; R2, P < 0.0001; R2*, P < 0.0001 and R2', P < 0.0001; Figure 5-27, Table 5-12). Following correction for multiple comparisons, R1 values were only significantly greater in WM than dGM (P = 0.001), with differences

between WM and MCL (P = 0.06) and MCL and dGM (P = 0.26) not significant (Figure 5-27A, Table 5-12). R2 values were significantly different between the three tissue regions following correction for multiple comparisons (P < 0.0001; Figure 5-27B, Table 5-12). R2* and R2' relaxometry however were only able to differentiate the WM values compared with MCL (both, P < 0.0001) and dGM (both, P < 0.0001), whereas dGM to MCL regions were similar to each other overall (R2*, P = 0.052 and R2', P = 0.614; Figure 5-27C-D, Table 5-12).

Paired statistical testing allowed identification of consistently increased relaxivity values in WM compared with GM for each sample (R1, P = 0.0006; R2, P < 0.0001; R2*, P < 0.0001 and R2', P < 0.0001; Figure 5-27). Similarly, R1, R2 and R2* values were consistently significantly increasing in the order of dGM < MCL < WM for each tissue sample when the different cortical layers were considered separately (R1, P = 0.0002; R2, P < 0.0001 and R2*, P < 0.0001; Figure 5-27A-C). R2' values however were only significantly higher in WM compared with MCL or dGM (both P < 0.0001), whilst R2' values in the dGM and MCL were similar (P = 0.338; Figure 5-27D).

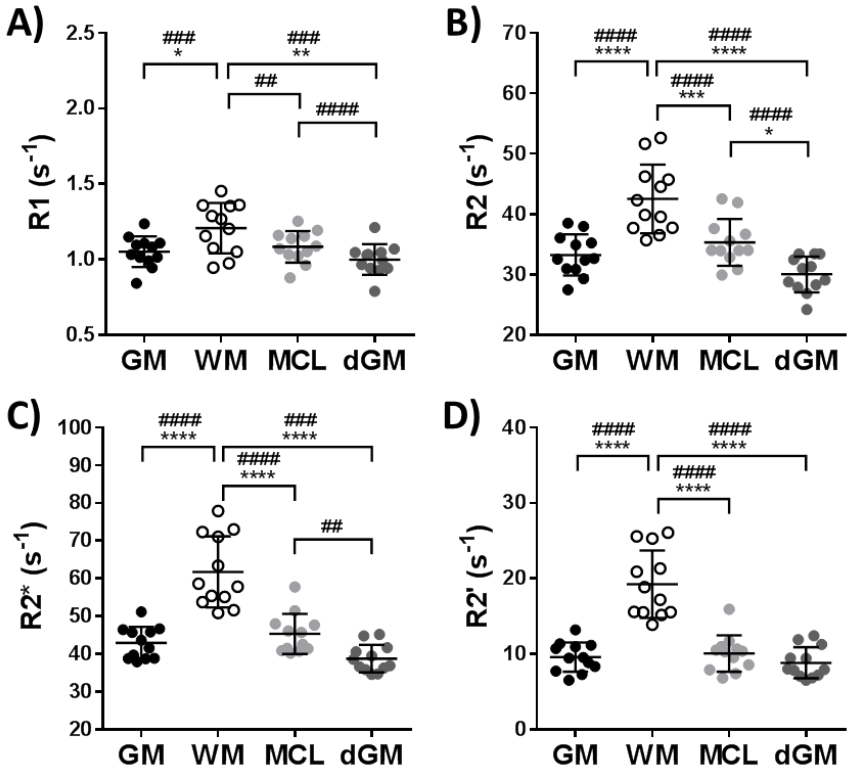

Figure 5-27 Relaxometry values in WM and GM tissue of AD samples

Graphs showing the mean GM and WM region relaxivity values for (A) R1, (B) R2, (C) R2 and (D) R2' from AD MTG samples. Significance was assessed using Student's unpaired (*), or paired (#) t-test between GM and WM. Mean MCL and dGM sub regions of GM ROIs were separately assessed with WM values, using one-way ANOVA (*), or repeated-measures one-way ANOVA (#), with Tukey's test for multiple comparisons. Graphs show mean values ± SD (n = 12).*

Table 5-12 Relaxivities and iron content from AD MTG samples

Tissue Region	R1 (s^{-1})	R2 (s^{-1})	R2* (s^{-1})	R2' (s^{-1})	Iron (ppm)
GM	1.05 ± 0.10	33.25 ± 3.38	42.94 ± 4.26	9.60 ± 1.95	142.1 ± 25.0
WM	1.21 ± 0.17	42.53 ± 5.70	61.75 ± 9.45	19.25 ± 4.48	213.6 ± 57.3
P-value	0.011	< 0.0001	< 0.0001	< 0.0001	0.0007
WM	1.21 ± 0.17	42.53 ± 5.70	61.75 ± 9.45	19.25 ± 4.48	213.6 ± 57.3
MCL	1.08 ± 0.10	35.33 ± 3.87	45.35 ± 5.31	10.07 ± 2.41	155.3 ± 29.4
dGM	1.00 ± 0.10	30.02 ± 2.97	38.78 ± 3.64	8.84 ± 2.05	123.7 ± 18.2
P-value	0.001	< 0.0001	< 0.0001	< 0.0001	< 0.0001

(GM) grey matter, (WM) white matter, (MCL) mid-cortical layer and (dGM) distal grey matter regions. Values are mean ± SD. Statistical testing between GM and WM performed using Student's unpaired t-test. Statistical testing between dGM, MCL and WM performed using one-way ANOVA with Tukey's test for multiple comparisons. Significance level set at $P \leq 0.05$ (n = 12).

5.5.3.2. XRF elemental iron assessment

Iron contents were significantly increased in AD MTG WM compared to GM using unpaired t-test (P = 0.0007; Figure 5-28, Table 5-12). Subdivision of the GM region into dGM and MCL demonstrated significantly different iron contents between these three tissue regions (P < 0.0001), with WM iron content significantly increased compared with dGM (P < 0.0001) and MCL (P = 0.002), but similar between MCL and dGM (P = 0.127; Figure 5-28, Table 5-12).

Paired statistical testing of the same data revealed that WM consistently showed increased iron content than GM within samples (P < 0.0001) and that across the three tissue regions, iron content increases consistently in the order of dGM < MCL < WM, in each sample (P < 0.0001; Figure 5-28).

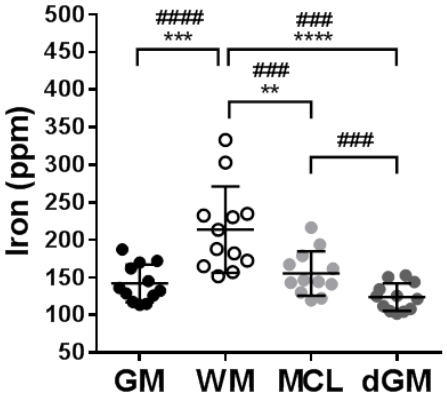

Figure 5-28 Elemental iron content in WM and GM tissue of AD samples

Graphs showing the mean GM and WM region iron contents from AD MTG samples. Significance was assessed using Student's unpaired (*), or paired (#) t-test. Mean MCL and dGM sub regions of the GM ROIs were separately assessed with WM iron contents, using one-way ANOVA (*), or repeated-measures one-way ANOVA (#), with Tukey's test for multiple comparisons. Graphs show mean values ± SD (n = 12).

5.5.3.3. Gender comparison

Comparing relaxivities in GM and WM were similar for male and female AD tissue (R1, P = 0.662; R2, P = 0.144; R2*, P = 0.081 and R2', P = 0.075), however a trend towards higher R2* and R2' values seem to be apparent for female AD samples compared with males, in WM regions (Figure 5-29A-D, Table 5-13). Separate assessment of the dGM and MCL with WM showed female AD samples with an overall trend towards significance of greater R2* values than males (P = 0.074), and R2' values were significantly higher overall in female AD samples than males (P = 0.048; Figure 5-29A-D, Table 5-13). Whilst no individual regions were significantly different between the genders following Holm-Sidak test for multiple comparisons, WM values showed the strongest difference in both R2* and R2' relaxometry. Similar R1 and R2 relaxivities were observed for male and female AD subjects (R1, P = 0.638 and R2, P = 0.166).

Interestingly, iron contents were significantly higher in WM tissue (P = 0.038) from female compared with male AD subjects when comparing WM with dGM and MCL (Figure 5-29E, Table 5-13). GM iron contents were similar between male and female AD samples (dGM, P = 0.975 and MCL, P = 0.559; Figure 5-29E).

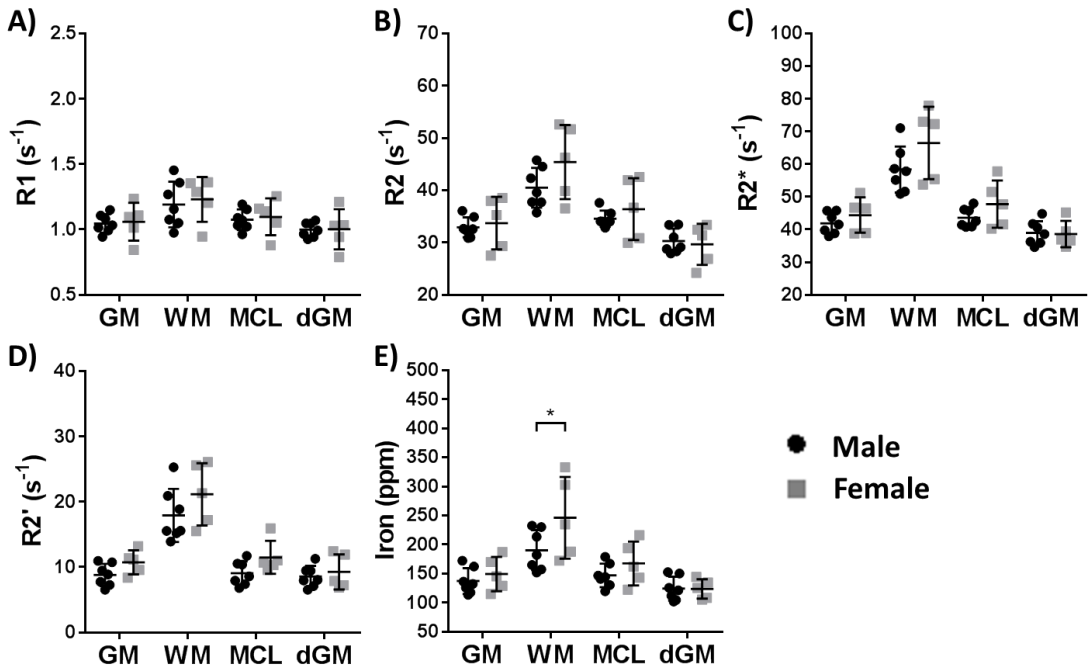

Figure 5-29 Gender comparison of relaxometry and elemental iron contents in AD samples

(A) R1, (B) R2, (C) R2, (D) R2' relaxometry values, and (E) elemental iron contents, from male (n = 7) and female (n = 5) subjects in GM and WM tissue, and in the MCL and dGM sub regions. Graphs show mean values ± SD. Significance assessed using two-way ANOVA, with Sidak test for multiple comparisons, with a level set to P ≤ 0.05 (*).*

Table 5-13 Relaxivities and iron content from AD MTG from male and female subjects

GM	R1 (s^{-1})	R2 (s^{-1})	R2* (s^{-1})	R2' (s^{-1})	Iron (ppm)
Male	1.05 ± 0.07	32.92 ± 1.92	41.89 ± 3.24	8.80 ± 1.70	137.1 ± 22.1
Female	1.06 ± 0.15	33.72 ± 5.04	44.40 ± 5.44	10.73 ± 1.85	149.2 ± 29.5
WM					
Male	1.19 ± 0.18	40.48 ± 3.79	58.38 ± 7.05	17.90 ± 4.06	190.3 ± 34.6*
Female	1.23 ± 0.17	45.39 ± 7.09	66.48 ± 11.10	21.14 ± 4.77	246.2 ± 70.3*
MCL					
Male	1.08 ± 0.08	34.58 ± 1.56	43.64 ± 2.93	9.05 ± 1.84	146.7 ± 20.4
Female	1.10 ± 0.14	36.39 ± 5.94	47.74 ± 7.23	11.50 ± 2.54	167.3 ± 37.9
dGM					
Male	1.00 ± 0.06	30.28 ± 2.37	38.92 ± 3.64	8.54 ± 1.63	124.0 ± 20.5
Female	1.00 ± 0.15	29.66 ± 3.95	38.59 ± 4.06	9.26 ± 2.70	123.4 ± 16.7

Values are mean ± SD. Statistical testing performed using two-way ANOVA, with Sidak test for multiple comparisons with a level set to P ≤ 0.05 (*) (male (n = 7) and female (n = 5)). Significant results highlighted blue.

5.5.4. Correlation of relaxometry to iron in AD samples

5.5.4.1. Correlation of whole tissue type ROIs

R1, R2, R2* and R2' measurements were significantly positively correlated with iron content, using all the dGM, MCL and WM tissue type values from AD samples (R1: r^2

= 0.17, P < 0.012; R2: r^2 = 0.71, P < 0.0001; R2*: r^2 = 0.71, P < 0.0001; R2': r^2 = 0.57, P < 0.0001; Figure 5-30A-D).

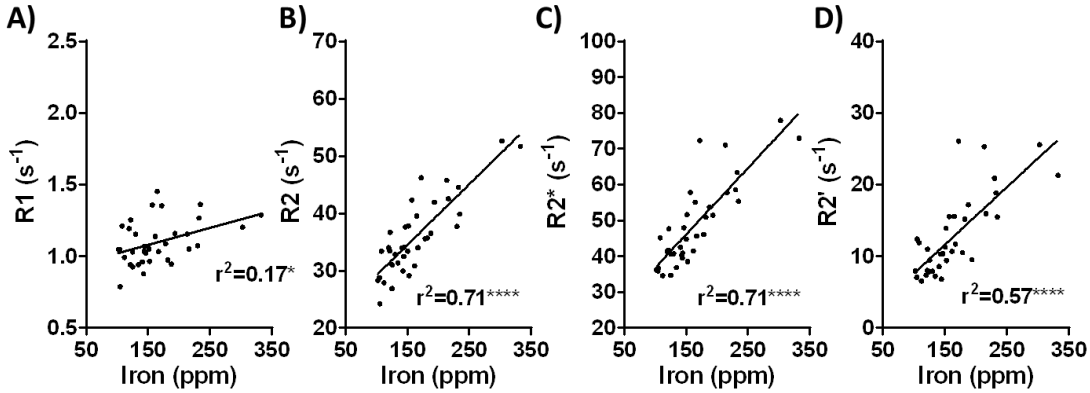

Figure 5-30 Whole tissue ROI correlations from AD samples

Mean (A) R1, (B) R2, (C) R2 and (D) R2' values correlated against iron content for AD tissue of all dGM, MCL and WM regions (n = 36). Correlation assessed using Pearson correlation with significance level set at P ≤ 0.05.*

5.5.4.2. Individual sample correlations

Twenty four 5x5 pixel ROIs were placed across the elemental iron and relaxometry maps, (see section 5.4.4.1, Figure 5-10), with eight ROIs in each of the three tissue regions identified in images (dGM, MCL and WM) to evaluate the consistency of relaxometry correlation to iron content within individual AD samples (Table 5-14). The mean correlations of individual samples were strongly significant between R1 (r^2 = 0.63 ± 0.23), R2 (r^2 = 0.79 ± 0.16), R2* (r^2 = 0.78 ± 0.14) and R2' (r^2 = 0.62 ± 0.19) measurements with iron content (Table 5-14). Whilst an overall significant difference was detected using one-way ANOVA (P = 0.038), R2 and R2* correlations

were only generally higher than R1 and R2' correlations, not quite reaching significance, following multiple comparisons testing.

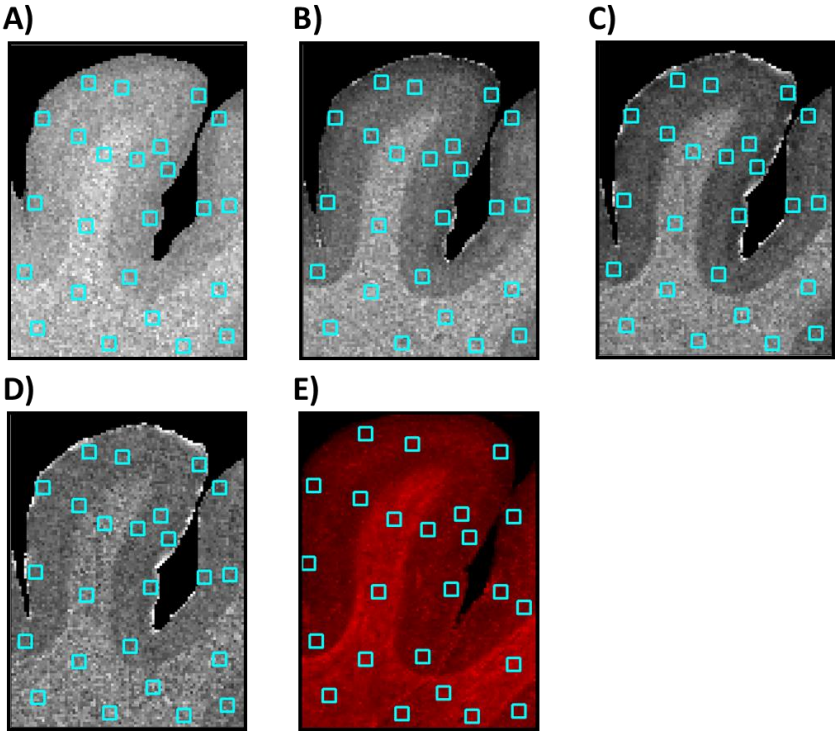

Figure 5-31 Representative relaxometry and elemental iron maps showing placement of 24 small ROIs in AD sample

Representative (A) R1, (B) R2, (C) R2, (D) R2' and (E) elemental iron maps, demonstrating the placement of the eight equally sized ROIs within each tissue region (twenty four ROIs in total across each sample).*

Table 5-14 The r^2 correlation values of relaxometry against iron content for each individual AD sample

Sample	R1	R2	R2*	R2'
1	0.46	0.53	0.70	0.71
2	0.85	0.85	0.81	0.61
3	0.55	0.87	0.68	0.21
4	0.50	0.86	0.85	0.77
5	0.73	0.82	0.90	0.87
6	0.77	0.89	0.86	0.61
7	0.84	0.86	0.85	0.50
8	0.72	0.90	0.87	0.74
9	0.83	0.93	0.94	0.84
10	0.48	0.42	0.44	0.38
11	0.07	0.66	0.69	0.59
12	0.72	0.84	0.75	0.61
Mean ± SD	0.63 ± 0.23	0.79 ± 0.16	0.78 ± 0.14	0.62 ± 0.19

Significance assessed using one-way ANOVA with Tukey's multiple comparisons test to significance set at $P \leq 0.05$ (n = 12).

5.5.4.3. Grouped correlations of AD samples

All of the mean relaxivity values from the 5x5 ROIs were correlated with iron contents together, as in section 5.4.4.4, allowing evaluation of inter-sample variability, as well as intra-sample variability (Figure 5-32). R1, R2, R2* and R2'

demonstrate significant correlations to iron contents (R1, r^2 = 0.18; R2, r^2 = 0.64; R2*, r^2 = 0.61 and R2' r^2 = 0.42; all P < 0.0001; Figure 5-32, Table 5-15 and Table 5-17). The strongest correlation to iron content was shown by R2 and R2*, which were similar to each other (P = 0.222; Figure 5-32B-C). R2' correlation with iron content was less than that for either R2 or R2* (both, P < 0.0001) and R1 correlation with iron content was substantially lower than the other three relaxometry measurements (R2, R2* and R2', P < 0.0001; Figure 5-32A, summarised in Table 5-17). Molar relaxivities for each relaxometry measurement to iron are also summarised in Table 5-15, as a measure of sensitivity.

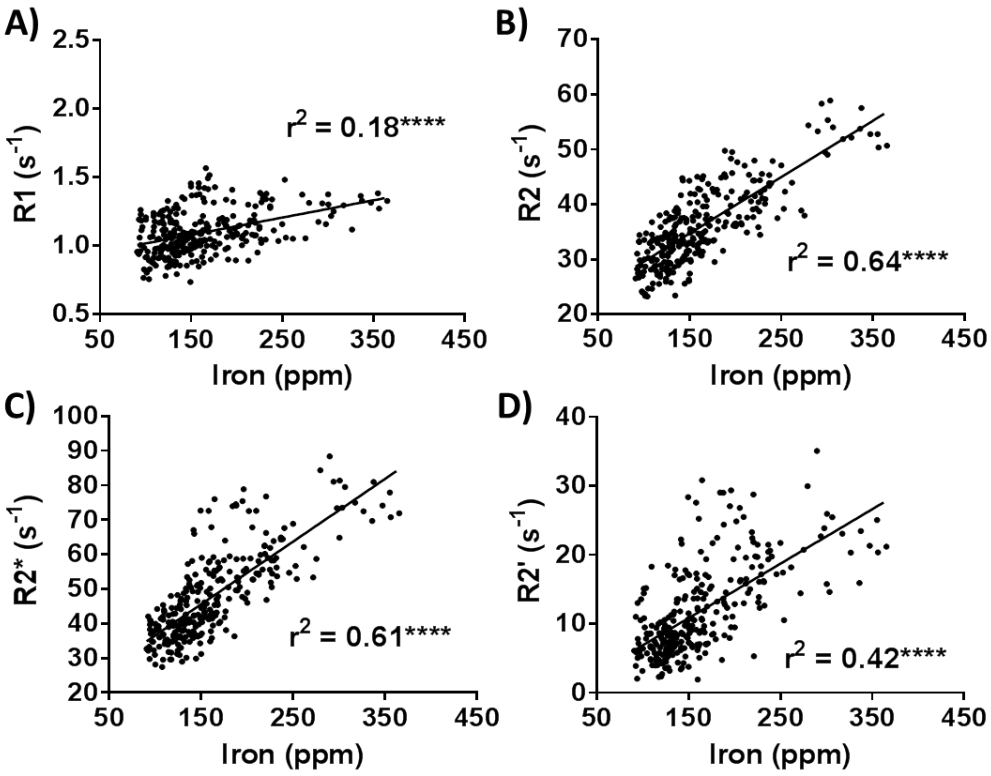

Figure 5-32 Correlation of relaxometry values against elemental iron content across all AD samples

Graphs of (A) R1, (B) R2, (C) R2 and (D) R2' correlation against iron content, as assessed using the twenty four 5x5 pixel ROIs for AD samples. Each point*

corresponds to one ROI pairing between the relaxometry map and elemental iron map. Correlation assessed using Pearson correlation with significance level set at P ≤ 0.05 (n = 288).

Individual sample regression lines were, again, placed together to evaluate the inter-sample variability in correlations between relaxometry and iron (see section 5.4.4.4). Wide variations in regression gradients, y-intercepts and ranges for relaxometry to iron contents were observed per subject, in AD tissue (Figure 5-33), as was observed in control samples (5.4.4.4).

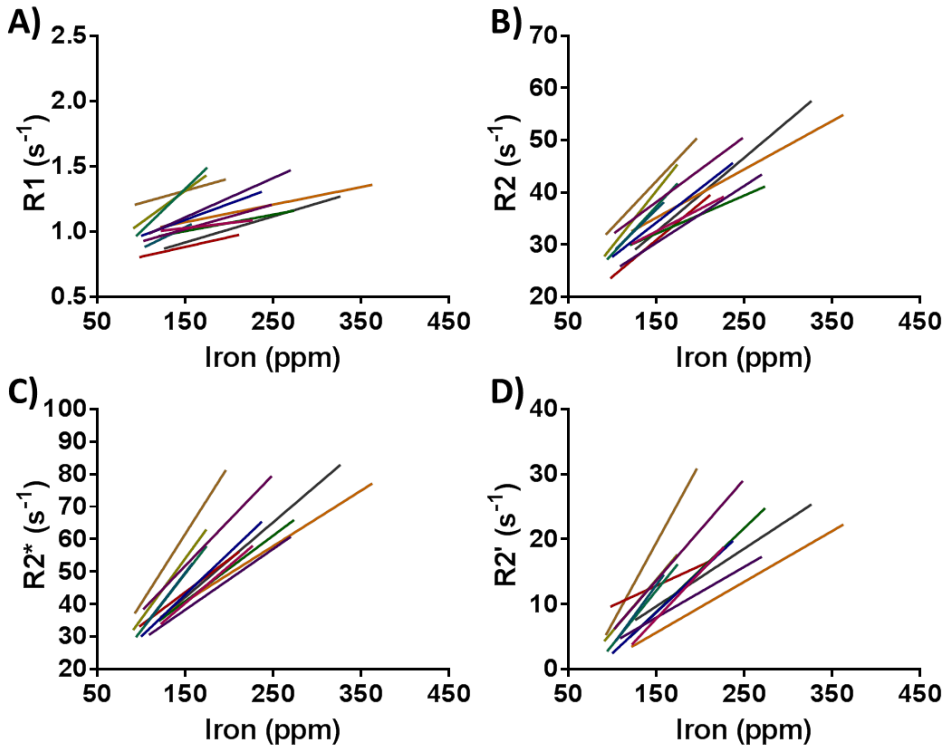

Figure 5-33 Variability in individual AD sample correlations for relaxometry measurements against elemental iron contents

Regression lines for (A) R1, (B) R2, (C) R2 and (D) R2' relaxometry values against iron content, for the 12 individual AD samples.*

5.5.4.4. Region-specific correlations in AD tissue

Evaluation of the 5x5 ROIs in separate WM or GM tissue demonstrated that R2, R2* and R2' relaxivity values were all still positively correlated to iron contents in both WM (R2: $r^2 = 0.45$, $P < 0.0001$, R2*: $r^2 = 0.33$, $P < 0.0001$, and R2', $r^2 = 0.09$, $P = 0.003$; Figure 5-34B-D) and GM (R2: $r^2 = 0.43$, $P < 0.0001$, R2*: $r^2 = 0.44$, $P < 0.0001$, and R2', $r^2 = 0.13$, $P < 0.0001$; Figure 5-34F-H). However region-specific correlations were substantially less than to correlations with both GM and WM ROIs together (Table 5-15). R1 values were not correlated within these regions (WM: $r^2 = 0.03$, $P = 0.122$, and GM: $r^2 = 0.02$, $P = 0.058$; Figure 5-34A and E).

Comparing WM to GM relaxometry correlations with iron content showed that R2 values were similarly correlated to iron content in WM and GM ($P = 0.853$), however with different molar relaxivity ($P = 0.020$; summarised in Table 5-16). Correlation of R2* values with iron content were also similar between GM and WM ($P = 0.255$), however with different molar relaxivity ($P = 0.028$; Table 5-16). Correlation of R2' values with iron content were similar between WM and GM ($P = 0.565$) and with similar molar relaxivity ($P = 0.237$, Table 5-16).

In AD WM, R2 correlated greater than R2* to iron content ($P = 0.009$), whilst R2' values were significantly less correlated to iron than both R2 and R2* values ($P < 0.0001$). AD GM provides similar correlations with iron for R2 and R2* values ($P = 0.867$), and R2' values were again significantly less correlated to iron than both R2 and R2* values ($P < 0.0001$; summarised in Table 5-15 and Table 5-17).

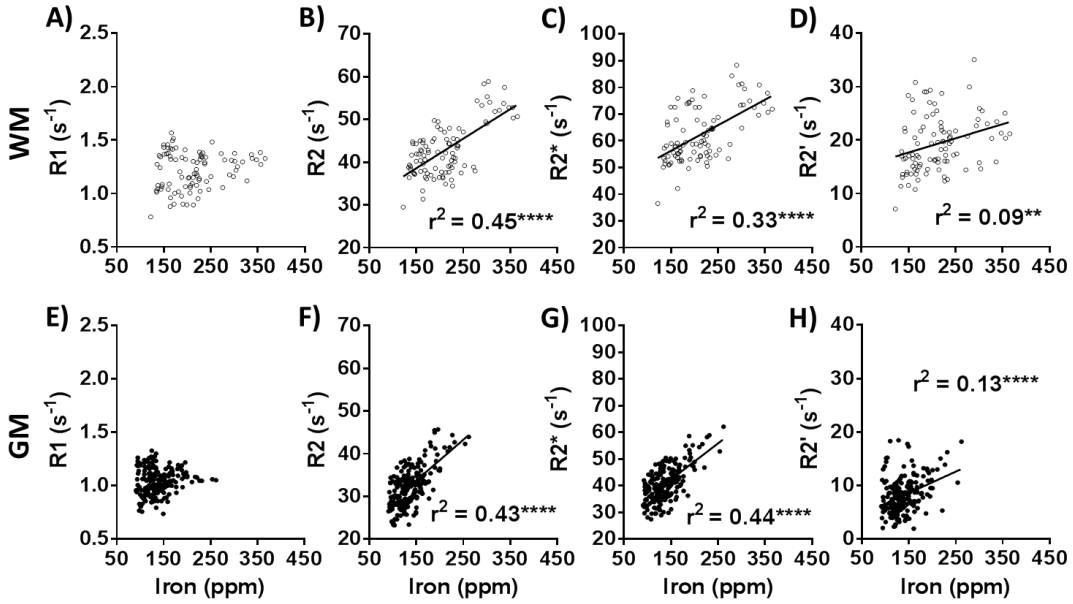

Figure 5-34 Correlation of relaxometry values against elemental iron content across AD samples in WM or GM tissue

Graphs showing (A-D) WM and (E-H) GM correlations to iron contents, using R1, R2, R2 and R2' relaxometry assessment in AD samples. Correlation assessed using Pearson correlation with significance at P ≤ 0.05. Solid circles are GM ROIs (n = 192), hollow circles are WM ROIs (n = 96).*

Table 5-15 Summary of correlations of all regions, WM only, or GM only regions between relaxometry values and iron content

Measure	All regions	WM only	GM only
R1 r^2	0.18	0.03	0.02
r_1 (s^{-1} ppm^{-1})	0.001	0.000	0.000
R2 r^2	0.64	0.45	0.43
r_2 (s^{-1} ppm^{-1})	0.102	0.069	0.096
R2* r^2	0.61	0.33	0.44
r_2* (s^{-1} ppm^{-1})	0.181	0.096	0.135
R2' r^2	0.42	0.09	0.13
r_2' (s^{-1} ppm^{-1})	0.079	0.027	0.040

Significance between correlations was assessed using Pearson and Filon's z, with level set to $P \leq 0.05$, and significant values summarised in Table 5-17. R1 values were not compared due to low correlation values and regression gradients.

Table 5-16 Summary of correlation and molar relaxivity comparisons, for each relaxometry measurement between WM and GM in AD tissue

Measurement	r^2	Molar relaxivity
R1	-	-
R2	GM = WM	GM > WM
R2*	GM = WM	GM > WM
R2'	GM = WM	GM = WM

> denotes values are significantly different, = denotes values are similar.

Table 5-17 Summary table of relaxometry to iron correlation comparisons in different tissue regions

Region Selection	Order of significance
All ROIs (WM and GM)	R2* = R2 > R2' > R1
WM only	R2 > R2* > R2' > R1
GM only	R2* = R2 > R2' > R1

Significance between correlations was assessed using Pearson and Filon's z, with level set to P ≤ 0.05. > denotes values are significantly different, = denotes values are similar.

5.5.5. Myelin assessment in AD samples

LFB stain was used to assess myelin content in AD MTG tissue samples, as performed for the control samples (see section 5.4.5). The effects of PMI, fixation time and age of subjects at death were evaluated first, before performing quantitative comparisons and correlations of relaxometry measurements and iron contents with myelin in the AD tissue and also in comparison between AD and control tissue. One male sample from the AD group had to be excluded from myelin assessments as there was not enough tissue remaining following SR-XRF.

5.5.5.1. Effect of PMI, fixation time and subjects' age, on myelin in AD samples

PMI length was significantly negatively correlated to myelin in the GM ($r^2 = 0.43$, P = 0.011), whereas WM was not affected by PMI (P = 0.925; Figure 5-35A).

Furthermore, neither fixation time nor subjects' age at death affected myelin content in either GM (fixation time, P = 0.583 and age, P = 0.671) or WM (fixation time, P = 0.417 and age, P = 0.442; Figure 5-35B-C). Separation of the GM into the dGM and MCL revealed similar results as that for GM, with both fixation time length and age demonstrating no significant correlations with myelin (fixation time: dGM, P = 0.558 and MCL, P = 0.590 and age: dGM, P = 0.613 and MCL, P = 0.778). However, myelin content was significantly negatively correlated to PMI length in the dGM (P = 0.001) and demonstrated a trend towards correlation in the MCL (P = 0.052).

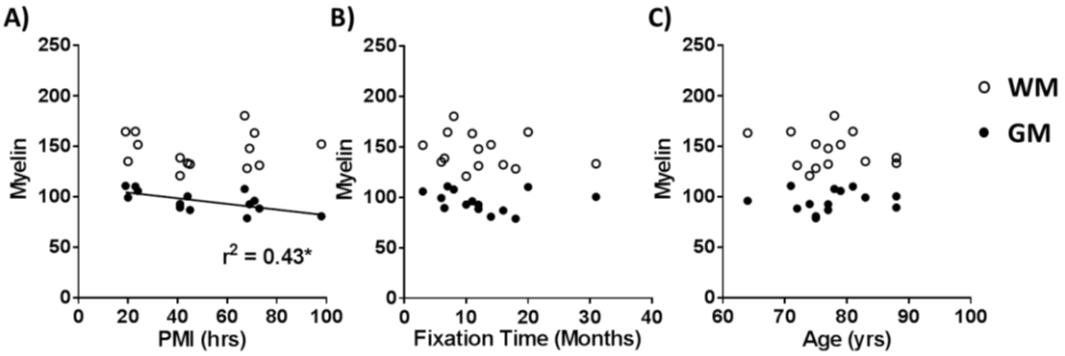

Figure 5-35 Effect of PMI, fixation time and subjects' age at death on myelin contents in AD samples

*Graphs showing myelin content against (A) PMI, (B) fixation time, and (C) subjects' age at death in AD samples. Correlation was assessed using Pearson's correlation with significance level set at P ≤ 0.05. * P ≤ 0.05, ** P < 0.01, *** P < 0.001 and **** P < 0.0001 (n = 14).*

5.5.5.2. Quantitative assessment of AD tissue myelin

As expected, more myelin was present in WM (147.2 ± 17.6) compared to GM (95.6 ± 9.5; P < 0.0001; Figure 5-36). Similarly, WM also had greater myelin than the dGM (89.2 ± 9.3; P < 0.0001) and MCL (100.5 ± 10.2; P < 0.0001; Figure 5-36). Whilst the dGM and MCL myelin levels were similar using one-way ANOVA (P = 0.118), evaluation using repeated-measures one-way ANOVA, showed that the increase in myelin was consistently in the order, dGM < MCL < WM (P < 0.0001; Figure 5-36).

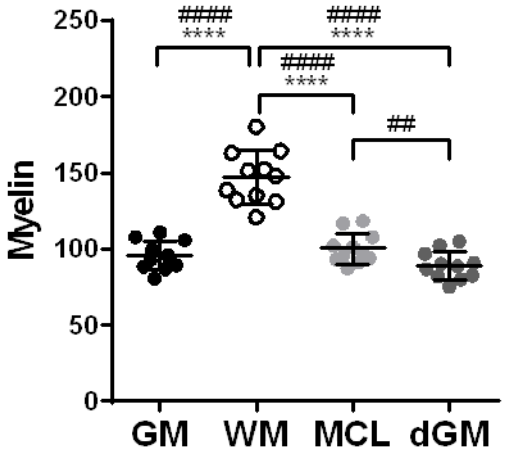

Figure 5-36 Myelin content in WM and GM tissue of AD samples

Graphs showing the mean GM and WM region LFB staining of myelin, from AD MTG samples. Significance was assessed using Student's unpaired (*), or paired (#) t-test. Mean MCL and dGM sub regions of the GM ROIs were separately assessed with WM iron contents, using one-way ANOVA (*), or repeated-measures one-way ANOVA (#), with Tukey's test for multiple comparisons. Graphs show mean values ± SD (n = 11).

5.5.5.3. Gender comparison of myelin in AD samples

Separation of myelin contents between male and female subjects demonstrated no significant differences in the amount of myelin between male and female subject samples in either GM or WM (GM: male, 91.84 ± 8.63; female, 100.04 ± 9.29 and WM: male, 141.96 ± 16.14; female, 153.41 ± 18.93, P = 0.115; Figure 5-37). Similarly, testing across the three tissue types also showed myelin to be comparable between males and females (dGM: male, 87.26 ± 10.54; female, 91.51 ± 7.99; MCL: male, 96.05 ± 7.54; female, 105.75 ± 11.07 and WM: male, 141.96 ± 16.14; female, 153.41 ± 18.93, P = 0.066; Figure 5-37).

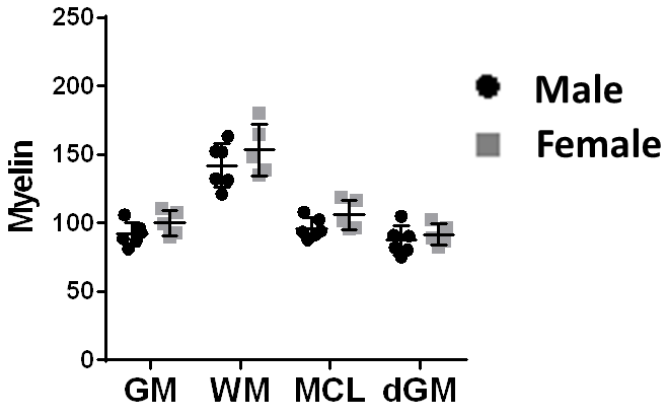

Figure 5-37 Gender comparison of myelin content in AD tissue

Myelin contents in the GM and WM tissue regions, as well as GM sub regions, separated between male (n = 6) and female (n = 5) samples. Significance assessed using two-way ANOVA, with Holm-Sidak test for multiple comparisons with level set at P ≤ 0.05. Graphs show mean values ± SD.

5.5.6. Correlation of myelin against relaxometry and iron in AD tissue

5.5.6.1. Correlation of whole tissue type ROIs

Whole tissue mean myelin contents were correlated against all AD sample elemental iron and R1, R2, R2* and R2' measurements, providing positive significant correlations between each assessment (iron, $r^2 = 0.70$, $P < 0.0001$; R1, $r^2 = 0.28$, $P = 0.002$; R2, $r^2 = 0.68$, $P < 0.0001$; R2*, $r^2 = 0.75$, $P < 0.0001$ and R2', $r^2 = 0.68$, $P < 0.0001$; Figure 5-38). Iron, R2, R2* and R2' showed similar correlations to myelin, but the myelin correlation for R1 was much lower.

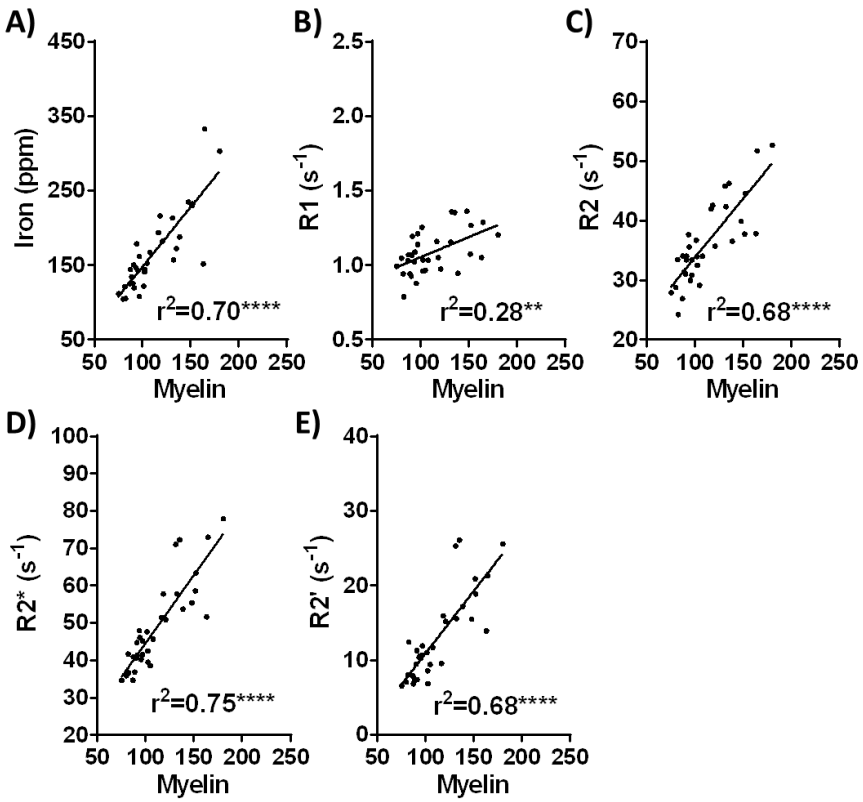

Figure 5-38 Whole tissue ROI correlations against myelin from AD samples

Correlation of myelin with (A) mean elemental iron content and (B) R1, (C) R2, (D) R2 and (E) R2' relaxometry values for the AD samples using the dGM, MCL and*

WM regions. Correlation assessed using Pearson correlation with significance level set at P ≤ 0.05 (n = 33).

5.5.6.2. Individual sample correlations

The 5x5 pixel ROI method (see section 5.4.4.1, Figure 5-10) was used again, to evaluate the individual sample correlations between elemental iron and relaxometry measurements with LFB assessment of myelin, to spatially correlate the variation in myelin content compared with iron or relaxometry values. Myelin was significantly positively correlated to iron content, R1, R2, R2* and R2' (iron, r^2 = 0.71 ± 0.22; R1, r^2 = 0.67 ± 0.19; R2, r^2 = 0.76 ± 0.24; R2*, r^2 = 0.83 ± 0.17 and R2', r^2 = 0.75 ± 0.17) all at similar levels (P = 0.391; Table 5-18).

Table 5-18 The r^2 correlation values of myelin against relaxometry and iron content for each individual AD sample

Sample	Iron	R1	R2	R2*	R2'
1	0.84	0.79	0.88	0.92	0.73
2	0.69	0.55	0.87	0.92	0.89
3	0.73	0.60	0.81	0.82	0.41
4	0.92	0.86	0.83	0.91	0.89
5	0.86	0.77	0.93	0.96	0.89
6	0.67	0.64	0.48	0.74	0.81
7	0.32	0.67	0.80	0.86	0.76
8	0.95	0.76	0.89	0.93	0.86
9	0.87	0.78	0.88	0.83	0.61
10	0.63	0.76	0.82	0.90	0.85
11	0.31	0.16	0.13	0.37	0.50
Mean ± SD	0.71 ± 0.22	0.67 ± 0.19	0.76 ± 0.24	0.83 ± 0.17	0.75 ± 0.17

Significance assessed using one-way ANOVA with Tukey's multiple comparisons test to significance set at $P \leq 0.05$ (n = 11).

5.5.6.3. Grouped sample correlations in AD tissue

To assess inter- and intra- sample variability of iron and relaxometry correlations to myelin, all the 5x5 pixel ROIs were evaluated together for each measurement, showing strongly significant positive correlations for each correlation to myelin (iron, $r^2 = 0.59$; R1, $r^2 = 0.29$; R2, $r^2 = 0.62$; R2*, $r^2 = 0.69$; R2', $r^2 = 0.57$, all P <

0.0001; Figure 5-39 and Table 5-20). R2* values were correlated to myelin significantly more than iron contents or R2 and R2' values were (iron, P = 0.005; R2, P = 0.016 and R2', P < 0.0001; Table 5-20 and Table 5-21). R2, R2' and iron contents showed similar correlation values with myelin as each other (R2 to R2', P = 0.181; iron to R2, P = 0.325 and iron to R2', P 0.676; Table 5-20 and Table 5-21). R1 values were less correlated than iron contents, or R2, R2* and R2' values were to myelin (all, P < 0.0001; Table 5-21). Regression gradients of each measurement to myelin are summarised in Table 5-20.

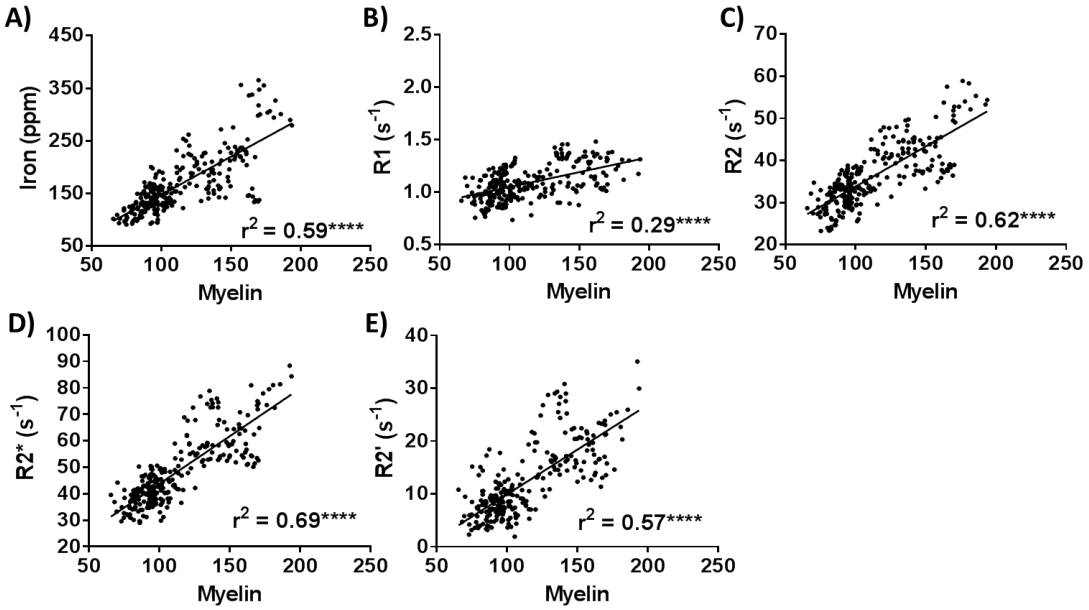

Figure 5-39 Correlation of relaxometry values and elemental iron contents against myelin across AD samples

Graphs of (A) elemental iron, (B) R1, (C) R2, (D) R2 and (E) R2' correlation against myelin content as assessed using the twenty-four 5x5 pixel ROIs for AD samples. Each point corresponds to one ROI pairing between the myelin image and elemental iron map/ relaxometry maps. Correlation assessed using Pearson correlation with significance level set at P ≤ 0.05 (n = 264).*

5.5.6.4. Region-specific correlations to myelin in AD tissue

Iron content, R2 and R2* measurements were correlated with myelin within WM and GM regions in AD tissue, in contrast to observations made using control tissue (see section 5.4.6.4) (WM: iron, $r^2 = 0.24$; R2, $r^2 = 0.20$ and R2*, $r^2 = 0.12$; and GM: iron, $r^2 = 0.48$; R2, $r^2 = 0.43$ and R2*, $r^2 = 0.39$; all $P < 0.0001$; summarised in Table 5-20). All correlations were still lower than correlations observed using both GM and WM regions together (Table 5-20).

Better correlations of R2 and R2* to myelin were observed in GM compared with WM regions (R2: correlation, P = 0.022 and regression gradient, P = 0.017; and R2*: correlation, P = 0.006 and regression gradient, P = 0.031; Table 5-19). Iron contents demonstrated better correlation to myelin in GM than in WM (P = 0.019), however with a similar gradient (P = 0.678; Table 5-19).

The correlation of R2 values to myelin in AD WM was higher than for R2* values (P = 0.019), whilst similar iron content correlations to myelin were detected against both R2 (P = 0.578) and R2* values correlation to myelin (P = 0.104; Table 5-20). Iron contents were similar to R2 and R2* correlations in GM (R2, P = 0.442 and R2*, P = 0.116), and R2 values were similarly correlated to myelin as R2* (P = 0.183; Table 5-20). Correlation values and regression gradients are summarised in Table 5-20.

Table 5-19 Summary of correlations and gradient comparisons, for relaxometry and iron measurements against myelin, between WM and GM in AD tissue

Measurement	r^2	Regression gradient
Iron	GM > WM	GM = WM
R2	GM > WM	GM > WM
R2*	GM > WM	GM > WM

> denotes values are significantly different, = denotes values are similar.

Table 5-20 Summary of r^2 correlation values for all regions, WM only, or GM only regions between relaxivities or iron contents, compared with myelin

	Iron	R1	R2	R2*	R2'
All regions r^2	0.59	0.29	0.62	0.69	0.57
All regions gradients	1.50	0.00	0.19	0.36	0.17
WM r^2	0.24	0.05	0.20	0.12	0.02
WM gradients	1.64	0.00	0.16	0.20	0.04
GM r^2	0.48	0.08	0.43	0.39	0.09
GM gradients	1.77	0.00	0.25	0.32	0.08

Significance between correlations was assessed using Pearson and Filon's z, with level set at $P \leq 0.05$. Significant values summarised in Table 5-21. R1 values were not compared due to low correlation values.

Table 5-21 Summary table of comparisons between relaxometry or iron content correlation with myelin

Region Selection	Order of significance
All ROIs (WM and GM)	R2* > iron = R2 = R2' > R1

Significance between correlations was assessed using Pearson and Filon's z, with level set at P ≤ 0.05. > denotes values are significantly different, = denotes values are similar.

5.5.7. Summary of AD human MTG assessments

- PMI and subjects' age at death did not affect relaxometry values or iron contents. Longer fixation times increased R1 values across all tissue regions, and decreased R2' values (see section 5.5.2, Table 5-11). R2, R2* and iron content were unaffected by fixation time. These were similar to control sample observations (see section 5.4.2). Myelin content was not affected by fixation time or subjects' age at death, however GM myelin was lower with PMI length (see section 5.5.5.1).
- All relaxivity values, iron contents and myelin contents in AD samples were higher in WM than GM (see section 5.5.3 and 5.5.5.2), as also detected in control samples (see section 5.4.3 and 5.4.5.3). R1, R2 and R2* relaxometry values and iron and myelin contents increased in the order of dGM < MCL < WM within each sample, whilst R2' values did not (see section 5.5.3.1).

- Females demonstrated higher iron content in WM than males, with a similar trend detected using R2* and R2' (see section 5.5.3.3). Myelin contents were similar between female and male AD samples (see section 5.5.5.3).
- Individual samples mean correlations demonstrated that R1, R2, R2* and R2' were all correlated similarly to iron within each AD sample (see section 5.5.4.2, Table 5-14). Mean correlations of individual samples were also similar for R1, R2, R2*, R2' and iron content correlations against myelin (see section 5.5.6.2).
- Grouped correlations assessing inter- and intra- sample variation together highlighted that R2* and R2 values correlated to iron similarly, and were both correlated to iron better than R2' or R1 values were. R1 correlation to iron was much lower than other relaxometry measurements (see section 5.5.4.3, Table 5-17). R2* was the most specific measurement for myelin, correlating to myelin better than iron content, R2 or R2' (see section 5.5.6.3).
- Region-specific correlations demonstrated R2 values were correlated better with iron content than R2* values were in WM. R2 and R2* correlated with iron content similarly to each other in GM (see section 5.5.4.4).
- Whilst region-specific correlations to myelin were substantially lower than correlations using all the ROIs, AD samples demonstrated that iron, R2 and R2* correlated to myelin within WM and GM tissue. Furthermore, R2 values demonstrated better correlation with myelin than R2* did in WM, whilst iron, R2 and R2* correlations to myelin in GM were similar to each other (see section 5.5.6.4).

5.6. Comparison of Results Between Control and AD Human MTG

5.6.1. Comparison of control and AD relaxometry values and iron contents

5.6.1.1. Relaxometry values and elemental iron content comparison

Comparing GM and WM tissue in control and AD MTG demonstrated similar R1, R2, R2* and R2' relaxometry values (R1, P = 0.203; R2, P = 0.326; R2*, P = 0.572 and R2', P = 0.881; Figure 5-40A-D). Iron contents were also similar (P = 0.956; Figure 5-40E). Furthermore, relaxometry values and iron contents in dGM, MCL and WM tissue were also similar between control and AD samples (R1, P = 0.154; R2, P = 0.346; R2*, P = 0.655; R2', P = 0.706 and iron, P = 0.912; Figure 5-40).

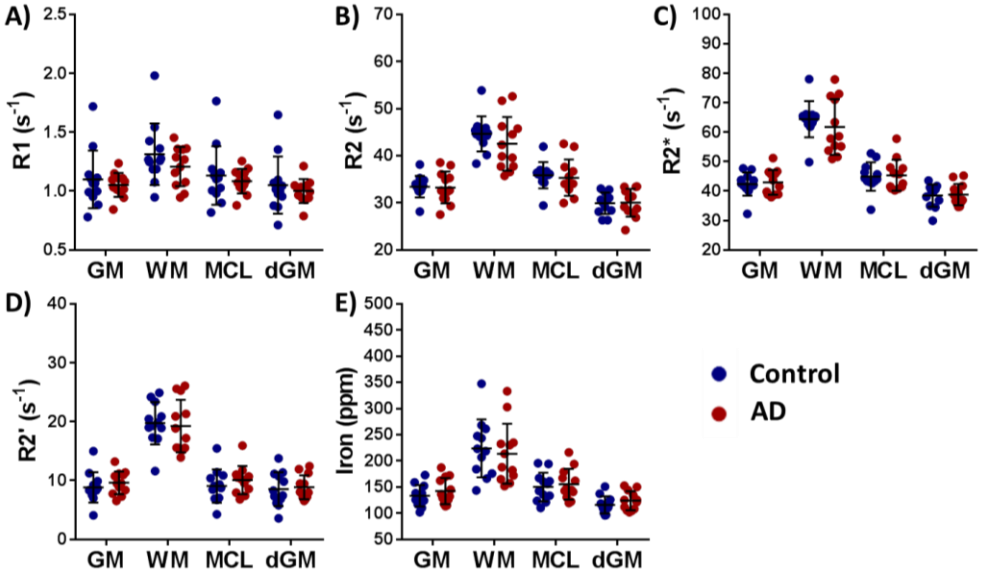

Figure 5-40 Relaxometry values and iron contents compared between control and AD samples

(A) R1, (B) R2, (C) R2, (D) R2' relaxometry values, and (E) elemental iron contents, compared between control (blue) (n = 12) and AD (red) (n = 12) MTG samples.*

Comparisons made between GM and WM tissue, and between dGM, MCL and WM. Significance assessed using two-way ANOVA, with Holm-Sidak test for multiple comparisons with level set to P ≤ 0.05. Graphs show mean values ± SD.

5.6.1.2. Gender comparison between control and AD tissue

Relaxivities and iron contents from Table 5-3 and Table 5-13 were compared to evaluate any differences between control and AD samples in GM or WM regions for each gender. Both males and females demonstrated similar relaxometry values and iron contents in GM regions, and within separated dGM and MCL sub regions, between control and AD samples. Relaxometry values and iron contents in WM were also similar between control and AD samples for each gender using two-way ANOVA (Figure 5-41).

It can be noted however that R2 and R2* values were significantly higher in male control WM than in male AD WM, assessed using Student's unpaired t-test (R2, P = 0.039 and R2*, P = 0.038), whilst female WM was similar between control and AD samples (R2, P = 0.615 and R2*, P = 0.450; Figure 5-41B-C).

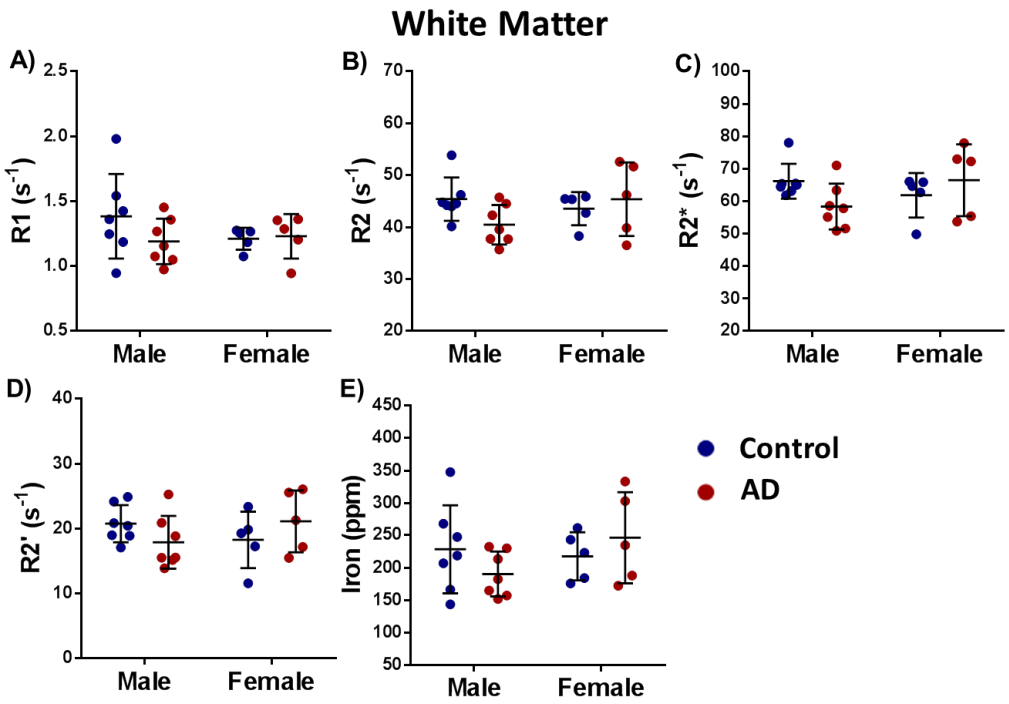

Figure 5-41 Gender comparison of relaxometry values and elemental iron contents in WM between control and AD samples

Comparison of control (blue), and AD (red), (A) R1, (B) R2, (C) R2, (D) R2' relaxometry values, and (E) elemental iron contents, in the WM from male and female subjects (male control (n = 7), male AD (n = 7), female control (n = 5), female AD (n = 5)). Significance assessed using two-way ANOVA, with Sidak test for multiple comparisons set at P ≤ 0.05. Graphs show mean values ± SD.*

5.6.2. Comparison of control and AD relaxometry to iron correlations

5.6.2.1. Comparison of relaxometry to iron correlations between control and AD individual samples

Mean correlations of individual samples were similar between control and AD samples using two-way ANOVA, with Sidak's test for multiple comparisons (R1:

control r^2 = 0.77 ± 0.12, AD r^2 = 0.63 ± 0.23, P = 0.112; R2: control r^2 = 0.81 ± 0.12, AD r^2 = 0.79 ± 0.16, P = 0.986; R2*: control r^2 = 0.83 ± 0.10, AD r^2 = 0.78 ± 0.14, P = 0.899 and R2': control r^2 = 0.65 ± 0.18, AD r^2 = 0.62 ± 0.19, P = 0.975; comparing Table 5-4 with Table 5-14).

5.6.2.2. Comparison of grouped control and AD correlations

Correlation values of both R2 and R2* against iron, were similar between control and AD samples (Figure 5-42B-C). R1 values correlated better with iron in AD samples than control samples (P = 0.005; Figure 5-42A), whilst R2' values correlated with iron better in control than in AD samples (P = 0.048; Figure 5-42D). Comparing the molar relaxivities between control and AD samples demonstrated similar values for r_1 (P = 0.368), r_2 (P = 0.318), r_2* (P = 0.941) and r_2' (P = 0.317; comparing results from Table 5-5 and Table 5-15). Furthermore, whilst R2* correlated better than R2 measurements with iron content in control samples, AD tissue was found to provide similar correlations with iron content between R2* and R2 (Table 5-23). These were both still correlated with iron better than either R2' or R1 values.

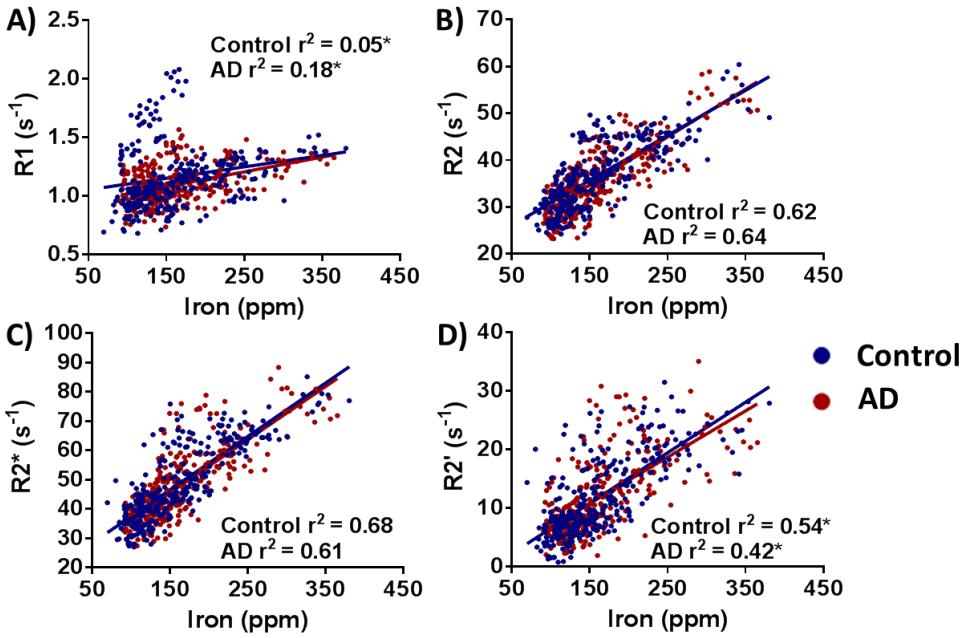

Figure 5-42 Correlation of relaxometry values against elemental iron content across all control and AD samples

Graphs of (A) R1, (B) R2, (C) R2 and (D) R2' against iron content, as assessed using the twenty-four 5x5 pixel ROIs for all control (blue) (n = 288), and AD (red) (n = 288) samples. Group correlation assessed using Pearson correlation and significance between control and AD correlations was assessed using Fisher's z test, with the level set at P ≤ 0.05. * denotes significance between control and AD correlation values.*

5.6.2.3. Comparison of control and AD region-specific correlations

Comparison of WM relaxometry correlations to iron content (Table 5-5 and Table 5-15) highlights R2 values as showing better correlation to iron in AD tissue than control (correlation, P = 0.019 and molar relaxivity, P = 0.001; Figure 5-43). R2* and R2' had similar correlations to iron between control and AD tissue within WM (R2*:

r^2 value, P = 0.870; molar relaxivity, P = 0.173 and R2', r^2 value, P = 0.249; molar relaxivity, P = 0.339; Figure 5-43). GM regions had similar R2, R2* and R2' relaxometry correlations to iron between control and AD tissue (R2: r^2 value, P = 0.555 and molar relaxivity, P = 0.521; R2*: r^2 value, P = 0.415, molar relaxivity, P = 0.779 and R2': r^2 value, P = 0.697, molar relaxivity, P = 0.818). R1 values were not compared due to low correlations to iron within WM and GM regions of both control and AD samples.

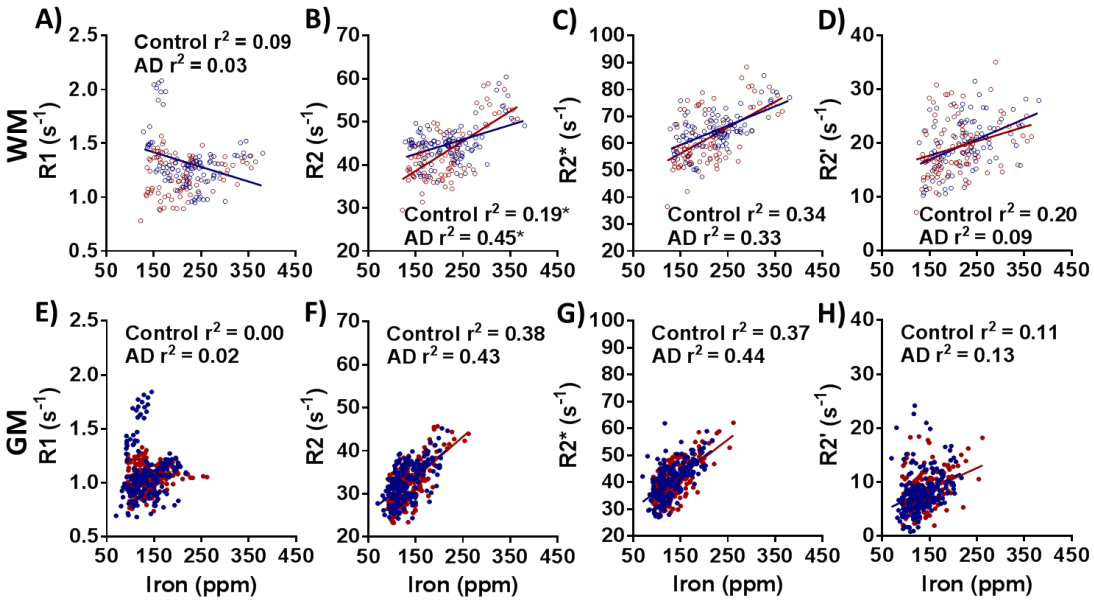

Figure 5-43 Correlation of relaxometry values against elemental iron content across control and AD samples in WM or GM tissue

Graphs showing (A-D) WM and (E-H) GM correlations to iron contents, using R1, R2, R2 and R2' relaxometry assessment in control (blue) and AD (red) samples (control GM (n = 192), AD GM (n = 192), control WM (n = 96), AD WM (n = 96)). Correlation assessed using Pearson correlation and significance between control and AD correlations was assessed using Fisher's z test with the level set at P ≤ 0.05. * denotes significance between control and AD correlation values.*

Table 5-22 Summary table of relaxometry values against iron content correlations and molar relaxivities for control and AD tissue in all, WM only or GM only regions

Model	Group and Region	Mol. Rel.	r^2	P-value
R1 vs Iron	CTR GM+WM	0.001	0.05	0.0003
R1 vs Iron	AD GM+WM	0.001	0.18	< 0.0001
R2 vs Iron	CTR GM+WM	0.096	0.62	< 0.0001
R2 vs Iron	AD GM+WM	0.102	0.64	< 0.0001
R2* vs Iron	CTR GM+WM	0.182	0.68	< 0.0001
R2* vs Iron	AD GM+WM	0.181	0.61	< 0.0001
R2’ vs Iron	CTR GM+WM	0.086	0.54	< 0.0001
R2’ vs Iron	AD GM+WM	0.079	0.42	< 0.0001
R1 vs Iron	CTR WM	-0.001	0.09	0.003
R1 vs Iron	AD WM	0.000	0.03	0.122
R2 vs Iron	CTR WM	0.034	0.19	< 0.0001
R2 vs Iron	AD WM	0.069	0.45	< 0.0001
R2* vs Iron	CTR WM	0.072	0.34	< 0.0001
R2* vs Iron	AD WM	0.096	0.33	< 0.0001
R2’ vs Iron	CTR WM	0.038	0.20	< 0.0001
R2’ vs Iron	AD WM	0.027	0.09	0.028
R1 vs Iron	CTR GM	0.000	0.00	0.748
R1 vs Iron	AD GM	0.001	0.02	0.058
R2 vs Iron	CTR GM	0.088	0.38	< 0.0001
R2 vs Iron	AD GM	0.096	0.43	< 0.0001

R2* vs Iron	CTR GM	0.130	0.37	< 0.0001
R2* vs Iron	AD GM	0.135	0.44	< 0.0001
R2’ vs Iron	CTR GM	0.043	0.11	< 0.0001
R2’ vs Iron	AD GM	0.040	0.13	< 0.0001

Mol. Rel. = Molar Relaxivity. Significant results between control and AD highlighted blue.

Table 5-23 Summary of relaxometry to iron correlation comparisons in different tissue regions between control and AD tissue

Region Selection	Order of significance						
All ROIs (WM and GM) – Control	R2*	>	R2	>	R2’	>	R1
All ROIs (WM and GM) – AD	R2*	=	R2	>	R2’	>	R1
WM only – Control	R2*	>	R2	=	R2’	>	R1
WM only – AD	R2	>	R2*	>	R2’	>	R1
GM only – Control	R2*	=	R2	>	R2’	>	R1
GM only – AD	R2*	=	R2	>	R2’	>	R1

Changes in correlation significance order are highlighted in blue.

5.6.3. Comparison of control and AD myelin contents

5.6.3.1. Quantitative comparison of control and AD myelin

WM from AD samples demonstrated less myelin compared to control samples using two-way ANOVA, with Sidak test for multiple comparisons (compared with GM

values, P = 0.041; or compared with dGM and MCL P = 0.037; Figure 5-44). Similar amounts of myelin were present in GM regions between control and AD samples (GM, P = 0.511; dGM, P = 0.430 and MCL, P = 0.623; Figure 5-44).

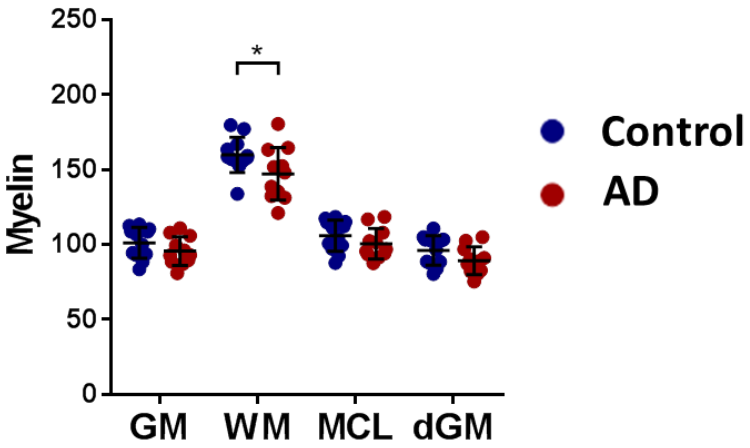

Figure 5-44 Comparison of myelin content in WM and GM tissue of control and AD samples

LFB staining of myelin in GM and WM regions, as well as in GM sub regions, compared between control (blue) (n = 12) and AD (red) (n = 11). Significance assessed using two-way ANOVA, with Sidak test for multiple comparisons, with levels set to P ≤ 0.05 (*). Graphs show mean values ± SD.

5.6.3.2. Gender comparison of myelin in control and AD tissue

Male samples showed significantly lower myelin content within all tissue regions evaluated (WM, P = 0.016; GM, P = 0.013; MCL, P = 0.013 and dGM, P = 0.021; Figure 5-45), between control and AD tissues. Female samples were similar between control and AD tissue however (WM, P = 0.991; GM, P = 0.432; MCL, P = 0.372 and dGM, P = 0.876; Figure 5-45).

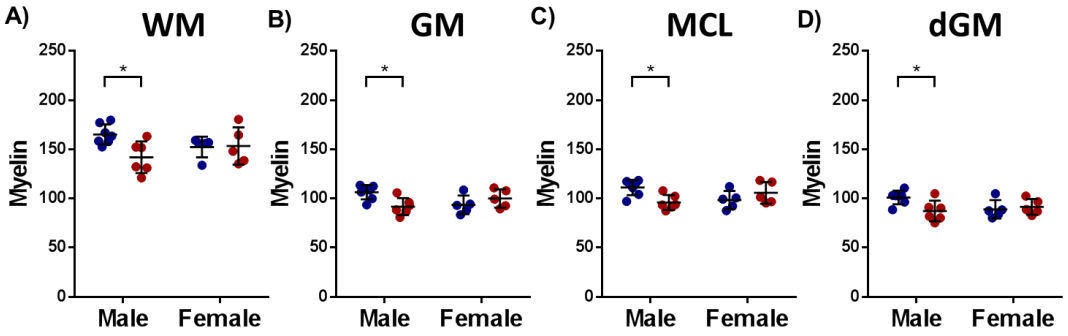

Figure 5-45 Gender comparison of myelin between control and AD tissue

(A) WM, (B) GM, (C) MCL and (D) dGM myelin contents between male and female, control (blue) and AD (red) samples (male control (n = 7), male AD (n = 6), female control (n = 5), female AD (n = 5)). Significance assessed using two-way ANOVA, with Sidak test for multiple comparisons, with levels set to P ≤ 0.05 (*). Graphs show mean values ± SD.

5.6.4. Comparison of control and AD myelin correlations to relaxometry or iron

5.6.4.1. Comparison of control and AD individual sample correlations

Individual sample correlations between myelin and relaxometry values or iron contents, demonstrated significant differences between AD and control samples using two-way ANOVA (P = 0.015), although none survived Sidak multiple comparisons test. However, comparisons using Student's unpaired t-test demonstrated that iron correlation and R1 correlations with myelin were generally lower in AD compared with control samples (iron, P = 0.059 and R1, P = 0.052; comparing Table 5-8 with Table 5-18).

5.6.4.2. Comparison of grouped control and AD correlations to myelin

Iron, R1, R2, R2* and R2' were all correlated to myelin similarly when comparing between control and AD tissue (iron, P = 0.700; R1, P = 0.061; R2, P = 0.851; R2*, P = 0.644 and R2', P = 0.854; Figure 5-46). Comparing regression gradients between relaxometry or iron contents with myelin also provided similar values between control and AD tissue for all measurements (iron, P = 0.539; R1, P = 0.273; R2, P = 0.246; R2*, P = 0.318 and R2', P = 0.649; Figure 5-46, and comparing values in Table 5-9 and Table 5-20). Furthermore, no changes in the correlation significance order were found between control and AD tissue, with R2* showing strongest correlation to myelin, ahead of iron, R2 and R2' correlations (Table 5-24).

The AD ROI values tended to show greater spread than the control data in relaxometry or iron content graphs against myelin (Figure 5-46 and Figure 5-47), which seems to be predominantly due to greater spread of WM ROI values (Figure 5-47).

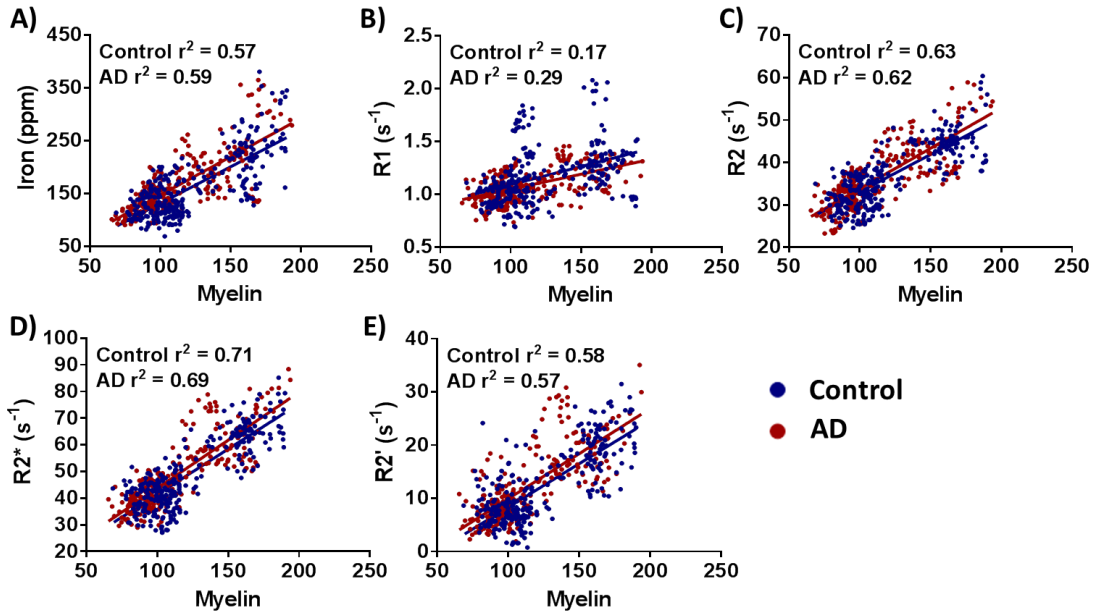

Figure 5-46 Correlation of relaxometry values and elemental iron contents against myelin between control and AD samples

Graphs of (A) elemental iron, (B) R1, (C) R2, (D) R2 and (E) R2' correlation against myelin, as assessed using the twenty four 5x5 pixel ROIs for control (blue) (n = 288), and AD (red) (n = 264) samples. Group correlation assessed using Pearson correlation and assessed for significance between control and AD correlations using Fisher's z test with the level set at $P \leq 0.05$.*

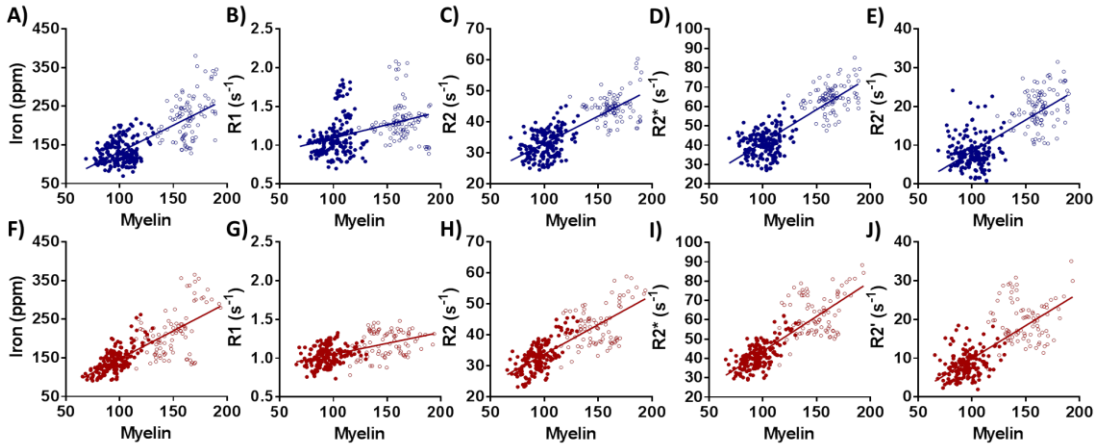

Figure 5-47 Separate GM and WM clustering in iron content and relaxometry correlations to myelin between control and AD tissue

Graphs of (A) iron content and (B) R1, (C) R2, (D) R2 and (E) R2' against myelin, in control (blue) samples (n = 288) and (F-J) AD (red) samples (n = 264). Solid circles are GM ROIs, hollow circles are WM ROIs.*

5.6.4.3. Comparison of control and AD region-specific correlations to myelin

Iron contents and R2* values were correlated similarly with myelin in WM tissue, between control and AD (iron: r^2, P = 0.685 and regression gradient, P = 0.694; and R2*, r^2, P = 0.779 and regression gradient, P = 0.614, comparing values from Table 5-9 and Table 5-20). R2 values correlated with myelin better in AD WM tissue, than control WM (r^2, P = 0.027 and regression gradient, P = 0.025). In GM however, iron contents, R2 and R2* values were all correlated to myelin better in AD samples than in control samples, and had better regression gradients (all, P < 0.0001, comparing values from Table 5-9 and Table 5-20).

Table 5-24 Summary of relaxometry and iron correlation comparisons against myelin, between control and AD tissue

Region Selection	Order of significance								
All ROIs – control	R2*	>	iron	=	R2	=	R2'	>	R1
All ROIs – AD	R2*	>	iron	=	R2	=	R2'	>	R1

> denotes values are significantly different, = denotes values are similar.

5.6.5. Summary of comparisons between control and AD human MTG

- Similar R1, R2, R2* and R2' relaxivity values, as well as similar elemental iron contents were detected between control and AD human MTG samples in GM and WM. These values were also similar in the MCL and dGM regions, between control and AD samples (see section 5.6.1.1). Myelin content however, was lower in AD WM than control WM.
- No changes in relaxometry values or iron content were detected between control and AD samples separated by gender. However separate assessment of R2 and R2* values demonstrated higher values in the WM from control males compared with AD males, whilst female R2 and R2* values were still similar (see section 5.6.1.2). Further evaluation of myelin contents identified that control male samples had higher myelin contents than AD male samples, within all the tissue regions evaluated (see section 5.6.3).
- Mean correlations of relaxometry to iron content in individual samples were similar between control and AD (see section 5.6.2.1), however mean correlations of individual samples when assessing all the relaxometry and

iron correlations with myelin were lower in AD tissue compared with controls (see section 5.6.4.1).

- Grouped correlations demonstrated better R1 correlations to iron, and lower R2' correlations to iron in AD samples than controls. Furthermore, whilst R2* correlated better with iron content than R2 did in control samples, these were similar in AD tissue (see section 5.6.2.2; Table 5-23).
- Grouped correlations of relaxometry and iron content with myelin were similar between control and AD samples, however a difference in the spread of ROI values seems to be apparent, with greater spreading of WM ROI values in AD samples, compared with more clustered control WM ROI values (see section 5.6.4.2).
- Region-specific correlations demonstrated that R2 values were better correlated to iron content in AD WM tissue than control WM tissue, whilst all other correlations and molar relaxivities were similar in WM and GM (see section 5.6.2.3, Table 5-22). Furthermore, whilst R2 values demonstrated lower correlation to iron content than R2* values did in control WM, R2 values became better correlated to iron content than R2* did in AD WM (see section 5.6.2.3, Table 5-23).
- Region-specific correlations demonstrated that R2 values were correlated with myelin better in AD WM tissue, than control WM. In GM, iron contents, R2 and R2* values were all better correlated to myelin in AD compared with control samples (see section 5.6.4.3).

5.7. Discussion

This chapter shows that WM regions consistently demonstrated greater levels of iron and myelin, and had higher R1, R2, R2* and R2' relaxometry values than GM tissue. Similar iron content, as well as R1, R2, R2* and R2' relaxometry values were obtained between control and AD tissues. Higher iron contents were detected in female AD WM, compared with male AD WM, and this can be attributed to myelin breakdown in the male AD WM tissue compared with control males. Whilst R1, R2, R2* and R2' all correlated strongly to iron within individual samples, inter-sample variability was especially high for R1. R2 and R2* relaxometry were able to detect changes in iron content within WM or GM regions for both control and AD tissue, however R2 values were better correlated to AD WM iron contents than control WM iron contents, potentially due to a breakdown in myelin content within WM of AD samples.

5.7.1. Post-mortem tissue factors

PMI and subjects' age at death did not affect R1, R2, R2* or R2' relaxivity values, or iron content, of control or AD human tissue samples (Table 5-1 and Table 5-11). Fixation time of samples however, influenced R1 values across all tissue regions in both control and AD tissue and demonstrated some effects on R2 and R2' values (Table 5-1 and Table 5-11).

5.7.1.1. PMI

Whilst certain MR techniques, such as ^{1}H-MRS, have been used for the detection of the biochemical or metabolic changes that occur early on in post mortem samples, (Petroff *et al.*, 1988, Ith *et al.*, 2002, Scheurer *et al.*, 2005), inconsistent findings have been observed using relaxometry assessment (Fagan *et al.*, 2008, Shepherd *et al.*, 2009). The method performed by Shepherd *et al*. more closely resembles the conditions of human tissue obtained as part of this study, in which they observed decreasing T1 and T2 values in rat cortical samples directly immersed in fixative, at various PMIs (Shepherd *et al.*, 2009). Despite the closely resembling model, our data demonstrates no impact of PMI length on relaxivity values in control or AD human brain tissue samples (Table 5-1 and Table 5-11). The discrepancies observed between our data and these two studies may be attributed not only to species differences with our assessment of human post-mortem tissue rather than rat cortex, but also due to our data evaluating PMI lengths of up to 100 hours, whilst both studies in rat only evaluated up to 24 hours PMI (Fagan *et al.*, 2008, Shepherd *et al.*, 2009). Relaxometry measurements are affected by tissue microstructure, water content and iron contents (Deoni, 2010), which are more likely to be affected by tissue degradation that can occur at longer PMIs. Given that no changes were detected for any relaxometry values due to PMI time here, we expect the level of degradation is not substantial enough to affect the environment of proton spins, measured through relaxometry assessment in these brain tissue samples, up to this length of PMI.

From the limited information available regarding the effects of PMI on iron content in control and AD human brain samples, no effect of PMI affecting iron content has been detected (Loeffler *et al.*, 1995). Here, we also show that over the course of up to 100 hours, no effects can be observed on global iron contents within either GM or WM tissue types due to PMI. Whilst, these results allow validation that PMI length does not influence any results obtained with this study, it is important that PMI effect on iron content be evaluated in a specific longitudinal study to validate these observations in greater detail.

5.7.1.2. Fixation time

Fixation of human tissue samples has been extensively explored, demonstrating decreasing T1 and T2 values (therefore increasing R1 and R2) during the fixation process (Tovi and Ericsson, 1992, Blamire *et al.*, 1999, Dawe *et al.*, 2009). T1 values of brain GM and WM became similar, with fixation reducing the contrast between them (Tovi and Ericsson, 1992). For this reason PD weighted images have been suggested for use with post-mortem samples to enhance GM to WM contrast (Tovi and Ericsson, 1992, Blamire *et al.*, 1999). T2 values also decrease with fixation although the decline is not as great as that for T1 (Tovi and Ericsson, 1992, Blamire *et al.*, 1999). Recently, a systematic study was performed showing that not only do T2 values vary with fixation time, but they also depend on the depth of the brain regions, with T2 values changing less rapidly in deep brain structures, reflecting the time taken for fixative to reach deeper brain regions (Dawe *et al.*, 2009). With these studies primarily focussed on evaluating the changes in relaxometry values

throughout the fixation process, the time points evaluated only range up to a maximum of 6 months post-mortem. Here, we find that prolonged fixation, beyond 6 months, and up to 33 months, of both control and AD samples in formalin continues to affect relaxometry measurements. The results showing that R1 values continue to increase in both control and AD WM and GM tissue are in agreement with the previously described, shorter length studies. The increase in R2 values within control GM is also in agreement with previous studies, however it was found that WM tissue did not continue to change at these prolonged fixation times. In AD samples, R2' values decreased in WM and GM tissue from AD samples, whilst R2 values showed no changes in any tissue regions. Fixation can affect relaxometry measurement of tissues due to the cross linking of proteins increasing tissue rigidity, and leading to a reduction in the mobility of water protons impacting on the T1 and T2 values (Dawe *et al.*, 2009). This discrepancy in R2 and R2' between control and AD tissue highlights that disease specific differences may be occurring with prolonged formalin fixation, with neurodegeneration playing varying roles on prolonged protein cross linking, compared with normal tissue. It should also be noted that all brain samples were sliced into thin sections prior to formalin fixation at the brain bank, and so it would be expected that tissue depth would play no role on the degree of fixation of samples, as has been documented by others (Dawe *et al.*, 2009).

These results may impact work requiring the use of human post-mortem tissue from brain banks however, which tend to have more readily-available formalin fixed tissue for assessment, than fresh or frozen tissue. Therefore, care should be taken

to ensure that samples obtained are also fixation time matched when carrying out post-mortem MRI studies, to compare between groups.

Formalin fixation demonstrated no effects on iron content over short-term fixation here, in agreement with previous studies (Bush *et al.*, 1995, Chua-anusorn *et al.*, 1997, Gellein *et al.*, 2008). The degree of iron leaching during storage in formalin is likely to be determined by the strength and mode of binding of iron to proteins, as well as length of time in fixative (Gellein *et al.*, 2008). Recently however, evidence has been shown that highlights decreased iron content following 4-6 years fixation (Schrag *et al.*, 2010). As no significant iron leaching has been demonstrated up to 18 months fixation (Gellein *et al.*, 2008), samples with fixation times greater than this have been excluded from subsequent group analyses.

5.7.1.3. Subjects' age at death

Much of the literature surrounding age of subject death on relaxometry values has involved evaluation of changes between young, adult and aged populations (Pujol *et al.*, 1992, Schenker *et al.*, 1993, Saito *et al.*, 2009). These relaxometry assessments predominantly evaluate changes in R2 and R2* in different brain areas demonstrating increases in R2 and R2* between young and adult subjects, with both relaxation rates reaching a plateau at around 40 years of age (Pujol *et al.*, 1992, Schenker *et al.*, 1993, Saito *et al.*, 2009). T1 values demonstrate inconsistent results with age, with some studies showing no change with age, whilst others shown an increase in certain brain regions (Breger *et al.*, 1991, Steen *et al.*, 1995,

Ogg and Steen, 1998, Saito *et al.*, 2009). Similar observations for iron content have been detected as for T2 and T2* relaxometry, with an increase in iron from young, until levels plateau at around 40 years of age (Hallgren and Sourander, 1958). Given that all the samples obtained for this thesis were from an aged population (60-95 years), it is unsurprising that no changes in any relaxometry values, or iron contents, are observed as a factor of age of subject, as the population has been sampled from the plateaus of relaxation times and iron contents for both control and AD subjects' samples.

5.7.2. Relaxometry values and elemental iron content assessments

The relaxometry values of medial temporal gyrus observed in this study are comparable to previously published literature using post-mortem formalin fixed human tissue (Dawe *et al.*, 2009, Antharam *et al.*, 2012) (Table 5-25). R1 values were comparable to both *in vivo* and frozen temporal cortex GM and WM values, within both control and AD samples. In line with the effects of fixation on relaxometry values in brain tissue, R2, R2* and R2' values detected here were slightly higher than those from studies performed using *in vivo* or fresh/ frozen brain tissue (see section 5.7.1.2 and Table 5-25) (Gelman *et al.*, 1999, House *et al.*, 2006, House *et al.*, 2007, Langkammer *et al.*, 2010, House *et al.*, 2012). R2 values measured here were approximately 30% greater than post mortem temporal cortex at similar field strength. The higher R2 values measured are thus due to the fixation of samples, and also due to the higher field strength used here, in comparison to other studies (Table 5-25). The R2* values measured were also comparable to other

studies using fixed tissue at similar field strength (Stuber *et al.*, 2014), however one study demonstrated slightly lower R2* values (Fukunaga *et al.*, 2010) (Table 5-25). This study however only performed measurements in one sample. Iron contents measured in this study were extremely comparable to previous literature in the same brain regions from both fixed and non-fixed post-mortem human tissue (Bush *et al.*, 1995, Deibel *et al.*, 1996, Leite *et al.*, 2008, Ramos *et al.*, 2014) (Table 5-25). This was the case for both control and AD samples. Furthermore, wet weight iron contents converted into dry weights by using dry-to-wet weight ratios (House *et al.*, 2007), also provided iron contents of similar value to that observed here (Table 5-25), verifying the validity in the use of SR-XRF.

Table 5-25 Comparison of cortical relaxometry and iron content measurements within literature

Measurement	Group	Region	Tissue	Values	Number of Samples	Sample type	B_0	Reference
R1	Control	Temporal cortex	GM	1.10 ± 0.25	12	Fixed	7 T	*This study*
(s^{-1})		Temporal cortex	WM	1.31 ± 0.26	12	Fixed	7 T	*This study*
	Control	Cortex	GM	0.72 ± 0.02	108	*In vivo*	1.5 T	(Ogg and Steen, 1998)
		Frontal cortex	WM	1.35 ± 0.02	112	*In vivo*	1.5 T	(Ogg and Steen, 1998)
	Control	Temporal Cortex	GM	0.90 ± 0.05 **	5	Frozen	1.4 T	(House *et al.*, 2008)
		Temporal Cortex	WM	1.55 ± 0.05 **	4	Frozen	1.4 T	(House *et al.*, 2008)
	Control	Hippocampus	CA4-DG	0.76 ± 0.01	3	Unfixed	14.1 T	(Antharam *et al.*, 2012)
	AD	Temporal cortex	GM	1.05 ± 0.10	12	Fixed	7 T	*This study*
		Temporal cortex	WM	1.21 ± 0.17	12	Fixed	7 T	*This study*
	AD	Temporal Cortex	GM	1.05 ± 0.15 **	5	Frozen	1.4 T	(House *et al.*, 2008)

		Temporal Cortex	WM	1.50 ± 0.10 **	5	Frozen	1.4 T	(House *et al.*, 2008)
	AD	Hippocampus	CA4-DG	0.66 ± 0.06	5	Unfixed	14.1 T	(Antharam *et al.*, 2012)
R2	Control	Temporal cortex	GM	33.42 ± 2.31	12	Fixed	7 T	*This study*
(s^{-1})		Temporal cortex	WM	44.64 ± 3.75	12	Fixed	7 T	*This study*
	Control	Cortex	GM	11.24 ± 0.88	5	P-M	2.35 T	(Brooks *et al.*, 1989)
		White Matter	WM	13.07 ± 1.88	5	P-M	2.35 T	(Brooks *et al.*, 1989)
	Control	Cortex	GM	23.67 ± 1.62	5	P-M	8.5 T	(Brooks *et al.*, 1989)
		White Matter	WM	27.84 ± 3.85	5	P-M	8.5 T	(Brooks *et al.*, 1989)
	Control	Prefrontal cortex	GM+WM	14.4 ± 1.8	6	*In vivo*	3 T	(Gelman *et al.*, 1999)
		Frontal WM	WM	18.0 ± 1.2	6	*In vivo*	3 T	(Gelman *et al.*, 1999)
	Control	Temporal cortex	GM	12.0 **	11	*In vivo*	1.5 T	(House *et al.*, 2006)
		Temporal cortex	WM	13.0 **	11	*In vivo*	1.5 T	(House *et al.*, 2006)
	Control	Temporal Cortex	GM	9.8 ± 1.0 **	5	Frozen	1.4 T	(House *et al.*, 2008)

		Temporal Cortex	WM	16.5 ± 1.5 **	4	Frozen	1.4 T	(House *et al.*, 2008)
	Control	Hemisphere	-	26.90 ± 2.93	5	Fixed	3 T	(Dawe *et al.*, 2009)
	Control	Hippocampus	CA4-DG	28.2 ± 2.8	3	Unfixed	14.1 T	(Antharam *et al.*, 2012)
	AD	Temporal cortex	GM	33.25 ± 3.38	12	Fixed	7 T	*This study*
		Temporal cortex	WM	42.53 ± 5.70	12	Fixed	7 T	*This study*
	Severe MCI	Temporal cortex	GM	12.9 **	11	*In vivo*	1.5 T	(House *et al.*, 2006)
		Temporal cortex	WM	11.9 **	11	*In vivo*	1.5 T	(House *et al.*, 2006)
	AD	Temporal Cortex	GM	11.0 ± 0.5 **	5	Frozen	1.4 T	(House *et al.*, 2008)
		Temporal Cortex	WM	15.0 ± 1.0 **	5	Frozen	1.4 T	(House *et al.*, 2008)
	AD	Hippocampus	CA4-DG	35.1 ± 3.8	5	Unfixed	14.1 T	(Antharam *et al.*, 2012)
R2*	Control	Temporal cortex	GM	42.38 ± 3.98	12	Fixed	7 T	*This study*
(s^{-1})		Temporal cortex	WM	64.39 ± 6.16	12	Fixed	7 T	*This study*
	Control	Cortex	GM	26.5	1	Fixed	7 T	(Fukunaga *et al.*, 2010)

		Cortex	WM	46.0	1	Fixed	7 T	(Fukunaga *et al.*, 2010)
	Control	Temporal cortex	WM	26 ± 3	36	P-M	3 T	(Langkammer *et al.*, 2010)
	Control	Hippocampus	CA4-DG	42.7 ± 4.7	3	Unfixed	14.1 T	(Antharam *et al.*, 2012)
	AD	Temporal cortex	GM	42.94 ± 4.26	12	Fixed	7 T	*This study*
		Temporal cortex	WM	61.75 ± 9.45	12	Fixed	7 T	*This study*
	AD	Hippocampus	CA4-DG	44.8 ± 2.6	5	Unfixed	14.1 T	(Antharam *et al.*, 2012)
R2’	Control	Temporal cortex	GM	8.82 ± 2.59	12	Fixed	7 T	*This study*
(s^{-1})		Temporal cortex	WM	19.74 ± 3.60	12	Fixed	7 T	*This study*
	Control	Prefrontal cortex	GM+WM	3.4 ± 1.1	6	*In vivo*	3 T	(Gelman *et al.*, 1999)
		Frontal WM	WM	3.9 ± 1.2	6	*In vivo*	3 T	(Gelman *et al.*, 1999)
	AD	Temporal cortex	GM	9.60 ± 1.95	12	Fixed	7 T	*This study*
		Temporal cortex	WM	19.25 ± 4.48	12	Fixed	7 T	*This study*

Measurement	Group	Region	Tissue	Concentration	Number of Samples	Sample type	Analysis	Reference
Iron	Control	Temporal cortex	GM	133.2 ± 20.4	12	Fixed	SR-XRF	*This study*
(μg/g dry wt)		Temporal cortex	WM	223.9 ± 55.2	12	Fixed	SR-XRF	*This study*
	Control	Temporal cortex	GM+WM	135.5 ‡	47	P-M	Colorimetry	(Hallgren and Sourander, 1958)
	Control	Temporal cortex	GM	222 ± 54.6	5	P-M	ICP-ES	(Bush *et al.*, 1995)
		Temporal cortex	WM	245 ± 85.9	5	P-M	ICP-ES	(Bush *et al.*, 1995)
	Control	Temporal cortex	GM+WM	266 ± 23.2 *	11	Frozen	INAA	(Deibel *et al.*, 1996)
	Control	Temporal cortex	GM	242.0 ‡	1	Frozen	GFAAS	(House *et al.*, 2007)
		Temporal cortex	WM	280.1 ‡	1	Frozen	GFAAS	(House *et al.*, 2007)
	Control	Frontal cortex	GM+WM	224.0 ± 41.5	21	Frozen	NAA	(Leite *et al.*, 2008)
	Control	Temporal cortex	WM	163.7 ‡	36	Fixed	ICP-MS	(Langkammer *et al.*, 2010)

Control	Temporal cortex	GM+WM	280 #	719	Frozen	GFAAS	(House *et al.*, 2012)
Control	Temporal cortex	GM+WM	287 ± 65	42	Frozen	GFAAS	(Ramos *et al.*, 2014)
AD	Temporal cortex	GM	142.1 ± 25.0	12	Fixed	SR-XRF	*This study*
	Temporal cortex	WM	213.6 ± 57.3	12	Fixed	SR-XRF	*This study*
AD	Temporal cortex	GM+WM	269 ± 37.9 *	10	Frozen	INAA	(Deibel *et al.*, 1996)
AD	Temporal cortex	GM	251.0 ‡	2	Frozen	GFAAS	(House *et al.*, 2007)
	Temporal cortex	WM	183.2 ‡	3	Frozen	GFAAS	(House *et al.*, 2007)
Dementia	Frontal cortex	GM+WM	235.7 ± 41.2	21	Frozen	NAA	(Leite *et al.*, 2008)

GM denotes Grey Matter, WM denotes White Matter, P-M denotes samples taken post-mortem, wt denotes weight, INAA denotes instrumental neutron activation analysis, ICP-ES denotes inductively coupled plasma emission spectroscopy, ICP-MS denotes inductively coupled plasma mass spectroscopy, GFAAS denotes graphite furnace atomic absorption spectrometry, SR-XRF denotes synchrotron radiation X-ray fluorescence.

** denotes conversion of SEM to SD, # denotes median value used, ** denotes approximate values given due to results presented as figures in the relevant references, ‡ denotes iron values converted from wet weight to dry weight using dry to wet weight ratios from (House et al., 2007).*

5.7.2.1. WM compared with GM in control and AD tissue

Using these MTG samples, both control and AD WM tissue were consistently found to hold greater iron contents than GM tissue, which were similarly detectable using R1, R2, R2* and R2' relaxometry assessment. This has also been shown in studies that evaluated cortical GM iron content or relaxometry values, compared to cortical WM values (House *et al.*, 2008, Fukunaga *et al.*, 2010, Stuber *et al.*, 2014). Furthermore, given the close similarities in tissue architecture detected between elemental iron and relaxometry maps, and the consistency of quantitative differences between WM and GM regions, it seems that iron content must be impacting on relaxometry measurements, at least to some extent. The detection of iron in this study was sensitive enough to investigate microstructural differences within the MTG, with identification of specific cortical layers, namely layers IV-V, within the GM (referred to as MCL). Identification of these cortical layers was also possible using high resolution R1, R2 and R2* relaxometry, again indicating that detection of these regions may be based on their iron contents. Indeed, assessment of this region separately provided relaxivity values increasing in the consistent order of dGM < MCL < WM using R1, R2 and R2* relaxometry, as was also observed for iron contents. It can be noted however that whilst R2 and R2* demonstrated similar differences as iron contents using unpaired statistical assessment between GM and WM regions, R1 values were generally less sensitive to this difference, only detecting differences consistently using paired statistics in both control and AD tissue. This may be due to lower reliability of R1 values for iron detection, as shown by the lower correlations of R1 to iron contents (see section 5.7.3.2). Furthermore,

R2’ values did not demonstrate this same consistent change between tissue types, with an inability to distinguish between the dGM and MCL. This may also be due to the lower correlations observed between R2’ and iron content than R2 or R2* relaxometry correlations to iron content (see section 5.7.3.2) or due to fewer effects from magnetic inhomogeneities within the MCL impacting R2’ measurement.

Both the WM and MCL layers have been identified previously within the MTG using Perls’ staining for iron and were found to contain cortical layers with greater levels of myelination (van Duijn *et al.*, 2013). With myelinated regions heavily populated with oligodendrocytes, the higher iron content observed in regions that contain greater numbers of oligodendrocytes is expected, given these cells contain the greatest amount of iron compared with other cell types in the brain (Connor *et al.*, 1990). However, given the differences in tissue microstructure and water content in myelin-rich WM regions compared with GM (House *et al.*, 2008), myelin itself has been shown to affect relaxometry values (Gelman *et al.*, 2001, Rooney *et al.*, 2007). Therefore it is important to consider changes in myelin content and iron content together, to understand the relaxometry observations in greater detail (see section 5.7.4).

Finally, it was determined that similar iron contents, as well as in R1, R2, R2* and R2’ relaxometry values were detected between control and AD tissue, in all WM and GM regions. Whilst other studies have also shown similar iron contents between controls and AD tissue (Hallgren and Sourander, 1960, Jellinger *et al.*, 1990, Magaki *et al.*, 2007, Schrag *et al.*, 2011), this work does however contradict

the hypothesis of increased iron content holding causal roles during neurodegeneration in AD (Goodman, 1953, Connor *et al.*, 1992a, Connor *et al.*, 1992b, Loeffler *et al.*, 1995, Deibel *et al.*, 1996, House *et al.*, 2008, Smith *et al.*, 2010). Histochemical approaches showing increased stainable iron have been used in many of these positive cases (Goodman, 1953, Connor *et al.*, 1992a, Smith *et al.*, 2010), however whilst these techniques provide excellent assessment of iron localisation, their quantitative interpretation can be complex (Meguro *et al.*, 2007) (see section 1.5.1). Furthermore, quantitative studies evaluating iron content in various brain regions have been performed in low sample numbers, with ten AD samples used in one study (Deibel *et al.*, 1996), whilst only five AD samples were used in another, of which two were specified as probable AD (House *et al.*, 2008). Finally, other previous studies have normalised iron content to protein content, demonstrating differences between AD and control in the frontal cortex (Loeffler *et al.*, 1995). Since protein content was also found to change during AD in that study, the results may be due to changes in protein content rather than solely changes in iron content (Loeffler *et al.*, 1995).

Similar iron contents have been detected in the hippocampus (Magaki *et al.*, 2007) and in cortical regions (Religa *et al.*, 2006) of AD subjects to control, supporting our elemental iron findings in the MTG. Furthermore, similar iron levels in CSF were found between control, MCI and AD patients (Lavados *et al.*, 2008). It should be noted, however, that these studies were also performed with low sample numbers. Studies also exist highlighting the use of histochemical assessment of iron to show

no overall iron content changes between control and AD tissue (Hallgren and Sourander, 1960, Jellinger *et al.*, 1990).

Alongside these similar iron contents observed between control and AD, we also found similar values using relaxometry measurements for these groups. These observations are also similar to some previous studies (Antharam *et al.*, 2012), whilst providing contradictory evidence to others (Schenck *et al.*, 2006, Qin *et al.*, 2011). Given that T1 and T2 changes in the brain with ageing closely match the profile of iron content changes with ageing, these measurements have been used as surrogate measurements for iron *in vivo* (Hallgren and Sourander, 1958, Schenker *et al.*, 1993, Ogg and Steen, 1998). Furthermore, strong correlations between relaxometry measurements and iron contents in the brain have been shown (Langkammer *et al.*, 2010) (also see chapter 4 and discussed in greater detail in section 5.7.3). Based on this premise, T2-weighted imaging highlighted iron deposition in AD subjects' hippocampus compared with controls (Schenck *et al.*, 2006), and increased R2' values were identified in both MCI and AD patients' hippocampus, caudate, putamen and parietal cortex (Qin *et al.*, 2011). More interesting are the correlations between relaxometry measurement changes to cognitive scores in both AD and even in normal healthy ageing (Pujol *et al.*, 1992, Qin *et al.*, 2011, Rodrigue *et al.*, 2012). Furthermore, increased ferritin iron in the caudate, globus pallidus and putamen from AD patients has been identified using approaches such as FDRI (Bartzokis *et al.*, 1994b, Bartzokis *et al.*, 2000). However, with all of these studies based in clinical populations, it is difficult to confirm that a change in iron content is truly being detected using these relaxometry

measurements. Finally, support for iron detection using relaxometry measurements has also been provided through studies evaluating the accumulation of iron in amyloid plaques, with loss of T2 and T2* specific to regions of Perls staining with amyloid deposition in animal models (Chamberlain *et al.*, 2009, Dhenain *et al.*, 2009, Wengenack *et al.*, 2011) or in human plaques (Meadowcroft *et al.*, 2009). However, given that these accumulations of iron provide clearly detectable foci by MRI, these observations are less relevant for global iron content changes being evaluated here. In support of the results shown here, R2 and R2* values were found to be similar between the hippocampus of AD compared with control subjects, despite detectably strong correlations with iron content also evaluated using SR-XRF (Antharam *et al.*, 2012).

Taken altogether, these results satisfied the objectives to perform quantitative R1, R2, R2* and R2' relaxometry using control and AD human MTG. These were then subsequently compared between control and AD, showing similar relaxometry values and iron contents in each tissue region assessed (see section 5.2). These results, along with others', may imply that changes in the distribution or forms of iron are being detected within brain tissue, as opposed to global iron content increase, with many studies demonstrating iron to have increased redox activity potential in AD pathology using histochemical or colorimetric approaches (Smith *et al.*, 1997, Magaki *et al.*, 2007, Lavados *et al.*, 2008, Smith *et al.*, 2010). Indeed, this hypothesis may be supported due to the various pathological forms of iron being detected at greater levels within AD tissue compared with control, such as

magnetite (Collingwood *et al.*, 2005, Pankhurst *et al.*, 2008) and hemosiderin (Quintana *et al.*, 2006). In this case, altered forms of iron during pathology may play a greater impact on relaxometry values, (as shown in chapter 4), however no evidence for this has been detected in the samples assessed here.

5.7.2.2. Gender comparison

Gender differences are rarely taken into account when measuring iron content or relaxivity values in post-mortem studies. However, we found no differences between control male and female subjects here, based on either of the iron content or relaxometry assessments, within WM or GM of the MTG. This is in line with iron estimation performed using phase imaging (Xu *et al.*, 2008) showing no discernible differences in brain iron, however others have detected lower female ferritin iron than in males using FDRI (Bartzokis *et al.*, 2007a). More recently, whilst no overall differences in iron content were detected between genders, a difference in the correlation of age and iron was detected, whereby male subjects showed a gradual increase in iron content with age, whilst females did not (Ramos *et al.*, 2014). This matches our data for overall iron content similarities between the genders, however no age-related correlations were observed in our results (see section 5.7.1.3).

Whilst control samples showed similar iron contents, R2* and R2' values between the genders, AD tissue demonstrated higher iron contents in female subjects' WM compared with males' WM, which seems to be mirrored with a trend towards

significance for R2* and R2' values. Further evaluation demonstrated that male AD samples had generally lower WM R2 and R2* values compared with male control WM tissue. These findings may be explained by a breakdown in myelin content in WM tissue from AD samples, which was specifically found to occur in males', but not females' samples (see section 5.7.4).

Iron therefore seems to affect relaxivity, most specifically R2 and R2*, in human post-mortem tissue. However, greater understanding of the specificity and sensitivity can be gained following correlation assessments between iron and relaxometry values (see section 5.7.3).

5.7.3. Correlation of iron to relaxometry

5.7.3.1. Individual samples

Most studies correlating quantitative iron contents to MR relaxometry measurements either involve *in vivo* clinical assessments correlated to previous iron contents established in literature (Ogg and Steen, 1998, House *et al.*, 2010, Qin *et al.*, 2011), or performing bulk analysis quantification of whole tissue regions for iron content and correlating this against averaged tissue relaxivities (House *et al.*, 2008, Langkammer *et al.*, 2010). Whilst these approaches provide important information regarding the overall regional correlations between iron and relaxometry, they do not allow for a full, specific and spatial assessment of

correlations between samples, or within regions, to fully understand the impact that iron may have on relaxivity changes within the brain (see section 1.6.5.1).

To spatially assess the correlation of iron content against relaxometry (see objectives in section 5.2), we employed a technique using 24 small 5x5 pixel ROIs placed across the GM and WM regions for each sample. These generally demonstrated strong, positive correlations for both control and AD tissue using R1, R2, R2* and R2' relaxometry measurements compared with iron content, as demonstrated by the mean correlation values across samples. Using this approach, R2' values were found to be correlated to iron contents worse than R1, R2 or R2* correlated to iron, in control samples. This result was unexpected given that R2' contains information on magnetic inhomogeneities, and should theoretically provide greater sensitivity for iron (Ordidge *et al.*, 1994, Haacke *et al.*, 2005). However, R2' maps demonstrated greater noise across maps, as indicated by the larger error bars in the representative single sample correlations compared with either R2 or R2* (Figure 5-12D). The reason for greater noise in R2' maps compared with the other relaxometry measurements is likely to be due to accumulation of error across pixels following the subtraction of R2 from R2* maps. To account for this in the future, acquisition of higher SNR data of both R2 and R2* maps should provide enhanced R2' maps for correlation against iron. The caveat to this, however, would be much longer scan times for each sample with a greater number of averages per scan. Relaxivities in AD tissue were all correlated with iron similarly, using the mean correlations of individual samples. Furthermore, comparison between control and AD correlations showed similar values detected for each

relaxometry measurement against iron, indicating that correlations within individual samples do not change during AD pathology.

5.7.3.2. Grouped and region-specific correlations

In order to assess both intra- and inter- sample variations in iron content correlations to relaxometry, all the individual 24 ROIs of each sample were pooled and correlated with iron, rather than using the mean of each samples' correlation. With this approach, R1 demonstrated extremely low correlation in both control and AD tissues (Table 5-22). This observation is in contradiction to the R1 correlations to iron observed in individual samples and likely indicates that other factors other than iron content have a great effect on R1 values across individual samples. Indeed, fixation time length was found to provide a significant effect on R1 values here, potentially impacting on the overall correlation with iron across multiple samples (Tovi and Ericsson, 1992, Blamire *et al.*, 1999). Similarly, given that fixation of samples involves protein cross-linking affecting water availability, differences in water content may also substantially effect R1 correlation to iron across multiple samples. However, water content was not measured within our study and so cannot be confirmed as an influencing factor.

R2 and R2* demonstrated strongest correlations to iron content in both control and AD tissues, however whilst R2* correlation to iron was higher than that for R2 correlation in control samples, the R2* correlation seems to be less in AD tissue. This leads to an equal correlation for both R2* and R2 to iron content in AD

samples. This may indicate that neurodegeneration in the AD tissue affects R2* correlation to iron. Molar relaxivities were similar between control and AD tissue, indicating that each relaxometry assessments' sensitivity to iron seems to be consistent in both control and AD samples.

Statistical analyses using linear regression and correlation were performed in order to draw comparisons to other studies. Comparison of our correlation values to others highlights agreement with combined GM and WM regions. The correlation values between R2 and iron from this study were $r^2 = 0.62$ in control and $r^2 = 0.64$ in AD, which are similar to that found using ICP-MS to compare against iron contents in the normal brain ($r^2 = 0.67$) (Langkammer *et al.*, 2010). These values are also similar to correlations found between R2 and iron content in control ($r^2 = 0.64$) and AD ($r^2 = 0.63$) tissue, following quantification of iron using AAS (House *et al.*, 2007). Using R2* correlation to iron, this study showed $r^2 = 0.68$ in control and 0.61 in AD, whereas a correlation value of $r^2 = 0.90$ was identified in the study of normal brains with ICP-MS (Langkammer *et al.*, 2010). The better correlation of iron to R2* observed in the latter study could be due to the bulk assessment of iron content from a number of different tissue regions, ranging from white matter, putamen, caudate and the globus pallidus, providing enhanced sampling of iron contents for comparability with relaxometry measurements. The samples acquired as part of the study here were substantially smaller, containing only WM and GM tissue from the MTG cortex, however we have been able to spatially correlate iron content with relaxometry.

From molar relaxivity values, this study demonstrated r_2 = 0.096 $s^{-1}ppm^{-1}$ and r_2* = 0.182 $s^{-1}ppm^{-1}$ in controls, and r_2 = 0.102 $s^{-1}ppm^{-1}$ and r_2* = 0.181 $s^{-1}ppm^{-1}$ in AD (Table 5-22). Using ICP-MS assessment of iron in control samples, R2 and R2* values provided r_2 = 0.04 $s^{-1}ppm^{-1}$ and r_2* = 0.27 $s^{-1}ppm^{-1}$ at 3T (Langkammer *et al.*, 2010). At 4.7T, R2 values correlated to iron with r_2 = 0.104 $s^{-1}ppm^{-1}$ in control and r_2 = 0.095 $s^{-1}ppm^{-1}$ in AD using GM and WM regions for assessment (House *et al.*, 2007). The values obtained in this study are relatively consistent to values obtained previously (House *et al.*, 2007, Langkammer *et al.*, 2010), with discrepancies potentially attributed to different field strengths used. These values allow the provision for predicting R2 or R2* values ($R2_{PRED}$ or $R2^*_{PRED}$) (House *et al.*, 2007), with a known iron content, [Fe], where,

$$R2_{PRED} \text{ or } R2^*_{PRED} = A[Fe] + B \qquad \text{(Eq.1)}$$

From the measurements taken within this work across both GM and WM regions, the following relationships can be outlined:

Control $R2_{PRED}$ = 0.096[Fe] + 21.30

Control $R2^*_{PRED}$ = 0.182[Fe] + 19.25

AD $R2_{PRED}$ = 0.102[Fe] + 19.38

AD $R2^*_{PRED}$ = 0.181[Fe] + 18.36

These relationships may also be used to evaluate the iron content present in the MTG following non-invasive R2 or R2* assessment.

The additional advantage with the approach taken here using 24 small ROIs is the potential to correlate relaxometry measurements to iron contents within regions, e.g. within the WM and GM tissue separately. In all cases of regional iron to relaxometry correlations, correlation values were substantially lower within regions compared with across regions. As the correlations were better with ROIs including both WM and GM, the correlations to iron appear to be predominantly driven by the larger differences in iron concentration between the WM and GM from each sample. Hence, MR relaxometry measures seem to be relatively insensitive to small changes in iron concentrations, given the lower correlation values when considering solely WM or GM ROIs. This is supported by the finding that an iron content change of 55 $\mu g\ g^{-1}$ wet tissue is required to provide correlative changes in MRI relaxometry values (House *et al.*, 2007).

Control GM provided greater R2 correlation to iron than in WM and showed greater molar relaxivity. R2* values between GM and WM were correlated to iron similarly, but demonstrated greater sensitivity with higher molar relaxivity in GM than WM (Table 5-6). These observations were similar in AD tissue, apart from R2 values also correlating to iron similarly between GM and WM, but still with greater sensitivity (Table 5-16). Altogether, these assessments show that R2 and R2* may show greater sensitivity for iron in GM than in WM, as had also been shown prior to this study using bulk assessment across multiple samples (House *et al.*, 2008, Langkammer *et al.*, 2010). R2' values however showed similar correlations and similar molar relaxivity to iron in both GM and WM tissue in both control and AD tissue, perhaps indicating that R2' is in fact a good measure of iron specifically,

irrespective of tissue types. However, the greater levels of noise in these particular maps have led to higher error and therefore correlation to iron to be worse overall.

Interestingly, a change in the regional correlations is detected between control and AD, whereby R2 values became better correlated, and with better molar relaxivity in AD WM tissue than in control WM. R2 became better correlated to iron content than R2* in AD WM tissue. GM regions were similar for both R2 and R2* correlations. This signifies again, that neurodegeneration seems to affect R2 and R2* correlation to iron, and more specifically within WM regions (see section 5.7.4).

Altogether, the results support iron shortening of T2 and T2* relaxation and therefore enhanced R2 and R2* values, by enhancing transverse relaxation of proton spins, as well as providing a source of magnetic field inhomogeneities. However, the degree of correlation and sensitivity of relaxometry values to iron seems to also depend substantially on the myelin content within the region (see section 5.7.4).

5.7.4. Myelin content assessment

Luxol fast blue staining of myelin content provides images demonstrating very similar cortical architecture as that observed in both elemental iron and MR images, for control and AD samples. Not only were the images qualitatively similar, but through quantitative assessment of the WM and GM tissue types in the control MTG samples, greater myelin was detected in WM than GM, as was also observed

for elemental iron content and R1, R2, R2* and R2' relaxometry measurements. Assessment of the cortical layers corresponding to the MCL and dGM also provide a consistent increase in myelin content within each sample, in the order of dGM < MCL < WM, similar to elemental iron and relaxometry values.

Myelin is produced by oligodendrocytes that create a sheath around long neuronal axons, speeding up axonal transduction of electrical stimuli across brain regions. Due to the high metabolic demand on oligodendrocytes for maintenance of these myelin sheaths, as well as the necessity of many of the enzymes involved in myelin production requiring iron cores, these cells have high iron content (Connor and Menzies, 1996, Todorich *et al.*, 2009). The data acquired here supports this concept in which WM regions hold significantly higher iron content than GM regions due to the presence of iron in myelin within WM. The finding that different cortical layers, such as layers IV and V (MCL) contain greater levels of both myelin and iron than dGM layers (van Duijn *et al.*, 2013) also substantiates the observations made in comparison to WM, whereby iron content was significantly higher in myelin rich regions.

Female samples demonstrated lower myelin contents than males in control post-mortem human MTG, however none of the tissue regions assessed were significantly different individually. This highlights that control populations may demonstrate altered levels of myelin by gender in aged populations and should be further explored. In AD tissue however, this difference between male and female samples did not exist. By comparing between control and AD tissue directly, lower myelin content in the WM regions of AD subjects was identified compared with

WM from controls. Separate evaluation of genders between control and AD demonstrated that male AD subjects had less myelin than male control samples, whilst myelin content in females was similar between control and AD. Given that myelin lipids and iron content can affect relaxivities in the same way (Rooney *et al.*, 2007), the findings demonstrating myelin loss in AD supports the results above (see section 5.7.2.2), in which R2 and R2* values in male AD WM were generally lower than male control WM. Therefore, a breakdown in myelin within WM regions detected using LFB staining may be driving subtle changes in R2 and R2* relaxometry values, especially in samples from male subjects, to provide the differences observed here. Furthermore, as iron content and myelin are strongly linked due to the presence of iron in oligodendrocytes, the breakdown of myelin in male AD WM may be driving the higher iron contents observed in female AD WM compared with male AD WM.

GM myelin was also decreased in male AD samples compared with male control samples, as observed for WM regions, whilst female samples remained similar between control and AD. The specific reason for lower GM myelin content detected in AD male samples in this study may be due to the global loss of myelin within tissue, therefore providing less myelin within the GM as well as in WM. In addition, greater neurodegeneration within AD tissue leads to greater axonal loss, which may provide less myelin staining in the GM. Furthermore, similar trends were detected between control and AD tissue relaxometry values, with a general lowering of GM values in male AD than male control, whilst providing similar female values, therefore supporting the findings observed with myelin content (Figure 5-41). The

extent and nature of myelin loss within GM requires further investigation beyond that performed in this study, especially given that PMI length also correlated with myelin loss within AD GM. This observation could be explained due to greater atrophy in these AD samples following death of the patient, however given that the main findings of myelin loss linked to relaxometry changes appeared in the WM, the overall conclusions can be retained.

A number of studies support our observation of myelin loss within the MTG of AD patients (Brun and Englund, 1986, Rose *et al.*, 2000, Bozzali *et al.*, 2002). *In vivo* diffusion based imaging studies have demonstrated WM loss in AD subjects and correlations to worsening cognition (Rose *et al.*, 2000, Bozzali *et al.*, 2002). Similarly, some of these changes in the temporal lobe have been identified even at the earliest stages of AD pathology (Huang *et al.*, 2007). Furthermore, post-mortem assessments have demonstrated WM loss in temporal lobe regions using LFB staining for myelin (Brun and Englund, 1986), and the loss of WM has been suggested to be due to vascular lining breakdown during AD (Scheltens *et al.*, 1995).

5.7.5. Correlation against myelin

In order to understand the effects of myelination on MRI-iron correlations to a greater degree, relaxometry values and iron contents were also correlated with myelin content spatially, using similarly placed 5x5 pixel ROIs across each sample image (see objectives section 5.2). The mean correlations of individual samples demonstrated that iron content and all relaxometry values were strongly correlated

to myelin in both control and AD tissue (Table 5-8 and Table 5-18). The correlation of iron with myelin is expected, due to the presence of iron in oligodendrocytes, and its requirement for myelin synthesis and maintenance (Connor *et al.*, 1990, Connor and Menzies, 1996, Todorich *et al.*, 2009). The correlation of relaxometry values to myelin has also been established previously, with studies demonstrating T1 correlation to myelin (Mottershead *et al.*, 2003). However, T1 correlation to myelin has been suggested to be indirect, and predominantly due to magnetisation transfer effects (Schmierer *et al.*, 2004). Furthermore, R1 was used as a surrogate for myelin content in an attempt to quantify iron and myelin from relaxometry maps of human cortical samples (Stuber *et al.*, 2014). More recently, methods using multi-echo T2 acquisition for evaluating the myelin water fraction specifically, have demonstrated strong correlations with myelin (Laule *et al.*, 2006).

Whilst the mean relaxometry and iron correlations to myelin in individual samples were high in controls, R2' demonstrated lower mean correlations to myelin, than R2, R2* and iron content did. The basis for this is, again, likely to be due to the greater noise in R2' calculation (see section 5.7.3.1). Interestingly, lower relaxometry and iron content correlations with myelin were observed in AD samples, compared with controls (see section 5.6.4.1), likely to be as a result of WM myelin breakdown in AD pathology.

The grouped correlations demonstrated that R2* was the most specific and sensitive measurement for myelin in both control and AD samples, and all relaxometry and iron correlations with myelin were similar between the two sample groups (Table 5-9 and Table 5-20, Figure 5-21 and Figure 5-39).

The measurements obtained within this work can, again, allow the provision for predicting R2* values or even iron content ($R2^*_{PRED}$ or $[Fe]_{PRED}$), with an understanding of myelin content, [Myelin], where,

$$R2^*_{PRED} \text{ or } [Fe]_{PRED} = C[Myelin] + D \qquad \text{(Eq.2)}$$

Using both GM and WM regions, the relationships provided are:

Control $R2^*_{PRED} = 0.340[Myelin] + 7.33$

AD $R2^*_{PRED} = 0.360[Myelin] + 7.71$

Control $[Fe]_{PRED} = 1.39[Myelin] – 6.73$

AD $[Fe]_{PRED} = 1.50[Myelin] + 2.64$

Given that relaxometry assessments are impacted by both iron and myelin contents, the equations described for iron (Eq.1) and myelin (Eq.2) can be combined to provide an overall relationship for R2 or R2* relaxometry signals (Eq.3) (House *et al.*, 2007, Stuber *et al.*, 2014). The new coefficients E and F can be obtained through multiple regression analysis:

$$R2_{PRED} \text{ or } R2^*_{PRED} = E[Fe] + F[Myelin] \qquad \text{(Eq.3)}$$

The relationship now described in Eq.3 could be used to determine the relaxometry signal when both iron and myelin content are known. Conversely, if an understanding of myelin content in a region is known, iron content could be evaluated following non-invasive R2 or R2* assessment and solving for [Fe].

R2* correlation to myelin is likely to be due to, in part, iron presence within myelin, as well as a direct effect of myelin lipids on both transverse relaxation and magnetic field inhomogeneities. Myelin was found to provide some residual contribution to R2* relaxometry following iron extraction from human cortical samples (Fukunaga *et al.*, 2010). More interestingly however, was that a difference in the spread of ROI values seems to be apparent between iron content and relaxometry value correlations with myelin in AD, compared with control samples (Figure 5-47). The control samples' relaxometry and iron correlations to myelin seem to be driven by two clusters, due to clear separation between WM and GM ROI values. The AD samples' relaxometry and iron correlations to myelin demonstrate greater spreading of ROI values, predominantly from within the WM. This is likely due to the myelin loss detected in WM as part of the AD pathology in these MTG samples (see section 5.7.4) causing partial volume effects in the tissue therefore providing a greater spread of ROI values. Indeed, assessment of AD WM-specific ROI values demonstrated enhanced R2 correlation to myelin compared with control WM ROI values, indicating that correlation depends mostly on tissue type in control samples, with very little variation within tissue types (see section 5.4.6.4). It should be noted however that region-specific correlations with myelin were still substantially lower than inclusion of both GM and WM ROI values.

5.7.6. Conclusion

Quantitative R1, R2, R2* and R2' relaxometry was successfully performed on control and AD MTG and correlated against SR-XRF elemental iron mapping (see

section 5.2). This allowed quantified iron contents to be compared against relaxometry values, to support the validation of iron detection using MRI relaxometry. One of the main advantages with acquisition of SR-XRF elemental iron maps, was the potential to spatially correlate iron content with relaxometry measurements, and to investigate the correlations within tissue types for better understanding of the sensitivity of MRI relaxometry for iron (see section 5.2).

WM tissue was found to consistently contain higher iron contents, with concomitantly higher relaxivity values in both control and AD samples. Similar relaxivities and iron contents were detected between control and AD samples, however a breakdown in myelin content was observed specifically in male AD samples compared with male control samples. This breakdown in WM myelin content provided an impact on the correlations of both relaxometry measurements with iron content, and on the correlations of relaxometry and iron contents with myelin. Therefore, whilst iron was clearly identified as providing substantial impact on relaxometry values through its effects on transverse relaxation and in generating magnetic field inhomogeneities, relaxometry values were also substantially affected by myelin content. Given that iron content demonstrates strong links with myelin content, the impact of myelination on iron-MRI correlations was evaluated further (see section 5.2) and showed that differences exist in relaxometry correlations between control and AD tissues. However, greater research is required to fully understand the effects of myelination on iron-detection using relaxometry, especially, in the cases of neurodegeneration, which may show altered correlations compared with control tissue.

6. Results: Direct Injection of Iron in the Mouse Hippocampus

6.1. Introduction

Iron was injected directly into the mouse hippocampus to provide a direct *in vivo*/ *ex vivo* model of iron accumulation. This approach allowed the assessment of non-invasive R1, R2, R2* and R2' relaxometry measurement for iron content detection and quantification, and to determine the direct toxicological effects of iron accumulation in the brain without interfering, detrimental, biological effects, commonly associated by using transgenic models of neurodegeneration.

Initially, pilot studies were performed in order to:

- Minimise harm and distress due to the direct injection of ferric citrate into the brain.
- Assess the ability to serially measure ME R2 and MGE R2* relaxometry values *in vivo*.
- To provide brain tissue sections for validating histological staining methods, prior to main study.

Following the pilot work, a full study was performed with the objectives outlined in section 6.3.

6.2. Pilot Work

6.2.1. Methods

Two mice were injected bilaterally with 0.5 µl of 2 mM ferric citrate prior to the main study, to validate the injection procedures and recovery for the main study animals. These mice were assessed serially using *in vivo* ME R2 and MGE R2* relaxometry on days 3, 5, 9 and 17, post-surgery, followed by perfusion fixation at day 17. Their brains were also scanned *ex vivo* using SE R1, SE R2 and GE R2* measurement (see section 3.2.3.4) and were subsequently sectioned for validation of ferritin and iba-1 immunohistochemistry, and neuronal histological staining.

6.2.2. Results

6.2.2.1. Toxic effects from direct injection of ferric citrate

Direct injection of 2 mM ferric citrate into the hippocampus was well tolerated by the two pilot mice. Mild seizures were observed immediately upon recovery from anaesthesia for both animals, however no future signs of distress, barbering or weight loss were observed within the period of assessment. During longitudinal scanning, one animal had a further minor seizure following recovery from anaesthesia at day 3, however no future seizures were observed either during, or outside scanning periods for both mice.

6.2.2.2. Serial in vivo ME R2 and MGE R2 measurement*

ME R2 relaxometry (Figure 6-1A-D) demonstrated substantially lower R2 values within the hippocampus at day 3 (Figure 6-1A) compared with the surrounding brain tissue. These lower R2 values continue to be observed at day 5 (Figure 6-1B), although at less of a difference to the surrounding tissue than at day 3. The hippocampal regions show consistent R2 values at day 9 (Figure 6-1C), as would be expected in normal mouse brain tissue with no change in R2 values in the region, which continues up to day 17 (Figure 6-1D). The corresponding *ex vivo* ME R2 map is shown adjacent to the *in vivo* images (Figure 6-1E). This image potentially highlights iron-rich areas in the hippocampus, due to the higher R2 values observed, compared with any *in vivo* R2 maps (Figure 6-1A-D, arrows).

MGE R2* relaxometry maps were heavily affected by image artefacts *in vivo* at days 3, 5 and 9 (Figure 6-1F-G), however potential iron containing regions or needle tracts can be observed *in vivo* at day 17 (Figure 6-1I, arrows), which correspond similarly in location to higher R2* values in the *ex vivo* image (Figure 6-1J, arrows).

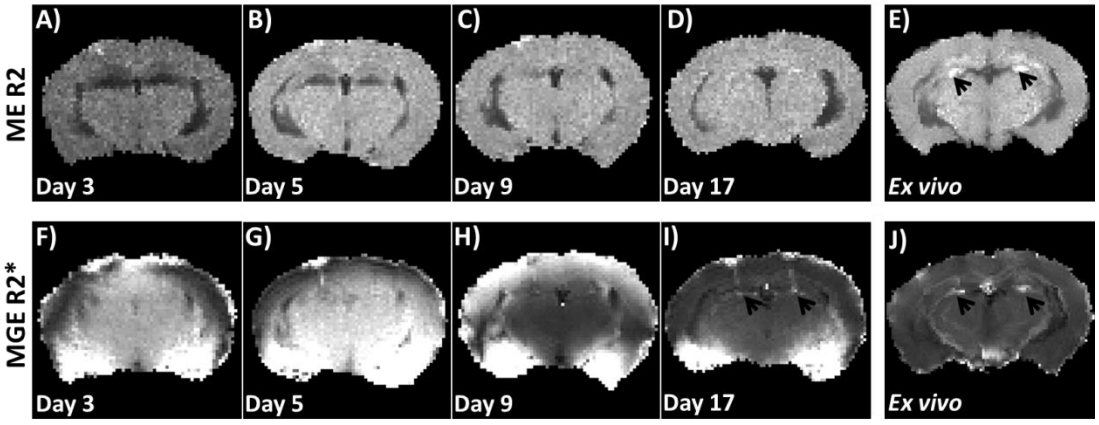

Figure 6-1 Serial ME R2 and MGE R2* assessment of mice in vivo following injection with ferric citrate into the hippocampus

Representative brain images showing (A-D) serial in vivo ME R2 hippocampal maps at days 3, 5, 9 and 17 post surgery, and (E) the corresponding image ex vivo, for a pilot 2mM ferric iron injected animal prior to the main study. (F-I) Serial in vivo MGE R2 maps at days 3, 5, 9 and 17 post surgery, and (J) the corresponding image ex vivo of the same animal brain. Arrows denote potential iron-rich areas.*

6.2.2.3. Summary of pilot work

From this pilot work, it was found that the injection of ferric citrate bilaterally into the mouse hippocampus was feasible and well tolerated, without causing major distress or suffering to animals. Furthermore, it was found that *in vivo* ME R2 values seem to decrease in the hippocampus following injection and return to normal by day 9. MGE R2* maps were heavily artefacted making *in vivo* R2* assessment difficult. Both ME R2 and MGE R2* *ex vivo* maps demonstrate areas of higher relaxivity values in the hippocampus, marking potential iron-rich areas compared with *in vivo* maps.

6.3. Objectives

The objectives for the main study of the mouse work were:

- To quantify and correlate *in vivo* ME R2 and MGE R2*, and *ex vivo* SE R1, SE R2, GE R2* and R2' values to the spatial distribution of iron content,

assessed using SR-XRF elemental mapping, in an animal model of iron overload.

- To evaluate the direct role iron plays on neurodegeneration and neuroinflammation using histological and behavioural assessments.

6.4. Methods

The methods for this work can be found in section 3.2.3. Mice were injected bilaterally into the hippocampus with 0.5 µl ferric citrate at 2 mM or 4 mM (n = 6/ group). Sodium citrate injections were used for controls (n = 6) (see section 3.2.3.2). Following injection, mice were left for 7 days to recover before performing a behaviour assessment (fear conditioning) from day 7. *In vivo* ME R2 and MGE R2* relaxometry assessments were performed at 10 days post-surgery, prior to perfusion fixation (see section 3.2.3.4) and brain excision (Figure 6-2). After 7 further days of fixation, brains were also scanned *ex vivo* to assess SE R1, SE R2, GE R2* and R2' in the hippocampus. ME R2 and MGE R2* were also evaluated for comparison with *in vivo* assessments. Brains were cryosectioned and SR-XRF elemental iron mapping was performed at slices corresponding to the hippocampus from T2W images, for comparison to MR relaxometry maps. Histological assessment of ferritin and iba-1, as well as haematoxylin and Nissl staining for neurons, was performed to evaluate the direct effects of iron accumulation on neuronal death and neuroinflammation (see section 3.2.3.5).

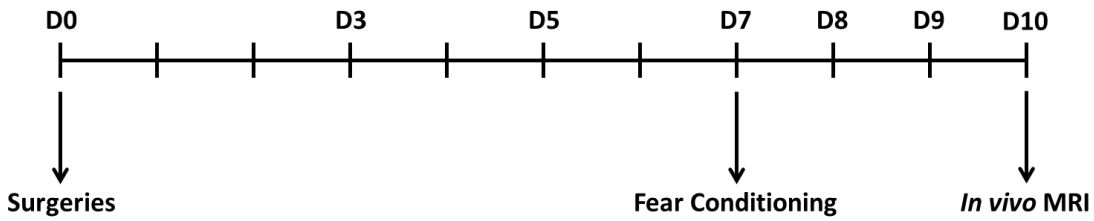

Figure 6-2 Outline of animal study over the 10 day period

6.5. Results

6.5.1. Animal health

Following surgeries, mice injected with iron frequently displayed minor seizures within the first 60 minutes post recovery from anaesthesia, whilst it was observed that control animals did not. No animals displayed any future seizures, signs of distress, barbering or weight loss within the 10 day experimental period. Furthermore, no significant differences were detected between animal body weights between the three treatment groups; control, 2mM or 4mM iron injections (Figure 6-3).

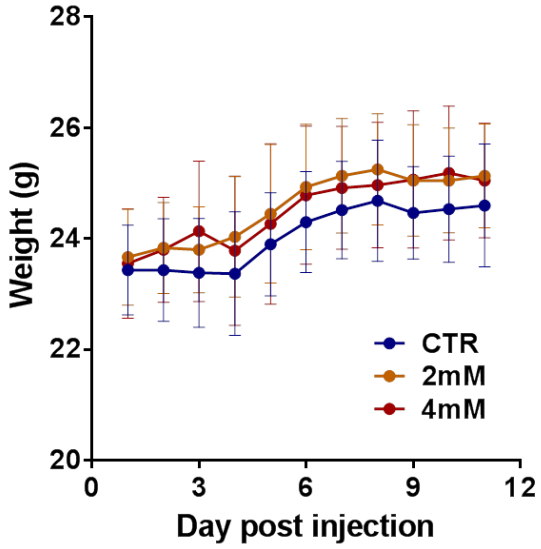

Figure 6-3 Mean body weights throughout the experiment period for each injection group

Graph showing the mean body weights during the 10 day experimental period for control (CTR, blue), 2 mM ferric iron (orange) and 4 mM ferric iron (red) intra-hippocampal injected mice. Significance assessed using two-way ANOVA for group differences to $P \leq 0.05$. Graphs show mean values ± SD.

6.5.2. Comparison of relaxometry and iron contents with ferric citrate injection into the mouse hippocampus

6.5.2.1. In vivo MRI relaxometry

Hippocampal ROIs were manually drawn over the first three imaging slices containing the hippocampus, to specifically match the three sections that were acquired using SR-XRF elemental mapping from each animal. ROIs were drawn on T2-weighted images of each brain, and overlaid onto R1, R2, R2* and R2'

relaxometry maps. Hippocampal *in vivo* ME R2 and MGE R2* values were similar between control and iron injected mice 10 days post-surgery (R2, P = 0.095 and R2*, P = 0.869) (Figure 6-4A-B and Figure 6-5). Mean MGE R2* values between animals were extremely varied, as can be seen from the size of error bars (Figure 6-4B), likely due to large susceptibility artefacts clearly observable within and between the MGE R2* maps themselves (arrows and arrowheads, Figure 6-5C-D). Susceptibility effects around the entorhinal cortex are expected due to presence of the nasal cavities nearby (arrowheads, Figure 6-5C-D), however differences in striatal and hippocampal basal values were detected in some animals, with higher pixel intensities across one brain than in another (arrows, Figure 6-5C-D). Therefore, maps with considerably higher basal striatal and hippocampal R2* values, with clear susceptibility artefacts were excluded from analysis (control n = 3, 2 mM n = 3 and 4 mM n = 5, remaining) (Figure 6-4C). Substantially less error in R2* assessment was observed, however R2* values were still similar between the control and iron injected mice (P = 0.165) (Figure 6-4C).

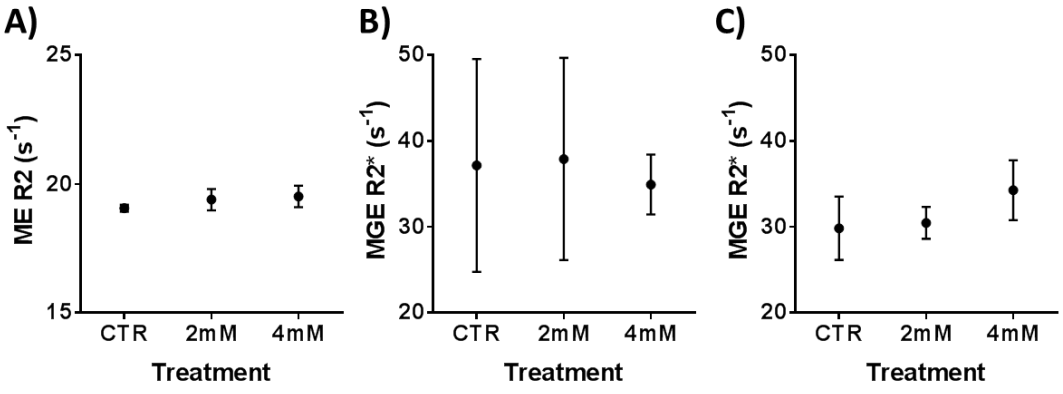

Figure 6-4 Mean in vivo ME R2 and MGE R2* values in the hippocampus of ferric citrate injected mice compared with controls

Graphs showing in vivo hippocampal (A) ME R2 and (B) MGE R2 values from the hippocampi of mice measured at 10 days post injection. (C) Graph showing mean MGE R2* values excluding mice with substantial image artefacts (control, n = 3; 2 mM, n = 3 and 4 mM, n = 5). Significance assessed using one-way ANOVA, with Tukey's test for multiple comparisons to P ≤ 0.05. Graphs show mean values ± SD.*

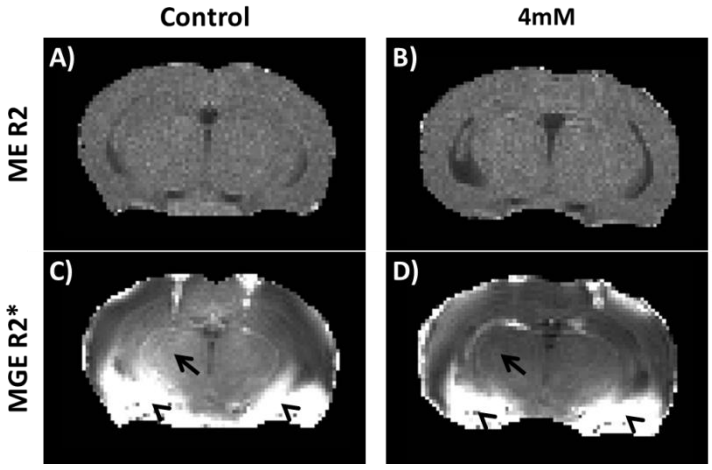

Figure 6-5 Representative in vivo ME R2 and MGE R2* maps of a ferric citrate injected animal

Representative in vivo images of a (A-B) ME R2 map and (C-D) MGE R2 map for a control and 4 mM injected mouse. Arrows highlight areas of different basal striatal and hippocampal R2* values between different brains; arrowheads highlight areas of susceptibility artefacts.*

6.5.2.2. Ex vivo MRI relaxometry

Standard, spin-echo (SE) R1 and R2, as well as gradient-echo (GE) R2* relaxometry assessments were performed on the mouse brains *ex vivo*. Furthermore, ME R2 and MGE R2* assessments were also performed of *ex vivo* tissue for comparison against *in vivo* measurements. R2' values were calculated by subtracting SE R2 maps from GE R2* maps.

Regions of higher SE R1, SE R2, GE R2* and R2' values were observed predominantly within the hippocampus of iron injected mice, compared with control mice across three MR slices (Figure 6-6). Higher values were also found outside the hippocampal regions, within the cortex (Figure 6-6C). Two mice injected with iron (one at 2 mM and one at 4 mM) were found not to contain bilateral lesions by relaxometry mapping, and were therefore excluded from further analyses to avoid bias.

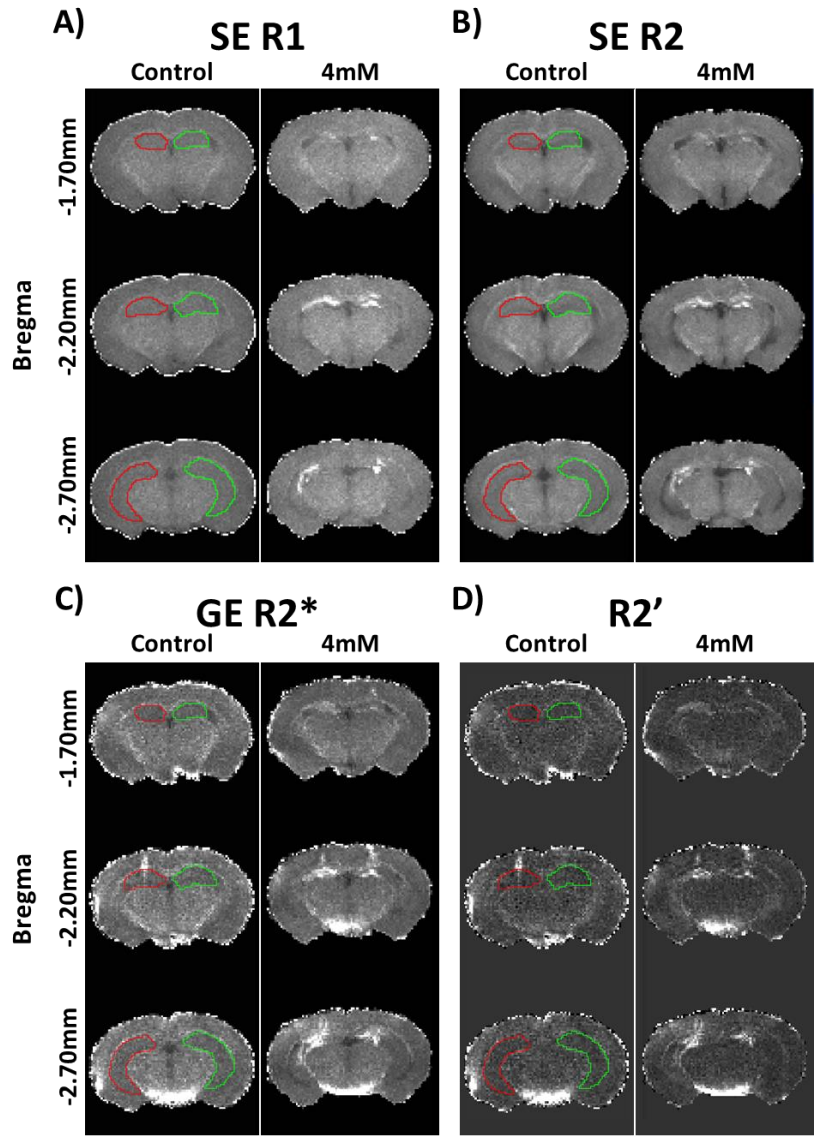

Figure 6-6 Ex vivo SE R1, SE R2, GE R2* and R2' images of the hippocampi from one control and one 4 mM ferric citrate injected mouse

Representative images demonstrating (A) SE R1, (B) SE R2, (C) GE R2 and (D) R2' relaxivity maps of a control and 4 mM injected mouse brain. Red and green ROIs represent left and right hippocampal regions from the control mouse brain. The hippocampal ROIs have been omitted from the 4 mM mouse brain so that the hyper-intense regions can be clearly observed within the hippocampus.*

ROIs were drawn around the hippocampus in the three slices that also corresponded to the sections that underwent SR-XRF (Figure 6-6; see section 6.5.2.3), for measurement of mean relaxivities and volumes of the hippocampus (Figure 6-7; Table 6-1). These ROIs were drawn on T2-weighted images of each brain, and overlaid onto R1, R2, R2* and R2' relaxometry maps. Standard SE R1 and SE R2 values were significantly higher between control and treated animals (SE R1: control = 0.66 ± 0.05 s^{-1}; 2 mM = 0.75 ± 0.05 s^{-1}; 4 mM = 0.80 ± 0.04 s^{-1}; P = 0.001, and SE R2: control = 24.60 ± 0.74 s^{-1}; 2 mM = 28.35 ± 2.00 s^{-1}; 4 mM = 29.74 ± 0.80 s^{-1}; P < 0.0001). No difference however, was observed between the 2 mM and 4 mM treatment groups by SE R1 and SE R2 (R1, P = 0.299 and R2, P = 0.235) following correction for multiple comparisons (Figure 6-7A-B). ME R2 values were also significantly different between control (19.98 ± 0.59 s^{-1}), 2 mM (21.37 ± 1.49 s^{-1}) and 4 mM (22.58 ± 0.90 s^{-1}; P = 0.004), however only the 4 mM injection showed significantly higher relaxivity values than control (P = 0.003; Figure 6-7C). Both, GE and MGE R2* relaxometry values led to significantly higher R2* in the iron injected mice hippocampi, compared with controls (GE R2*: control = 30.24 ± 1.96 s^{-1}; 2 mM = 37.44 ± 2.77 s^{-1}; 4 mM = 40.77 ± 2.02 s^{-1}; P < 0.0001, and MGE R2*: control = 27.26 ± 1.14 s^{-1}; 2 mM = 34.47 ± 3.41 s^{-1}; 4 mM = 39.91 ± 2.82 s^{-1}; P < 0.0001; Figure 6-7D-E). The MGE R2* acquisition method was able to distinguish between the 2 mM and 4 mM injections (P = 0.013), as well as comparison to control injections, whilst GE R2* was not able to distinguish between the two ferric citrate concentrations (P = 0.086; Figure 6-7D-E). Finally, R2' relaxivity assessment showed significantly higher values within the hippocampus of both the 2mM and 4mM injection groups compared to control (R2': control = 5.63 ± 1.28 s^{-1}; 2 mM = 9.08 ±

1.44 s^{-1}; 4 mM = 11.02 ± 1.59 s^{-1}; P < 0.0001), however again, the 2 mM and 4 mM iron injections were not significantly different to each other (P = 0.119).

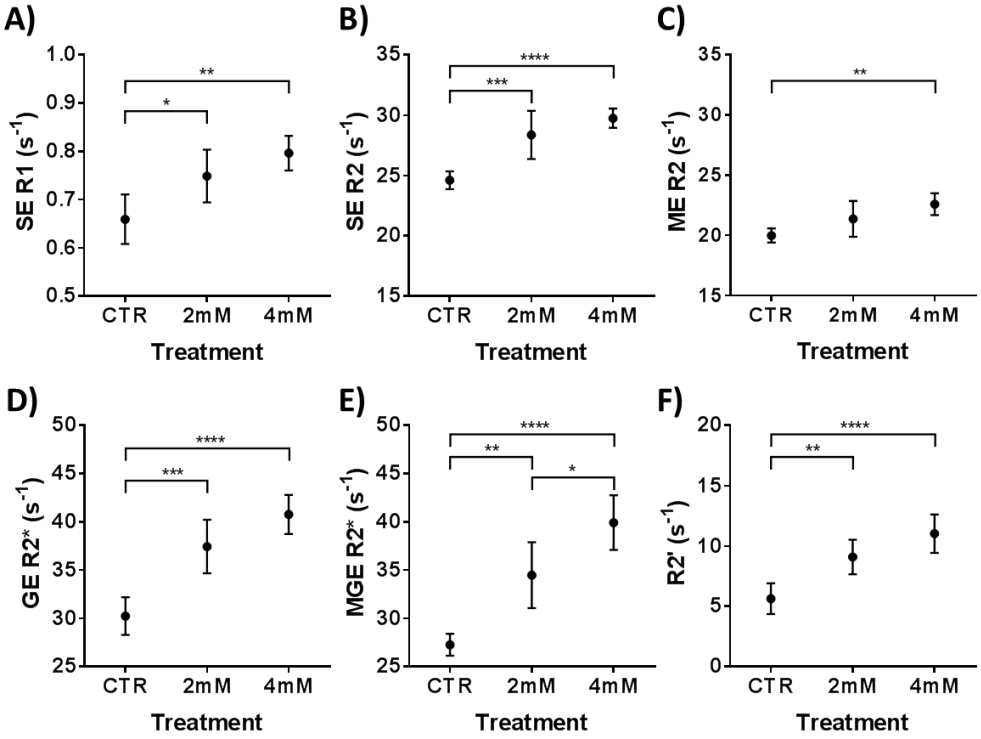

Figure 6-7 Mean ex vivo relaxometry values in the hippocampus of control, 2 mM and 4 mM ferric citrate injected mice

Graphs of the mean (A) SE R1, (B) SE R2, (C) ME R2, (D) GE R2, (E) MGE R2* and (F) R2' relaxivity values obtained in the whole hippocampal regions from each injection treatment. Graphs show mean values ± SD, with significance obtained using one-way ANOVA and Tukey's multiple comparisons correction to P ≤ 0.05 (*).*

To assess the iron accumulation lesions from the two iron injection treatment groups, ROIs were drawn around areas in the hippocampus with higher GE R2* values than a threshold value, based on control treated animals hippocampi (Figure

6-8). The lesioned areas showed similar SE R1, SE R2, GE R2* and R2' relaxometry measurements between the 2 mM and 4 mM injections (R1, P = 0.714; R2, P = 0.089; R2*, P = 0.828, and R2', P = 0.564; Figure 6-9).

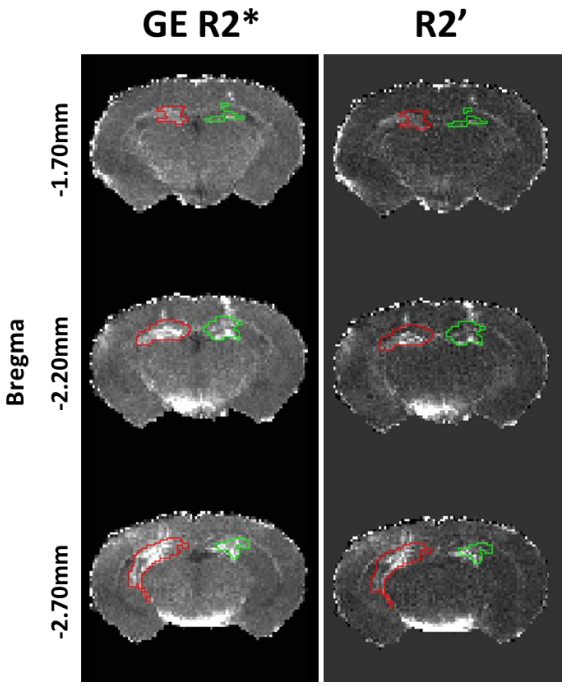

Figure 6-8 Example ROIs manually drawn around the iron lesion in the hippocampus from a 4 mM ferric citrate injected mouse, using GE R2* and R2'

Representative GE R2 and R2' images of a 4 mM iron injected brain, highlighting lesion ROIs based on hyper-intense pixels above that of control brains, within the hippocampus.*

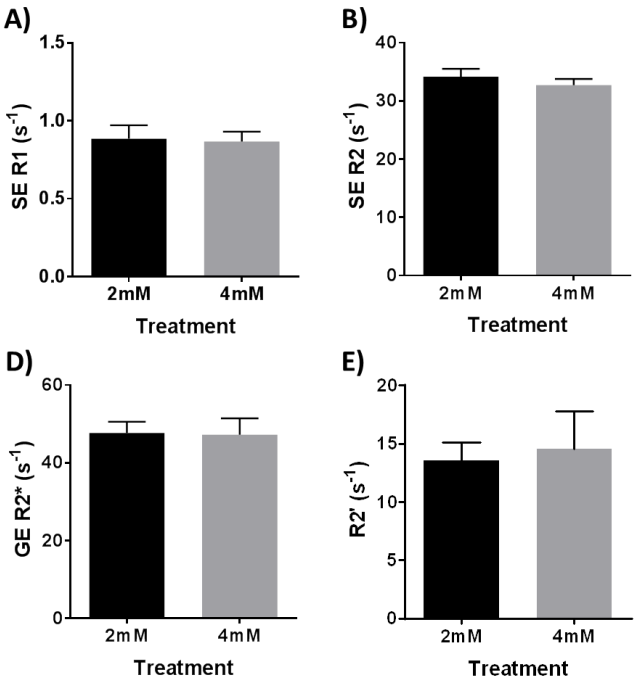

Figure 6-9 Mean relaxometry values in the iron lesion of 2 mM and 4 mM ferric citrate injected mice

Graphs showing the (A) SE R1, (B) SE R2, (C) GE R2 and (D) R2' relaxivity values within the iron accumulation lesions in the hippocampi of only iron injected mice, with significance assessed using unpaired t-test to $P \leq 0.05$.*

6.5.2.3. XRF elemental mapping

Qualitatively, SR-XRF elemental iron maps showed regions of higher intensities, predominantly within the hippocampus of iron injected mice, indicating higher iron contents, compared with control mice across three slices corresponding to MR (Figure 6-10). As highlighted in some relaxometry maps (Figure 6-6), regions of increased iron content were also found outside the hippocampal regions, within the cortex (Figure 6-10B).

Significantly higher iron levels were observed in the hippocampus in iron injected animals compared to controls (control = 14.22 ± 1.18 ppm, 2 mM = 30.50 ± 5.36 ppm, 4 mM = 44.58 ± 7.74 ppm, P = 0.002) and significant differences were detected between all three treatment groups to each other (CTR to 2 mM, P = 0.025; CTR to 4 mM, P = 0.001 and 2 mM to 4 mM, P = 0.045; Figure 6-11A, Table 6-1). Hippocampal iron lesions were also measured, showing similar iron contents in both the 2 mM and 4 mM treatments (2 mM = 63.18 ± 4.70 ppm and 4 mM = 73.78 ± 7.07 ppm, P = 0.097) (Figure 6-11B).

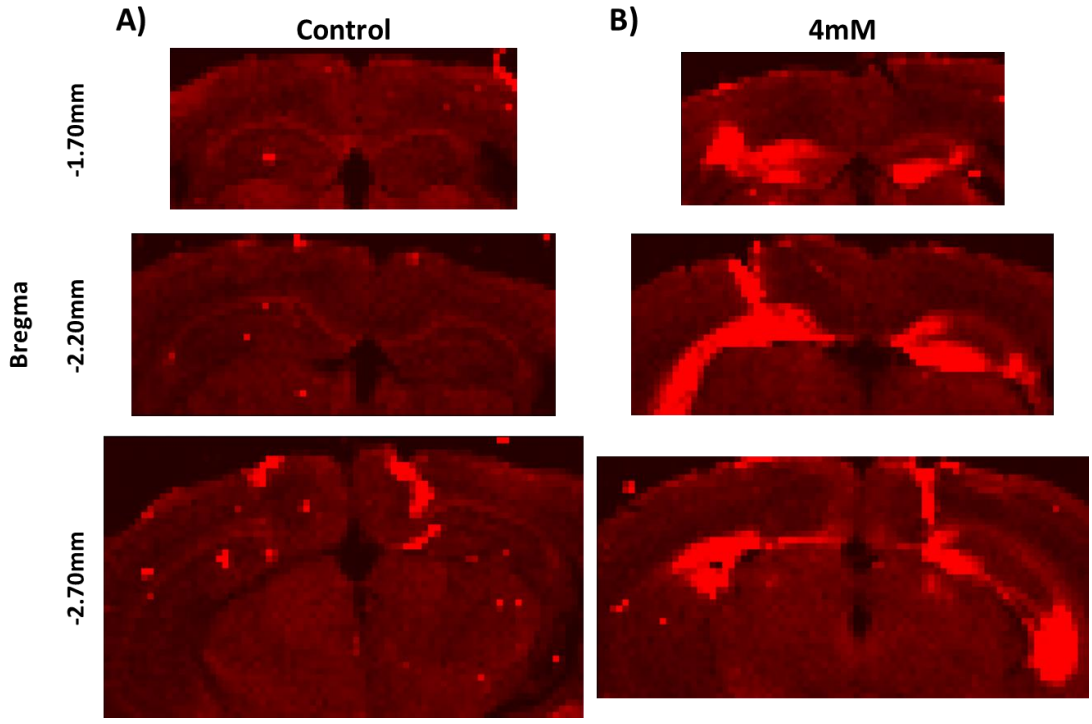

Figure 6-10 SR-XRF elemental iron maps of the hippocampi from one control and one 4 mM ferric citrate injected mouse

Representative elemental iron maps of (A) one control and (B) one 4 mM ferric citrate injected brain, at corresponding bregma positions (left hand side) as relaxivity maps.

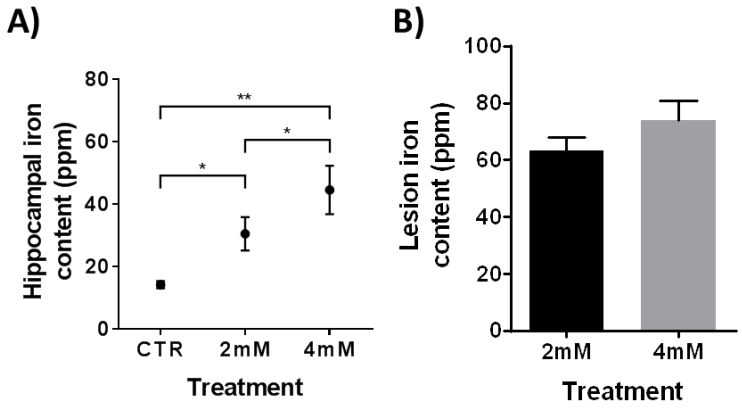

Figure 6-11 Mean elemental iron contents in the hippocampus of control, 2 mM and 4 mM ferric citrate injected mice, and in the iron lesion of 2 mM and 4 mM injected mice

Graphs of (A) the mean iron content obtained in the hippocampus from each injection treatment, with significance obtained using one-way ANOVA and Tukey's multiple comparisons correction to $P \leq 0.05$ (*), and (B) the mean iron content observed within the iron lesions of the hippocampi of only ferric citrate injected mice, with significance assessed using unpaired t-test to $P \leq 0.05$. Graphs show mean values ± SD.

Table 6-1 Summary of the iron content and relaxivities from the hippocampus of each treatment group

	Iron	SE R1	SE R2	ME R2	GE R2*	MGE R2*	R2'
CTR	14.22 ± 1.18	0.66 ± 0.05	24.60 ± 0.74	19.98 ± 0.59	30.24 ± 1.96	27.26 ± 1.14	5.63 ± 1.28
2 mM	30.50 ± 5.36 [a]	0.75 ± 0.05 [a]	28.35 ± 2.00 [a]	21.37 ± 1.49	37.44 ± 2.77 [a]	34.47 ± 3.41 [a]	9.08 ± 1.44 [a]
4 mM	44.58 ± 7.74 [a,b]	0.80 ± 0.04 [a]	29.74 ± 0.80 [a]	22.58 ± 0.90 [a]	40.77 ± 2.02 [a]	39.91 ± 2.82 [a,b]	11.02 ± 1.59 [a]
P-value	0.0002	0.001	< 0.0001	0.004	< 0.0001	< 0.0001	< 0.0001

For relaxivities, n = 6, 5 and 5 per group, for control, 2 mM and 4 mM injections respectively. For iron contents, n = 3 per group. Significance obtained using one-way ANOVA, with Tukey's multiple comparisons correction to $P \leq 0.05$. [a] denotes significance compared with controls, and [b] denotes significance compared with 2 mM.

6.5.2.4. Iron lesion volume assessment

Whole hippocampal ROIs had similar volumes across the three treatment groups (control = 15.36 ± 1.70 pixels, 2 mM = 14.29 ± 1.78 pixels and 4 mM = 14.79 ± 2.25 pixels, P = 0.658; Figure 6-12A). The iron lesion volumes, delineated using GE R2* maps, were significantly higher in the 4 mM, compared to the 2 mM, treatment groups (2 mM = 5.48 ± 2.83 pixels and 4 mM = 9.08 ± 1.07 pixels, P = 0.029; Figure 6-12B). Similarly, the iron lesion volumes delineated from the elemental iron maps were also significantly higher in the 4 mM compared with the 2 mM treatment groups (2 mM = 398.70 ± 50.46 pixels and 4 mM = 588.70 ± 83.94 pixels, P = 0.028; Figure 6-12C).

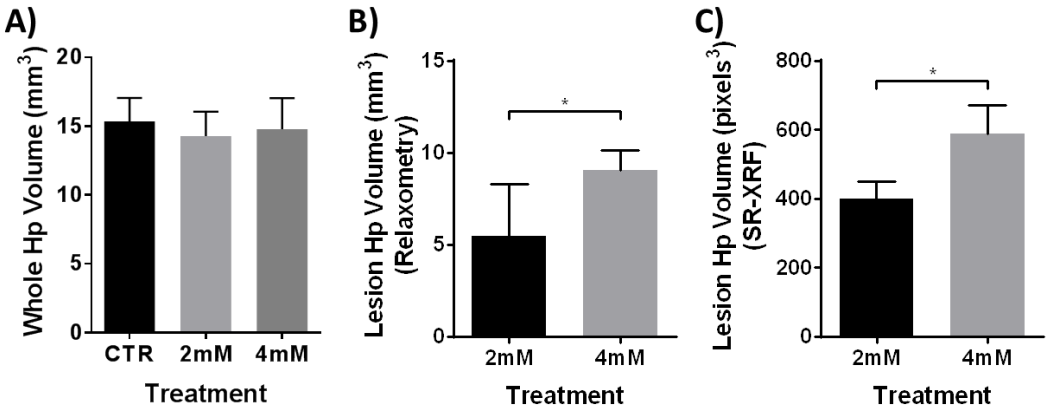

Figure 6-12 Lesion volumes in the hippocampus delineated using relaxometry and elemental iron maps

Graphs showing (A) mean whole hippocampal volumes obtained by T2W images, and mean hippocampal iron lesion volumes assessed (B) from GE R2 maps and (C) from elemental iron maps.*

Total iron content in the iron lesion was calculated by: lesion mean x lesion volume. The same calculation was also performed for each relaxometry measurement (Table 6-2) for assessment of how well each measurement is able to detect total iron content. A 1.74-fold increase in total iron content is measured using XRF mapping of the three slices of hippocampus, between the 2 mM and 4 mM injected brains (Table 6-2). Using relaxometry assessments, R2' was closest to total iron content, at 1.79-fold increase between the 2 mM to 4 mM injected brains. SE R1 (1.65-fold), SE R2 (1.59-fold) and GE R2* (1.65-fold) also detect total iron content similarly with XRF mapping (Table 6-2).

Table 6-2 Total iron content and relaxivities in the iron lesions between the 2mM and 4mM ferric citrate injection groups

	Iron (pixels^3 ppm)	SE R1 (mm^3 s^{-1})	SE R2 (mm^3 s^{-1})	GE R2* (mm^3 s^{-1})	R2' (mm^3 s^{-1})
2 mM	25140 ± 3060	4.75 ± 2.13	186.13 ± 91.17	259.21 ± 124.24	73.08 ± 33.55
4 mM	43800 ± 9880	7.84 ± 0.82	296.44 ± 30.48	427.44 ± 51.68	131.00 ± 30.12
Fold change	1.74	1.65	1.59	1.65	1.79
P value	0.0002	0.017	0.033	0.023	0.021

Values are mean ± SD. Significance assessed using unpaired t-test, to $P \leq 0.05$.

6.5.2.5. Summary and discussion of relaxometry and iron contents in ferric citrate injected into the mouse hippocampus

Ferric citrate injections into the hippocampus were well tolerated in the main study, with no signs of long-term distress or suffering, and no weight loss in any of the groups throughout the experiment. *In vivo* ME R2 and MGE R2* relaxometry assessment demonstrated no significant differences between the hippocampus of each treatment group and MGE R2* maps were heavily affected with susceptibility artefacts, adding to error using this measurement. *Ex vivo* SE R1, SE R2, GE R2* and R2' relaxometry all detected differences between the ferric citrate treated and control hippocampus, however could not differentiate between the 2 mM and 4 mM ferric citrate injections. ME R2 measurement demonstrated less clarity between the treatment groups, only differentiating between the 4 mM ferric citrate injection and control hippocampi, whilst the MGE R2* measurement demonstrated comparable detection capability to the elemental iron maps, distinguishing between all three treatment groups in this study.

The SE R1, SE R2, GE R2* and R2' values were similar in the iron lesions between the 2 mM and 4 mM ferric citrate injections, as were the elemental iron contents. The iron lesion volumes however, were significantly larger with the 4 mM than with the 2 mM ferric citrate injections, and demonstrated a near doubling in measured total iron content between these two treatment groups. This was comparably detected using the four relaxometry assessments.

6.5.3. Correlation of hippocampal iron and relaxometry measurements

Qualitatively, areas of high iron content corresponded to areas of higher SE R1, SE R2, GE R2* and R2' values in *ex vivo* samples (Figure 6-13). The precise position of iron lesions also corresponded to relaxivity maps at each of the three bregma distances evaluated within the brain. The arrows highlight areas where iron is detected within all the relaxometry maps compared to the elemental iron maps (Figure 6-13). In some cases however, iron-rich regions identified in elemental iron maps were only observed in R2* and R2' maps, but not in R1 or R2 maps (Figure 6-13, arrowheads), such as those found within the cortex.

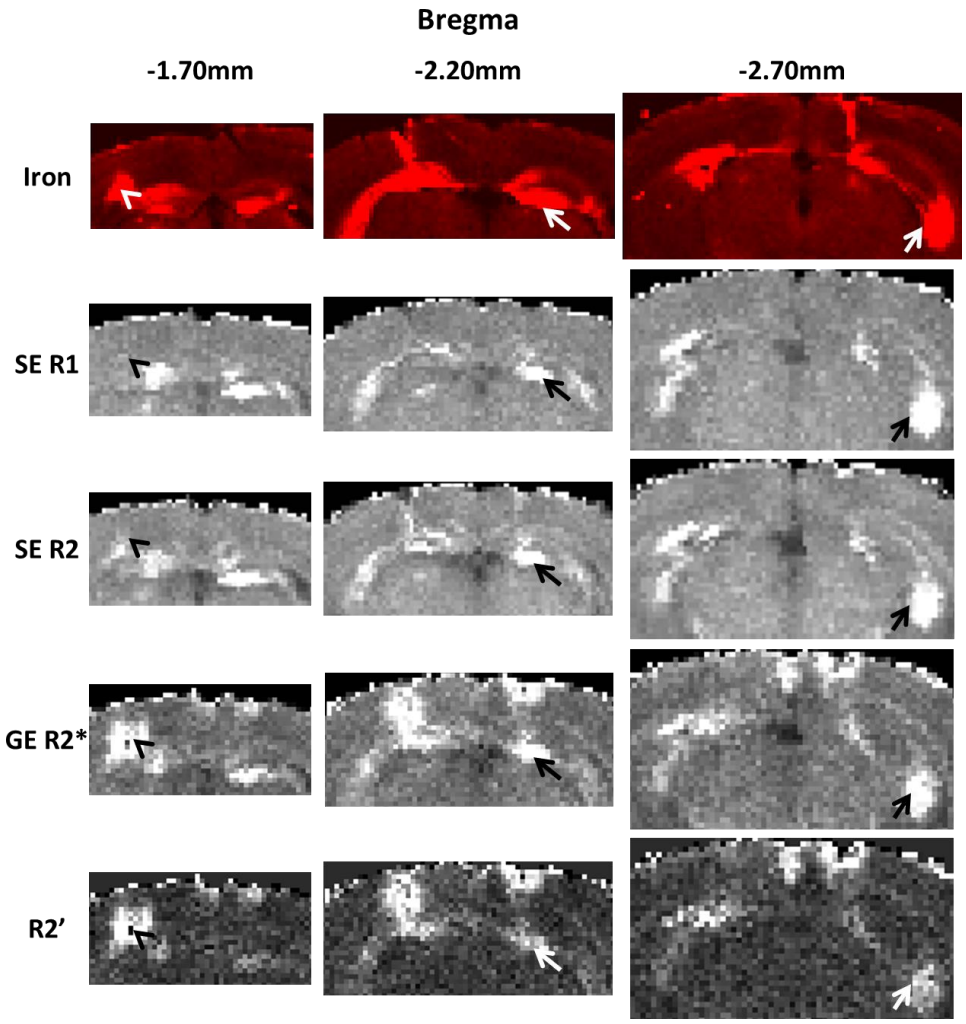

Figure 6-13 Correlation of elemental iron maps against relaxometry maps from the mouse hippocampus

Representative images of the three slices from elemental iron maps, co-registered with the corresponding brain and slice of SE R1, SE R2, GE R2 and R2' relaxometry maps. Arrows highlight iron lesions that are observable in all four relaxivity maps, whilst arrowheads denote iron rich regions that are only picked up using certain MR relaxometry methods.*

A significant correlation was detected between all four relaxometry measurements and the mean iron contents using all of the whole hippocampal ROIs, with R2' showing strongest correlation to iron levels (SE R1, r^2 = 0.33; SE R2, r^2 = 0.33; GE R2*, r^2 = 0.58 and R2', r^2 = 0.61; all correlations, P < 0.001) (Figure 6-14). R1 and R2 correlations to iron content were similar to each other (P = 0.985), however both R1 and R2 correlations to iron were less than R2* correlation to iron (R2* compared with R1, P = 0.011 and R2* compared with R2, P = 0.001) or to R2' correlation to iron (R2' compared to R1, P = 0.017 and R2' compared to R2, P = 0.100). R2* and R2' values were similarly correlated against iron content (P = 0.456). Correlation gradients (or molar relaxivity) of R1, R2, R2* and R2' values to iron were, r_1 = 0.003 $s^{-1}ppm^{-1}$, r_2 = 0.086 $s^{-1}ppm^{-1}$, r_2* = 0.253 $s^{-1}ppm^{-1}$ and r_2' = 0.168 $s^{-1}ppm^{-1}$.

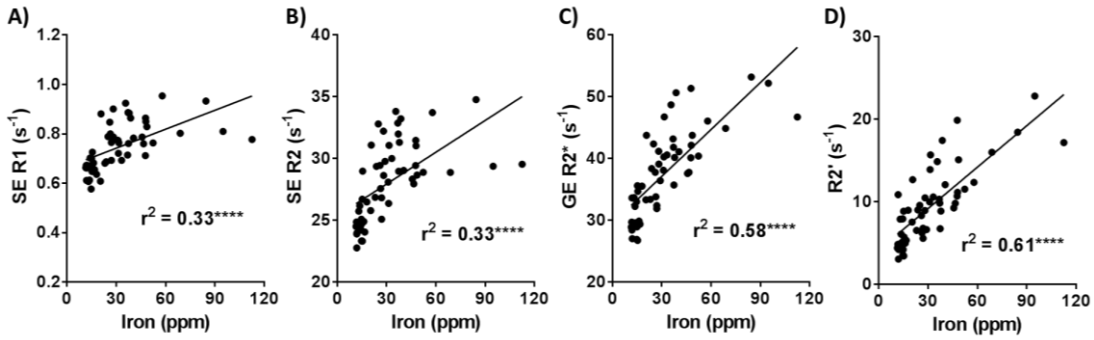

Figure 6-14 Correlation of hippocampal ROIs from elemental iron maps against each relaxometry measurements

Graphs showing the correlation of whole hippocampal ROIs between mean (A) SE R1, (B) SE R2, (C) GE R2 and (D) R2' relaxivities, and mean iron content. Correlation assessed using Pearson correlation with significance at P ≤ 0.05.*

6.5.3.1. Summary of correlation of hippocampal iron and relaxometry measurements

In general, high elemental iron contents corresponded to regions of high relaxometry values within the hippocampus, using SE R1, SE R2, GE R2* and R2' assessment. Some regions of high iron content outside the hippocampus were only detectable using R2* and R2' relaxometry, highlighting that these measurements seem to be enhanced at iron-specific detection. Correlation of all relaxometry to elemental iron hippocampi values demonstrates that GE R2* and R2' were superior to SE R1 and SE R2 at iron detection within the mouse hippocampus.

6.5.4. Behaviour assessment

Mice learnt the contextual fear memory test equally across the three treatment groups, with no significant differences between control, 2 mM or 4 mM injections affecting learning (P = 0.594; Figure 6-15A). Contextual memory assessment of mice 7 days post-surgery provided no significant differences between the three groups (control = 72.11 ± 13.01 %, 2 mM = 60.24 ± 11.27 % and 4 mM = 56.43 ± 21.30 %, P = 0.252; Figure 6-15B).

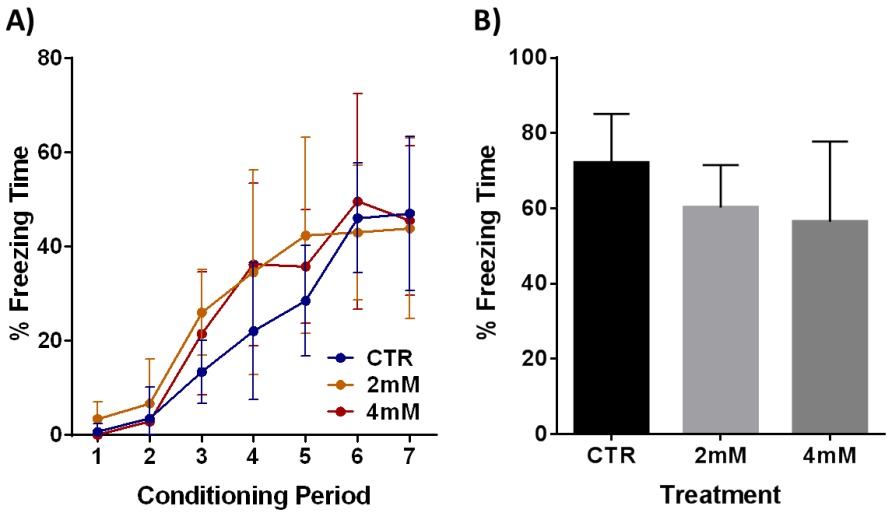

Figure 6-15 Effects of ferric citrate injection on contextual memory fear conditioning behaviour

Graphs showing the behavioural assessment of mice injected with ferric iron, with (A) percentage freezing times during the training periods, and (B) percentage freezing time for control, 2 mM and 4 mM injected mice during contextual memory assessment.

6.5.5. Histological assessment of ferric citrate injection pathology

6.5.5.1. Ferritin immunohistochemistry

Ferritin is the iron storage protein expressed in cells, and so immunohistochemistry was performed to detect the storage capacity in the hippocampus upon injection with ferric citrate. Very few ferritin-positive cells were detected following control injections into the hippocampus (Figure 6-16A), with cells that were positive evenly spread throughout the whole hippocampus and within both the dentate gyrus (DG) and CA3 regions, without any clustering (Figure 6-16A-C). The 2 mM ferric citrate

injection into the hippocampus caused substantial increases in ferritin immunoreactivity 10 days post-surgery, with many more positive cells observed in the hippocampus, and in the DG and CA3 regions (Figure 6-16D-F). The ferritin positive cells were also clustered tightly to the granular neuronal layers in the DG and CA3 (Figure 6-16E-F). The 4 mM ferric citrate injection similarly shows substantially increased ferritin immunoreactivity in the hippocampus compared with controls, and clustering to the neuronal layers of the DG and CA3 regions, as detected in 2 mM injected brains (Figure 6-16G-I).

Co-staining with haematoxylin to label cell nuclei of the ferritin stained sections, predominantly highlights the neuronal architecture in control injected hippocampus for clear definition of the DG and CA3 neuronal layers (Figure 6-16B-C). Whilst the 2 mM ferric citrate injection allows approximate architecture delineation within the DG and CA3 regions (Figure 6-16E-F), 4 mM injection led to complete loss of integrity in these layers (Figure 6-16H-I).

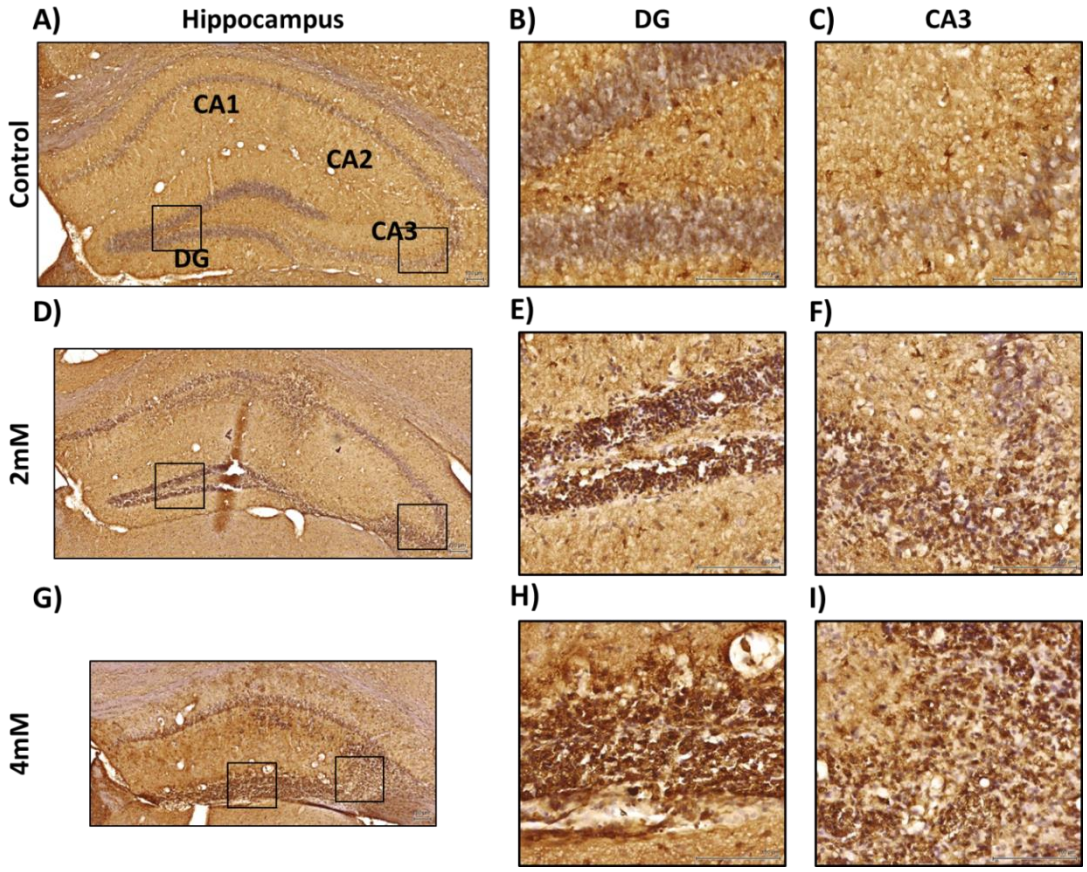

Figure 6-16 Ferritin immunoreactivity in the hippocampus of one control, one 2 mM and one 4 mM ferric citrate injected animal

Ferritin immunoreactivity (dark brown) and haematoxylin staining (pale blue) in the hippocampus of (A-C) a control, (D-F) a 2 mM ferric citrate and (G-I) a 4 mM ferric citrate injected mouse. Boxes in the left images highlight the area selected for evaluation at 20X magnification in the DG and CA3 regions.

6.5.5.2. Iba-1 immunohistochemistry

Iba-1 protein is a calcium-binding adaptor protein that is found specifically in microglial cells in the brain (Ito *et al.*, 1998) and frequently used as a marker for microglial counting and morphological assessment (Ahmed *et al.*, 2007). Iba-1

positive cells were spread evenly throughout the hippocampus of control injected mice (Figure 6-17A), and were evenly spread throughout both the DG and CA3 hippocampal sub-regions (Figure 6-17B-C). Furthermore, the morphology of the microglia was predominantly non-reactive, with few processes (Figure 6-18A). The 2 mM ferric citrate injection led to a substantial increase in the number of Iba-1 positive cells across the hippocampus (Figure 6-17D) and whilst being identified throughout the hippocampus, did show some clustering to the neuronal architecture of the DG and CA3 regions (Figure 6-17E-F). Morphologically, Iba-1 positive cells demonstrated more aggressive appearance, with many processes exuding from the cell bodies (Figure 6-17E-F, Figure 6-18B, arrowheads). Finally, assessment of the 4 mM ferric citrate injected hippocampus demonstrated similar observations as made in the 2 mM injections, with substantially increased iba-1 positive cell numbers throughout the hippocampus compared to controls (Figure 6-17G), with clustering to the DG and CA3 neuronal layers (Figure 6-17H-I). Extremely aggressive microglial morphologies could be observed with many processes from each cell body as well as many overlapping cells (Figure 6-18C, arrowheads). Amoeboid-like morphologies seemed to also be observed within the granular neuronal layers in the 4 mM ferric citrate injected hippocampus.

Nissl co-staining of sections labelled with Iba-1 allowed clear delineation of the neuronal cell architecture within the control injected hippocampus (Figure 6-17A), with both the DG and CA3 regions demonstrating healthy neuronal layers (Figure 6-17B-C, Figure 6-18A). Whilst the 2 mM ferric citrate injection allowed the neuronal layers to remain discernible throughout the whole hippocampus (Figure

6-17D), regions of greater neuronal death could be detected with highly intensely stained pyknotic nuclei in the DG and CA3 regions (Figure 6-17E-F, Figure 6-18B, arrows). The 4 mM ferric citrate injections provided less clarity in the neuronal layers throughout the hippocampus (Figure 6-17G) and demonstrated a near complete loss of integrity in neuronal cells in the DG and CA3 regions, with no layer structure and many intensely stained pyknotic nuclei (Figure 6-17H-I, Figure 6-18C, arrows).

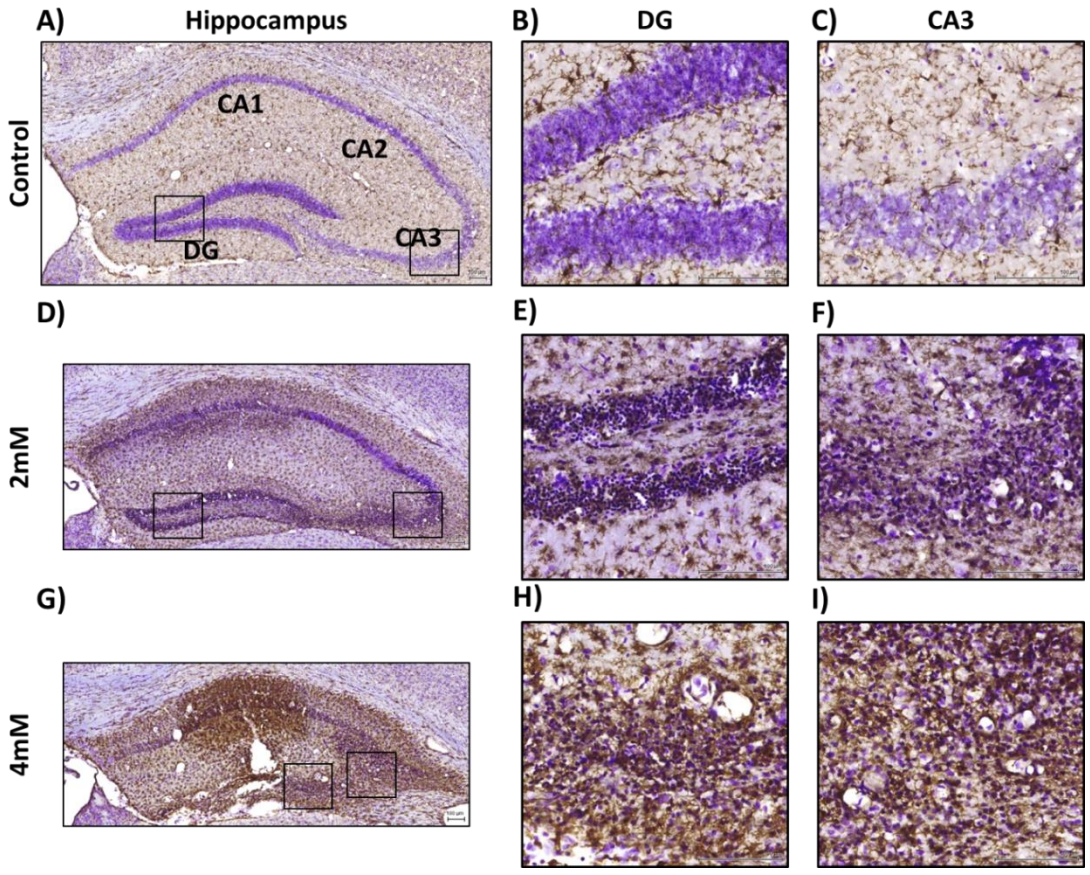

Figure 6-17 Iba-1 immunoreactivity in the hippocampus of one control, one 2 mM and one 4 mM ferric citrate injected animal

Iba-1 immunoreactivity (dark brown) and nissl staining (blue/ purple) in the hippocampus of (A-C) a control, (D-F) a 2 mM ferric citrate and (G-I) a 4 mM ferric

citrate injected mouse. Boxes in the left images highlight the area selected for evaluation at 20X magnification in the DG and CA3 regions.

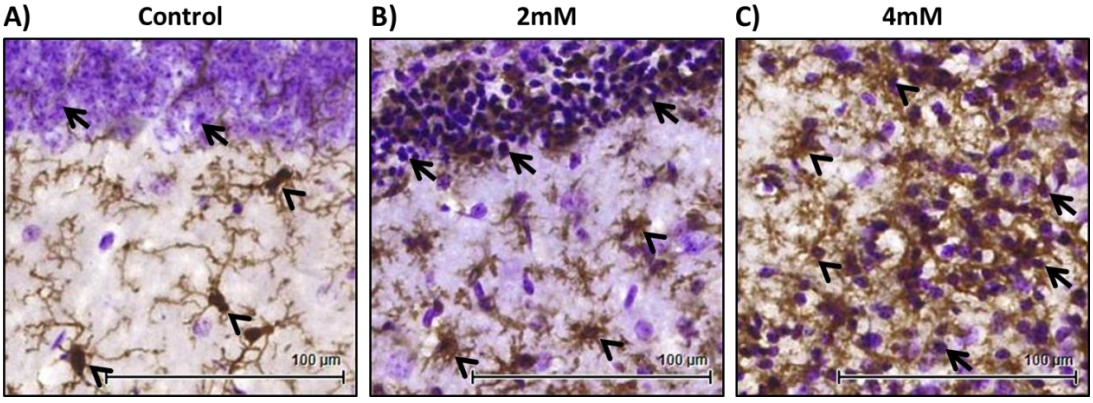

Figure 6-18 Microglial morphologies and pyknotic nuclei in control, 2 mM and 4 mM ferric citrate injected hippocampus

Microglial cells (arrowheads) show different morphologies between (A) control, (B) 2 mM and (C) 4 mM ferric citrate injected animals. Neuronal cells (arrows) highlight healthy neuronal cell bodies in (A) control, compared with pyknotic cells in (B) 2 mM and (C) 4 mM ferric citrate injections. The 4 mM ferric citrate injection has led to loss of neuronal layer integrity.

6.5.5.3. Correlation of histology to iron content

Histological evaluation of ferritin, Iba-1 and neuronal cell death were compared alongside elemental iron maps to understand the pathology in greater detail. Mice injected with control solution demonstrated no regions of high iron content, evaluated by XRF, within the hippocampus (Figure 6-10 and Figure 6-19A).

Histological assessment of the adjacent slices revealed no substantial increase in ferritin or Iba-1 staining within the hippocampus either (Figure 6-19B-C) and the granular neuronal layers of the hippocampus (CA1, CA2, CA3 and DG) can be clearly delineated using both haematoxylin (Figure 6-19B), and more specifically, Nissl (Figure 6-19C) stains. In the representative hippocampal section from the 2 mM ferric citrate injected animals, the localisation of iron is predominantly within the DG and CA3 regions, with lower intensity of iron content also within the CA1 region (Figure 6-19D). Comparison against ferritin and Iba-1 immunohistochemistry demonstrates substantial positive cell staining for both markers within these same three regions (DG, CA3 and CA1), whilst the CA2 does not show much immunoreactivity (Figure 6-16E-F, Figure 6-17E-F and Figure 6-19E-F). An intense accumulation of iron was also observed in this sample just above the hippocampus (Figure 6-19D; arrow), matching a ferritin positive area in the adjacent slice (Figure 6-19E; arrow), whilst demonstrating less staining for Iba-1 in the same area (Figure 6-19F; arrow). Furthermore, haematoxylin and Nissl staining of neurons revealed damaged regions of the granular layers in the same sub-regions of hippocampus containing high iron, high ferritin and high Iba-1 clusters (Figure 6-19E-F). Similar to 2 mM treatment, the 4 mM ferric citrate injected animal demonstrated a global increase in iron content throughout the hippocampal section (Figure 6-19G), with a concomitant increase in ferritin and Iba-1 staining localised to the granular layers from the DG, CA3, CA2 and CA1 (Figure 6-19H-I). The integrity of the granular neuronal layers was also substantially compromised in regions containing high iron, high ferritin and high Iba-1 positivity (Figure 6-19H-I). A region of high iron content was again observed above the hippocampus (Figure 6-19G; arrow), which again

demonstrated ferritin positive staining, but limited Iba-1 positive staining (Figure 6-19H-I; arrows). Finally, it was also notable that many of the hippocampal sections evaluated from the 4 mM ferric citrate injections demonstrated large cavities in their structure (Figure 6-19I; arrowhead).

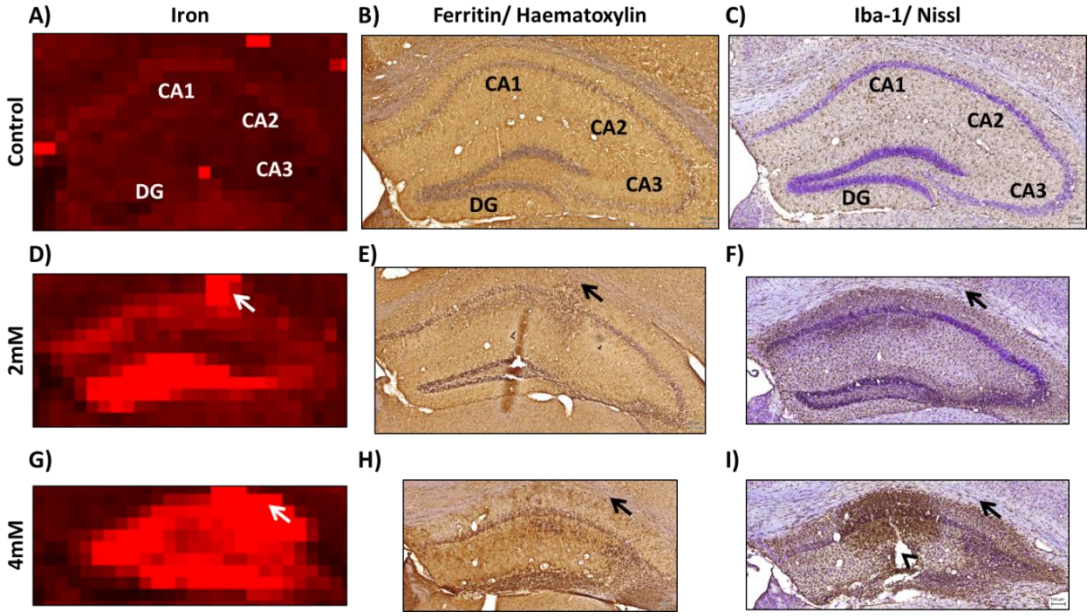

Figure 6-19 Elemental iron maps compared alongside ferritin and Iba-1 immunohistochemistry

Representative images of the whole hippocampus comparing the (A, D, G) elemental iron maps with (B, E, H) ferritin and (C, F, I) Iba-1 immunohistochemistry, in control, 2 mM and 4 mM ferric citrate injected mice. Arrows denote specific regions of iron content increase across each image; the arrowhead denotes a large cavity in the hippocampal structure, likely due to iron injection.

6.5.5.4. Injection site

Further evaluation of the cortical regions where high iron content is observed above the hippocampus, demonstrated that these areas coincided with the injection site, and correlated with regions of higher ferritin and some Iba-1 staining than the surrounding tissue (Figure 6-20A-B; arrows). Furthermore, strong ferritin immunoreactivity, with low Iba-1 positive staining, can be observed within the WM tracts above the hippocampus of mice that show areas of high iron content at comparable locations (Figure 6-20B; arrowheads).

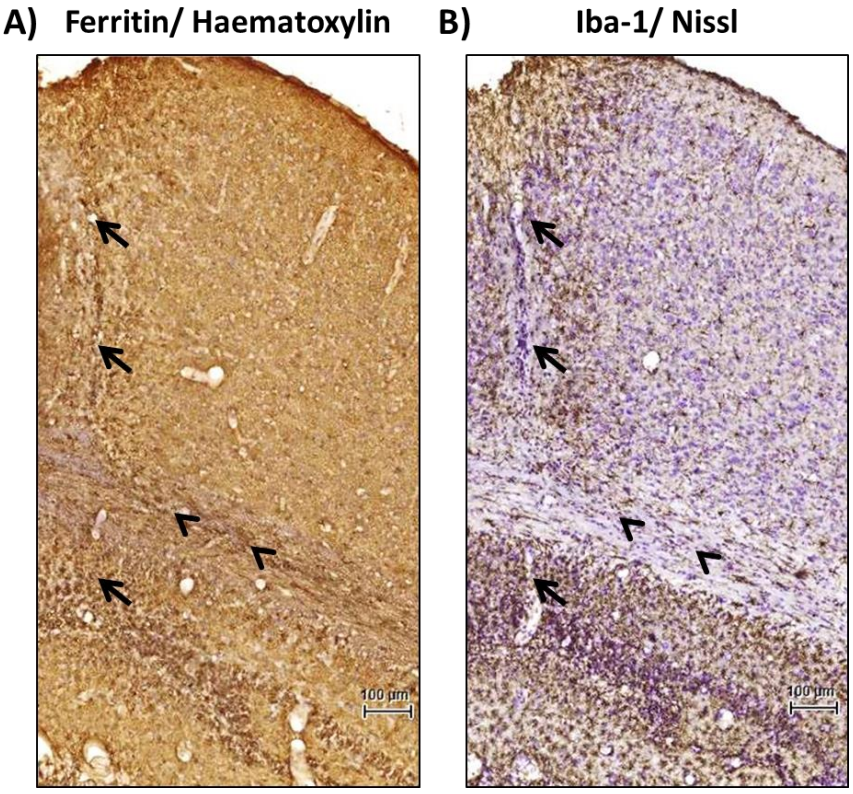

Figure 6-20 Injection site of ferric citrate from mouse with high iron content outside the hippocampus

Histological images of (A) ferritin/ haematoxylin and (B) Iba-1/ Nissl of a 4 mM ferric citrate injected mouse, demonstrating a region of increased iron content above the

hippocampus. Arrows denote the needle tract into the hippocampus; arrowheads denote regions in the WM with greater ferritin, and comparably less Iba-1 staining.

6.5.5.5. Summary of histological assessment of ferric citrate injection pathology

Greater ferritin expression was found in ferric citrate injected animals than controls, and clustered predominantly at the neuronal layers of the DG and CA3 regions. Iba-1 staining was also greater in ferric citrate injected animals and again clustered at the DG and CA3 regions of the hippocampus. Iba-1 staining also demonstrated more aggressive morphologies of microglial cells (as activated, rather than resting morphology) than observed in controls. Nissl assessment of neurons specifically highlighted greater levels of neuronal cell death in ferric citrate injected mice than controls, with greater numbers of pyknotic nuclei and loss of the architectural integrity of the neuronal layers in the DG and CA3 regions. Furthermore, the regions with greatest ferritin and Iba-1 localisation and with greater neuronal cell death, correlated to similar locations of higher elemental iron contents.

6.6. Discussion

A model system for developing and validating MRI measurements for the *in vivo* detection of iron within the brain is described here, also allowing for the assessment of the direct toxic effects iron may play towards neuronal cell death.

Much of the previous literature involving injection of iron into the brain has evaluated the biochemical and cellular nature of iron toxicity from unilateral hippocampal injections, or injections within cortical areas (Willmore *et al.*, 1983, Triggs and Willmore, 1984, Sloot *et al.*, 1994, Armstrong *et al.*, 2001, Bishop and Robinson, 2001, 2003, Bostanci and Bagirici, 2007). This study is the first to perform bilateral injection of iron into the hippocampus, to allow evaluation of behavioural or cognitive deficits, and demonstrates this as a tolerable model of iron toxicity in mice. Animals remained free from seizures throughout the experimental period, and did not show changes in weight between the treatment groups. Furthermore, this approach allows for a novel method to validate MRI measurements for the evaluation of brain iron.

6.6.1. *Ex vivo* hippocampal iron detection

SE R1, SE R2, GE R2* and R2' were all able to detect the change in iron content between ferric citrate injected, versus control injected hippocampi, however they were unable to distinguish between the two ferric citrate concentrations. R2* relies on susceptibility effects, as well as the R2 transverse relaxation of protons for iron detection (Langkammer *et al.*, 2010), thus clarifying the enhanced sensitivity of R2* within this study. R2' provides a measure of inhomogeneities in tissue, (Haacke *et al.*, 2005), and given the strong correlation of R2' to iron content in this model, as was also observed with R2* to iron, these findings highlight that susceptibility effects seem to be a major factor contributing to sensitivity here.

R1 and R2 values demonstrated lower correlations to iron content than R2* and R2' values, despite all four relaxometry measurements equally capable for detecting iron in the ferric citrate-injected, versus control-injected mice. Iron has been demonstrated to play a direct role on both the longitudinal and transverse relaxometry measurements within tissue (Ogg and Steen, 1998, Schenck, 2003), due to the paramagnetic effects impacting on both R1 and R2 relaxation rates (Vymazal *et al.*, 1996b). The lower correlations of iron content to R1 and R2 may be due to less of an impact on longitudinal and transverse relaxation, than by also including inhomogeneity detection, within this model. This difference was most apparent with regions of the cortex showing iron accumulation only detected using R2* and R2' mapping, whilst they were not detected in R1 or R2 maps.

The finding that the MGE R2* assessment was able to detect the changes in iron content between the two ferric citrate concentrations, comparably to elemental iron mapping, is likely due to this acquisition sequence demonstrating enhanced differences between low and high R2* values compared to the GE R2* sequence (see sections 4.4.3). Also, given that this sequence can be performed at substantially faster acquisition times than the standard GE R2* method, the number of averages used was greater, providing improved SNR for better detection of the changes between treatment groups compared with GE R2*. The ME R2 assessment was less clear at detecting the changes in iron content than SE R2 measurement, and again this can be explained due to the ME R2 measurement consistently demonstrating lower R2 values than the SE sequence, especially at higher R2 values (see section 4.4.3).

6.6.2. *In vivo* hippocampal iron detection

Whilst *ex vivo* imaging demonstrated clear differences between injection groups, neither ME R2 nor MGE R2* was able to detect differences between ferric citrate injected and control injected animals, *in vivo*. The results in this study can be best understood using current knowledge and models of haemorrhaging in the brain, whereby blood leakage from vessels occurs into the brain tissue. The stages for clearance of a brain haemorrhage have been established, with an understanding of how each stage might affect MRI signals differently, especially using T1W and T2W imaging. Five stages can be classified using MRI, predominantly dependent on the forms of iron present and the localisation of these iron substances (Bradley, 1993). The first three stages involve the conversion of oxyhaemoglobin to deoxyhaemoglobin, and subsequently to methemoglobin within the red cells that have leaked into the brain tissue (Bradley, 1993). The ferric chloride injections performed as part of this study resemble the stages following these, in which the red cells lyse and release their contents into the brain tissue (Huang *et al.*, 2002). This release of haemoglobin and iron from red cells into the brain leads to oedema, which involves fluid accumulation at the site of injury (Huang *et al.*, 2002). Oedema can lead to a lengthening of T2, and therefore lower R2 values due to the increase in fluid (Kato *et al.*, 1986) and T2W imaging has been used to evaluate oedema in animal models (Schneider *et al.*, 2002, Sironi *et al.*, 2004). ME R2 values were lower in the hippocampus at days 3 and 5 compared with the surrounding tissue in this study, as assessed from the serial *in vivo* acquisitions in the pilot work. The lower R2 values observed in the hippocampi *in vivo* at this time may therefore be due to

oedema presence within the iron lesioned hippocampi post-surgery. Following this stage, iron is finally taken up into macrophages and stored as ferritin or hemosiderin, which provide a shortening of T2 values due to their paramagnetic nature (Bradley, 1993). Indeed, during further recovery of animals in this study, the *in vivo* ME R2 values become normal for the hippocampus at days 9 and 17 post-surgery, likely due to a reduction of oedema during recovery, as well as an increase in ferritin and hemosiderin. It therefore seems that at these later stages, conflicting relaxometry signals may be occurring within the hippocampus *in vivo*, with a combination of low R2 values from oedema, whilst higher R2 values come from iron content, present as ferritin. Clearly, once brains are perfusion-fixed, excised and then further PFA fixed, oedema is cleared and no longer plays any role in R2 signal, allowing iron-rich regions to be clearly delineated *ex vivo* (see section 6.6.1). Therefore, allowing a greater recovery time post-surgery would potentially provide better detection of iron *in vivo*, once oedema has been completely reduced.

Given that neurodegenerative diseases tend to provide some level of neuroinflammation that may lead to oedema during pathology (Dheen *et al.*, 2007), these findings may need to be taken into consideration if comparing iron contents between control subjects and neurodegenerative disease patients *in vivo*, as there may be interference with observed relaxometry values.

MGE R2* maps were unable to differentiate between iron injected and control animals due to large susceptibility effects *in vivo*, likely due to local inhomogeneities and from susceptibility changes between tissue, skull and air (Czervionke *et al.*, 1988).

6.6.3. Iron accumulation in lesion

We found that iron content, as well as R1, R2, R2* and R2' relaxivity values, were identical within the iron accumulation lesions of the hippocampus between the 2 mM and 4 mM ferric citrate injections. This implies the densities of iron within the lesions are comparable. However, there was a greater iron accumulation lesion volume for the 4 mM compared with 2 mM group. This suggests greater spreading of injected iron throughout the hippocampus after the 4 mM ferric citrate injections, which led to a near doubling of detected total iron content in the 4 mM compared with the 2 mM injected mice. Both of these findings are reasonable, given that ferritin protein is only able to store a certain number of iron atoms prior to saturation, reflecting the similar iron contents, as well as relaxivity values, between the two treatment groups (Harrison and Arosio, 1996). However, given that more iron was injected in the 4 mM than 2 mM treatments, the greater amount of iron has clearly been distributed further around the hippocampus leading to greater lesion volumes in the 4 mM treatment. Whilst no studies have evaluated this spreading of iron in the hippocampus using MRI previously, total damage and cytotoxicity was shown to increase in a concentration dependent manner using ferric citrate injections (Armstrong *et al.*, 2001).

The greater spreading of iron within the lesion may have occurred either through passive diffusion within the hippocampus, or may have been through active movement, given that the same volume (500 nl) of 2 mM and 4 mM ferric citrate was injected into the hippocampus. Iron is transported within the brain by transferrin and lactoferrin and is exported from cells, such as neurons, through

ferroportin (Moos *et al.*, 2007). If active movement of iron was occurring within the hippocampus following ferric citrate injection, it would be expected that these proteins would be expressed at greater levels in the 4 mM ferric citrate injected animals, than in the 2 mM injected animals. Evaluation of both transferrin and ferroportin immunohistochemically gave rise to non-specific and high background staining in mouse tissue. Therefore, western blotting of digested hippocampal material could be used in subsequent studies to evaluate the changes in expression of these proteins following ferric citrate injection (Chen *et al.*, 2011).

Despite injecting twice as many iron atoms in the 4 mM treatment, compared with 2 mM ferric citrate injections, a slightly less than doubling of total iron content was detected. This discrepancy is likely due to only three slices of hippocampus being assessed using XRF elemental mapping, rather than coverage of the whole brain region across 4-5 slices, due to time constraints for XRF acquisition. With a greater spreading of iron content in the higher treatment group, as discussed above, movement of some injected iron may have occurred more ventrally in the hippocampus than was assessed by XRF mapping. Similarly, iron may have been transported away from the hippocampus entirely. Therefore, total iron content may have been underestimated in the 4 mM group compared with the 2 mM injection group. These findings were comparable with the relaxometry assessments across the 3 slices of hippocampus, also showing a slight underestimation of relaxivities in 4 mM ferric citrate injections compared with the 2 mM injections.

6.6.4. Correlation of iron to ferritin and Iba-1 immunoreactivity

We found that higher elemental iron contents within the hippocampus, seem to correspond to regions of high R1, R2, R2* and R2' values in relaxivity maps. Furthermore, we have demonstrated that higher iron contents correspond to regions of greater ferritin and Iba-1 immunohistochemistry, as well as to regions with greater neuronal cell death.

Unsurprisingly, ferritin localisation was similar to that observed for iron contents within the hippocampi, especially given that ferritin is the storage protein for iron (Harrison and Arosio, 1996) and that iron overload can directly increase ferritin translation (see section 1.3.3) (Theil, 1990). Furthermore, the observation that higher iron contents, as well as ferritin and Iba-1 staining, were predominantly located at the DG and CA3 regions of the hippocampus, was expected given that this was the physical site of injection of ferric citrate within the hippocampus. The appearance of iron, ferritin and Iba-1 within the CA1 regions of some mice may also be as a direct result from surgeries, whereby any iron leakage whilst the needle was removed may have occurred into this hippocampal region.

Ferritin and Iba-1 positive cells clustering at the neuronal layers within the DG and CA3 highlight that microglia may be involved in mediating the effects of iron toxicity on neuronal cells. Microglial cells have been suggested to be the predominant cells in the brain responsible for iron storage, given their higher expression of L-ferritin, involved in storage of iron (Connor *et al.*, 1994, Han *et al.*, 2002). Furthermore, injection of iron into the rat cortex alone, led to increased expression of ferritin-positive microglia and neuronal death at the injection site (Bishop and Robinson,

2001). Similarly, ferritin-positive microglia were reported following the intracerebral injection of blood into rabbits, along with the potential identification of factors that may lead to recruitment of more microglial cells to the region (Koeppen *et al.*, 1995). Therefore, microglial presence surrounding neurons may hold relevance for mediating the iron-induced toxicity of ferric citrate in the hippocampus. However whether this inflammatory response is pro-survival or deleterious to neuronal cells is unknown from this study, as we are unable to specify whether neuronal degeneration preceded microglial aggregation to the granular layers. Whilst microglia presence may provide a means for uptake and storage of injected iron away from regions where it would otherwise cause toxic effects, microglial cells can also play a role in the clearance of cell debris, following necrotic cell death (Graeber, 2010).

Microglial cells seem to show a ramified morphology in control-injected hippocampus, however in the 2 mM injections, these cells appear activated. Whilst similar morphologies to these activated microglia are also detected in the 4 mM ferric citrate injected mice, the presence of amoeboid microglia are also apparent, especially across the granular neuronal layers. These amoeboid microglia imply phagocytosis of cell debris may be occurring around the DG and CA3 regions, following ferric citrate injection at the higher concentration (Graeber, 2010).

The expression of ferritin within the WM of certain mice that also show higher iron content in this area highlights that other cell types may also be responsible for clearance of iron in the brain, given the lower expression of Iba-1 detected. Whilst this has not been definitively proven in this study, it is hypothesised that

oligodendrocytes may be responsible for accumulating the iron in these WM areas, given their presence within WM for myelin synthesis, along with demonstrated expression of ferritin in the brain (Connor *et al.*, 1994).

6.6.5. Neuronal death

Neuronal cell death seems to be ongoing at 10 days post-injection, based on the detection of pyknotic nuclei within the hippocampal sub regions (de Torres *et al.*, 1997). The precise mechanism surrounding neuronal cell death has not been fully evaluated here, however is likely to be, at least in part, due to the generation of ROS (Willmore *et al.*, 1983). Furthermore, neuronal death was demonstrated using Fluoro-Jade labelling following ferric ammonium citrate injection into the cortex, and continued to 7 days post-injection (Bishop and Robinson, 2001). Given that neuronal cells do not seem to have stopped undergoing cell death, this may explain the lack of significance observed in the contextual memory task at only 10 days post-injection. It may therefore be conceivable that allowing a longer time post-surgery prior to behavioural testing may allow for greater levels of neuronal cell death to occur, providing a greater memory reduction following ferric citrate injections.

6.6.6. Conclusion

In conclusion, the direct injection of iron into the mouse hippocampus provides a novel approach for developing and validating MRI measurements for the *in vivo* detection of iron within the brain.

In order to quantify *in vivo* ME R2 and MGE R2* for iron detection (see section 6.3), endpoint *in vivo* MRI was carried out using the ferric citrate injected mice compared with controls. Whilst ME R2 and MGE R2* were unable to detect changes in iron content in the mouse brain *in vivo* after 10 days post injection, attention can be drawn to confounding factors affecting the relaxometry values *in vivo*. Furthermore, R1, R2, R2* and R2' were then evaluated *ex vivo* for quantification and correlation of iron detection capability, compared with SR-XRF elemental iron assessment, as noted in objectives (see section 6.3). All relaxometry assessments were able to detect ferric iron injected, versus control injected hippocampus *ex vivo*, and all demonstrated strong correlation to overall iron contents. This study highlights R2* and R2' as the most sensitive methods for iron detection *ex vivo*. Greater optimisation of the R2* acquisition is still required for iron detection *in vivo* however.

Finally, using this animal model, the direct role iron plays on neuronal cell death and neuroinflammation could be evaluated by histological and behavioural assessments (see section 6.3) without the additional, detrimental phenotypes from transgenic approaches. Iron led to an increase in ferritin immunoreactivity and Iba-1 microglial presence in the hippocampus, and highlighted roles for microglia in mediating the iron-induced toxicity of neurons, given their clustering to the

neuronal layers in this brain region. The applicability of this model for testing therapeutic interventions of iron overload may provide a future goal, along with enhanced validation methods for iron detection using MRI.

7. Discussion

The work in this thesis supports the approaches using MR relaxometry for the non-invasive detection of iron content in brain tissue during neurodegeneration. Using a variety of systems, greater knowledge into the direct effects that iron plays on R1, R2, R2* and R2' measurements have been gained, and greater understanding of iron-induced neurodegeneration has also been obtained.

With MRI evaluation of iron content in live, biological samples complicated by the variety of tissue environments, unconfirmed iron contents and heterogeneous forms of iron found (see section 2) simple model standards were first used to confirm and validate the direct effect of iron content and form on R1, R2, R2* and R2' (see section 4). The direct, linear relationships between iron content and R1, R2 and R2* for both ferric and ferrous iron, as well as using ferritin bound iron, supports the direct evaluation of iron content using relaxometry measurement, as outlined in the hypotheses (see section 2). These results satisfy the main objectives for the thesis in understanding the basic principles of iron content detection using MR relaxometry. However, given that the different forms of iron clearly impact relaxometry values irrespective of concentration, these observations may have considerable effects for the use of these techniques to quantitatively assess iron content during neurodegeneration.

Spatially correlating elemental iron content against relaxometry measurements in individual, as well as multiple human post-mortem samples, demonstrated that R2

and R2* were found to be correlated most consistently with iron, in both control and AD MTG. This fits the evaluations performed using iron agarose standards, whereby both systems demonstrate linear correlation between iron content and R2 or R2*. The lower correlation values obtained in human post-mortem tissue compared with the iron agarose standards can be attributed to the presence of many different cell types and therefore tissue microstructures in human tissue, compared with the homogenous nature of the iron agarose standards. Water content differences between post-mortem tissue and the agarose standards may also have impacted correlation values. R1 values demonstrated significant correlations when assessing individual human post-mortem samples with iron content, as expected from the work using iron agarose standards. However, its use as a specific measure of iron seems to be severely hindered by effects from other influencing factors between samples. An example of this includes prolonged fixation time in human post-mortem tissue strongly affecting R1.

R2' provided a sensitive measure for iron content in the human post-mortem samples, whereas the iron agarose standards did not allow for quantification of iron content using this measurement. This can be attributed due to the agarose standards' greater homogeneity than the human post-mortem samples. However, despite R2' being sensitive to iron from human post-mortem tissue, the low SNR associated with the acquisition of this parameter here seems to have led to lower correlation values against iron content, than that obtained using R2 and R2* relaxometry.

The results provided within this thesis using post-mortem human tissue allow far greater understanding of iron-sensitive MRI capabilities through correlation against quantitative SR-XRF evaluation of iron, rather than by comparison against non-quantitative histological Perls' staining. This satisfies the main aims of the thesis for validating iron-sensitive MRI methods during neurodegeneration (see section 2).

Comparison of control and AD tissue provided similar iron and relaxometry values within both GM and WM regions, as well as separation of the GM into the separate cortical layers of dGM and MCL. Whilst some studies have shown changes in iron content or relaxation between AD and control tissue (Goodman, 1953, Deibel *et al.*, 1996, Schenck *et al.*, 2006, Smith *et al.*, 2010), our results are still in agreement others (Schrag *et al.*, 2011, Antharam *et al.*, 2012). However, a decrease in WM myelin was identified in male AD samples compared with male control subjects and this loss of myelin in WM allowed for greater sensitivity in the detection of iron using R2 relaxometry assessment. This highlights that myelin can strongly affect relaxometry values, and therefore with their estimation of iron content, as was hypothesised (see section 2). Future work could therefore employ the use of multiple regression analysis in order to provide greater understanding of the impact of myelin, water or other factors, on the measurement of iron using relaxometry assessment.

Finally, by directly injecting iron into the mouse hippocampus, *in vivo* MRI methods for quantitative detection of iron could be assessed. R2 and R2* *in vivo* assessments of iron were similar in the hippocampus of control and ferric citrate injected

animals. This was likely due to 10 days recovery of animals only just allowing for reduced oedema within the injection sites, as well as large image artefacts hampering the R2* findings *in vivo*.

Iron detection was achievable *ex vivo* however, using R1, R2, R2* and R2'. R2* and R2' provided the strongest correlation to elemental iron. These results were expected, given the basis of iron content changes on relaxometry values using agarose standards. In mouse *ex vivo* tissue, R2' provided strongest correlation to iron, whereas this measurement was poorer than R2 and R2* in human post-mortem tissue and non-existent in the agarose standards. The improved R2' correlation in mouse tissue may be due to the smaller ID RF coil used for the animal work, providing greater SNR than that obtained in the human post-mortem studies. Furthermore, differences in the tissue types investigated may impact the correlation of R2' for iron content, with human post mortem tissue performed in the MTG, a cortical region with low changes in iron content, whilst the mouse injections were performed in the hippocampus, using greater concentrations of iron.

A greater amount of iron spreading within the hippocampus was identified with increased ferric citrate injection concentration, whilst iron levels were saturated within the hippocampal iron lesion. This was attributed to ferritin saturation, with positive cell staining identified in similar regions of the hippocampus, as elemental iron was located following injection. This animal model therefore provided a very useful approach to validate iron-sensitive MR measurements in a controlled, *in vivo*,

system and to explore the direct effect of iron overload on neuronal cell death, without the detrimental effects associated with transgenic models.

The results taken together from the three different systems used in this thesis are consistent with iron-lengthening of MRI relaxivity, and imply R2, R2* and R2' relaxometry can be used to provide non-invasive, quantitative information on the iron content of brain tissue, during neurodegeneration.

7.1. Limitations and future directions

Whilst attempts were made to perform studies in the most systematic and methodical manner, there remains some limitations to the studies within this thesis, highlighted below. Future investigations based on the observed results are also outlined.

7.1.1. Iron agarose standards

With ferric iron detectable compared to ferrous iron based on their individual molar relaxivities in agarose standards, it would beneficial to also characterise alternative, pathological forms of iron using this approach, such as magnetite or hemosiderin, given that these forms are reportedly higher during AD (Collingwood *et al.*, 2005, Quintana *et al.*, 2006, Pankhurst *et al.*, 2008). Furthermore, it would then be of interest to evaluate the application of this assay using purified iron from human

post-mortem control and AD brain samples, or from transgenic animal models of AD. This may aid our understanding of whether changes in the forms of iron from neurodegenerative disease samples, compared with control tissue, can be detected by molar relaxivity measurement. Similarly, extraction of ferritin from control and AD human post-mortem brain tissue followed by the subsequent comparison of molar relaxivities may also be of interest. These experiments should clarify whether any changes observed between AD and control tissue using relaxometry measurement in clinical environments are as a direct result from changes in iron content, or whether there is a change in the form of iron during AD pathology.

7.1.2. Iron measurement in control and AD human MTG

A limitation of the work using human post-mortem tissue is that many other factors excluding iron or myelin content may play a substantial role in relaxometry signal generation, which were not fully explored here. Water content, for example, can show major effects on relaxivity values based on the greater proportion of freely moving water protons within the environment. Water content has been shown by others to correlate with relaxometry values in control and AD post-mortem tissue, with differences in GM and WM (House *et al.*, 2008). However, with all of the samples obtained for this study being formalin fixed, we expect that any effects of water content will be equalised between samples.

Another limitation to this study was that the only iron-sensitive MRI measurements performed here were relaxometry evaluations, whereas many other MRI

approaches may also support these findings against SR-XRF elemental iron, such as using FDRI, QSM or MFC. It would therefore be of interest to establish how well these alternative approaches for iron-detection correlate to post-mortem tissue elemental iron in the future. Furthermore, other more general MRI approaches using post-mortem tissue may provide greater understanding of the overall physiology of AD compared with controls for evaluating against iron content, such as using magnetisation transfer ratio or diffusion weighted imaging.

Limitations with the histological assessments performed in this thesis are that only myelin content was evaluated using luxol fast blue staining. To strengthen the conclusions derived here, immunohistochemical staining for myelin basic protein (MBP) could be performed as another marker of myelin health. Similarly, immunohistochemical staining of physiological changes between control and AD tissue may also provide greater insights into the results observed using iron-sensitive MRI approaches, such as by staining for ferritin expression. Indeed, ferritin showed direct correlation to relaxometry values in the agarose standards, however has only demonstrated modest correlation within human post-mortem tissue by others (Fukunaga *et al.*, 2010). Greater general physiological understanding into the relaxometry signals detected can also be gained by evaluating specific cellular presence, such as astrocytic or microglial presence in AD compared with controls.

Finally, the observations of ROI clustering differences within graphs correlating iron with relaxometry between AD and control samples, highlights that there may be a change in how pixel intensities are spread within tissue regions. This may be especially identified in WM regions, given the observed loss of myelin during AD.

Therefore, texture based analysis of specific regions from human samples may provide a novel approach for assessment of relaxometry maps, for the clinical evaluation of patients with neurodegenerative diseases, such as AD.

7.1.3. Direct injection of iron in the mouse hippocampus

A clear limitation of this study is that the iron clearly present in the hippocampus from *ex vivo* assessment could not be detected *in vivo*. This was due to the injections leading to oedema in the hippocampus, producing conflicting signals by relaxometry assessment, and R2* imaging *in vivo* was heavily impacted by imaging artefacts. Therefore to address these issues, a longer recovery period for animals should be allowed prior to evaluation using iron-sensitive MRI methods, and greater optimisation of R2* *in vivo* imaging is required. Indeed, a longer recovery time post-injection may even allow functional behavioural deficits to be more clearly derived, with iron-induced neurodegeneration allowed to progress for a longer period.

Furthermore, this study could only provide cross-sectional evidence for the role of iron during neurodegeneration with no understanding of the temporal mechanisms of neurodegeneration assessed. Therefore, evaluation of animals at multiple time points following ferric citrate injection would allow greater understanding of these mechanisms and the cell types responsible. Indeed, rats were followed over a 10 day period to show increase of ferritin up to this point and a plateau in neuronal death (Armstrong *et al.*, 2001). However, with this thesis study performed in mice,

neuronal loss may be occurring at a different rate than in rats. Double or triple immunohistochemistry for combinations of protein markers would also provide beneficial evidence in understanding mechanisms of iron-induced neurodegeneration using this animal model, complementing work performed by others showing that both ROS and oxidation products are raised immediately following iron injection (Willmore *et al.*, 1983, Triggs and Willmore, 1984).

Finally, to understand how a greater spread of iron within the lesion is observed following greater amounts of ferric iron injection, the expression of certain iron regulatory proteins, such as transferrin, transferrin receptor and ferroportin, can be evaluated. Given that immunohistochemical staining methods were not sufficient to establish the expression of these proteins in the present study, Western blot analysis can be utilised in a subsequent study.

It should also be noted that whilst the scope of this thesis has been focussed on the impact of iron on MRI and in understanding the roles that iron may play during neurodegeneration, exploration of how other metals, such as zinc or copper, are affected during neurodegeneration may also be of interest in the potential for developing novel therapeutic interventions against AD.

Appendix A

Improved Correlation of Iron to R2 and R2* in Alzheimer's Disease-Affected White Matter

Christos Michaelides[1], David J. Lythgoe[1], Harold G. Parkes[1,2], Claire Troakes[3], Istvan Bodi[4], Tina Geraki[5], Amy H. Herlihy[6], Po-Wah So[1]

[1]Department of Neuroimaging, Institute of Psychiatry, King's College London, London. [2]CR-UK Clinical MR Research Group, Institute of Cancer Research, Sutton, Surrey. [3]MRC London Neurodegenerative Diseases Brain Bank, Department of Clinical Neuroscience, Institute of Psychiatry, King's College London, London. [4]Clinical Neuropathology & London Neurodegenerative Diseases Brain Bank, King's College London, King's College Hospital, London. [5]Diamond Light Source, Harwell Science and Innovation Campus, Didcot, Oxfordshire. [6]Agilent Technologies, Yarnton, Oxfordshire.

Target Audience: This work is relevant for scientific researchers interested in neurodegenerative diseases and the basis of MR relaxometry measurements, more specifically, against iron.

Purpose: Non-invasive assessment of iron may provide a feasible method for diagnosis of neurodegenerative diseases, such as Alzheimer's disease, due to increasing evidence highlighting iron dysregulation during pathology[1]. The paramagnetic properties of iron also provide an ideal candidate for detection by MRI, with iron shortening of T2 relaxation times within tissues. Thus, T2 and T2* measurement have been used in clinical studies as surrogate methods for iron detection[2], however measurement of iron by MRI has yet to be validated against a gold standard method. Iron quantities have been correlated against published post-mortem results in current clinical literature[3], whilst animal studies predominantly utilise MRI measurements correlated against Perl's staining for iron. Whilst this staining method highlights iron accumulation, it remains a qualitative assessment[4]. The purpose of this study was to identify factors that may influence the correlation of MR relaxometry measurements in human AD brain samples, by utilising gold-standard, quantitative methods for iron assessment, using synchrotron radiation X-ray fluorescence (SR-XRF) elemental mapping.

Methods: Formalin-fixed post-mortem medial temporal gyri from AD (n=15) and control (n=15) human subjects were immersed in perfluoropolyether and positioned in a 7T MRI scanner. R1 and R2 relaxometry were performed using a spin-echo sequence with varying TR (300-4000ms) and TE (12-60ms), respectively. R2* relaxometry was performed using a gradient-echo sequence with varying TE (5-50ms). In-plane resolution was 0.11x0.15mm, thickness of 0.50mm. Magnetisation Transfer Ratio (MTR) was acquired at TR=1100ms, TE=4ms, offset at 100000Hz and 4500Hz. Following MRI, samples were processed and sectioned at 7µm for SR-XRF elemental iron mapping at 100µm resolution. Relaxometry and SR-XRF maps had 20 small ROIs of 5x5 pixels placed in each co-registered map to assess correlation of iron to MRI measurements using r^2 linear regression analysis (Fig. 1). 14µm thick sections were used for luxol fast blue (LFB) staining of myelin.

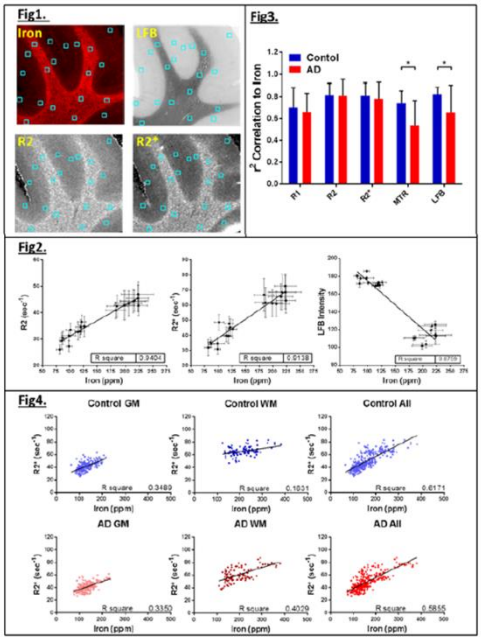

Fig.1. *Representative elemental iron, LFB and relaxometry maps.* ***Fig.2.*** *Representative correlation graphs of iron to R2, R2* and LFB staining in one tissue sample.* ***Fig.3.*** *Comparison of correlations between AD and control tissue.* ***Fig.4.*** *Correlation of R2* with iron changes in WM regions potentially due to changes in myelin.*

Results and Discussion: For each sample, individual r^2 correlations were calculated across the 20 ROIs for iron against R1, R2, R2*, MTR and LFB (representative graphs shown in Fig. 2). The correlation between iron and R1, R2 and R2* were similar between AD and control samples (Fig. 3). However, the correlation between iron and MTR or LFB differed between AD and control (MTR mean r^2 is 0.74±0.12 and 0.54±0.23 for control and AD, respectively, P=0.022; LFB mean r^2 is 0.83±0.06 and 0.66±0.25 for control and AD, respectively, P=0.050; Fig3). This indicates a breakdown between the relationship of white matter (WM) to iron content in AD compared to control. Further investigation indicates better correlation of R2* with iron in WM of AD compared to control (r^2=0.403 and r^2=0.163, respectively; Fig. 4). Grey matter (GM) regions show similar correlation values between control (r^2=0.349) and AD (r^2=0.335) samples, therefore highlighting the specificity of this correlation disparity to WM.

Conclusion: R2 and R2* correlated well with iron content in the GM, irrespective of disease. Their correlation in normal WM was poorer than that in AD-affected WM and appears to be dependent on myelination, therefore may have clinical relevance when applying R2 and R2* relaxometry to assess iron *in vivo*. **References:** (1) Zecca L, et al. *Nature Reviews: Neuroscience*. 2004; 5:863-873. (2) Langkammer C, et. al. *Radiology* 2010; 257:2 :455-462. (3) Rodrigue KM, et al. *NeuroImage*. 2011; 54:750-759. (4) Wengenack TM, et al. *NeuroImage*. 2011; 54:113-122.

1884

MRI Relaxometry Correlation against Iron in Alzheimer's Disease

Christos Michaelides[1], David J Lythgoe[1], Harold G Parkes[2], Claire Troakes[3], Istvan Bodi[4], Tina Geraki[5], Amy H Herlihy[6], and Po-Wah So[1]

[1]*Department of Neuroimaging, Institute of Psychiatry, King's College London, London, London, United Kingdom,* [2]*CR-UK Clinical MR Research Group, Institute of Cancer Research, Sutton, Surrey, United Kingdom,* [3]*MRC London Neurodegenerative Diseases Brain Bank, Department of Clinical Neuroscience, Institute of Psychiatry, King's College London, London, United Kingdom,* [4]*Clinical Neuropathology & London Neurodegenerative Diseases Brain Bank, King's College London, King's College Hospital, London, United Kingdom,* [5]*Diamond Light Source, Harwell Science and Innovation Campus, Didcot, Oxfordshire, United Kingdom,* [6]*Agilent Technologies, Yarnton, Oxfordshire, United Kingdom*

Target Audience: This work is relevant for scientific researchers interested in neurodegenerative diseases and the basis of MR relaxometry measurements, more specifically, against iron.

Purpose: Iron dysregulation is being increasingly identified as a supporting mechanism for oxidative stress and cell death of neurons during neurodegenerative diesases[1], such as Alzheimer's disease (AD). Iron is highly paramagnetic and detection of iron *in vivo* may provide a viable method for non-invasive diagnosis or assessment of disease progression. Studies have shown clinical correlation of T2 and T2* measurements with iron in neurodegeneration, however iron quantities can only be correlated against published post-mortem results[2]. In animal experiments, relaxometry measurements can be correlated against Perl's staining, but whilst this method highlights iron accumulation, it remains a qualitative assessment[3]. The purpose of this study was to therefore correlate MR relaxometry measurement in human AD and control brain samples, against a quantitative method for iron assessment, using synchrotron radiation X-ray fluorescence (SR-XRF) elemental mapping.

Methods: Formalin-fixed post-mortem medial temporal gyri from AD (n=9) and control (n=11) human subjects were immersed in perfluoropolyether and positioned in a 7T MRI scanner. R1 and R2 relaxometry were performed using a spin-echo sequence with varying TR (300-4000ms) and TE (12-60ms), respectively. R2* relaxometry was performed using a gradient-echo sequence with varying TE (5-50ms). In-plane resolution was 0.11x0.15mm, thickness of 0.50mm. Following MRI, samples were processed and sectioned at 7µm for SR-XRF elemental iron mapping at 100µm resolution. Relaxometry and SR-XRF maps were manually registered in ImageJ and regions of interest (ROIs) drawn around the grey (GM) and white matter (WM), using a T2-weighted image as reference. Furthermore, for each sample, 20 small ROIs of 5x5 pixels were placed in each co-registered map to assess correlation of iron to relaxometry measurements (Fig.1).

Results and Discussion: Mean WM iron concentrations, R1, R2 and R2* values were significantly increased compared to GM ($P<0.001$) (Fig.1). A mid-layer of cortex was identified within the GM of each sample adjacent to the WM and an ROI of this region (Fig.2) showed higher amounts of iron and increased R1, R2 and R2* values compared to GM, but were lower than that in WM ($P<0.001$). This highlights the sensitivity of relaxometry measurements to different iron concentrations in human tissue[4]. Similar iron and relaxometry values were observed between control and AD samples in both WM and GM.

R1, R2 and R2* relaxometry correlated strongly to iron concentrations in individual samples (mean r^2 0.70±0.18, 0.81±0.12 and 0.80±0.13 respectively). However, pooling all the ROIs across all samples showed poor iron correlation against R1 (r^2=0.002), but remained good for R2 and R2* (r^2=0.480 and 0.567, respectively) (Fig.3). R1 values were subsequently found to be significantly affected by long term fixation of the samples ($P<0.001$), potentially driving the low R1 correlation against iron.

Good correlation of iron, R2 and R2* values with Luxol Fast Blue (LFB) staining for myelin was observed in both AD and control samples (Fig.4). Our results, taken together, are consistent with increased concentrations of iron within white matter myelin.

Conclusion: Iron levels and MR relaxometry were similar between control and AD, however R2 and R2* were shown to correlate with iron in both healthy and AD tissue, supporting their use in the non-invasive assessment of brain iron.

References: (1) Zecca L, et al. *Nature Reviews: Neuroscience.* 2004; 5:863-873. (2) Rodrigue KM, et al. *NeuroImage.* 2011; 54:750-759. (3) Wengenack TM, et al. *NeuroImage.* 2011; 54:113-122. (4) Fukunaga M, et al. *PNAS.* 2010; 8:3834-3839.

Fig 1

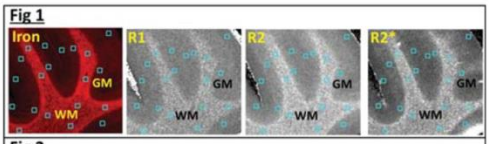

Fig 2

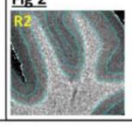

Fig.1 *Typical elemental iron and relaxometry maps with 20 small 5x5 pixel ROIs.* ***Fig.2*** *Representative R2 map showing the GM, mid-cortical GM and WM ROIs.*

Fig 3

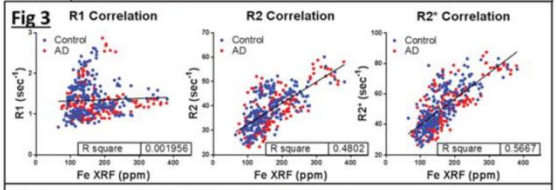

Fig 4

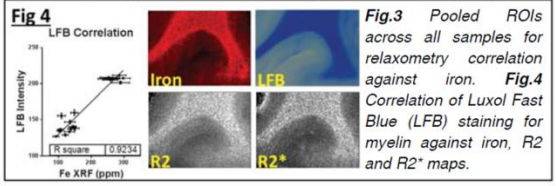

Fig.3 *Pooled ROIs across all samples for relaxometry correlation against iron.* ***Fig.4*** *Correlation of Luxol Fast Blue (LFB) staining for myelin against iron, R2 and R2* maps.*

387

MRI Relaxometry Correlation to Iron Levels Using Synchrotron Radiation X-Ray Fluorescence Mapping in Alzheimer's Disease

C. Michaelides[1], D.J. Lythgoe[1], H.G. Parkes[2], C. Troakes[3], I. Bodi[4], T. Geraki[5], A.H. Herlihy[6], P.W. So[1]
[1]Institute of Psychiatry, King's College London, London/UNITED KINGDOM, [2]CR-UK Clinical MR Research Group, Institute of Cancer Research, London/UNITED KINGDOM, [3]Institute of Psychiatry, MRC London Neurodegenerative Diseases Brain Bank, King's College London, London/UNITED KINGDOM, [4]Clinical Neuropathology and MRC London Neurodegenerative Diseases Brain Bank, King's College London, London/UNITED KINGDOM, [5]Diamond Light Source, Harwell Science and Innovation Campus, Didcot/UNITED KINGDOM, [6]Agilent Technologies, Yarnton, Oxford/UNITED KINGDOM

Purpose/Introduction: Alzheimer's disease (AD) is a neurodegenerative disease involving the gradual loss of neuronal cells within the central nervous system. Whilst a definitive cause for AD remains unknown, iron dysregulation is suggested to play a role during neurodegeneration by increasing oxidative stress, subsequently leading to cell death of neurons[1]. Iron is also highly paramagnetic, leading to changes in image contrast using certain MRI sequences including relaxometry measurements. This study was performed to correlate and evaluate the specificity of relaxometry measurements for iron using synchrotron radiation X-ray fluorescence (SR-XRF) mapping, between AD and control brain samples.

Subjects and Methods: R1, R2 and R2* relaxometry maps were generated of formalin fixed post-mortem medial temporal gyri from AD (n=6) and control (n=9) human brains. Samples were sectioned and elemental iron maps obtained using SR-XRF. Twenty regions of interest were drawn across each relaxometry map for comparison against registered iron maps within both grey (GM) and white (WM) matter. Individual sample data was normalised to correlate all relaxometry values against iron across multiple samples. Histological assessment of tissue was also performed.

Results: Iron and relaxometry values show significant correlation across all samples (R1: r^2=0.676, R2: r^2=0.786 and R2*: r^2=0.734, P<0.001). Separating AD and control samples provides equally good correlations for R2 (control: r^2=0.786, AD: r^2=0.790) and R2* (control: r^2=0.774, AD: r^2=0.702), however R1 correlation decreased in AD samples (control: r^2=0.728, AD: r^2=0.580, P=0.03), highlighting other tissue changes may potentially be occurring within AD tissue to affect R1 values, other than iron levels.

A significant increase in iron and all relaxometry values was identified in WM to GM (P<0.001), however comparison of control against AD relaxometry and iron values did not show significantly different results.

Subsequent histological analysis of tissue suggests strong correlation between myelin and iron, as well as R2 and R2* values.

Discussion/Conclusion: The correlations between relaxometry and iron observed in our study are comparable to previously published literature[2,3], however we have also been able to show correlation across multiple samples rather than within one sample as performed in the published studies. Our data also suggests increased R2 and R2* may be attributed to higher iron concentrations within myelin.

Although iron may play a role during AD, we, like others[2], were unable to detect elevated iron levels using SR-XRF between control and AD medial temporal gyri, a brain region affected during pathology.

References:

[1]Zecca L, 2004 Nat Rev Neurosci 863-873, [2]Antharam V, 2012 Neuroimage 1249-1260, [3]Zheng W, 2013 Neuroimage 68-74

Poster #206

A DECREASE IN NEURONAL FERROPORTIN ACCOMPANIES CHRONIC BRAIN INFLAMMATION WITH IRON DEPOSITION

Michelle Vandborg Andersen, BSc, Pia Rægaard Christoffersen, BSc, Malene Duedal Jensen, BSc, Jacek Lichota, MSc, PhD and Torben Moos
Aalborg University
(Presented By: Torben Moos)

Introduction: Conditions with neurodegeneration lead to significant accumulation of iron in the brain. The mechanisms for this accumulation of iron remain unresolved but two possible causes are denoted by: 1) the incapability of affected neurons to excrete iron mediated by ferroportin and 2) iron-containing inflammatory cells accumulating in brain areas with neurodegeneration. An experimental model of neurodegeneration can be generated by denervation of GABAergic striatal inputs to the substantia nigra via stereotactic injection of the glutamatergic receptor ligand ibotenic acid, which leads to deprivation in inhibitory inputs to the neurons of the substantia nigra pars reticulate due to a relative abundance of glutamate originating from excitatory projections from the subthalamic nucleus.
Methods and Materials: Accordingly, adult male Sprague-Dawley rats were injected unilaterally with ibotenic acid in the striatum, and brain stems were examined at one, four or thirteen weeks following surgery. In spite of being anatomically localized in distance from the striatum, the substantia nigra pars reticulate was clearly affected, indicating that remote surgery leads to an excitotoxic lesion. The substantia nigra pars reticulate contained numerous inflammatory cells expressing the clone-markers ED1 and CD11b suggesting these cells to be derived from the myelo-monocytic cell lineage. Notably, these cells also contained ferritin, and it was found that the substantia nigra pars reticulate continued to express these inflammatory markers over time together with an increase in ferritin. Neurons of the substantia nigra pars reticulate decreased their density with time, and surviving neurons contained less ferroportin with time. Supporting the latter observation, ferroportin mRNA was also less abundant with increasing time in the substantia nigra pars reticulate, whereas ferritin mRNA increased with time in the substantia nigra pars reticulate.
Results: The results show that chronic neurodegeneration can be induced in the brain with an accompanying inflammatory process that leads to deposition of iron in the affected area. The iron deposition was followed by an increase in ferritin mRNA and protein. In contrast the quantity of ferroportin mRNA was lower, an observation that was adjoined by lower ferroportin content in surviving neurons. The latter observation indicates that ferroportin is not upregulated in surviving neurons when iron increases as a mechanism to scavenge iron excess.
Conclusion: In additional explanation to the fall in ferroportin expression, the inflammatory process leading to migration of monocytes and macrophages to the brain leads to that these cells probably downregulate ferroportin via their release of hepcidin. In conclusion, experimentally induced chronic neurodegeneration leads to iron accumulation, upregulation of ferritin mRNA and protein, but a decrease in ferroportin mRNA and protein.

Poster #207

EVALUATION OF IRON LEVELS IN ALZHEIMER'S DISEASE USING MRI RELAXOMETRY

Christos Michaelides[1], David J. Lythgoe[1], Harold G. Parkes[2], Claire Troakes[1], Istvan Bodi[1], Tina Geraki[3], Amy H. Herlihy[4] and Po-Wah So[1]
[1]King's College London, London; [2]Institute of Cancer Research, London; [3]Diamond Light Source, Oxford; [4]Agilent Technologies, Oxford
(Presented By: Christos Michaelides)

Introduction: Alzheimer's disease (AD) is a neurodegenerative disease involving the gradual loss of neuronal cells within the central nervous system. Therapeutic strategies remain anti-symptomatic and methods for diagnosis and monitoring disease progression remain poorly validated. Iron dysregulation is being increasingly identified as a supporting mechanism for oxidative stress and cell death of neurons[1]. Increased levels of iron have been identified in brain regions most associated with AD[2] and iron has been found associated with β-amyloid plaques and neurofibrillary tangles, two major hallmarks of AD[3]. This study was performed to evaluate whether changes in iron can be detected between AD and control brain samples using MRI relaxometry.
Methods: Formalin-fixed post-mortem medial temporal gyri from AD (n=5) and control (n=5) human subjects were immersed in perfluoropolyether and positioned within a 7T Agilent Technologies VNMRS scanner. R1 and R2 relaxometry were performed using spin-echo sequences with varying TR and TE, respectively. R2* relaxometry was performed using a gradient-echo sequence with varying TE. Voxel sizes were 0.11x0.15x0.50mm. Elemental iron maps were obtained from a 10μm thick section of each sample using synchrotron radiation X-ray fluorescence, at 100μm resolution. Regions of interest were drawn around grey and white matter in R1, R2, R2* and iron elemental maps to compare mean values between control and AD samples.
Results and Discussion: Mean white and grey matter relaxometry values obtained using all five samples within each group were highly variable due to fixation time effects. R1 increased, whilst R2 and R2* values decreased with longer fixation times. Whilst changes in relaxometry during the fixation process have been characterised previously[4], our data highlights potential long term effects of fixation on human brain tissue, consistent with previous findings[5]. Thus, samples fixed for longer than 18 months were removed from statistical analysis and remaining control and AD samples (n=3/group) were paired according to

fixation time. Levels of iron appear to be increased in AD grey matter (152.9±20.2 ppm, Mean±SEM) compared to controls (118.2±15.4 ppm, P=0.062), with a concomitant increase in R2 (AD 36.7±2.7 sec^{-1}, Control 32.0±2.5 sec^{-1}, P=0.006) and R2* (AD 46.9±4.9 sec^{-1}, Control 38.5±4.1 sec^{-1}, P=0.036) relaxometry values. R1 were similar between control and AD. Our findings are consistent with iron−enhancement of T2 relaxation and lengthening of R2 and R2* values[6], and imply R2 and R2* relaxometry may provide information on the iron content in tissue. White matter showed similar values for iron levels, R1, R2 and R2* between AD and control tissue.

Conclusion: These results highlight a potential role for iron during AD within the medial temporal gyrus, and outline methods for non−invasive assessment using MR relaxometry. This may also substantiate the application of novel therapeutic strategies such as iron chelation therapies against AD.

References: (1) Zecca L, et al. Nature Reviews: Neuroscience. 2004 (2) Smith MA, et al. Journal of Alzheimer's disease. 2010 (3) Lovell MA, et al. Journal of Neurological Sciences. 1998 (4) Yong-Hing, et al. Magnetic Resonance in Medicine 2005 (5) Gellein K, et al. Biol Trace Elem Res. 2008 (6) Haacke EM, et al. Magnetic Resonance Imaging. 2005.

Poster #208

ALTERED BRAIN IRON HOMEOSTASIS IN PARKINSON'S DISEASE AND THE POTENTIAL FOR IRON CHELATION THERAPY

David Dexter, PhD[2], Roberta Ward, PhD[2], Robert Crichton, PhD[3], Veronica Kallo, PhD[1] and Surjit K. Srai, PhD[1]
[1]University College, London; [2]Imperial College, London; [3]University Catholique de Louvain
(Presented By: David Dexter)

Introduction: There is ample evidence which shows that excessive accumulation of iron occurs in specific brain regions in many neurodegenerative diseases, including Parkinson's disease, which may exacerbate the progression of the disease. A common feature in many neurodegenerative diseases is the occurrence of neuro-inflammation which is associated with the neurodegenerative process. The etiology of iron accumulation remains undefined although it maybe as a result of the inflammatory process triggering iron sequestration into neurons, within certain brain regions.

Methods and Materials: In our cell culture studies, the supernatant from cultured N9 microglia, activated with lipopolysaccharide (LPS) for 24h, was incubated with either dopaminergic neurons (N27) or astrocytic (C6) cell lines for time periods up to 24h. The expression of ferritin, transferrin receptors, DMT1 and ferroportin was assayed in the cells at the different time periods. Intracellular iron uptake in the N27 neurons was assessed by the ferrocene assay. The results showed that genes, which are involved in systemic iron homeostasis, transferrin receptors, DMT1 and ferroportin, were expressed on both astrocytes and neurons.

Results: Exposure of N27 neurons to supernatant from activated microglia stimulated a persistent increased neuronal expression of DMT1 and transferrin receptor, whilst the expression of ferroportin and ferritin were unchanged over the 24 hour period. This was mirrored by an increase in neuronal iron uptake. In contrast in the C6 astrocytes exposed to supernatants from activated microglia there was a transient increase in DMT1 expression which declined over 24 hours and there was a reduction in transferrin receptor expression at 12 and 24 hours. Ferroportin expression increased over the 24 hour period in the astrocytic cells. Hepcidin expression was evident in both microglia and astrocytes; and LPS activation of microglia was associated with a time dependent increase in hepcidin expression. The removal of such excesses of iron, via various iron chelators has been extolled in various publication although caution is needed because of the possible adverse effects of the administration of iron chelators to patients with otherwise normal iron homeostasis. A clinical trial to investigate the possibility of iron chelation in Parkinson's patients has commenced. Parkinson's patients received the oral ion chelator deferiprone at low doses, of either 20 or 30 mg/kg/day, for a period of 6 months. Such low doses of the oral iron chelator were well tolerated by the patients, showed minimal toxic effects, and induced decreases in iron in specific brain regions assayed by MRI T2*
Such iron chelation may represent a new therapeutic tool to slow the progression of PD.

Conclusion: Furthermore by increasing our knowledge of brain homeostasis, it should become possible to more closely control the expression of genes which are responsible for iron accumulation in specific glial and neuronal cells.

Poster #209

ANALYSIS OF IRON METABOLISM IN TFR2 TARGETED ANIMALS BRAIN

Rosa Maria Pellegrino, Enrica Boda, Martina Boero, Francesac Montarolo, Alessandro Volpengo, Giuseppe Saglio, Annalisa Buffo and Antonella Roetto
University of Torino – Dept. of Oncology
(Presented By: Antonella Roetto)

Introduction: It is well known that iron is an essential element for all cells and in brain also it is involved in important functions as neurotransmission and myelination as well as in neuronal cells division (Moos et al, 2007). Iron metabolism in the brain must be tightly regulated since iron overload has been evidenced in quite common neurodegenerative disorders like Parkinson and Alzheimer diseases. Hepcidin (Hamp), a key iron regulator, resulted to be present in the brain (Hanninen et al 2009) but it is not clear how Hamp and its regulating proteins modify iron availability in the nervous tissues.

Methods and Materials: Transferrin receptor 2 (TFR2) is one of the proteins involved Hamp regulation. The TFR2 gene is transcribed in two main isoforms, tfr2 alpha, an iron sensor that contributes to hepatic regulation of Hamp, and Tfr2 beta that seems to be involved in transcriptional regulation of iron exporter Ferroportin 1 (Fpn1). To get inside on Tfr2 isoforms functions

Appendix B

List of all obtained human tissue samples; with associated gender, age at death, PMD, PMI, and fixation time.

Control Samples					
Sample #	**Gender**	**Age (years)**	**PMD (months)**	**PMI (months)**	**Fixation Time (months)**
A319-11	Male	74	22.5	24	13
A114-12	Male	82	24	25	7
A261-12	Male	63	23	51	5
A388-12	Male	65	26	28	2
A213-12	Male	78	24	24	6
A127-11	Male	73	23	23	20
A53-11	Male	77	10	11	13
A346-10	Female	84	34	34	14
A33-11	Male	82	47	47	14
A130-09	Male	54	31	32	33
A136-10	Female	89	41	65	21

A404-12	Female	90	83	87	13
A329-12	Female	92	66	66	15
A382-12	Female	85	45	51	13
A152-13	Female	78	45	70	8

AD Samples

Sample #	Gender	Age (years)	PMD (months)	PMI (months)	Fixation Time (months)
A277-12	Male	79	20	24	3
A356-11	Female	77	42	69	12
A206-12	Female	88	41	41	6.5
A195-12	Female	83	20	20	6
A220-11	Female	71	18	19	7
A195-11	Female	78	39	67	8
A282-10	Male	68	25	25	16
A200-10	Female	81	23	23	20
A216-09	Female	88	22	44	31
A348-12	Male	75	69	98	14

A276-12	Male	77	43	45	16
A3-13	Male	64	48	71	11
A244-12	Male	75	27	68	18
A50-13	Male	74	15.5	41	10
A38-13	Male	72	73	73	12

References

Achterberg HC, van der Lijn F, den Heijer T, Vernooij MW, Ikram MA, Niessen WJ & de Bruijne M (2013) Hippocampal shape is predictive for the development of dementia in a normal, elderly population. *Hum Brain Mapp*.

Adams CW (1988) Perivascular iron deposition and other vascular damage in multiple sclerosis. *J Neurol Neurosurg Psychiatry* 51:260-265.

Adlard PA & Bush AI (2006) Metals and Alzheimer's disease. *J Alzheimers Dis* 10:145-163.

Ahmed Z, Shaw G, Sharma VP, Yang C, McGowan E & Dickson DW (2007) Actin-binding proteins coronin-1a and IBA-1 are effective microglial markers for immunohistochemistry. *J Histochem Cytochem* 55:687-700.

Alafuzoff I *et al.* (2008) Staging of neurofibrillary pathology in Alzheimer's disease: a study of the BrainNet Europe Consortium. *Brain Pathol* 18:484-496.

Alderson NL, Rembiesa BM, Walla MD, Bielawska A, Bielawski J & Hama H (2004) The human FA2H gene encodes a fatty acid 2-hydroxylase. *J Biol Chem* 279:48562-48568.

Alonso A, Zaidi T, Novak M, Grundke-Iqbal I & Iqbal K (2001) Hyperphosphorylation induces self-assembly of tau into tangles of paired helical filaments/straight filaments. *Proc Natl Acad Sci U S A* 98:6923-6928.

Alzheimer's Association, (2014) 2014 Alzheimer’s Disease Facts and Figures. 1-80

Alzheimer's Disease International, (2010) World Alzheimer Report 2010: The Global Economic Impact of Dementia. 1-56

Alzheimer's Disease International, (2013) Policy Brief for Heads of Government: The Global Impact of Dementia 2013–2050. 1-8

Alzheimer's Society, (2014a) Dementia UK: Update. 1-136

Alzheimer's Society, (2014b) Dementia 2014: Opportunity for Change. 1-86

Alzheimer A (1907) Über eine eigenartige Erkrankung der Hirnrinde. *Allgemeine Zeitschrift für Psychiatrie und Psychisch-Gerichtliche Medizin* 64:146-148.

Anders A, Gilbert S, Garten W, Postina R & Fahrenholz F (2001) Regulation of the alpha-secretase ADAM10 by its prodomain and proprotein convertases. *Faseb J* 15:1837-1839.

Anderson CP, Shen M, Eisenstein RS & Leibold EA (2012) Mammalian iron metabolism and its control by iron regulatory proteins. *Biochim Biophys Acta* 1823:1468-1483.

Antharam V, Collingwood JF, Bullivant JP, Davidson MR, Chandra S, Mikhaylova A, Finnegan ME, Batich C, Forder JR & Dobson J (2012) High field magnetic resonance microscopy of the human hippocampus in Alzheimer's disease: quantitative imaging and correlation with iron. *Neuroimage* 59:1249-1260.

Appleby A, Christman EA & Leghrouz A (1987) Imaging of spatial radiation dose distribution in agarose gels using magnetic resonance. *Med Phys* 14:382-384.

Armstrong C, Leong W & Lees GJ (2001) Comparative effects of metal chelating agents on the neuronal cytotoxicity induced by copper (Cu+2), iron (Fe+3) and zinc in the hippocampus. *Brain Res* 892:51-62.

Avramovich-Tirosh Y, Rezrlichenko D, Amit T, Zheng H, Fridkin M, Weinreb O, Mandel S & Youdim MBH (2007) Neurorescue activity, APP regulation and amyloid-beta peptide reduction by novel multi-functional brain permeable iron- chelating-antioxidants, m-30 and green tea polyphenol, EGCG. *Curr Alzheimer Res* 4:403-411.

Baba M, Nakajo S, Tu PH, Tomita T, Nakaya K, Lee VM, Trojanowski JQ & Iwatsubo T (1998) Aggregation of alpha-synuclein in Lewy bodies of sporadic Parkinson's disease and dementia with Lewy bodies. *Am J Pathol* 152:879-884.

Ball MJ, Fisman M, Hachinski V, Blume W, Fox A, Kral VA, Kirshen AJ, Fox H & Merskey H (1985) A new definition of Alzheimer's disease: a hippocampal dementia. *Lancet* 1:14-16.

Ballatore C, Lee VM & Trojanowski JQ (2007) Tau-mediated neurodegeneration in Alzheimer's disease and related disorders. *Nat Rev Neurosci* 8:663-672.

Bartzokis G, Aravagiri M, Oldendorf WH, Mintz J & Marder SR (1993) Field dependent transverse relaxation rate increase may be a specific measure of tissue iron stores. *Magn Reson Med* 29:459-464.

Bartzokis G, Cummings J, Perlman S, Hance DB & Mintz J (1999) Increased basal ganglia iron levels in Huntington disease. *Arch Neurol* 56:569-574.

Bartzokis G, Mintz J, Sultzer D, Marx P, Herzberg JS, Phelan CK & Marder SR (1994a) In vivo MR evaluation of age-related increases in brain iron. *AJNR Am J Neuroradiol* 15:1129-1138.

Bartzokis G, Sultzer D, Mintz J, Holt LE, Marx P, Phelan CK & Marder SR (1994b) In vivo evaluation of brain iron in Alzheimer's disease and normal subjects using MRI. *Biol Psychiatry* 35:480-487.

Bartzokis G, Sultzer D, Cummings J, Holt LE, Hance DB, Henderson VW & Mintz J (2000) In vivo evaluation of brain iron in Alzheimer disease using magnetic resonance imaging. *Arch Gen Psychiatry* 57:47-53.

Bartzokis G, Tishler TA, Lu PH, Villablanca P, Altshuler LL, Carter M, Huang D, Edwards N & Mintz J (2007a) Brain ferritin iron may influence age- and gender-related risks of neurodegeneration. *Neurobiol Aging* 28:414-423.

Bartzokis G, Lu PH, Tishler TA, Fong SM, Oluwadara B, Finn JP, Huang D, Bordelon Y, Mintz J & Perlman S (2007b) Myelin breakdown and iron changes in Huntington's disease: pathogenesis and treatment implications. *Neurochemical Research* 32:1655-1664.

Becker JS, Matusch A, Palm C, Salber D, Morton KA & Becker JS (2010) Bioimaging of metals in brain tissue by laser ablation inductively coupled plasma mass spectrometry (LA-ICP-MS) and metallomics. *Metallomics* 2:104-111.

Beharry C, Cohen LS, Di J, Ibrahim K, Briffa-Mirabella S & Alonso Adel C (2014) Tau-induced neurodegeneration: mechanisms and targets. *Neurosci Bull* 30:346-358.

Bennett KM, Shapiro EM, Sotak CH & Koretsky AP (2008) Controlled aggregation of ferritin to modulate MRI relaxivity. *Biophys J* 95:342-351.

Beutler E, Gelbart T, Lee P, Trevino R, Fernandez MA & Fairbanks VF (2000) Molecular characterization of a case of atransferrinemia. *Blood* 96:4071-4074.

Bishop GM & Robinson SR (2001) Quantitative analysis of cell death and ferritin expression in response to cortical iron: implications for hypoxia-ischemia and stroke. *Brain Res* 907:175-187.

Bishop GM & Robinson SR (2003) Human Abeta1-42 reduces iron-induced toxicity in rat cerebral cortex. *J Neurosci Res* 73:316-323.

Blamire AM, Rowe JG, Styles P & McDonald B (1999) Optimising imaging parameters for post mortem MR imaging of the human brain. *Acta Radiol* 40:593-597.

Bolognin S, Messori L, Drago D, Gabbiani C, Cendron L & Zatta P (2011) Aluminum, copper, iron and zinc differentially alter amyloid-A beta(1-42) aggregation and toxicity. *Int J Biochem Cell B* 43:877-885.

Bonda DJ, Lee HG, Blair JA, Zhu X, Perry G & Smith MA (2011) Role of metal dyshomeostasis in Alzheimer's disease. *Metallomics* 3:267-270.

Borchelt DR, Ratovitski T, van Lare J, Lee MK, Gonzales V, Jenkins NA, Copeland NG, Price DL & Sisodia SS (1997) Accelerated amyloid deposition in the brains of transgenic mice coexpressing mutant presenilin 1 and amyloid precursor proteins. *Neuron* 19:939-945.

Bostanci MO & Bagirici F (2007) Neuroprotection by 7-nitroindazole against iron-induced hippocampal neurotoxicity. *Cell Mol Neurobiol* 27:933-941.

Boyd-Kimball D, Sultana R, Poon HF, Lynn BC, Casamenti F, Pepeu G, Klein JB & Butterfield DA (2005) Proteomic identification of proteins specifically oxidized by intracerebral

injection of amyloid beta-peptide (1-42) into rat brain: implications for Alzheimer's disease. *Neuroscience* 132:313-324.

Bozoki A, Giordani B, Heidebrink JL, Berent S & Foster NL (2001) Mild cognitive impairments predict dementia in nondemented elderly patients with memory loss. *Arch Neurol* 58:411-416.

Bozzali M, Falini A, Franceschi M, Cercignani M, Zuffi M, Scotti G, Comi G & Filippi M (2002) White matter damage in Alzheimer's disease assessed in vivo using diffusion tensor magnetic resonance imaging. *J Neurol Neurosurg Psychiatry* 72:742-746.

Braak H & Braak E (1991) Neuropathological stageing of Alzheimer-related changes. *Acta Neuropathol* 82:239-259.

Bradbury MW (1997) Transport of iron in the blood-brain-cerebrospinal fluid system. *Journal of Neurochemistry* 69:443-454.

Bradley MA, Markesbery WR & Lovell MA (2010) Increased levels of 4-hydroxynonenal and acrolein in the brain in preclinical Alzheimer disease. *Free Radic Biol Med* 48:1570-1576.

Bradley WG, Jr. (1993) MR appearance of hemorrhage in the brain. *Radiology* 189:15-26.

Brandt J, Spencer M & Folstein M (1988) The telephone interview for cognitive status. *Neuropsychiatry Neuropsychol Behav Neurol* 1:111–117.

Breger RK, Yetkin FZ, Fischer ME, Papke RA, Haughton VM & Rimm AA (1991) T1 and T2 in the cerebrum: correlation with age, gender, and demographic factors. *Radiology* 181:545-547.

Brewer GJ (2012) Copper excess, zinc deficiency, and cognition loss in Alzheimer's disease. *Biofactors* 38:107-113.

Brooks DJ, Luthert P, Gadian D & Marsden CD (1989) Does signal-attenuation on high-field T2-weighted MRI of the brain reflect regional cerebral iron deposition?

Observations on the relationship between regional cerebral water proton T2 values and iron levels. *J Neurol Neurosurg Psychiatry* 52:108-111.

Brun A & Englund E (1986) A white matter disorder in dementia of the Alzheimer type: a pathoanatomical study. *Ann Neurol* 19:253-262.

Buee L, Bussiere T, Buee-Scherrer V, Delacourte A & Hof PR (2000) Tau protein isoforms, phosphorylation and role in neurodegenerative disorders. *Brain Res Brain Res Rev* 33:95-130.

Bush AI (2013) The metal theory of Alzheimer's disease. *J Alzheimers Dis* 33 Suppl 1:S277-281.

Bush VJ, Moyer TP, Batts KP & Parisi JE (1995) Essential and toxic element concentrations in fresh and formalin-fixed human autopsy tissues. *Clin Chem* 41:284-294.

Butterfield DA, Reed T, Newman SF & Sultana R (2007) Roles of amyloid beta-peptide-associated oxidative stress and brain protein modifications in the pathogenesis of Alzheimer's disease and mild cognitive impairment. *Free Radic Biol Med* 43:658-677.

Butterfield DA, Poon HF, St Clair D, Keller JN, Pierce WM, Klein JB & Markesbery WR (2006) Redox proteomics identification of oxidatively modified hippocampal proteins in mild cognitive impairment: insights into the development of Alzheimer's disease. *Neurobiol Dis* 22:223-232.

Cairo G, Rappocciolo E, Tacchini L & Schiaffonati L (1991) Expression of the Genes for the Ferritin-H and Ferritin-L Subunits in Rat-Liver and Heart - Evidence for Tissue-Specific Regulations at Pretranslational and Posttranslational Levels. *Biochemical Journal* 275:813-816.

Casey JL, Koeller DM, Ramin VC, Klausner RD & Harford JB (1989) Iron regulation of transferrin receptor mRNA levels requires iron-responsive elements and a rapid

turnover determinant in the 3' untranslated region of the mRNA. *The EMBO journal* 8:3693-3699.

Catala A (2009) Lipid peroxidation of membrane phospholipids generates hydroxy-alkenals and oxidized phospholipids active in physiological and/or pathological conditions. *Chem Phys Lipids* 157:1-11.

Chamberlain R, Reyes D, Curran GL, Marjanska M, Wengenack TM, Poduslo JF, Garwood M & Jack CR, Jr. (2009) Comparison of amyloid plaque contrast generated by T2-weighted, T2*-weighted, and susceptibility-weighted imaging methods in transgenic mouse models of Alzheimer's disease. *Magn Reson Med* 61:1158-1164.

Chen J, Marks E, Lai B, Zhang Z, Duce JA, Lam LQ, Volitakis I, Bush AI, Hersch S & Fox JH (2013) Iron accumulates in Huntington's disease neurons: protection by deferoxamine. *PLoS One* 8:e77023.

Chen JC, Borson S & Scanlan JM (2000) Stage-specific prevalence of behavioral symptoms in Alzheimer's disease in a multi-ethnic community sample. *Am J Geriatr Psychiatry* 8:123-133.

Chen Z, Gao C, Hua Y, Keep RF, Muraszko K & Xi G (2011) Role of iron in brain injury after intraventricular hemorrhage. *Stroke* 42:465-470.

Cheng HL, Stikov N, Ghugre NR & Wright GA (2012) Practical medical applications of quantitative MR relaxometry. *J Magn Reson Imaging* 36:805-824.

Chetelat G, Desgranges B, de la Sayette V, Viader F, Eustache F & Baron JC (2003) Mild cognitive impairment: Can FDG-PET predict who is to rapidly convert to Alzheimer's disease? *Neurology* 60:1374-1377.

Chong YH, Shin YJ, Lee EO, Kayed R, Glabe CG & Tenner AJ (2006) ERK1/2 activation mediates Abeta oligomer-induced neurotoxicity via caspase-3 activation and tau cleavage in rat organotypic hippocampal slice cultures. *J Biol Chem* 281:20315-20325.

Chua-anusorn W, Webb J, Macey DJ, Pootrakul P & St Pierre TG (1997) The effect of histological processing on the form of iron in iron-loaded human tissues. *Biochim Biophys Acta* 1360:255-261.

Citron M, Oltersdorf T, Haass C, McConlogue L, Hung AY, Seubert P, Vigo-Pelfrey C, Lieberburg I & Selkoe DJ (1992) Mutation of the beta-amyloid precursor protein in familial Alzheimer's disease increases beta-protein production. *Nature* 360:672-674.

Clark PR, Chua-Anusorn W & St Pierre TG (2003) Proton transverse relaxation rate (R2) images of liver tissue; mapping local tissue iron concentrations with MRI [corrected]. *Magn Reson Med* 49:572-575.

Cleveland DW, Hwo SY & Kirschner MW (1977) Physical and chemical properties of purified tau factor and the role of tau in microtubule assembly. *J Mol Biol* 116:227-247.

Cole SL & Vassar R (2008) The role of amyloid precursor protein processing by BACE1, the beta-secretase, in Alzheimer disease pathophysiology. *J Biol Chem* 283:29621-29625.

Collingwood J & Dobson J (2006) Mapping and characterization of iron compounds in Alzheimer's tissue. *J Alzheimers Dis* 10:215-222.

Collingwood JF, Mikhaylova A, Davidson M, Batich C, Streit WJ, Terry J & Dobson J (2005) In situ characterization and mapping of iron compounds in Alzheimer's disease tissue. *J Alzheimers Dis* 7:267-272.

Connor JR & Menzies SL (1996) Relationship of iron to oligodendrocytes and myelination. *Glia* 17:83-93.

Connor JR, Menzies SL, St Martin SM & Mufson EJ (1990) Cellular-Distribution of Transferrin, Ferritin, and Iron in Normal and Aged Human Brains. *J Neurosci Res* 27:595-611.

Connor JR, Menzies SL, St Martin SM & Mufson EJ (1992a) A histochemical study of iron, transferrin, and ferritin in Alzheimer's diseased brains. *J Neurosci Res* 31:75-83.

Connor JR, Boeshore KL, Benkovic SA & Menzies SL (1994) Isoforms of Ferritin Have a Specific Cellular-Distribution in the Brain. *J Neurosci Res* 37:461-465.

Connor JR, Snyder BS, Beard JL, Fine RE & Mufson EJ (1992b) Regional distribution of iron and iron-regulatory proteins in the brain in aging and Alzheimer's disease. *J Neurosci Res* 31:327-335.

Cook SE, Marsiske M & McCoy KJ (2009) The use of the Modified Telephone Interview for Cognitive Status (TICS-M) in the detection of amnestic mild cognitive impairment. *J Geriatr Psychiatry Neurol* 22:103-109.

Corrigan FM, Reynolds GP & Ward NI (1993) Hippocampal tin, aluminum and zinc in Alzheimer's disease. *Biometals* 6:149-154.

Craelius W, Migdal MW, Luessenhop CP, Sugar A & Mihalakis I (1982) Iron deposits surrounding multiple sclerosis plaques. *Arch Pathol Lab Med* 106:397-399.

Cruts M & Van Broeckhoven C (1998) Presenilin mutations in Alzheimer's disease. *Hum Mutat* 11:183-190.

Curtis ARJ, Fey C, Morris CM, Bindoff LA, Ince PG, Chinnery PF, Coulthard A, Jackson MJ, Jackson AP, McHale DP, Hay D, Barker WA, Markham AF, Bates D, Curtis A & Burn J (2001) Mutation in the gene encoding ferritin light polypeptide causes dominant adult-onset basal ganglia disease. *Nat Genet* 28:350-354.

Czervionke LF, Daniels DL, Wehrli FW, Mark LP, Hendrix LE, Strandt JA, Williams AL & Haughton VM (1988) Magnetic susceptibility artifacts in gradient-recalled echo MR imaging. *AJNR Am J Neuroradiol* 9:1149-1155.

Dadras A, Riazi GH, Afrasiabi A, Naghshineh A, Ghalandari B & Mokhtari F (2013) In vitro study on the alterations of brain tubulin structure and assembly affected by

magnetite nanoparticles. *Journal of biological inorganic chemistry : JBIC : a publication of the Society of Biological Inorganic Chemistry* 18:357-369.

Daubner SC, Le T & Wang S (2011) Tyrosine hydroxylase and regulation of dopamine synthesis. *Arch Biochem Biophys* 508:1-12.

Dawe RJ, Bennett DA, Schneider JA, Vasireddi SK & Arfanakis K (2009) Postmortem MRI of human brain hemispheres: T2 relaxation times during formaldehyde fixation. *Magn Reson Med* 61:810-818.

De Felice FG, Wu D, Lambert MP, Fernandez SJ, Velasco PT, Lacor PN, Bigio EH, Jerecic J, Acton PJ, Shughrue PJ, Chen-Dodson E, Kinney GG & Klein WL (2008) Alzheimer's disease-type neuronal tau hyperphosphorylation induced by A beta oligomers. *Neurobiol Aging* 29:1334-1347.

de Pasquale F, Cherubini A, Peran P, Caltagirone C & Sabatini U (2013) Influence of white matter fiber orientation on R2* revealed by MRI segmentation. *J Magn Reson Imaging* 37:85-91.

de Rochefort L, Liu T, Kressler B, Liu J, Spincemaille P, Lebon V, Wu J & Wang Y (2010) Quantitative susceptibility map reconstruction from MR phase data using bayesian regularization: validation and application to brain imaging. *Magn Reson Med* 63:194-206.

de Souza LC, Chupin M, Lamari F, Jardel C, Leclercq D, Colliot O, Lehericy S, Dubois B & Sarazin M (2012) CSF tau markers are correlated with hippocampal volume in Alzheimer's disease. *Neurobiol Aging* 33:1253-1257.

de Toledo-Morrell L, Dickerson B, Sullivan MP, Spanovic C, Wilson R & Bennett DA (2000) Hemispheric differences in hippocampal volume predict verbal and spatial memory performance in patients with Alzheimer's disease. *Hippocampus* 10:136-142.

de Torres C, Munell F, Ferrer I, Reventos J & Macaya A (1997) Identification of necrotic cell death by the TUNEL assay in the hypoxic-ischemic neonatal rat brain. *Neurosci Lett* 230:1-4.

Dedman DJ, Treffry A, Candy JM, Taylor GA, Morris CM, Bloxham CA, Perry RH, Edwardson JA & Harrison PM (1992) Iron and aluminium in relation to brain ferritin in normal individuals and Alzheimer's-disease and chronic renal-dialysis patients. *Biochem J* 287 (Pt 2):509-514.

Deibel MA, Ehmann WD & Markesbery WR (1996) Copper, iron, and zinc imbalances in severely degenerated brain regions in Alzheimer's disease: possible relation to oxidative stress. *J Neurol Sci* 143:137-142.

Delay C, Mandemakers W & Hebert SS (2012) MicroRNAs in Alzheimer's disease. *Neurobiol Dis* 46:285-290.

den Heijer T, van der Lijn F, Koudstaal PJ, Hofman A, van der Lugt A, Krestin GP, Niessen WJ & Breteler MM (2010) A 10-year follow-up of hippocampal volume on magnetic resonance imaging in early dementia and cognitive decline. *Brain* 133:1163-1172.

Deoni SC (2010) Quantitative relaxometry of the brain. *Top Magn Reson Imaging* 21:101-113.

Devos D *et al.* (2014) Targeting chelatable iron as a therapeutic modality in Parkinson's disease. *Antioxid Redox Signal* 21:195-210.

Dexter DT, Wells FR, Agid F, Agid Y, Lees AJ, Jenner P & Marsden CD (1987) Increased nigral iron content in postmortem parkinsonian brain. *Lancet* 2:1219-1220.

Dexter DT, Wells FR, Lees AJ, Agid F, Agid Y, Jenner P & Marsden CD (1989) Increased nigral iron content and alterations in other metal ions occurring in brain in Parkinson's disease. *Journal of Neurochemistry* 52:1830-1836.

Dexter DT, Carayon A, Javoy-Agid F, Agid Y, Wells FR, Daniel SE, Lees AJ, Jenner P & Marsden CD (1991) Alterations in the levels of iron, ferritin and other trace metals

in Parkinson's disease and other neurodegenerative diseases affecting the basal ganglia. *Brain* 114 (Pt 4):1953-1975.

Dheen ST, Kaur C & Ling EA (2007) Microglial activation and its implications in the brain diseases. *Curr Med Chem* 14:1189-1197.

Dhenain M, El Tannir El Tayara N, Wu TD, Guegan M, Volk A, Quintana C & Delatour B (2009) Characterization of in vivo MRI detectable thalamic amyloid plaques from APP/PS1 mice. *Neurobiol Aging* 30:41-53.

Diedenhofen B & Musch J (2015) cocor: A Comprehensive Solution for the Statistical Comparison of Correlations. *PLoS One* 10:e0121945.

Dietrich O, Levin J, Giese A, Plate A, Bötzel K, Reiser MF & Ertl-Wagner B (2013) Differentiation of Fe2+ and Fe3+ with iron-sensitive MRI. *Proc Intl Soc Mag Reson Med* (ISMRM Abstract) 21:2482.

Dobson J & Grassi P (1996) Magnetic properties of human hippocampal tissue--evaluation of artefact and contamination sources. *Brain Res Bull* 39:255-259.

Duce JA *et al.* (2010) Iron-export ferroxidase activity of beta-amyloid precursor protein is inhibited by zinc in Alzheimer's disease. *Cell* 142:857-867.

Emre M, Heckers S, Mash DC, Geula C & Mesulam MM (1993) Cholinergic innervation of the amygdaloid complex in the human brain and its alterations in old age and Alzheimer's disease. *J Comp Neurol* 336:117-134.

Everett J, Cespedes E, Shelford LR, Exley C, Collingwood JF, Dobson J, van der Laan G, Jenkins CA, Arenholz E & Telling ND (2014a) Evidence of redox-active iron formation following aggregation of ferrihydrite and the Alzheimer's disease peptide beta-amyloid. *Inorg Chem* 53:2803-2809.

Everett J, Cespedes E, Shelford LR, Exley C, Collingwood JF, Dobson J, van der Laan G, Jenkins CA, Arenholz E & Telling ND (2014b) Ferrous iron formation following the

co-aggregation of ferric iron and the Alzheimer's disease peptide beta-amyloid (1-42). *J R Soc Interface* 11:20140165.

Ewers M, Mattsson N, Minthon L, Molinuevo JL, Antonell A, Popp J, Jessen F, Herukka SK, Soininen H, Maetzler W, Leyhe T, Burger K, Taniguchi M, Urakami K, Lista S, Dubois B, Blennow K & Hampel H (2015) CSF biomarkers for the differential diagnosis of Alzheimer's disease. A large-scale international multicenter study. *Alzheimers Dement*.

Fagan AJ, Mullin JM, Gallagher L, Hadley DM, Macrae IM & Condon B (2008) Serial postmortem relaxometry in the normal rat brain and following stroke. *J Magn Reson Imaging* 27:469-475.

Falangola MF, Lee S-P, Nixon RA, Duff K & Helpern JA (2005) Histological Co-Localization of Iron in A beta Plaques of PS/APP Transgenic Mice. *Neurochemical Research* 30:201-205.

Folstein MF, Folstein SE & McHugh PR (1975) "Mini-mental state". A practical method for grading the cognitive state of patients for the clinician. *J Psychiatr Res* 12:189-198.

Fox CH, Johnson FB, Whiting J & Roller PP (1985) Formaldehyde fixation. *J Histochem Cytochem* 33:845-853.

Fox NC & Freeborough PA (1997) Brain atrophy progression measured from registered serial MRI: validation and application to Alzheimer's disease. *J Magn Reson Imaging* 7:1069-1075.

Fox NC, Scahill RI, Crum WR & Rossor MN (1999) Correlation between rates of brain atrophy and cognitive decline in AD. *Neurology* 52:1687-1689.

Fukunaga M, Li TQ, van Gelderen P, de Zwart JA, Shmueli K, Yao B, Lee J, Maric D, Aronova MA, Zhang G, Leapman RD, Schenck JF, Merkle H & Duyn JH (2010) Layer-specific variation of iron content in cerebral cortex as a source of MRI contrast. *Proc Natl Acad Sci U S A* 107:3834-3839.

Gabbita SP, Lovell MA & Markesbery WR (1998) Increased nuclear DNA oxidation in the brain in Alzheimer's disease. *Journal of Neurochemistry* 71:2034-2040.

Gauthier S, Reisberg B, Zaudig M, Petersen RC, Ritchie K, Broich K, Belleville S, Brodaty H, Bennett D, Chertkow H, Cummings JL, de Leon M, Feldman H, Ganguli M, Hampel H, Scheltens P, Tierney MC, Whitehouse P & Winblad B (2006) Mild cognitive impairment. *Lancet* 367:1262-1270.

Ge Y, Jensen JH, Lu H, Helpern JA, Miles L, Inglese M, Babb JS, Herbert J & Grossman RI (2007) Quantitative assessment of iron accumulation in the deep gray matter of multiple sclerosis by magnetic field correlation imaging. *AJNR Am J Neuroradiol* 28:1639-1644.

Geekiyanage H, Jicha GA, Nelson PT & Chan C (2012) Blood serum miRNA: non-invasive biomarkers for Alzheimer's disease. *Exp Neurol* 235:491-496.

Gellein K, Flaten TP, Erikson KM, Aschner M & Syversen T (2008) Leaching of trace elements from biological tissue by formalin fixation. *Biol Trace Elem Res* 121:221-225.

Gelman N, Ewing JR, Gorell JM, Spickler EM & Solomon EG (2001) Interregional variation of longitudinal relaxation rates in human brain at 3.0 T: relation to estimated iron and water contents. *Magnetic resonance in medicine* 45:71-79.

Gelman N, Gorell JM, Barker PB, Savage RM, Spickler EM, Windham JP & Knight RA (1999) MR imaging of human brain at 3.0 T: preliminary report on transverse relaxation rates and relation to estimated iron content. *Radiology* 210:759-767.

Gomme PT & McCann KB (2005) Transferrin: structure, function and potential therapeutic actions. *Drug Discov Today* 10:267-273.

Good PF, Perl DP, Bierer LM & Schmeidler J (1992) Selective accumulation of aluminum and iron in the neurofibrillary tangles of Alzheimer's disease: a laser microprobe (LAMMA) study. *Ann Neurol* 31:286-292.

Goodman L (1953) Alzheimer's disease; a clinico-pathologic analysis of twenty-three cases with a theory on pathogenesis. *J Nerv Ment Dis* 118:97-130.

Gossuin Y, Muller RN & Gillis P (2004) Relaxation induced by ferritin: a better understanding for an improved MRI iron quantification. *NMR Biomed* 17:427-432.

Gossuin Y, Gillis P, Muller RN & Hocq A (2007) Relaxation by clustered ferritin: a model for ferritin-induced relaxation in vivo. *NMR Biomed* 20:749-756.

Gossuin Y, Roch A, Muller RN, Gillis P & Lo Bue F (2002) Anomalous nuclear magnetic relaxation of aqueous solutions of ferritin: an unprecedented first-order mechanism. *Magn Reson Med* 48:959-964.

Graeber MB (2010) Changing face of microglia. *Science* 330:783-788.

Guillozet AL, Weintraub S, Mash DC & Mesulam MM (2003) Neurofibrillary tangles, amyloid, and memory in aging and mild cognitive impairment. *Arch Neurol* 60:729-736.

Gupta VB, Anitha S, Hegde ML, Zecca L, Garruto RM, Ravid R, Shankar SK, Stein R, Shanmugavelu P & Jagannatha Rao KS (2005) Aluminium in Alzheimer's disease: are we still at a crossroad? *Cellular and molecular life sciences : CMLS* 62:143-158.

Gyorffy-Wagner Z, Englund E, Larsson EM, Brun A, Cronqvist S & Persson B (1986) Proton magnetic resonance relaxation times T1 and T2 related to postmortem interval. An investigation on porcine brain tissue. *Acta Radiol Diagn (Stockh)* 27:115-118.

Haacke EM, Xu Y, Cheng YC & Reichenbach JR (2004) Susceptibility weighted imaging (SWI). *Magn Reson Med* 52:612-618.

Haacke EM, Cheng NY, House MJ, Liu Q, Neelavalli J, Ogg RJ, Khan A, Ayaz M, Kirsch W & Obenaus A (2005) Imaging iron stores in the brain using magnetic resonance imaging. *Magn Reson Imaging* 23:1-25.

Haacke EM, Ayaz M, Khan A, Manova ES, Krishnamurthy B, Gollapalli L, Ciulla C, Kim I, Petersen F & Kirsch W (2007) Establishing a baseline phase behavior in magnetic

resonance imaging to determine normal vs. abnormal iron content in the brain. *J Magn Reson Imaging* 26:256-264.

Hallgren B & Sourander P (1958) The effect of age on the non-haemin iron in the human brain. *Journal of Neurochemistry* 3:41-51.

Hallgren B & Sourander P (1960) The non-haemin iron in the cerebral cortex in Alzheimer's disease. *Journal of Neurochemistry* 5:307-310.

Han J, Day JR, Connor JR & Beard JL (2002) H and L ferritin subunit mRNA expression differs in brains of control and iron-deficient rats. *J Nutr* 132:2769-2774.

Hardy J (1997) Amyloid, the presenilins and Alzheimer's disease. *Trends Neurosci* 20:154-159.

Hardy J & Selkoe DJ (2002) The amyloid hypothesis of Alzheimer's disease: progress and problems on the road to therapeutics. *Science* 297:353-356.

Harrison PM & Arosio P (1996) The ferritins: molecular properties, iron storage function and cellular regulation. *Biochimica et Biophysica Acta (BBA) - Bioenergetics* 1275:161-203.

Helpern JA, Jensen J, Lee SP & Falangola MF (2004) Quantitative MRI assessment of Alzheimer's disease. *J Mol Neurosci* 24:45-48.

Hem JD & Cropper WH. U.S Geological Survey, (1962) Survey of Ferrous-Ferric Chemical Equilibria and Redox Potentials. Chemistry of Iron in Natural Water, 1-32

Hennig J (1988) Multiecho Imaging Sequences with Low Refocusing Flip Angles. *J Magn Reson* 78:397-407.

Henriksen K, O'Bryant SE, Hampel H, Trojanowski JQ, Montine TJ, Jeromin A, Blennow K, Lonneborg A, Wyss-Coray T, Soares H, Bazenet C, Sjogren M, Hu W, Lovestone S, Karsdal MA & Weiner MW (2014) The future of blood-based biomarkers for Alzheimer's disease. *Alzheimers Dement* 10:115-131.

Hensley K, Hall N, Subramaniam R, Cole P, Harris M, Aksenov M, Aksenova M, Gabbita SP, Wu JF, Carney JM & et al. (1995) Brain regional correspondence between Alzheimer's disease histopathology and biomarkers of protein oxidation. *Journal of Neurochemistry* 65:2146-2156.

Hentze MW, Muckenthaler MU & Andrews NC (2004) Balancing acts: molecular control of mammalian iron metabolism. *Cell* 117:285-297.

Hirose W, Ikematsu K & Tsuda R (2003) Age-associated increases in heme oxygenase-1 and ferritin immunoreactivity in the autopsied brain. *Legal Medicine* 5:S360-S366.

Hirsch EC, Brandel JP, Galle P, Javoy-Agid F & Agid Y (1991) Iron and aluminum increase in the substantia nigra of patients with Parkinson's disease: an X-ray microanalysis. *Journal of Neurochemistry* 56:446-451.

Hodges JR & Patterson K (1995) Is semantic memory consistently impaired early in the course of Alzheimer's disease? Neuroanatomical and diagnostic implications. *Neuropsychologia* 33:441-459.

Holmes C, Boche D, Wilkinson D, Yadegarfar G, Hopkins V, Bayer A, Jones RW, Bullock R, Love S, Neal JW, Zotova E & Nicoll JA (2008) Long-term effects of Abeta42 immunisation in Alzheimer's disease: follow-up of a randomised, placebo-controlled phase I trial. *Lancet* 372:216-223.

House E, Esiri M, Forster G, Ince PG & Exley C (2012) Aluminium, iron and copper in human brain tissues donated to the Medical Research Council's Cognitive Function and Ageing Study. *Metallomics* 4:56-65.

House MJ, St Pierre TG & McLean C (2008) 1.4T study of proton magnetic relaxation rates, iron concentrations, and plaque burden in Alzheimer's disease and control postmortem brain tissue. *Magn Reson Med* 60:41-52.

House MJ, St Pierre TG, Foster JK, Martins RN & Clarnette R (2006) Quantitative MR imaging R-2 relaxometry in elderly participants reporting memory loss. *Am J Neuroradiol* 27:430-439.

House MJ, St Pierre TG, Milward EA, Bruce DG & Olynyk JK (2010) Relationship between brain R(2) and liver and serum iron concentrations in elderly men. *Magn Reson Med* 63:275-281.

House MJ, St Pierre TG, Kowdley KV, Montine T, Connor J, Beard J, Berger J, Siddaiah N, Shankland E & Jin LW (2007) Correlation of proton transverse relaxation rates (R2) with iron concentrations in postmortem brain tissue from alzheimer's disease patients. *Magn Reson Med* 57:172-180.

Huang FP, Xi G, Keep RF, Hua Y, Nemoianu A & Hoff JT (2002) Brain edema after experimental intracerebral hemorrhage: role of hemoglobin degradation products. *J Neurosurg* 96:287-293.

Huang J, Friedland RP & Auchus AP (2007) Diffusion tensor imaging of normal-appearing white matter in mild cognitive impairment and early Alzheimer disease: preliminary evidence of axonal degeneration in the temporal lobe. *AJNR Am J Neuroradiol* 28:1943-1948.

Huang X, Atwood CS, Hartshorn MA, Multhaup G, Goldstein LE, Scarpa RC, Cuajungco MP, Gray DN, Lim J, Moir RD, Tanzi RE & Bush AI (1999) The A beta peptide of Alzheimer's disease directly produces hydrogen peroxide through metal ion reduction. *Biochemistry* 38:7609-7616.

Hwang EM, Kim SK, Sohn JH, Lee JY, Kim Y, Kim YS & Mook-Jung I (2006) Furin is an endogenous regulator of alpha-secretase associated APP processing. *Biochem Biophys Res Commun* 349:654-659.

Hye A, Lynham S, Thambisetty M, Causevic M, Campbell J, Byers HL, Hooper C, Rijsdijk F, Tabrizi SJ, Banner S, Shaw CE, Foy C, Poppe M, Archer N, Hamilton G, Powell J,

Brown RG, Sham P, Ward M & Lovestone S (2006) Proteome-based plasma biomarkers for Alzheimer's disease. *Brain* 129:3042-3050.

Hyman BT, Van Hoesen GW, Damasio AR & Barnes CL (1984) Alzheimer's disease: cell-specific pathology isolates the hippocampal formation. *Science* 225:1168-1170.

Ibach B, Haen E, Marienhagen J & Hajak G (2005) Clioquinol treatment in familiar early onset of Alzheimer's disease: a case report. *Pharmacopsychiatry* 38:178-179.

Ith M, Bigler P, Scheurer E, Kreis R, Hofmann L, Dirnhofer R & Boesch C (2002) Observation and identification of metabolites emerging during postmortem decomposition of brain tissue by means of in situ 1H-magnetic resonance spectroscopy. *Magn Reson Med* 48:915-920.

Ito D, Imai Y, Ohsawa K, Nakajima K, Fukuuchi Y & Kohsaka S (1998) Microglia-specific localisation of a novel calcium binding protein, Iba1. *Brain Res Mol Brain Res* 57:1-9.

Izquierdo A, Wellman CL & Holmes A (2006) Brief uncontrollable stress causes dendritic retraction in infralimbic cortex and resistance to fear extinction in mice. *J Neurosci* 26:5733-5738.

Jack CR, Jr., Knopman DS, Jagust WJ, Shaw LM, Aisen PS, Weiner MW, Petersen RC & Trojanowski JQ (2010) Hypothetical model of dynamic biomarkers of the Alzheimer's pathological cascade. *Lancet Neurol* 9:119-128.

Jack CR, Jr., Petersen RC, Xu YC, O'Brien PC, Smith GE, Ivnik RJ, Boeve BF, Waring SC, Tangalos EG & Kokmen E (1999) Prediction of AD with MRI-based hippocampal volume in mild cognitive impairment. *Neurology* 52:1397-1403.

Jack CR, Jr., Shiung MM, Gunter JL, O'Brien PC, Weigand SD, Knopman DS, Boeve BF, Ivnik RJ, Smith GE, Cha RH, Tangalos EG & Petersen RC (2004) Comparison of different MRI brain atrophy rate measures with clinical disease progression in AD. *Neurology* 62:591-600.

Jack CR, Jr., Lowe VJ, Weigand SD, Wiste HJ, Senjem ML, Knopman DS, Shiung MM, Gunter JL, Boeve BF, Kemp BJ, Weiner M & Petersen RC (2009) Serial PIB and MRI in normal, mild cognitive impairment and Alzheimer's disease: implications for sequence of pathological events in Alzheimer's disease. *Brain* 132:1355-1365.

Jellinger K, Paulus W, Grundke-Iqbal I, Riederer P & Youdim MB (1990) Brain iron and ferritin in Parkinson's and Alzheimer's diseases. *J Neural Transm Park Dis Dement Sect* 2:327-340.

Jensen JH, Chandra R, Ramani A, Lu H, Johnson G, Lee SP, Kaczynski K & Helpern JA (2006) Magnetic field correlation imaging. *Magn Reson Med* 55:1350-1361.

Jensen JH, Szulc K, Hu C, Ramani A, Lu H, Xuan L, Falangola MF, Chandra R, Knopp EA, Schenck J, Zimmerman EA & Helpern JA (2009) Magnetic field correlation as a measure of iron-generated magnetic field inhomogeneities in the brain. *Magn Reson Med* 61:481-485.

Jomova K & Valko M (2011) Advances in metal-induced oxidative stress and human disease. *Toxicology* 283:65-87.

Jomova K, Vondrakova D, Lawson M & Valko M (2010) Metals, oxidative stress and neurodegenerative disorders. *Mol Cell Biochem* 345:91-104.

Jucker M (2010) The benefits and limitations of animal models for translational research in neurodegenerative diseases. *Nat Med* 16:1210-1214.

Kasarskis EJ, Tandon L, Lovell MA & Ehmann WD (1995) Aluminum, calcium, and iron in the spinal cord of patients with sporadic amyotrophic lateral sclerosis using laser microprobe mass spectroscopy: a preliminary study. *J Neurol Sci* 130:203-208.

Kato H, Kogure K, Ohtomo H, Izumiyama M, Tobita M, Matsui S, Yamamoto E, Kohno H, Ikebe Y & Watanabe T (1986) Characterization of experimental ischemic brain edema utilizing proton nuclear magnetic resonance imaging. *J Cereb Blood Flow Metab* 6:212-221.

Kaur D, Yantiri F, Rajagopalan S, Kumar J, Mo JQ, Boonplueang R, Viswanath V, Jacobs R, Yang L, Beal MF, DiMonte D, Volitaskis I, Ellerby L, Cherny RA, Bush AI & Andersen JK (2003) Genetic or pharmacological iron chelation prevents MPTP-induced neurotoxicity in vivo: a novel therapy for Parkinson's disease. *Neuron* 37:899-909.

Kayed R & Lasagna-Reeves CA (2013) Molecular mechanisms of amyloid oligomers toxicity. *J Alzheimers Dis* 33 Suppl 1:S67-78.

Keller JN, Schmitt FA, Scheff SW, Ding Q, Chen Q, Butterfield DA & Markesbery WR (2005) Evidence of increased oxidative damage in subjects with mild cognitive impairment. *Neurology* 64:1152-1156.

Kiddle SJ, Sattlecker M, Proitsi P, Simmons A, Westman E, Bazenet C, Nelson SK, Williams S, Hodges A, Johnston C, Soininen H, Kloszewska I, Mecocci P, Tsolaki M, Vellas B, Newhouse S, Lovestone S & Dobson RJ (2014) Candidate blood proteome markers of Alzheimer's disease onset and progression: a systematic review and replication study. *J Alzheimers Dis* 38:515-531.

Kirschvink JL, Kobayashi-Kirschvink A & Woodford BJ (1992) Magnetite biomineralization in the human brain. *Proc Natl Acad Sci U S A* 89:7683-7687.

Kjos BO, Ehman RL & Brant-Zawadzki M (1985) Reproducibility of T1 and T2 relaxation times calculated from routine MR imaging sequences: phantom study. *AJR Am J Roentgenol* 144:1157-1163.

Klatzo I, Wisniewski H & Streicher E (1965) Experimental Production of Neurofibrillary Degeneration. I. Light Microscopic Observations. *J Neuropathol Exp Neurol* 24:187-199.

Klausner RD, Rouault TA & Harford JB (1993) Regulating the fate of mRNA: the control of cellular iron metabolism. *Cell* 72:19-28.

Klein WL (2013) Synaptotoxic amyloid-beta oligomers: a molecular basis for the cause, diagnosis, and treatment of Alzheimer's disease? *J Alzheimers Dis* 33 Suppl 1:S49-65.

Koeppen AH, Dickson AC & McEvoy JA (1995) The cellular reactions to experimental intracerebral hemorrhage. *J Neurol Sci* 134 Suppl:102-112.

Kopeikina KJ, Hyman BT & Spires-Jones TL (2012) Soluble forms of tau are toxic in Alzheimer's disease. *Transl Neurosci* 3:223-233.

Krasuski JS, Alexander GE, Horwitz B, Daly EM, Murphy DG, Rapoport SI & Schapiro MB (1998) Volumes of medial temporal lobe structures in patients with Alzheimer's disease and mild cognitive impairment (and in healthy controls). *Biol Psychiatry* 43:60-68.

Krebs N, Langkammer C, Goessler W, Ropele S, Fazekas F, Yen K & Scheurer E (2014) Assessment of trace elements in human brain using inductively coupled plasma mass spectrometry. *J Trace Elem Med Biol* 28:1-7.

Langkammer C, Krebs N, Goessler W, Scheurer E, Ebner F, Yen K, Fazekas F & Ropele S (2010) Quantitative MR imaging of brain iron: a postmortem validation study. *Radiology* 257:455-462.

Lanphear BP, Hornung R, Khoury J, Yolton K, Baghurst P, Bellinger DC, Canfield RL, Dietrich KN, Bornschein R, Greene T, Rothenberg SJ, Needleman HL, Schnaas L, Wasserman G, Graziano J & Roberts R (2005) Low-level environmental lead exposure and children's intellectual function: an international pooled analysis. *Environ Health Perspect* 113:894-899.

Laule C, Leung E, Lis DK, Traboulsee AL, Paty DW, MacKay AL & Moore GR (2006) Myelin water imaging in multiple sclerosis: quantitative correlations with histopathology. *Mult Scler* 12:747-753.

Lavados M, Guillon M, Mujica MC, Rojo LE, Fuentes P & Maccioni RB (2008) Mild cognitive impairment and Alzheimer patients display different levels of redox-active CSF iron. *Journal of Alzheimers Disease* 13:225-232.

Lee HG, Zhu X, Castellani RJ, Nunomura A, Perry G & Smith MA (2007) Amyloid-beta in Alzheimer disease: the null versus the alternate hypotheses. *J Pharmacol Exp Ther* 321:823-829.

Lei P, Ayton S, Finkelstein DI, Spoerri L, Ciccotosto GD, Wright DK, Wong BX, Adlard PA, Cherny RA, Lam LQ, Roberts BR, Volitakis I, Egan GF, McLean CA, Cappai R, Duce JA & Bush AI (2012) Tau deficiency induces parkinsonism with dementia by impairing APP-mediated iron export. *Nat Med* 18:291-295.

Leissring MA (2008) The AbetaCs of Abeta-cleaving proteases. *J Biol Chem* 283:29645-29649.

Leite REP, Jacob-Filho W, Saiki M, Grinberg LT & Ferretti REL (2008) Determination of trace elements in human brain tissues using neutron activation analysis. *J Radioanal Nucl Ch* 278:581-584.

LeVine SM (1997) Iron deposits in multiple sclerosis and Alzheimer's disease brains. *Brain Res* 760:298-303.

Lill R, Hoffmann B, Molik S, Pierik AJ, Rietzschel N, Stehling O, Uzarska MA, Webert H, Wilbrecht C & Muhlenhoff U (2012) The role of mitochondria in cellular iron-sulfur protein biogenesis and iron metabolism. *Biochim Biophys Acta* 1823:1491-1508.

Loeffler DA, Sima AA & LeWitt PA (2001) Ceruloplasmin immunoreactivity in neurodegenerative disorders. *Free Radic Res* 35:111-118.

Loeffler DA, Connor JR, Juneau PL, Snyder BS, Kanaley L, DeMaggio AJ, Nguyen H, Brickman CM & LeWitt PA (1995) Transferrin and iron in normal, Alzheimer's disease, and Parkinson's disease brain regions. *Journal of Neurochemistry* 65:710-724.

Lopes KO, Sparks DL & Streit WJ (2008) Microglial dystrophy in the aged and Alzheimer's disease brain is associated with ferritin immunoreactivity. *Glia* 56:1048-1060.

Lovell MA & Markesbery WR (2007) Oxidative DNA damage in mild cognitive impairment and late-stage Alzheimer's disease. *Nucleic Acids Res* 35:7497-7504.

Lovell MA, Ehmann WD, Butler SM & Markesbery WR (1995) Elevated thiobarbituric acid-reactive substances and antioxidant enzyme activity in the brain in Alzheimer's disease. *Neurology* 45:1594-1601.

Lovell MA, Robertson JD, Teesdale WJ, Campbell JL & Markesbery WR (1998) Copper, iron and zinc in Alzheimer's disease senile plaques. *J Neurol Sci* 158:47-52.

Lyubartseva G & Lovell MA (2012) A potential role for zinc alterations in the pathogenesis of Alzheimer's disease. *Biofactors* 38:98-106.

Magaki S, Raghavan R, Mueller C, Oberg KC, Vinters HV & Kirsch WM (2007) Iron, copper, and iron regulatory protein 2 in Alzheimer's disease and related dementias. *Neurosci Lett* 418:72-76.

Mandelkow EM, Stamer K, Vogel R, Thies E & Mandelkow E (2003) Clogging of axons by tau, inhibition of axonal traffic and starvation of synapses. *Neurobiol Aging* 24:1079-1085.

Mangialasche F, Solomon A, Winblad B, Mecocci P & Kivipelto M (2010) Alzheimer's disease: clinical trials and drug development. *Lancet Neurol* 9:702-716.

Mantyh PW, Ghilardi JR, Rogers S, DeMaster E, Allen CJ, Stimson ER & Maggio JE (1993) Aluminum, iron, and zinc ions promote aggregation of physiological concentrations of beta-amyloid peptide. *Journal of Neurochemistry* 61:1171-1174.

Markesbery WR (1997) Oxidative stress hypothesis in Alzheimer's disease. *Free Radic Biol Med* 23:134-147.

Markesbery WR & Lovell MA (1998) Four-hydroxynonenal, a product of lipid peroxidation, is increased in the brain in Alzheimer's disease. *Neurobiol Aging* 19:33-36.

Maynard CJ, Cappai R, Volitakis I, Cherny RA, White AR, Beyreuther K, Masters CL, Bush AI & Li QX (2002) Overexpression of Alzheimer's disease amyloid-beta opposes the age-dependent elevations of brain copper and iron. *J Biol Chem* 277:44670-44676.

McCrea RP, Harder SL, Martin M, Buist R & Nichol H (2008) A comparison of rapid-scanning X-ray fluorescence mapping and magnetic resonance imaging to localize brain iron distribution. *Eur J Radiol* 68:S109-113.

McKhann G, Drachman D, Folstein M, Katzman R, Price D & Stadlan EM (1984) Clinical diagnosis of Alzheimer's disease: report of the NINCDS-ADRDA Work Group under the auspices of Department of Health and Human Services Task Force on Alzheimer's Disease. *Neurology* 34:939-944.

McLachlan CDR, Dalton AJ, Kruck TP, Bell MY, Smith WL, Kalow W & Andrews DF (1991) Intramuscular desferrioxamine in patients with Alzheimer's disease. *Lancet* 337:1304-1308.

Meadowcroft MD, Connor JR, Smith MB & Yang QX (2009) MRI and histological analysis of beta-amyloid plaques in both human Alzheimer's disease and APP/PS1 transgenic mice. *J Magn Reson Imaging* 29:997-1007.

Meadowcroft MD, Peters DG, Dewal RP, Connor JR & Yang QX (2015) The effect of iron in MRI and transverse relaxation of amyloid-beta plaques in Alzheimer's disease. *NMR Biomed* 28:297-305.

Mecocci P, MacGarvey U & Beal MF (1994) Oxidative damage to mitochondrial DNA is increased in Alzheimer's disease. *Ann Neurol* 36:747-751.

Meguro R, Asano Y, Iwatsuki H & Shoumura K (2003) Perfusion-Perls and -Turnbull methods supplemented by DAB intensification for nonheme iron histochemistry: demonstration of the superior sensitivity of the methods in the liver, spleen, and stomach of the rat. *Histochem Cell Biol* 120:73-82.

Meguro R, Asano Y, Odagiri S, Li C, Iwatsuki H & Shoumura K (2007) Nonheme-iron histochemistry for light and electron microscopy: a historical, theoretical and technical review. *Arch Histol Cytol* 70:1-19.

Meunier B, de Visser SP & Shaik S (2004) Mechanism of oxidation reactions catalyzed by cytochrome p450 enzymes. *Chem Rev* 104:3947-3980.

Miller LM, Wang Q, Telivala TP, Smith RJ, Lanzirotti A & Miklossy J (2006) Synchrotron-based infrared and X-ray imaging shows focalized accumulation of Cu and Zn co-localized with beta-amyloid deposits in Alzheimer's disease. *J Struct Biol* 155:30-37.

Miszkiel KA, Paley MN, Wilkinson ID, Hall-Craggs MA, Ordidge R, Kendall BE, Miller RF & Harrison MJ (1997) The measurement of R2, R2* and R2' in HIV-infected patients using the prime sequence as a measure of brain iron deposition. *Magn Reson Imaging* 15:1113-1119.

Mitchell AJ (2009) A meta-analysis of the accuracy of the mini-mental state examination in the detection of dementia and mild cognitive impairment. *J Psychiatr Res* 43:411-431.

Mitchell MD, Kundel HL, Axel L & Joseph PM (1986) Agarose as a tissue equivalent phantom material for NMR imaging. *Magn Reson Imaging* 4:263-266.

Moos T, Rosengren Nielsen T, Skjorringe T & Morgan EH (2007) Iron trafficking inside the brain. *Journal of Neurochemistry* 103:1730-1740.

Morris CM, Candy JM, Oakley AE, Bloxham CA & Edwardson JA (1992) Histochemical distribution of non-haem iron in the human brain. *Acta Anat (Basel)* 144:235-257.

Morris JC (1993) The Clinical Dementia Rating (CDR): current version and scoring rules. *Neurology* 43:2412-2414.

Morris JC, Storandt M, Miller JP, McKeel DW, Price JL, Rubin EH & Berg L (2001) Mild cognitive impairment represents early-stage Alzheimer disease. *Arch Neurol* 58:397-405.

Mottershead JP, Schmierer K, Clemence M, Thornton JS, Scaravilli F, Barker GJ, Tofts PS, Newcombe J, Cuzner ML, Ordidge RJ, McDonald WI & Miller DH (2003) High field MRI correlates of myelin content and axonal density in multiple sclerosis--a post-mortem study of the spinal cord. *J Neurol* 250:1293-1301.

Mullan M, Crawford F, Axelman K, Houlden H, Lilius L, Winblad B & Lannfelt L (1992) A pathogenic mutation for probable Alzheimer's disease in the APP gene at the N-terminus of beta-amyloid. *Nat Genet* 1:345-347.

Nasreddine ZS, Phillips NA, Bedirian V, Charbonneau S, Whitehead V, Collin I, Cummings JL & Chertkow H (2005) The Montreal Cognitive Assessment, MoCA: a brief screening tool for mild cognitive impairment. *J Am Geriatr Soc* 53:695-699.

Netz DJ, Stith CM, Stumpfig M, Kopf G, Vogel D, Genau HM, Stodola JL, Lill R, Burgers PM & Pierik AJ (2012) Eukaryotic DNA polymerases require an iron-sulfur cluster for the formation of active complexes. *Nat Chem Biol* 8:125-132.

Neve RL, Boyce FM, McPhie DL, Greenan J & Oster-Granite ML (1996) Transgenic mice expressing APP-C100 in the brain. *Neurobiol Aging* 17:191-203.

Nilsberth C, Westlind-Danielsson A, Eckman CB, Condron MM, Axelman K, Forsell C, Stenh C, Luthman J, Teplow DB, Younkin SG, Naslund J & Lannfelt L (2001) The 'Arctic' APP mutation (E693G) causes Alzheimer's disease by enhanced Abeta protofibril formation. *Nat Neurosci* 4:887-893.

Nunez MT, Urrutia P, Mena N, Aguirre P, Tapia V & Salazar J (2012) Iron toxicity in neurodegeneration. *Biometals* 25:761-776.

O'Brien RJ & Wong PC (2011) Amyloid precursor protein processing and Alzheimer's disease. *Annu Rev Neurosci* 34:185-204.

Oddo S, Caccamo A, Shepherd JD, Murphy MP, Golde TE, Kayed R, Metherate R, Mattson MP, Akbari Y & LaFerla FM (2003) Triple-transgenic model of Alzheimer's disease

with plaques and tangles: intracellular Abeta and synaptic dysfunction. *Neuron* 39:409-421.

Ogg RJ & Steen RG (1998) Age-related changes in brain T1 are correlated with iron concentration. *Magn Reson Med* 40:749-753.

Ordidge RJ, Gorell JM, Deniau JC, Knight RA & Helpern JA (1994) Assessment of relative brain iron concentrations using T2-weighted and T2*-weighted MRI at 3 Tesla. *Magn Reson Med* 32:335-341.

Pal A, Siotto M, Prasad R & Squitti R (2015) Towards a unified vision of copper involvement in Alzheimer's disease: a review connecting basic, experimental, and clinical research. *J Alzheimers Dis* 44:343-354.

Pankhurst Q, Hautot D, Khan N & Dobson J (2008) Increased levels of magnetic iron compounds in Alzheimer's disease. *J Alzheimers Dis* 13:49-52.

Panza F, Logroscino G, Imbimbo BP & Solfrizzi V (2014) Is there still any hope for amyloid-based immunotherapy for Alzheimer's disease? *Curr Opin Psychiatry* 27:128-137.

Paxinos G & Franklin KB (2001) The Mouse Brain: in Stereotaxic Coordinates; Second Edition.

Perry TL, Hansen S & Gandham SS (1981) Postmortem changes of amino compounds in human and rat brain. *Journal of Neurochemistry* 36:406-410.

Perutz MF (1979) Regulation of oxygen affinity of hemoglobin: influence of structure of the globin on the heme iron. *Annu Rev Biochem* 48:327-386.

Petersen RC (2004) Mild cognitive impairment as a diagnostic entity. *J Intern Med* 256:183-194.

Petersen RC, Roberts RO, Knopman DS, Boeve BF, Geda YE, Ivnik RJ, Smith GE & Jack CR, Jr. (2009) Mild cognitive impairment: ten years later. *Arch Neurol* 66:1447-1455.

Petersen RC, Parisi JE, Dickson DW, Johnson KA, Knopman DS, Boeve BF, Jicha GA, Ivnik RJ, Smith GE, Tangalos EG, Braak H & Kokmen E (2006) Neuropathologic features of amnestic mild cognitive impairment. *Arch Neurol* 63:665-672.

Petroff OA, Ogino T & Alger JR (1988) High-resolution proton magnetic resonance spectroscopy of rabbit brain: regional metabolite levels and postmortem changes. *Journal of Neurochemistry* 51:163-171.

Poon CS & Henkelman RM (1992) Practical T2 quantitation for clinical applications. *J Magn Reson Imaging* 2:541-553.

Pratico D (2008) Evidence of oxidative stress in Alzheimer's disease brain and antioxidant therapy: lights and shadows. *Ann N Y Acad Sci* 1147:70-78.

Prusiner SB, Scott MR, DeArmond SJ & Cohen FE (1998) Prion protein biology. *Cell* 93:337-348.

Puchtler H & Meloan SN (1985) On the chemistry of formaldehyde fixation and its effects on immunohistochemical reactions. *Histochemistry* 82:201-204.

Pujol J, Junque C, Vendrell P, Grau JM, Marti-Vilalta JL, Olive C & Gili J (1992) Biological significance of iron-related magnetic resonance imaging changes in the brain. *Arch Neurol* 49:711-717.

Qin Y, Zhu W, Zhan C, Zhao L, Wang J, Tian Q & Wang W (2011) Investigation on positive correlation of increased brain iron deposition with cognitive impairment in Alzheimer disease by using quantitative MR R2' mapping. *J Huazhong Univ Sci Technolog Med Sci* 31:578-585.

Quintana C (2007) About the presence of hemosiderin in the hippocampus of Alzheimer patients. *J Alzheimers Dis* 12:157-160.

Quintana C, Cowley JM & Marhic C (2004) Electron nanodiffraction and high-resolution electron microscopy studies of the structure and composition of physiological and pathological ferritin. *J Struct Biol* 147:166-178.

Quintana C, Bellefqih S, Laval JY, Guerquin-Kern JL, Wu TD, Avila J, Ferrer I, Arranz R & Patino C (2006) Study of the localization of iron, ferritin, and hemosiderin in Alzheimer's disease hippocampus by analytical microscopy at the subcellular level. *J Struct Biol* 153:42-54.

Ramos P, Santos A, Pinto NR, Mendes R, Magalhaes T & Almeida A (2014) Iron levels in the human brain: a post-mortem study of anatomical region differences and age-related changes. *J Trace Elem Med Biol* 28:13-17.

Rapoport M, Dawson HN, Binder LI, Vitek MP & Ferreira A (2002) Tau is essential to beta -amyloid-induced neurotoxicity. *Proc Natl Acad Sci U S A* 99:6364-6369.

Reddy PH (2011) Abnormal tau, mitochondrial dysfunction, impaired axonal transport of mitochondria, and synaptic deprivation in Alzheimer's disease. *Brain Res* 1415:136-148.

Regland B, Lehmann W, Abedini I, Blennow K, Jonsson M, Karlsson I, Sjogren M, Wallin A, Xilinas M & Gottfries CG (2001) Treatment of Alzheimer's disease with clioquinol. *Dement Geriatr Cogn Disord* 12:408-414.

Religa D, Strozyk D, Cherny RA, Volitakis I, Haroutunian V, Winblad B, Naslund J & Bush AI (2006) Elevated cortical zinc in Alzheimer disease. *Neurology* 67:69-75.

Rissman RA, Trojanowski JQ, Shaw LM & Aisen PS (2012) Longitudinal plasma amyloid beta as a biomarker of Alzheimer's disease. *J Neural Transm* 119:843-850.

Rivera-Mancia S, Perez-Neri I, Rios C, Tristan-Lopez L, Rivera-Espinosa L & Montes S (2010) The transition metals copper and iron in neurodegenerative diseases. *Chem Biol Interact* 186:184-199.

Robson KJH, Lehmann DJ, Wimhurst VLC, Livesey KJ, Combrinck M, Merryweather-Clarke AT, Warden DR & Smith AD (2004) Synergy between the C2 allele of transferrin and the C282Y allele of the haemochromatosis gene (HFE) as risk factors for developing Alzheimer's disease. *J Med Genet* 41:261-265.

Rodrigue KM, Haacke EM & Raz N (2011) Differential effects of age and history of hypertension on regional brain volumes and iron. *Neuroimage* 54:750-759.

Rodrigue KM, Daugherty AM, Haacke EM & Raz N (2012) The Role of Hippocampal Iron Concentration and Hippocampal Volume in Age-Related Differences in Memory. *Cereb Cortex*.

Rogers JT, Bush AI, Cho HH, Smith DH, Thomson AM, Friedlich AL, Lahiri DK, Leedman PJ, Huang X & Cahill CM (2008) Iron and the translation of the amyloid precursor protein (APP) and ferritin mRNAs: riboregulation against neural oxidative damage in Alzheimer's disease. *Biochem Soc Trans* 36:1282-1287.

Rogers JT, Randall JD, Cahill CM, Eder PS, Huang X, Gunshin H, Leiter L, McPhee J, Sarang SS, Utsuki T, Greig NH, Lahiri DK, Tanzi RE, Bush AI, Giordano T & Gullans SR (2002) An iron-responsive element type II in the 5'-untranslated region of the Alzheimer's amyloid precursor protein transcript. *J Biol Chem* 277:45518-45528.

Rondeau V, Jacqmin-Gadda H, Commenges D, Helmer C & Dartigues JF (2009) Aluminum and silica in drinking water and the risk of Alzheimer's disease or cognitive decline: findings from 15-year follow-up of the PAQUID cohort. *Am J Epidemiol* 169:489-496.

Rooney WD, Johnson G, Li X, Cohen ER, Kim SG, Ugurbil K & Springer CS, Jr. (2007) Magnetic field and tissue dependencies of human brain longitudinal 1H2O relaxation in vivo. *Magnetic resonance in medicine* 57:308-318.

Rose SE, Chen F, Chalk JB, Zelaya FO, Strugnell WE, Benson M, Semple J & Doddrell DM (2000) Loss of connectivity in Alzheimer's disease: an evaluation of white matter tract integrity with colour coded MR diffusion tensor imaging. *J Neurol Neurosurg Psychiatry* 69:528-530.

Rosen WG, Mohs RC & Davis KL (1984) A new rating scale for Alzheimer's disease. *Am J Psychiatry* 141:1356-1364.

Ross CA & Poirier MA (2004) Protein aggregation and neurodegenerative disease. *Nat Med* 10 Suppl:S10-17.

Rottkamp CA, Raina AK, Zhu X, Gaier E, Bush AI, Atwood CS, Chevion M, Perry G & Smith MA (2001) Redox-active iron mediates amyloid-beta toxicity. *Free Radic Biol Med* 30:447-450.

Rouault TA (2001) Systemic iron metabolism: a review and implications for brain iron metabolism. *Pediatr Neurol* 25:130-137.

Saito N, Sakai O, Ozonoff A & Jara H (2009) Relaxo-volumetric multispectral quantitative magnetic resonance imaging of the brain over the human lifespan: global and regional aging patterns. *Magn Reson Imaging* 27:895-906.

Sayre LM, Perry G, Harris PL, Liu Y, Schubert KA & Smith MA (2000) In situ oxidative catalysis by neurofibrillary tangles and senile plaques in Alzheimer's disease: a central role for bound transition metals. *Journal of Neurochemistry* 74:270-279.

Scahill RI, Frost C, Jenkins R, Whitwell JL, Rossor MN & Fox NC (2003) A longitudinal study of brain volume changes in normal aging using serial registered magnetic resonance imaging. *Arch Neurol* 60:989-994.

Scheltens P, Barkhof F, Leys D, Wolters EC, Ravid R & Kamphorst W (1995) Histopathologic correlates of white matter changes on MRI in Alzheimer's disease and normal aging. *Neurology* 45:883-888.

Schenck JF (2003) Magnetic resonance imaging of brain iron. *J Neurol Sci* 207:99-102.

Schenck JF, Zimmerman EA, Li Z, Adak S, Saha A, Tandon R, Fish KM, Belden C, Gillen RW, Barba A, Henderson DL, Neil W & O'Keefe T (2006) High-field magnetic resonance imaging of brain iron in Alzheimer disease. *Top Magn Reson Imaging* 17:41-50.

Schenker C, Meier D, Wichmann W, Boesiger P & Valavanis A (1993) Age distribution and iron dependency of the T2 relaxation time in the globus pallidus and putamen. *Neuroradiology* 35:119-124.

Scherzinger E, Lurz R, Turmaine M, Mangiarini L, Hollenbach B, Hasenbank R, Bates GP, Davies SW, Lehrach H & Wanker EE (1997) Huntingtin-encoded polyglutamine expansions form amyloid-like protein aggregates in vitro and in vivo. *Cell* 90:549-558.

Scheuner D *et al.* (1996) Secreted amyloid beta-protein similar to that in the senile plaques of Alzheimer's disease is increased in vivo by the presenilin 1 and 2 and APP mutations linked to familial Alzheimer's disease. *Nat Med* 2:864-870.

Scheurer E, Ith M, Dietrich D, Kreis R, Husler J, Dirnhofer R & Boesch C (2005) Statistical evaluation of time-dependent metabolite concentrations: estimation of post-mortem intervals based on in situ 1H-MRS of the brain. *NMR Biomed* 18:163-172.

Schipper HM, Cisse S & Stopa EG (1995) Expression of heme oxygenase-1 in the senescent and Alzheimer-diseased brain. *Ann Neurol* 37:758-768.

Schmierer K, Scaravilli F, Altmann DR, Barker GJ & Miller DH (2004) Magnetization transfer ratio and myelin in postmortem multiple sclerosis brain. *Ann Neurol* 56:407-415.

Schmierer K, Tozer DJ, Scaravilli F, Altmann DR, Barker GJ, Tofts PS & Miller DH (2007) Quantitative magnetization transfer imaging in postmortem multiple sclerosis brain. *J Magn Reson Imaging* 26:41-51.

Schneider G, Fries P, Wagner-Jochem D, Thome D, Laurer H, Kramann B, Mautes A & Hagen T (2002) Pathophysiological changes after traumatic brain injury: comparison of two experimental animal models by means of MRI. *Magma* 14:233-241.

Schneider LS, Mangialasche F, Andreasen N, Feldman H, Giacobini E, Jones R, Mantua V, Mecocci P, Pani L, Winblad B & Kivipelto M (2014) Clinical trials and late-stage drug development for Alzheimer's disease: an appraisal from 1984 to 2014. *J Intern Med* 275:251-283.

Schrag M, Mueller C, Oyoyo U, Smith MA & Kirsch WM (2011) Iron, zinc and copper in the Alzheimer's disease brain: a quantitative meta-analysis. Some insight on the influence of citation bias on scientific opinion. *Prog Neurobiol* 94:296-306.

Schrag M, Dickson A, Jiffry A, Kirsch D, Vinters HV & Kirsch W (2010) The effect of formalin fixation on the levels of brain transition metals in archived samples. *Biometals* 23:1123-1127.

Selkoe DJ (2004) Cell biology of protein misfolding: the examples of Alzheimer's and Parkinson's diseases. *Nat Cell Biol* 6:1054-1061.

Serrano-Pozo A, Frosch MP, Masliah E & Hyman BT (2011) Neuropathological alterations in Alzheimer disease. *Cold Spring Harb Perspect Med* 1:a006189.

Shachar DB, Kahana N, Kampel V, Warshawsky A & Youdim MBH (2004) Neuroprotection by a novel brain permeable iron chelator, VK-28, against 6-hydroxydopamine lession in rats. *Neuropharmacology* 46:254-263.

Shaw LM, Vanderstichele H, Knapik-Czajka M, Clark CM, Aisen PS, Petersen RC, Blennow K, Soares H, Simon A, Lewczuk P, Dean R, Siemers E, Potter W, Lee VM & Trojanowski JQ (2009) Cerebrospinal fluid biomarker signature in Alzheimer's disease neuroimaging initiative subjects. *Ann Neurol* 65:403-413.

Sheehan JP, Swerdlow RH, Miller SW, Davis RE, Parks JK, Parker WD & Tuttle JB (1997) Calcium homeostasis and reactive oxygen species production in cells transformed by mitochondria from individuals with sporadic Alzheimer's disease. *J Neurosci* 17:4612-4622.

Shepherd TM, Flint JJ, Thelwall PE, Stanisz GJ, Mareci TH, Yachnis AT & Blackband SJ (2009) Postmortem interval alters the water relaxation and diffusion properties of rat nervous tissue--implications for MRI studies of human autopsy samples. *Neuroimage* 44:820-826.

Silvestri L & Camaschella C (2008) A potential pathogenetic role of iron in Alzheimer's disease. *J Cell Mol Med* 12:1548-1550.

Silvestri L, Pagani A & Camaschella C (2008) Furin-mediated release of soluble hemojuvelin: a new link between hypoxia and iron homeostasis. *Blood* 111:924-931.

Sironi L, Guerrini U, Tremoli E, Miller I, Gelosa P, Lascialfari A, Zucca I, Eberini I, Gemeiner M, Paoletti R & Gianazza E (2004) Analysis of pathological events at the onset of brain damage in stroke-prone rats: a proteomics and magnetic resonance imaging approach. *J Neurosci Res* 78:115-122.

Sloot WN, van der Sluijs-Gelling AJ & Gramsbergen JB (1994) Selective lesions by manganese and extensive damage by iron after injection into rat striatum or hippocampus. *Journal of Neurochemistry* 62:205-216.

Smith MA, Harris PL, Sayre LM & Perry G (1997) Iron accumulation in Alzheimer disease is a source of redox-generated free radicals. *Proc Natl Acad Sci U S A* 94:9866-9868.

Smith MA, Kutty RK, Richey PL, Yan SD, Stern D, Chader GJ, Wiggert B, Petersen RB & Perry G (1994) Heme Oxygenase-1 Is Associated with the Neurofibrillary Pathology of Alzheimers-Disease. *American Journal of Pathology* 145:42-47.

Smith MA, Zhu X, Tabaton M, Liu G, McKeel DW, Jr., Cohen ML, Wang X, Siedlak SL, Dwyer BE, Hayashi T, Nakamura M, Nunomura A & Perry G (2010) Increased iron and free radical generation in preclinical Alzheimer disease and mild cognitive impairment. *J Alzheimers Dis* 19:363-372.

Smith ME, Stapleton JM & Halgren E (1986) Human medial temporal lobe potentials evoked in memory and language tasks. *Electroencephalogr Clin Neurophysiol* 63:145-159.

Snoeyink VL & Jenkins D (1980) Water Chemistry. 266

Somayajulu M, McCarthy S, Hung M, Sikorska M, Borowy-Borowski H & Pandey S (2005) Role of mitochondria in neuronal cell death induced by oxidative stress; neuroprotection by Coenzyme Q10. *Neurobiol Dis* 18:618-627.

Sperling RA *et al.* (2011) Toward defining the preclinical stages of Alzheimer's disease: recommendations from the National Institute on Aging-Alzheimer's Association workgroups on diagnostic guidelines for Alzheimer's disease. *Alzheimers Dement* 7:280-292.

Spillantini MG, Crowther RA, Jakes R, Hasegawa M & Goedert M (1998) alpha-Synuclein in filamentous inclusions of Lewy bodies from Parkinson's disease and dementia with lewy bodies. *Proc Natl Acad Sci U S A* 95:6469-6473.

Squitti R, Cassetta E, Dal Forno G, Lupoi D, Lippolis G, Pauri F, Vernieri F, Cappa A & Rossini PM (2004) Copper perturbation in 2 monozygotic twins discordant for degree of cognitive impairment. *Arch Neurol* 61:738-743.

Squitti R, Lupoi D, Pasqualetti P, Dal Forno G, Vernieri F, Chiovenda P, Rossi L, Cortesi M, Cassetta E & Rossini PM (2002) Elevation of serum copper levels in Alzheimer's disease. *Neurology* 59:1153-1161.

Steen RG, Gronemeyer SA & Taylor JS (1995) Age-related changes in proton T1 values of normal human brain. *J Magn Reson Imaging* 5:43-48.

Stuber C, Morawski M, Schafer A, Labadie C, Wahnert M, Leuze C, Streicher M, Barapatre N, Reimann K, Geyer S, Spemann D & Turner R (2014) Myelin and iron concentration in the human brain: A quantitative study of MRI contrast. *Neuroimage* 93 Pt 1:95-106.

Su JH, Deng G & Cotman CW (1997) Bax protein expression is increased in Alzheimer's brain: correlations with DNA damage, Bcl-2 expression, and brain pathology. *J Neuropathol Exp Neurol* 56:86-93.

Subbarao KV, Richardson JS & Ang LC (1990) Autopsy samples of Alzheimer's cortex show increased peroxidation in vitro. *Journal of Neurochemistry* 55:342-345.

Tao Y, Wang Y, Rogers JT & Wang F (2014) Perturbed iron distribution in Alzheimer's disease serum, cerebrospinal fluid, and selected brain regions: a systematic review and meta-analysis. *J Alzheimers Dis* 42:679-690.

Terry RD, Masliah E, Salmon DP, Butters N, DeTeresa R, Hill R, Hansen LA & Katzman R (1991) Physical basis of cognitive alterations in Alzheimer's disease: synapse loss is the major correlate of cognitive impairment. *Ann Neurol* 30:572-580.

Theil EC (1990) Regulation of ferritin and transferrin receptor mRNAs. *J Biol Chem* 265:4771-4774.

Theil EC (2011) Ferritin protein nanocages use ion channels, catalytic sites, and nucleation channels to manage iron/oxygen chemistry. *Curr Opin Chem Biol* 15:304-311.

Thinakaran G & Koo EH (2008) Amyloid precursor protein trafficking, processing, and function. *J Biol Chem* 283:29615-29619.

Thompson SM, Craven RA, Nirmalan NJ, Harnden P, Selby PJ & Banks RE (2013) Impact of pre-analytical factors on the proteomic analysis of formalin-fixed paraffin-embedded tissue. *Proteomics Clin Appl* 7:241-251.

Thomson AM, Rogers JT & Leedman PJ (1999) Iron-regulatory proteins, iron-responsive elements and ferritin mRNA translation. *Int J Biochem Cell Biol* 31:1139-1152.

Todorich B, Pasquini JM, Garcia CI, Paez PM & Connor JR (2009) Oligodendrocytes and myelination: the role of iron. *Glia* 57:467-478.

Tokuhiro T, Appleby A, Leghrouz A, Metcalf R & Tokarz R (1996) Proton spin-lattice relaxation of water molecules in ferrous–ferric/agarose gel system. *J Chem Phys* 105:3761-3769.

Tokutake S, Nagase H, Morisaki S & Oyanagi S (1995) Aluminium detected in senile plaques and neurofibrillary tangles is contained in lipofuscin granules with silicon, probably as aluminosilicate. *Neurosci Lett* 185:99-102.

Tovi M & Ericsson A (1992) Measurements of T1 and T2 over time in formalin-fixed human whole-brain specimens. *Acta Radiol* 33:400-404.

Treusch S, Cyr DM & Lindquist S (2009) Amyloid deposits: protection against toxic protein species? *Cell Cycle* 8:1668-1674.

Triggs WJ & Willmore LJ (1984) In vivo lipid peroxidation in rat brain following intracortical Fe2+ injection. *Journal of Neurochemistry* 42:976-980.

Urrutia P, Aguirre P, Esparza A, Tapia V, Mena NP, Arredondo M, Gonzalez-Billault C & Nunez MT (2013) Inflammation alters the expression of DMT1, FPN1 and hepcidin, and it causes iron accumulation in central nervous system cells. *Journal of Neurochemistry* 126:541-549.

van Duijn S, Nabuurs RJ, van Duinen SG & Natte R (2013) Comparison of histological techniques to visualize iron in paraffin-embedded brain tissue of patients with Alzheimer's disease. *J Histochem Cytochem* 61:785-792.

Van Hoesen GW, Hyman BT & Damasio AR (1991) Entorhinal cortex pathology in Alzheimer's disease. *Hippocampus* 1:1-8.

Vanhoutte G, Dewachter I, Borghgraef P, Van Leuven F & Van der Linden A (2005) Noninvasive in vivo MRI detection of neuritic plaques associated with iron in APP[V717I] transgenic mice, a model for Alzheimer's disease. *Magn Reson Med* 53:607-613.

Vassar R (2004) BACE1: the beta-secretase enzyme in Alzheimer's disease. *J Mol Neurosci* 23:105-114.

Vassiliev V, Harris ZL & Zatta P (2005) Ceruloplasmin in neurodegenerative diseases. *Brain Res Brain Res Rev* 49:633-640.

Vidal R, Miravalle L, Gao X, Barbeito AG, Baraibar MA, Hekmatyar SK, Widel M, Bansal N, Delisle MB & Ghetti B (2008) Expression of a mutant form of the ferritin light chain

gene induces neurodegeneration and iron overload in transgenic mice. *J Neurosci* 28:60-67.

von Bernhardi R, Tichauer JE & Eugenin J (2010) Aging-dependent changes of microglial cells and their relevance for neurodegenerative disorders. *Journal of Neurochemistry* 112:1099-1114.

Vymazal J, Zak O, Bulte JW, Aisen P & Brooks RA (1996a) T1 and T2 of ferritin solutions: effect of loading factor. *Magn Reson Med* 36:61-65.

Vymazal J, Brooks RA, Baumgarner C, Tran V, Katz D, Bulte JW, Bauminger R & Di Chiro G (1996b) The relation between brain iron and NMR relaxation times: an in vitro study. *Magn Reson Med* 35:56-61.

Wallis LI, Paley MN, Graham JM, Grunewald RA, Wignall EL, Joy HM & Griffiths PD (2008) MRI assessment of basal ganglia iron deposition in Parkinson's disease. *J Magn Reson Imaging* 28:1061-1067.

Wang J, Markesbery WR & Lovell MA (2006) Increased oxidative damage in nuclear and mitochondrial DNA in mild cognitive impairment. *Journal of Neurochemistry* 96:825-832.

Ward RJ, Zucca FA, Duyn JH, Crichton RR & Zecca L (2014) The role of iron in brain ageing and neurodegenerative disorders. *Lancet Neurol* 13:1045-1060.

Watt NT, Whitehouse IJ & Hooper NM (2010) The role of zinc in Alzheimer's disease. *Int J Alzheimers Dis* 2011:971021.

Weisskopf MG, Proctor SP, Wright RO, Schwartz J, Spiro A, 3rd, Sparrow D, Nie H & Hu H (2007) Cumulative lead exposure and cognitive performance among elderly men. *Epidemiology* 18:59-66.

Welsh KA, Breitner JC & Magruder-Habib KM (1993) Detection of dementia in the elderly using telephone screening of cognitive status. *Neuropsychiatry Neuropsychol Behav Neurol* 6:103–110.

Wengenack TM, Reyes DA, Curran GL, Borowski BJ, Lin J, Preboske GM, Holasek SS, Gilles EJ, Chamberlain R, Marjanska M, Jack CR, Jr., Garwood M & Poduslo JF (2011) Regional differences in MRI detection of amyloid plaques in AD transgenic mouse brain. *Neuroimage* 54:113-122.

Wharton S & Bowtell R (2012) Fiber orientation-dependent white matter contrast in gradient echo MRI. *Proc Natl Acad Sci U S A* 109:18559-18564.

World Health Organization, (2006) Neurological disorders: public health challenges. 1-232

World Health Organization, (2012) Dementia: a public health priority. 1-112

Willmore LJ, Hiramatsu M, Kochi H & Mori A (1983) Formation of superoxide radicals after FeCl3 injection into rat isocortex. *Brain Res* 277:393-396.

Wood JC (2007) Magnetic resonance imaging measurement of iron overload. *Curr Opin Hematol* 14:183-190.

Wu LJ, Leenders AG, Cooperman S, Meyron-Holtz E, Smith S, Land W, Tsai RY, Berger UV, Sheng ZH & Rouault TA (2004) Expression of the iron transporter ferroportin in synaptic vesicles and the blood-brain barrier. *Brain Res* 1001:108-117.

Xu X, Wang Q & Zhang M (2008) Age, gender, and hemispheric differences in iron deposition in the human brain: an in vivo MRI study. *Neuroimage* 40:35-42.

Yamamoto A, Shin RW, Hasegawa K, Naiki H, Sato H, Yoshimasu F & Kitamoto T (2002) Iron (III) induces aggregation of hyperphosphorylated tau and its reduction to iron (II) reverses the aggregation: implications in the formation of neurofibrillary tangles of Alzheimer's disease. *Journal of Neurochemistry* 82:1137-1147.

Yao B, Li TQ, Gelderen P, Shmueli K, de Zwart JA & Duyn JH (2009) Susceptibility contrast in high field MRI of human brain as a function of tissue iron content. *Neuroimage* 44:1259-1266.

Yassin MS, Ekblom J, Xilinas M, Gottfries CG & Oreland L (2000) Changes in uptake of vitamin B(12) and trace metals in brains of mice treated with clioquinol. *J Neurol Sci* 173:40-44.

Youdim MB, Fridkin M & Zheng H (2005) Bifunctional drug derivatives of MAO-B inhibitor rasagiline and iron chelator VK-28 as a more effective approach to treatment of brain ageing and ageing neurodegenerative diseases. *Mech Ageing Dev* 126:317-326.

Zecca L, Youdim MB, Riederer P, Connor JR & Crichton RR (2004) Iron, brain ageing and neurodegenerative disorders. *Nat Rev Neurosci* 5:863-873.

Zetterberg H, Wilson D, Andreasson U, Minthon L, Blennow K, Randall J & Hansson O (2013) Plasma tau levels in Alzheimer's disease. *Alzheimers Res Ther* 5:9.

Zheng W, Nichol H, Liu S, Cheng YC & Haacke EM (2013) Measuring iron in the brain using quantitative susceptibility mapping and X-ray fluorescence imaging. *Neuroimage* 78C:68-74.